Anisotropic spinrelaxation in graphene

Dissertation
zur Erlangung des Doktorgrades der Naturwissenschaften
(Dr. rer. nat.)
der Fakultät für Physik
an der Universität Regensburg

vorgelegt von
Sebastian Johannes Ringer
aus Geretsried

2018

Promotionsgesuch eingereicht am: 10. Mai 2011
Die Arbeit wurde angeleitet von: Prof. Dr. Dieter Weiss

Prüfungsausschuss:

Vorsitzende: Prof. Dr. Jaroslav Fabian
1. Gutachter: Prof. Dr. Dieter Weiss
2. Gutachter: Prof. Dr. Günther Bayreuther
weiterer Prüfer: Prof. Dr. Rupert Huber

Termin Promotionskolloquium: 23. Juli 2018

Contents

Chapter 1

Introduction

The technological advances of the past decades have largely been driven by the continuous rapid increase in power of micro processors. This was achieved through miniaturization and is described by Moore's law, which states that the number of transistors in a dense integrated circuit doubles approximately every two years [1]. However, structure sizes are approaching dimensions where in the not too distant future of 10 years, transistors based on silicon will face fundamental physical obstacles that make further miniaturization increasingly difficult if not impossible [2]. To continue the advance in microprocessor technology then requires a different approach.

One possibility is to replace silicon with a different material that has better electric properties. Graphene, a one atom thick sheet of graphite, is a potential candidate [3]. Like a semiconductor, its conductance can be manipulated by the field effect which is needed to build transistors. The improvement it offers over silicon is a much higher conductivity and charge carrier mobility, leading to faster switching circuitry that needs less power.

Another approach to advance microprocessor technology is to develop new ways to build logic circuits. Spintronics, which is a blend of the words spin and electronics, expands electronics from using only the charge of the electron to also utilizing its spin property [4]. So far, spintronic devices have only been used for data storage, but concepts exist for also building spin based logic circuitry [5–7]. As these work with magnetic switches that don't need a constant charge refresh to keep their state, a device utilizing them would need no boot time and use considerably less power.

Spintronic devices have four basic building blocks: spin generation, spin detection, spin transport and spin manipulation. The biggest obstacle for larger scale spintronic circuitry is the spin transport, as electron spin is fragile and short lived. In currently used materials such as Si and GaAs, spin information decays on the length scale of micrometers, which is a severe constriction for device design [8, 9]. Research effort is now directed at getting a better understanding of the spin relaxation in materials, to then be able to design effective countermeasures [10]. While the fundamental processes of spin relaxation are quite well understood, the application to real world conditions are still lacking. The problem is that spin relaxation is not a fixed material parameter but rather a mechanism that is greatly influenced by impurities and the surroundings. The inclusion of these factors into the models is complex and the focus of current research [11–14].

When looking for long spin lifetimes and spin relaxation length, a particular material of interest is graphene [15]. It has similar features to the well known carbon nanotubes, which can be considered as rolled up graphene, but is a lot easier to fabricate. So far, graphene is the most favorable candidate for spin channel material in spin logic applications [15]. As it is also suitable for regular semiconductor electronics, this opens the possibility of hybrid designs on a single material. This powerful combination gives graphene great potential as a candidate to replace silicon in the next generation of microprocessor technology.

However, graphene is also a prime example to demonstrate the limits of the current models of spin relaxation. Based on the spin orbit interaction, which is the basic source for most spin relaxation processes, graphene should have a spin lifetime upwards of 50 ns [16]. This is three orders of magnitude higher than the 100 ps that were actually measured in the first experiments [17]. The difference can be attributed to invasive effects of the contacts, impurities and the substrate. Since then, researchers have been trying to properly model these invasive effects and have been somewhat successful in mitigating them [18]. Although progress has been made, the question which is the dominant spin relaxation mechanism in graphene is still not solved. The motivation to find an answer is high, as that would allow to design effective countermeasures and perform experiments with record breaking spin lifetimes.

The focus of this work is the study of the spin relaxation processes in graphene. Particularly, the experiments focus on a precise measurement of the anisotropy parameter of the spin relaxation, which can be used to identify the different proposed relaxation mechanisms [19, 20]. Several models exist that at least give results for the spin lifetime that match the experiment. What is missing however, is to unambiguously identify a proposed mechanism by also matching its other characteristics like the spin lifetime anisotropy and the energy dependence. So far, what is the limiting factor for the spin lifetime in graphene is still open for debate.

The second part of this work is the report of a newly discovered property of a Co/MgO/graphene tunnel contact, where the spin polarization of the tunnel current can be tuned and even inverted by the applied current bias and back gate voltage. By using this contact in a non-local spin valve geometry, spin transistor action is demonstrated where the transistor is switched on or off by a back gate that controls the spin injection.

Chapter 2

Theoretical Background

2.1 Graphene

Graphite consists of layers of carbon atoms in a hexagonal lattice. If the graphite is so thin that is has just a few of these layers, it is called graphene. The graphene is then differentiated by the number of layers it has and is accordingly called single layer graphene, bilayer graphene, trilayer graphene etc. When it is called just graphene, usually the single layer variant is meant.

The name „graphene“ was coined by Hanns-Peter Boehm *et al.* [21], who were the first to observe it in 1961 [22]. Although graphene has unintentionally been produced over the centuries through the use of pencils, the challenge is to isolate it. Boehm, who had studied chemistry in Regensburg from 1947 to 1951 [23], obtained graphene through the reduction of graphite oxide. He then used a „Siemens Übermikroskop 100 e“, an early commercial TEM, to measure the thickness of the obtained thin carbon films. With the method of graphite oxide reduction, the graphene sheets are first in solution and when placed on a substrate will be crumpled and full of wrinkles. As the article of Boehm *et al.* mostly just stated that atomically thin graphite films exist and are thermodynamically stable (a disputed fact up to that point), it did not gather much attention. What was missing were measurements hinting at the extraordinary properties of this material.

Graphene was then largely forgotten until 2004, when Konstantin Novoselov and Andre Geim published an article in *Science* titled „Electric field effect in atomically thin carbon films“ [24]. They obtained high quality, wrinkle free single layer graphene by mechanical exfoliation (repeated peeling) of a graphite block with scotch tape. Their article demonstrated that graphene has multiple electric properties (2DEG, electric field effect, ballistic transport) that were previously very hard or impossible to obtain in other materials. As their method to fabricate graphene was cheap, reliable and easy to copy, this animated research groups worldwide to also start experimenting with the material. The response in the science community was so huge that K. Novoselov and A. Geim were awarded the 2010 Nobel prize for enabling this development. Since then, the study of graphene has revealed so many record breaking properties that is must be called a wonder material. A review article in *Science* by A. Geim states:

> *Graphene is a wonder material with many superlatives to its name. It is the thinnest known material in the universe and the strongest ever measured. Its charge carriers exhibit giant intrinsic mobility, have zero effective mass, and can travel for micrometers without scattering at room temperature. Graphene can sustain current densities six orders of magnitude higher than that of copper, shows record thermal conductivity and stiffness, is impermeable to gases, and reconciles such conflicting qualities as brittleness and ductility. Electron transport in graphene is described by a Dirac-like equation, which allows the investigation of relativistic quantum phenomena in a benchtop experiment.* [25]

2.1.1 Crystal lattice

The unique properties of graphene arise from its crystal structure. In the hexagonal graphene lattice, each carbon atom is about $a = 1.42$Å from its three neighbors [28]. The ground state electronic configuration of carbon is $1s^2 2s^2 2p^2$, with single electrons in two of the three 2p orbitals and one unoccupied 2p orbital [29]. To form more than two bonds, one of the 2s electrons is promoted to the free 2p orbital, resulting in four unpaired electrons. In graphene, the remaining 2s electron hybridizes with two of the 2p orbitals to form three sp^2 hybrid orbitals. These are located in the graphene plane and form a strong σ bond with each neighbor [30]. The σ bonds are responsible for the

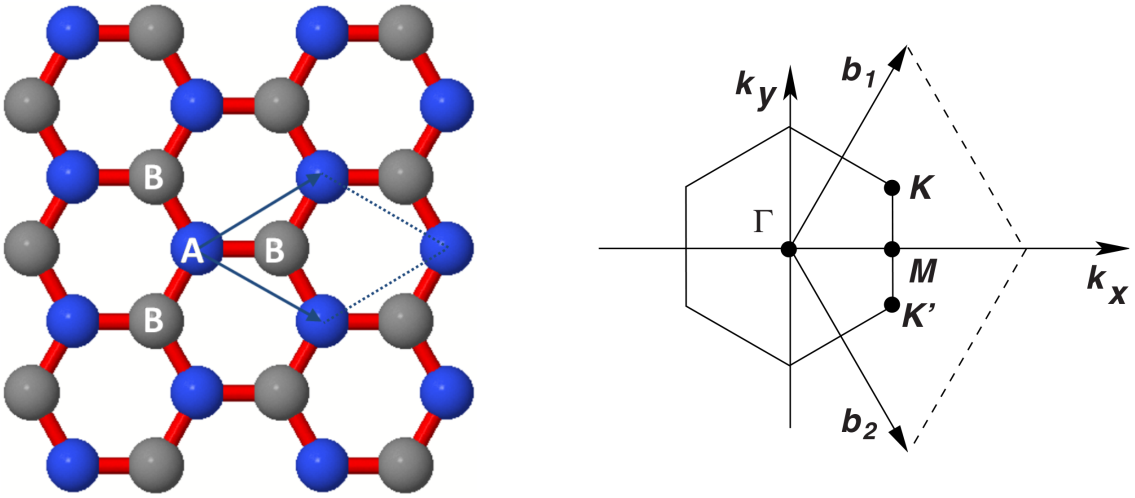

Figure 2.1: Left: Graphene lattice, depicting the diamond shaped unit cell containing two carbon atoms marked A (blue) and B (gray). Adapted from [26]. Right: Brillouin zone of graphene, showing the location of the K and K' points. Adapted from [27].

superb mechanical stability of graphene.
The remaining p orbital is oriented out-of-plane and forms π bonds with its neighbors. Like in benzene rings, these π bonds are delocalised and the resulting electronic band-structure is half filled. The π bonds are responsible for the electric properties of graphene [26].
The honeycomb lattice of graphene can be described as a hexagonal Bravais lattice with a diamond shaped unit cell containing two atoms, as shown in Fig. 2.1. The two atoms are both carbon, but in the lattice their properties are not identical. Each atom forms a sub lattice in the Bravais lattice, named A and B in Fig. 2.1 [29].

2.1.2 Band structure

The π bonds of the carbon atoms hybridize to form π- and $\pi*$-bands. The π-band is the valence band while the $\pi*$-band is the conduction band. They touch only at the K and K' points of the Brillouin zone (see Fig. 2.1), but do not overlap [26]. These points are called Dirac points, because of the unique properties of the band structure in these spots. The existence of two K points arises from the two atoms in the unit cell of the Bravais lattice.
The Fermi level lies at the Dirac point and here the density of states (DOS) is zero. This makes graphene a zero-gap semiconductor. The energy dispersion at the Dirac point and thus at the Fermi level is linear [29]:

$$E_{\pm}(\vec{k}) = \pm v_F \hbar |\vec{k}| \tag{2.1}$$

This formula is valid for both K and K'. The energy E is the difference of energy to the Fermi level, $\vec{k}$ is the wave vector originating from the K or K' point, $\hbar$ is the reduced

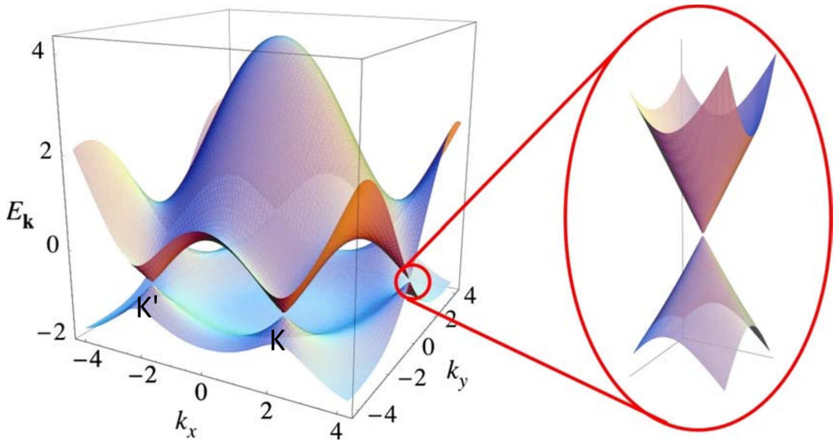

Figure 2.2: Electric dispersion of graphene, with a zoom in of the energy bands close to the Dirac points. Adapted from [27].

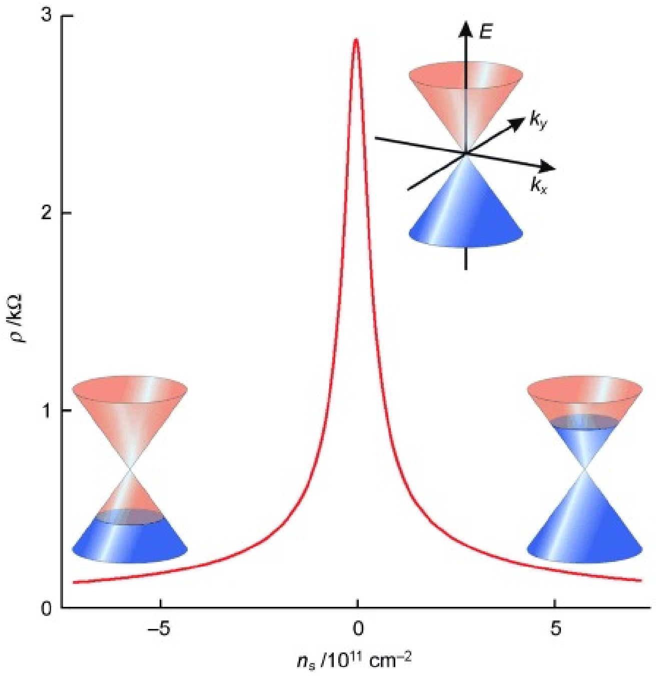

Figure 2.3: Ambipolar field effect in graphene, resulting in the typical Dirac curve of the graphene sheet resistance when changing the charge carrier concentration in graphene with a gate. The sketches of the Dirac cones show the Fermi level and the corresponding charge carrier type. Adapted from [31].

Planck constant and v_F is the Fermi velocity. The full dispersion relation of graphene is depicted in Fig. 2.2, with a zoom of the Dirac cone that is a result of the linear energy dispersion at the Dirac point described by equation 2.1.

A consequence of this linear dispersion relation is that both electrons and holes have a constant velocity that is independent of their energy. As they can not be accelerated by increasing their energy, they have infinite effective mass. The Hamiltonian describing these particles at the Dirac point is equivalent to a Dirac Hamiltonian for massless fermions, with the speed of light substituted by the Fermi velocity in graphene $v_F \approx \frac{c}{300}$ [26]. The word „Dirac point“ was coined by this similarity.

Calculating the DOS for the band structure at the Dirac point reveals a linear energy dependency: [27]

$$\nu(E) = \frac{g_s g_v}{2\pi} \frac{|E|}{\hbar^2 {v_F}^2} \tag{2.2}$$

Here, g_s represents the degeneracy due to the spin degree of freedom and g_v represents the degeneracy due to the valley degree of freedom that arises from the K and K' points. As the field effect can be used to change the charge carrier concentration in graphene, the DOS can easily be observed experimentally. The usual setup for this is to exfoliate graphene on a Si/SiO$_2$ silicon chip, where the SiO$_2$ is the isolating top layer. The Si underneath is highly doped and serves as a back gate. Measuring the graphene sheet resistance while sweeping the back gate will result in the graph shown in Fig. 2.3.

Applying a gate voltage will move the Fermi level up or down in the Dirac cone. The charge carrier concentration n changes accordingly, resulting in a different sheet resistance $R_{sq} = (ne\mu)^{-1}$, where μ is the electron mobility and e the electron charge [32]. When the Fermi level is at the Dirac point, there are very few charge carriers and the resistance is highest. Moving the Fermi level in any direction away from the Dirac point will symmetrically lower the resistance. This measurement can be used to extract the electron mobility μ in graphene.

According to the formula, R_{sq} should be infinity when the Fermi level is at the Dirac point, as there are no states there. However, measurements show that graphene has a minimum conductivity [32, 33], which is referred to as quantum-limited resistivity [29].

2.2 Spin transport in diffusive systems

2.2.1 Spintronic basics - spin and spin valve

Spintronics expands electronics from only using the charge of the electron to also using its spin property [4]. The spin of an electron is a quantum mechanical state that is called „spin“ because its mathematical description has similarities to the angular momentum of a spinning object. To obtain the spin quantum number, the spin vector is compared against a quantization axis. For the electron, this will return „points in the same direction“ (spin up) or „does not point in the same direction“ (spin down). If the quantization axis is inverted, the result will be exactly opposite.

The spin gives electrons a magnetic moment, similar to the magnetic dipole created when an electrically charged object is spinning [34]. As a result of this magnetic dipole, the electron spin interacts with a magnetic field. The spin vector will precess around a magnetic field and over time relax into a parallel (spin up) or antiparallel (spin down) orientation.

Because of this interaction with magnetism, ferromagnets (FM) play a central role in spintronic applications. While in a regular metal (N) the spin of an electron is irrelevant to its conductance, in an FM spin up and spin down experience different electrical resistances [35]. The electric current flowing in a FM is dominated by the spins with the higher conductance, which is called a current spin polarization. Current flowing from a FM to a N material will keep this spin polarization for some time, effectively injecting the spin polarization into the N material [36]. Depending on the FM material, the orientation of the injected spin is either parallel or antiparallel to its magnetization direction. The orientation of the spins injected into N can then be controlled by manipulating the magnetization of the FM.

When it is the other way around and a spin polarized current flows into a FM, the FM acts as a spin detector [36]. The current will have the least resistance if the high conductance spin state in the FM is aligned with the majority spins of the current. By having current flow through two FM in series, this creates a so called spin valve, where the resistance is low for a parallel orientation of the two FM and high for an antiparalell orientation. This is schematically shown in Fig. 2.4. This device utilizes the vector property of the spin, demonstrating the enhanced functionality that spintronics offers over regular electronics.

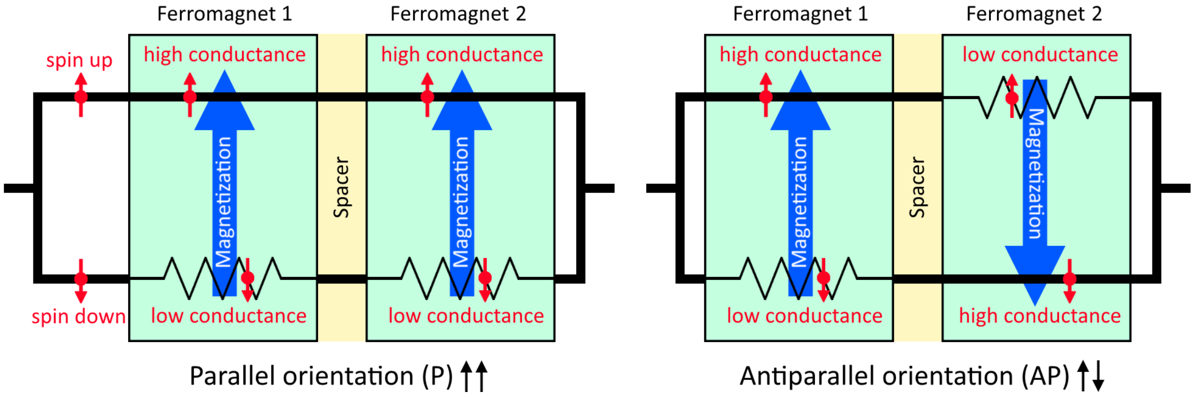

Figure 2.4: Schematic function of a spin valve. In the parallel orientation, the spin up electrons can pass through both ferromagnets unhindered while the spin down electrons experience a high resistance. In the antiparallel orientation, the spin up electrons become spin down electrons and vice versa in the second ferromagnet. Now both spin channels experience a high resistance in one of the magnets and the overall resistance is higher than in the parallel state.

A spin valve is not the only possible spintronic device, but so far it is the most successful one [37]. Several types of spin valves exist. The spin valve depicted in Fig. 2.4 is based on the giant magnetoresistive effect (GMR). Actual devices consist of two thin magnetic layers, separated by a thin nonmagnetic layer. The non-magnetic layer in between is needed to decouple the magnetization of the magnetic layers.

The commercial success of spintronics started with spin valves based on the GMR effect. The GMR effect was discovered in 1988 simultaneously by Albert Fert and Peter Grünberg [38, 39], who were awarded the 2007 nobel Prize for its discovery. A remarkable fact about the GMR effect is that it only took 10 years from the discovery until commercial products were available. Stuart Parkin perfected GMR devices for IBM so they could be used as hyper sensitive magnetic field sensors [37]. These were then used in hard disk read heads, which enabled a huge leap in hard disk storage capacity from 1.6 GB per platter in 1996 (Quantum Fireball ST) to 5.6 GB per platter in 1998 (IBM Deskstar 16GP).

The function of a GMR spin valve device seems simple enough that the question must be asked why this was not discovered sooner. The reason is spin flip processes and spin relaxation. The spin valve effect as depicted in Fig. 2.4 depends on the electrons keeping their spin state between the first and the second FM. Electron spin is generally short-lived and fragile, the time electrons stay in one spin state is usually in the order of pico seconds. Depending on which material is used as a spacer, the two FM need to have a separation of just a few nanometers to still work as a spin valve [37]. For larger distances, the effect is nullified by spin relaxation.

2.2.2 Two current model

In the experiments presented in this work, a spin polarization in graphene is created by spin injection from a FM. The mathematics to describe the related spin phenomena employ a two current model that was established by Mott *et al* [40]. This model is based on the conductance in FMs, where spin up and spin down have a separate density of states (DOS) and can be treated as if flowing in different conductors. The model is valid when the chance of a spin flip during a scattering event is small, so that the coupling between the spin channels is weak.
For the following definitions, the index ↑ signifies spin up while ↓ signifies spin down. The nomenclature is according to J. Fabian *et al.* [35].

$$\text{Electron density:} \qquad n = n_\uparrow + n_\downarrow \tag{2.3}$$

$$\text{Spin density:} \qquad s = n_\uparrow - n_\downarrow \tag{2.4}$$

$$\text{Density polarization:} \qquad P_n = \frac{n_\uparrow - n_\downarrow}{n_\uparrow + n_\downarrow} = \frac{s}{n} \tag{2.5}$$

The spin density s is defined as the difference between spin up and spin down electron density, it is the density of spins that have no counterpart. The density polarization P_n describes the fraction of electrons that have a spin without counterpart. When the term 'spin' is used as in „spin is injected into graphene“, what is meant by 'spin' is the parameter s of electrons at the Fermi level. When it is further stated that „the injected spins create a spin polarization in graphene“, the term 'spin polarization' refers to the parameter P_n of electrons at the Fermi level in graphene.
As spin is a vector, the question must be asked how that is represented in this two current model. In a FM where the spins align parallel or antiparallel to the magnetization, any other orientation of spin gets projected onto this axis. Spins perpendicular to the magnetization are treated as if unpolarized (mapped to 50% spin up + 50% spin down). In an N material where there is no preferred direction for the spin, the spin density is a vector with the three components s_x, s_y and s_z:

$$\vec{s} = \begin{pmatrix} s_x \\ s_y \\ s_z \end{pmatrix} \tag{2.6}$$

A spin density of any orientation is then treated as a linear combination of spin density s_x, s_y and s_z on the x, y and z axis, respectively.

In section 2.2.1 it was stated that the current flowing in a FM is spin polarized. This is because in a FM, the electronic bands for spin up and spin down are shifted relative to each other as shown in Fig. 2.5. As a result, at the Fermi level there is a difference between $n_\uparrow$ and $n_\downarrow$ in equilibrium and current flowing in a FM is spin polarized. The

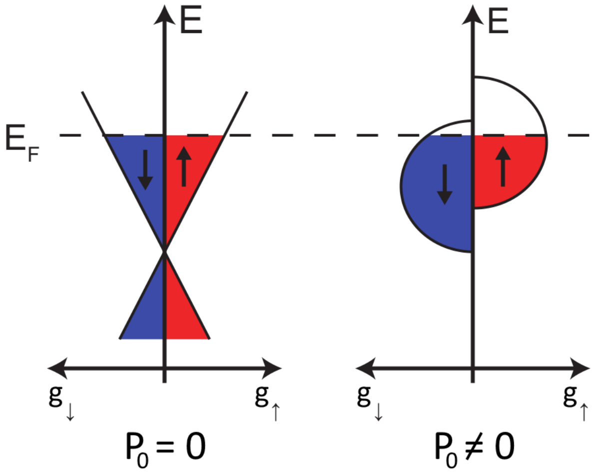

Figure 2.5: DOS at the Fermi level E_F of a nonmagnetic conductor (N, left), in this case n-doped graphene, and a ferromagnetic conductor (FM, right). In N there is an equal number of spin up and spin down electrons in equilibrium. In the FM, the densities are different due to the exchange splitting causing the minima of the two spin bands to be displaced. The spin of the larger electronic density is called majority spin; the spin of the smaller density is called minority spin. However, usually the density of states at the Fermi level is higher for the minority than for the majority electrons. Adapted from [35].

formula for the spin polarization in equilibrium P_0 is then [35]:

$$P_0 = \left| \frac{g_\uparrow - g_\downarrow}{g_\uparrow + g_\downarrow} \right| \tag{2.7}$$

With $g_\uparrow$ and $g_\downarrow$ being the density of states at the Fermi level for spin up and spin down electrons, respectively. Graphene as a nonmagnetic material has the same density of states for spin up and spin down electrons and thus no spin polarization in equilibrium. It should be noted that for the spin polarization in general there is no simple formula, as that is affected by temperature, the electronic band structure, electric fields, chemical potentials, doping, etc [35]. Formula 2.7 for P_0 is a simplification as it lacks a temperature dependence. Some materials like cobalt have an insignificant variation of P_0 with temperature, so for cobalt this formula is quite accurate. Other materials like permalloy have a stronger variation of P_0 with temperature and require a different formula [41].
The difference in conductance for spin up and spin down in a FM also originates from the spin split DOS. In general, the conductivity σ of a material is described by the Einstein relation [35]:

$$\sigma = e^2 D g \tag{2.8}$$

Here, D is the charge carrier diffusion coefficient, e is the electron charge and $g = g_\uparrow + g_\downarrow$ is the density of states at the Fermi level. In a FM where the DOS is spin dependent, σ then needs to be calculated separately for each spin state:

$$\sigma_\uparrow = e^2 D_\uparrow g_\uparrow \qquad , \qquad \sigma_\downarrow = e^2 D_\downarrow g_\downarrow \tag{2.9}$$

The diffusivity D is then also spin dependent.

2.2.3 Spin injection and relaxation

When doing spin injection with a FM/N junction, we seek an answer to the following question:

> *Given the equilibrium spin polarization P_0 in the ferromagnet, what is the spin accumulation in the nonmagnetic conductor if electric current j flows through the junction?*[36]

The word 'spin accumulation' signifies the difference of the spin polarization to the equilibrium state. In the N material this is equivalent to the spin polarization, but 'accumulation' is a better description of the situation.

The spin polarized current coming from the FM creates a spin density s at the N side of the FM/N interface. This spin density propagates in N by drift and diffusion, but is also subject to spin relaxation. The spin polarization in the N material is highest at the FM/N interface, the spin 'accumulates' there. This is shown in Fig. 2.6.

The spin accumulation in N is a static out of equilibrium state that is reached as a balance of spin source and spin drain. The spin source is the current j through the FM/N junction. We discuss a one dimensional model, so the current j is equivalent to the current density. The particle current (density) is then $j/(-e)$. The number of unpaired spins arriving in N per unit of time would then be $j_{s0}/(-e)$, with the spin current [36]:

$$j_{s0} = P_0 j \tag{2.10}$$

This is a rough estimate of what to expect but neglects several things. Spin also accumulates in the FM which increases the junction resistance (spin bottleneck effect) [35]. Depending on the relative electrical resistances of the FM and N region, a spin polarization in the FM might not matter when the resistance of the N region is much higher than the resistance of the FM (conductivity mismatch problem, see section 2.2.5). We also assumed that the spin is conserved when crossing the interface, which is actually a good approximation [35].

Note that $j_{s0} \neq 0$ is achieved for both current directions. When the current flows into the FM this is called spin extraction. The current in the FM is carried by the majority spins at the Fermi level, so these will be the ones that predominantly enter the FM. The minority spins will be left behind in the N, where they are now in the majority as spins of the other type are extracted into the FM.

The spin sinks in N that counteract a spin accumulation from the spin injection are spin diffusion, spin drift and spin relaxation. These are described by the drift diffusion equation for the spin density $s(x,t)$ [35]:

$$\frac{\partial s}{\partial t} = D\frac{\partial^2 s}{\partial x^2} - \mu_e E\frac{\partial s}{\partial x} - \frac{s}{\tau_s} \tag{2.11}$$

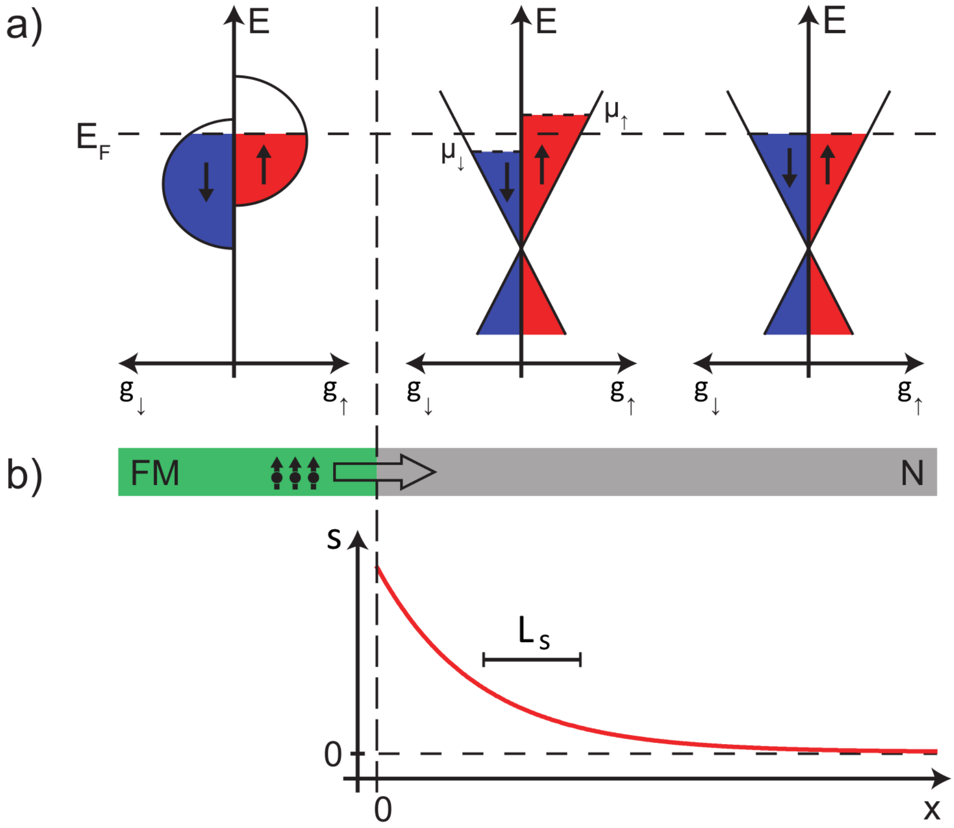

Figure 2.6: (a) Creating a spin accumulation in a non magnetic conductor (N) by means of spin injection from a ferromagnet (FM). Left: Spin dependent DOS of the FM. Middle: DOS of N, in this case n-doped graphene, with a spin accumulation. Right: DOS of N in equilibrium. (b) The spin accumulation $s(x)$ in N decays as a function of the position x with the spin relaxation length L_s. Adapted from [42].

This formula does not account for spin precession and is only valid for $B = 0$. On the right hand side, the first term describes diffusion with the diffusion coefficient D. The second term describes drift with the electron mobility μ_e and the electric field E, the product of which equals the drift velocity v_d. The electron mobility μ_e is written here with index e to avoid confusion with the quasichemical potential μ that will be introduced in the next section. The last term on the right hand side describes spin relaxation with the spin relaxation time τ_s. Note that equation 2.11 is strictly speaking just for the one dimensional case, but under the right circumstances can also be used for 2D or 3D. The experiments in this work use the non-local spin valve geometry that can create a purely diffusive spin current without drift (see section 2.2.6). When the spin accumulation has reached an equilibrium and the system can be considered in a steady state ($\partial s/\partial t = 0$), the equation for the N region is then reduced to [35]:

$$0 = D\frac{\partial^2 s}{\partial x^2} - \frac{s}{\tau_s} \tag{2.12}$$

This is then rearranged to:

$$\frac{\partial^2 s}{\partial x^2} = \frac{s}{D\tau_s} = \frac{s}{{L_s}^2} \tag{2.13}$$

With the spin relaxation length $L_s = \sqrt{D\tau_s}$. Using the boundary condition that the spin density vanishes at infinity $s(\infty) = 0$, the solution for s in the interval of $(0, \infty)$ is then:

$$s(x) = s_{x=0}e^{-x/L_s} \tag{2.14}$$

So the spin accumulation at the FM/N interface $s_{x=0}$ decays in N exponentially and L_s is the length after which the spin density has dropped by a factor of $1/e$. The mechanisms that cause the spin relaxation are discussed in section 2.3.

The influence of the N region on the spin accumulation $s_{x=0}$ can now be calculated by specifying the spin source. We use the non-local geometry as an example, were a spin current $j_{s,nl}$ enters the N region at $x = 0$ only by diffusion [36]:

$$j_{s,nl}(x = 0) = eD\left.\frac{\partial s}{\partial x}\right|_{x=0} \tag{2.15}$$

The differential equation for $j_{s,nl}$ is another boundary condition that must be fulfilled by $s(x)$ and we get:

$$s(x) = \frac{j_{s,nl}}{-e}\frac{L_s}{D}e^{-x/L_s} \tag{2.16}$$

The spin density at $x = 0$ is now

$$s(0) = \frac{j_{s,nl}}{-e}\frac{L_s}{D} \tag{2.17}$$

The spin accumulation at the FM/N interface on the N side is dependent not only on the spin current $j_{s,nl}$ flowing into N but also on the properties of N. The spin accumulation is higher for a long spin relaxation length (slow spin relaxation), while a high diffusivity D lowers the spin accumulation (the spins disperse faster).

2.2.4 Quasichemical potentials

In the model described so far, electrons and therefore spin move through either drift or diffusion. As the result of these two forces is the same (the electron is moving), drift and diffusion can be combined into a single parameter called the quasichemical potential μ. To find out what force is acting on an electron, it is then sufficient to look at the gradient of the quasichemical potential. With the conductivity σ, the electrical current can then be written as [35]:

$$j = \sigma \nabla \mu \tag{2.18}$$

As was already shown in Fig. 2.6, each spin state can have a separate quasichemical potential $\mu_\uparrow$ and $\mu_\downarrow$. The individual spin currents are then:

$$j_\uparrow = \sigma_\uparrow \nabla \mu_\uparrow \tag{2.19}$$

$$j_\downarrow = \sigma_\downarrow \nabla \mu_\downarrow \tag{2.20}$$

For σ and μ, spin dependent parameters can be defined:

$$\sigma = \sigma_\uparrow + \sigma_\downarrow, \qquad \sigma_s = \sigma_\uparrow - \sigma_\downarrow \tag{2.21}$$

$$\mu = \frac{1}{2}(\mu_\uparrow + \mu_\downarrow), \qquad \mu_s = \frac{1}{2}(\mu_\uparrow - \mu_\downarrow) \tag{2.22}$$

As was seen in Fig. 2.6, a spin accumulation leads to $\mu_\uparrow \neq \mu_\downarrow$ and therefore $\mu_s \neq 0$. Because of this, the spin quasichemical potential μ_s is also called a spin accumulation. These definitions can now be used to formulate equations for the charge current j and spin current j_s based on the quasichemical potentials and conductivities [35]:

$$j = j_\uparrow + j_\downarrow = \sigma \nabla \mu + \sigma_s \nabla \mu_s \tag{2.23}$$

$$j_s = j_\uparrow - j_\downarrow = \sigma_s \nabla \mu + \sigma \nabla \mu_s \tag{2.24}$$

These equations allow for an easy description of several situations. In a nonmagnetic conductor $\sigma_s = 0$ (no difference in spin up and spin down conductivities), so j is decoupled from j_s. A spin current j_s is driven only by the gradient of the spin accumulation μ_s and can be present without a charge current j. This is then a pure spin current where spin up electrons move in one direction while an equal number of spin down electrons move in the opposite direction. The spin density is changing without changing the electrical charge.

In a ferromagnet $\sigma_s \neq 0$, the different spin channels have different conductivities. As a consequence of that, a gradient in the spin accumulation μ_s can create an electrical current while a gradient of the quasichemical potential μ can create a spin current.

The relationship between spin density s and spin quasichemical potential μ_s is [35]:

$$\delta s = s - s_0 = 4e\mu_s \frac{g_\uparrow g_\downarrow}{g} \tag{2.25}$$

With s_0 the spin density in equilibrium. As can be seen, the non equilibrium spin density δs is proportional to the spin quasichemical potential μ_s and both can be called a spin accumulation. In a normal conductor where $s_0 = 0$ and $g_\uparrow = g_\downarrow = \frac{1}{2}g$, equation 2.25 can be simplified to $s = e\mu_s g$. This is the number of electron states in the interval of $e\mu_s$ at the Fermi level.

2.2.5 Spin injection efficiency: The conductivity mismatch problem

In section 2.2.3 we have assumed that the spin current j_s entering N at a FM/N junction through spin injection is simply $j_s = P_0 j$, with P_0 the spin polarization of the FM. It was already stated that this omits several effects that are present at a FM/N junction. Using the introduced formalism of quasichemical potentials allows a more accurate description of the problem, which is called the standard model of electrical spin injection [35, 43].
The first addition is to expand the FM/N junction to FM/C/N, to additionally include the contact C at $x = 0$ into the calculation. The generalized current polarization $P_j = j_s/j$ is then modeled using μ and μ_s for each region FM, C and N. To solve the system, it is assumed that P_j must be continuous across the interface [36]:

$$P_j = P_{jFM}(0) = P_{jN}(0) = P_{jC} \tag{2.26}$$

Since the contact region C is defined as a single point at $x = 0$, the quasichemical potential μ is allowed to have a discontinuity there. The current polarization P_j across the interface can then be expressed as a function of the effective resistances R_{FM}, R_C and R_N of the FM, C and N region, respectively, and the conductivity spin polarization $P_{\sigma FM} = \sigma_s/\sigma$ of the FM region and P_Σ of the C region [36]:

$$P_j \equiv \frac{R_{FM}P_{\sigma FM} + R_c P_\Sigma}{R_{FM} + R_c + R_N} = \langle P_\sigma \rangle_R \tag{2.27}$$

This P_j is then called the spin injection efficiency. Qualitatively, P_j is the conductivity spin polarization averaged over the three regions $\langle P_\sigma \rangle$, weighted by the effective resistances.
The conductivity spin polarization P_Σ of the contact is not a material parameter. It would make sense in case of a tunnel contact when there is actually a material between FM and N, but not for a direct FM/N contact. P_Σ must be understood as a parameter depending on both FM and N. The best example would be a tunnel contact, where the tunneling probability according to Fermi's golden rule is proportional to the density of states g on both sides. In the FM $g_\uparrow \neq g_\downarrow$, so the tunneling probability, which is equivalent to the conductivity, is different for spin up and spin down. This difference in conductivity is then expressed by P_Σ.

Equation 2.27 can now be used to explain the conductivity mismatch problem that was first discussed by Schmidt *et al.* [44]. The essence of the problem is that the spin injection efficiency P_j depends on the conductivities (resistances) of the FM and N material.

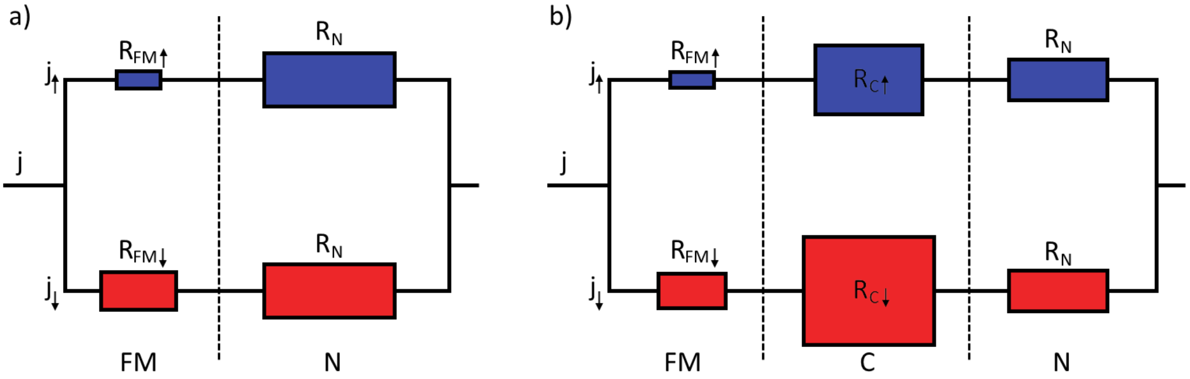

Figure 2.7: The equivalent circuit diagram to explain the conductivity mismatch problem, in a) for a FM/N junction with $R_N > R_{FM}$ and in b) with an additional tunnel barrier R_C. In a) the resistance in both spin channels is dominated by R_N and the resulting spin polarization in N is very low. In b) the resistance is dominated by the spin dependent R_C, resulting in a much better spin polarization in N.

In the case of a direct FM/N contact with low contact resistance, $R_C \ll R_{FM}, R_N$. Equation 2.27 is then reduced to:

$$P_j = \frac{R_{FM}}{R_{FM} + R_N} P_{\sigma FM} \tag{2.28}$$

As can be seen, the injected current P_j retains most of the spin polarization $P_{\sigma FM}$ of the FM if the resistance of the N material R_N is lower or of the same order of magnitude as R_{FM}. In the case of Co as the FM and graphene as N however, $R_N > R_{FM}$ and the spin injection efficiency is severely reduced. The problem is most prominent when spin injection into a semiconductor is attempted ($R_N \gg R_{FM}$).
The conductivity mismatch problem can be reduced or circumvented when the contact resistance is artificially increased, for example by introducing a tunnel barrier. In the case of $R_C \gg R_{FM}, R_N$, equation 2.27 is reduced to:

$$P_j \approx P_\Sigma \tag{2.29}$$

As has been stated before, P_Σ still depends on the FM and N material.

The conductivity mismatch problem can be qualitatively explained by looking at the equivalent circuit diagram in Fig. 2.7. For a direct FM/N contact shown in Fig. 2.7a) with $R_N > R_{FM}$, the resistance in each spin channel is dominated by R_N. The difference in resistance of $R_{FM\uparrow}$ and $R_{FM\downarrow}$ does not change the total resistance much. When a high resistance tunnel contact is inserted between FM and N as shown in Fig. 2.7b), the resistance in each spin channel is dominated by $R_{C\uparrow}$ and $R_{C\downarrow}$. Then the current flowing in N has a much higher spin polarization.

2.2.6 Non-local spin valve geometry: Johnson-Silsbee spin injection experiment

When studying spin transport in a material, the most popular setup to do so is the non-local spin valve geometry shown in Fig. 2.8, established by M. Johnson and R. H. Silsbee [46]. The major benefit of this setup is that it creates a pure spin current that propagates by diffusion, excluding the spurious effects of the charge current in a regular (local) spin valve setup.

The principle of the non-local spin valve geometry is to separate the injector circuit from the detector circuit. The spin channel then needs to have four contacts, two for the injector circuit and two for the detector circuit. In Fig. 2.8, the injector circuit is connected to FM1 and the left end of the N spin channel. When a current is applied to inject spins under FM1, the electric field that causes the electron drift in N is confined to the left side of FM1. The region of N that is to the right of FM1, called the non-local region, is then free of an electric field and electron drift. This is an accurate description when a 2D material like graphene is used as a spin channel. For thicker 3D spin channels, there may still be spurious effects of the injector current in the non-local region [47].

A spin accumulation is created under FM1 by spin injection. Through electron diffusion driven by the quasichemical potential, a pure spin current propagates to the right of FM1 into the non-local region. There is no charge current, as a spin up electron moving in one

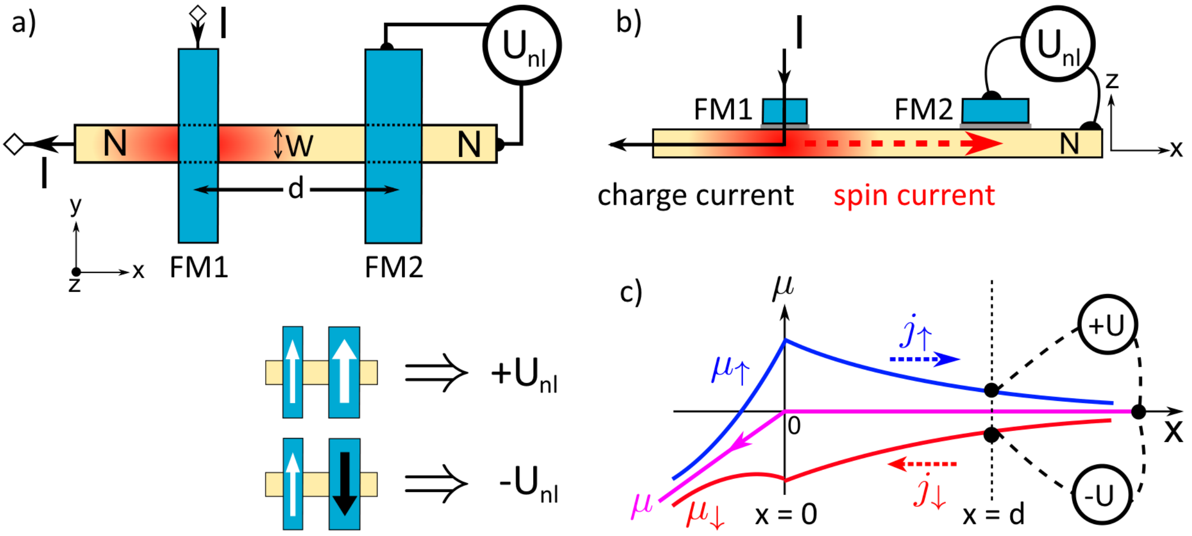

Figure 2.8: Sketch of the lateral non-local spin valve geometry in a) top view and b) side view. A spin accumulation (red) is created under FM1 by spin injection, the charge current I is flowing towards the left end of the spin channel. On the right side of FM1, a pure spin current propagates by diffusion to contact FM2, where it is detected as the non-local voltage U_{nl}. c) Display of the corresponding quasichemical potentials μ, $\mu_\uparrow$ and $\mu_\downarrow$ in the spin channel. For a P orientation of FM1 and FM2 U_{nl} is positive, while for an AP orientation U_{nl} is negative. Adapted from [45].

direction is counterbalanced by a spin down electron moving in the opposite direction. The spin accumulation in the non-local region can be detected by the detector circuit, which consists of FM2 and a non magnetic reference electrode at the right end of the spin channel. Because of the so called „Silsbee-Johnson spin-charge coupling“ [48], a spin accumulation μ_s at the FM2/N interface will result in a non-local voltage U_{nl} proportional to μ_s in the open detector circuit.
With the applied current I_{inj} at the injector circuit, the non-local voltage U_{nl} is then [42]:

$$U_{nl} = \pm I_{inj} \frac{P_{inj} P_{det} R_{sq} L_s}{2W} e^{-d/L_s} \tag{2.30}$$

Here, P_{inj} and P_{det} are the spin injection efficiencies of FM1 and FM2, respectively. $R_{sq} = 1/\sigma$ is the sheet resistance of N, W is the width of the spin channel, d is the distance between the centers of FM1 and FM2 and L_s is the spin relaxation length in N. When reporting experimental results, it is common practice to not state U_{nl} but rather the non-local resistance $R_{nl} = U_{nl}/I_{inj}$.
The '±' in equation 2.30 is for parallel and antiparallel orientation of FM1 and FM2. If the orientation of $\vec{s}$ is not P or AP to the magnetization in FM2, $\vec{s}$ is projected onto that magnetization and the signal strength is reduced accordingly. This happens for instance during Hanle measurements and can be used to probe the orientation of $\vec{s}$.

2.2.7 Spin dynamics: Hanle precession

The standard method to to measure the spin relaxation time τ_s of a spin channel in a non-local spin valve setup is a Hanle measurement, depicted in Fig. 2.9a). Here, a magnetic field $\vec{B}$ is applied perpendicular to the direction of the injected spins, usually the z direction as shown in Fig. 2.9a). The spins then precess around the magnetic field while diffusing from injector to detector. The orientation the spins have when they reach the detector is now dependent on their travel time and the strength of the magnetic field. By performing a magnetic sweep in both P and AP configuration, one obtains the non-local resistance R_{nl} with the characteristic Hanle oscillations as shown in Fig. 2.9c). By fitting the traces, the spin relaxation time τ_s can be extracted.
For a mathematical description of the effect, the diffusion equation for the spin density $\vec{s}$ is expanded to also include spin precession $\vec{s} \times \vec{\omega}$, with the Larmor frequency $\vec{\omega_0} = \gamma \vec{B}$ and the gyromagnetic ratio γ. [35]:

$$\frac{\partial \vec{s}}{\partial t} = \vec{s} \times \vec{\omega} + D \frac{\partial^2 \vec{s}}{\partial x^2} - \frac{\vec{s}}{\tau_s} \tag{2.31}$$

Note that the diffusion equation now needs to be calculated with $\vec{s}$ as a vector, but the equation is still for a 1D model. For the orientation of electrodes and magnetic field as shown in Fig. 2.9a), the solution to this equation that is used to fit the Hanle oscillations is:

$$R_{nl} = \frac{U_{nl}}{I_{inj}} = \pm \frac{P_{inj} P_{det} R_{sq} D}{W} \int_0^\infty dt \frac{1}{\sqrt{4\pi D t}} e^{-d^2/4Dt} e^{-t/\tau_s} \cos(\omega_0 t) \tag{2.32}$$

The „±“ is to account for P or AP alignment of the electrodes. For $B = 0$, this formula is identical to equation 2.30. If the electrodes are not parallel or antiparallel, this solution is not valid.

Formula 2.32 consists of four parts. The prefactor in front of the integral is responsible for the height of the central peak at $B = 0$. If it is sufficient to only extract τ_s, the prefactor can be ignored and the normalized data fitted with a normalized function. The term $\frac{1}{\sqrt{4\pi Dt}}e^{-d^2/4Dt}$ is a (gaussian) probability distribution, which represents the spacial profile of diffusing particles. The term e^{-t/τ_s} is the spin relaxation. The final term $\cos(\omega_0 t)$ is the projection of the spin vector onto the magnetization axis (with $\omega_0 = |\vec{\omega_0}|$), which changes over time because of Larmor precession.

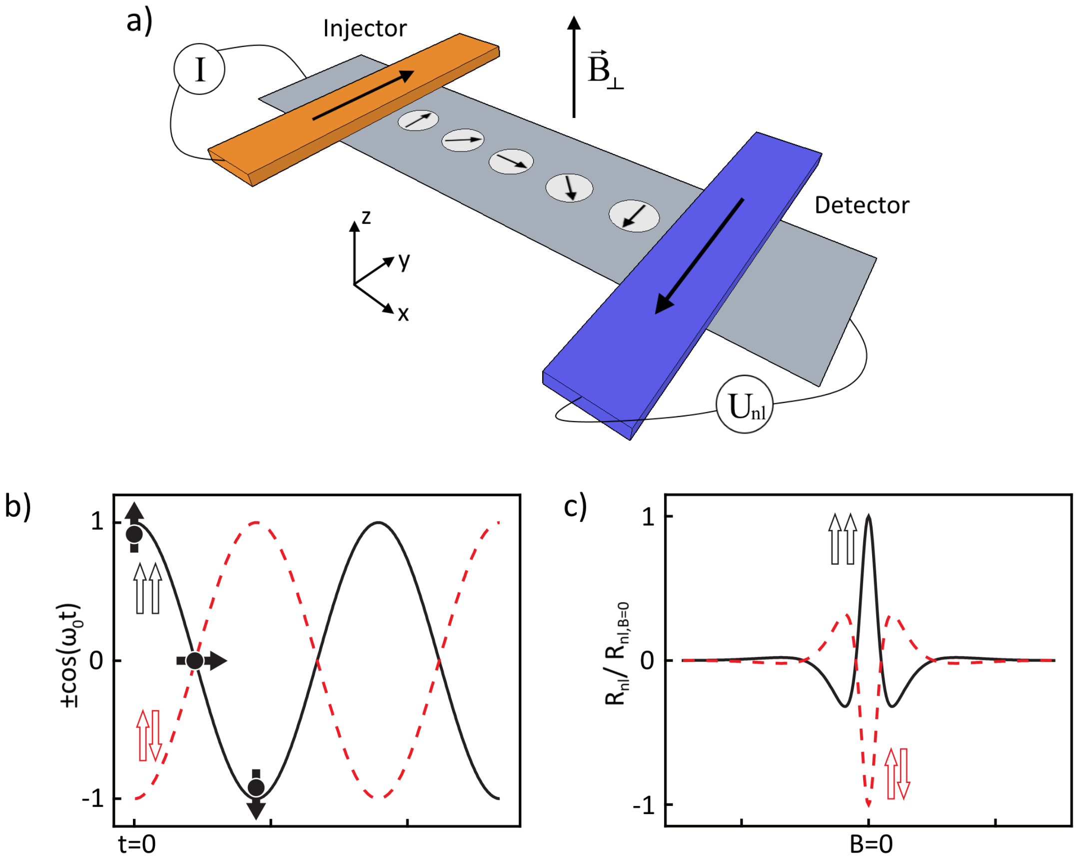

Figure 2.9: a) Sketch of a Hanle measurement in a non-local spin valve geometry. b) Projection of the spin vector onto the magnetization axis which changes over time due to Larmor precession, for P and AP orientation. c) Normalized Hanle oscillations in the non-local resistance R_{nl}, obtained by performing magnet sweeps in P and AP orientation. b) and c) adapted from [42].

2.3 Spin relaxation mechanisms in graphene

Spin-orbit interaction is the source of various spin relaxation and dephasing mechanisms. The interaction is a relativistic effect that results from the electrons moving in the electric field of the positively charged nuclei. In the electron's frame of reference, the nuclei are moving and produce a magnetic field that the electron spin interacts with. The strength of the interaction scales with the charge of the nuclei. For graphene, which is entirely made of carbon atoms, the spin-orbit interaction is very weak compared to other materials as carbon has just six protons [49, 50].

As a result, graphene should have very long spin-lifetimes and would be an ideal candidate for a spin channel in spintronic applications [15, 51]. Based on the spin-orbit interaction, calculations predict a spin lifetime exceeding 50 ns [16]. However, experiments up to now could only measure spin-lifetimes of a few nanoseconds [52–54]. Because of this discrepancy between calculation and experiment, it is apparent that the model the calculation is based on (perfectly flat, defect free graphene in vacuum) is of limited use. Since then, there has been an ongoing discussion of what additional spin relaxation mechanisms exist in graphene that are limiting the measured spin-lifetimes. Several sources for additional spin relaxation in graphene have been proposed [15]: impurities (adatoms) [55], the substrate [56], polymer residues [57–59], ripples[60], resonant magnetic scattering at magnetic impurities [11, 61] and contact induced spin relaxation [62–64].

In a real world sample it is expected to have several of these relaxation mechanisms at once, which increases the difficulty of identifying them. Each mechanism has an associated relaxation rate τ, and they are added to a total spin relaxation rate τ_{total} according to this formula:

$$\frac{1}{\tau_{total}} = \frac{1}{\tau_1} + \frac{1}{\tau_2} + \dots \tag{2.33}$$

To determine which is the dominant effect, experiments focused on finding a correlation between the momentum scattering time τ_p of electrons and their spin relaxation time τ_s [65–67]. This would allow to differentiate between Elliott-Yafet type scattering, where $\tau_s \sim \tau_p$, and Dyakonov-Perel type scattering, where $\tau_s \sim 1/\tau_p$. This approach has so far produced no conclusive results [15].

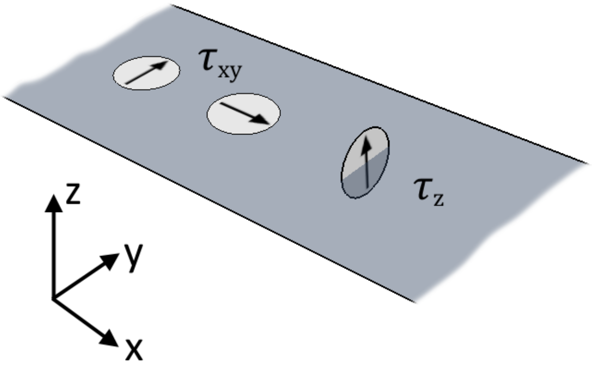

Figure 2.10: In graphene, the relaxation rate of the spins can depend on their orientation. Spins that are oriented in plane experience τ_{xy} while spins oriented out of plane experience τ_z.

Another signature of spin relaxation mechanisms is the anisotropy or isotropy of the spin relaxation time. The out-of-plane spin relaxation time, which we will call τ_z, can be different from the in-plane spin relaxation time, which we will call τ_{xy} (see Fig. 2.10). For convenience, we introduce $\zeta := \frac{\tau_z}{\tau_{xy}}$. If $\zeta = 1$, the spin relaxation is isotropic, while $\zeta \neq 1$ is called anisotropic spin relaxation.

The third characteristic of a spin relaxation mechanism is the dependence on the Fermi energy. Resonant magnetic scattering at magnetic impurities is called resonant because it is enhanced when the Fermi energy is at the resonance energy. Manipulating the Fermi energy with a gate can then be used to map the energy dependence of the spin relaxation time as well as the spin relaxation anisotropy. Observed features then allow a clear attribution to specific relaxation mechanisms.

2.3.1 Pristine graphene: Elliott-Yafet spin relaxation

The spin relaxation based on the intrinsic spin-orbit field of graphene is of the Elliot-Yafet type (see Fig. 2.11) [16]. Spins relax because the electron wave functions normally associated with a given spin have an admixture of the opposite-spin states, due to spin-orbit coupling induced by ions [4]. Then, a spin flip can occur only during a scattering event [68, 69]. As a result, τ_s is then proportional to the momentum scattering time τ_p of electrons. The formula for this mechanism is [16]:

$$\frac{1}{\tau_{xy}} \approx \frac{{\Delta_I}^2}{{\epsilon_F}^2}\frac{1}{\tau_p} \tag{2.34}$$

With the interaction strength parameter Δ_I and the Fermi energy ϵ_F, measured from the band-crossing point. For perfectly flat graphene, this mechanism only relaxes in plane spins (τ_{xy}) and not out of plane spins ($\tau_z \to \infty$) [16], so there is a very strong spin relaxation anisotropy. However, graphene on a real sample is not perfectly flat but corrugated, which reduces this anisotropy. This spin relaxation mechanism is stronger the further the Fermi energy is from the Dirac point. In corrugated graphene, the intrinsic

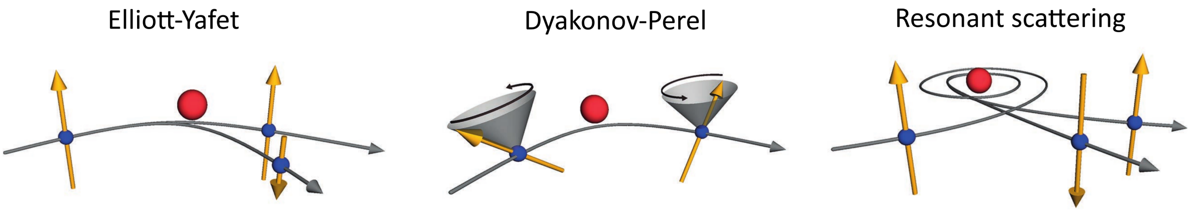

Figure 2.11: Sketch of three possible spin relaxation mechanisms for graphene: Elliott-Yafet, Dyakonov-Perel and resonant scattering by local magnetic moments. The blue dots indicate the electrons/holes with yellow arrows as their spin orientation. The red dots represent the scattering centres. Grey cones with circular arrows represent the spin precession. Adapted from [15].

spin-orbit field will also cause Dyakonov-Perel type spin relaxation.

For the intrinsic spin-orbit field of graphene, experiments have managed to place an upper bound of $\sim 100\,\mu$eV on Δ_I [70], which then leads to the mentioned worst case $\sim$50 ns spin relaxation time (assuming a mobility of $3000\,\mathrm{cm}^2\mathrm{V}^{-1}\mathrm{s}^{-1}$ and a carrier density of $\sim 10^{12}\,\mathrm{cm}^{-2}$). However, the mid-range of theoretical estimates for Δ_I is at $\sim 10\,\mu$eV, resulting in spin-lifetimes exceeding a microsecond [16]. These calculations are the source for the speculated record breaking spin-lifetimes in graphene.

2.3.2 Rashba type spin-orbit fields: Dyakonov-Perel spin relaxation

When graphene is placed on a substrate, this breaks the inversion symmetry and results in Dyakonov-Perel spin relaxation [72]. Ripples in the graphene, adatoms or an electric field induced by a back gate have a similar effect [16]. They induce a Rashba type spin-orbit field that changes locally or is dependent on the movement direction. The electron spins precess in these fields and will flip or eventually dephase (see Fig. 2.11). When scattering, the electrons change direction and the orientation and/or value of the Rashba spin-orbit field changes. The result is a random fluctuation of the field the electrons precess in, which delays spin flip and dephasing. The frequency of the fluctuations correlate with the momentum scattering time, so in this mechanism more

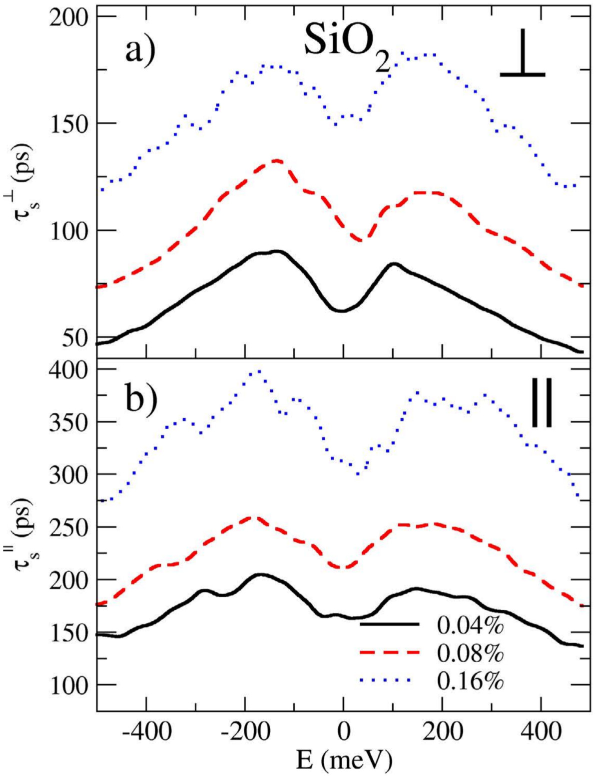

Figure 2.12: Spin-lifetimes calculated by Dinh Van Tuan *et al.* for graphene on SiO$_2$. The different colored traces represent different impurity densities of 0.04% (black solid curves), 0.08% (red dashed curves), and 0.16% (blue dotted curves). Panel a) is calculated for out-of-plane spin orientation while panel b) is calculated for in-plane spin orientation. The anisotropy is $\zeta \approx 0.5$. Adapted from [71].

momentum scattering lowers spin relaxation. This concept is called motional narrowing. The formula for the Dyakonov-Perel mechanism is [16]:

$$\tau_s \approx \frac{\hbar^2}{{\Delta_R}^2 \tau_p} \tag{2.35}$$

with the Rashba spin-orbit coupling strength Δ_R. Although this mechanism does not have an intrinsic energy dependence, the Rashba field can have one. For example, it is common practice to manipulate the Fermi energy in graphene with a gate. This gate induces a Rahsba field that changes strength as the gate voltage is changed, which will appear as an energy dependent spin relaxation when the gate is used to probe different Fermi energies.

Rashba spin-orbit coupling usually not only leads to the Dyakonov-Perel type spin relaxation but also induces Elliott-Yafet type spin relaxation [73]. The Dyakonov-Perel mechanism is still the dominating process, which then leads to the overall $\tau_s \sim 1/\tau_p$ scaling. If the Elliott-Yafet part is sufficiently strong, this will add an energy dependence.

Dinh Van Tuan *et al.* calculated the spin-lifetimes for graphene on SiO_2. The SiO_2 substrate produces a global uniform Rashba field that is superimposed by potential fluctuations because of electron-hole puddles [74]. The resulting spin-lifetimes are shown in Fig. 2.12. As expected for Dyakonov-Perel type spin relaxation, a higher impurity density leads to longer spin-lifetimes. The spin relaxation has an M-shaped energy dependence as well as an anisotropy of $\zeta \approx 0.5$.

2.3.3 Resonant scattering at magnetic impurities

Another relaxation mechanism that can reproduce the order of magnitude of experimentally observed spin-lifetimes is resonant scattering by magnetic impurities [11]. Here, a realistically low concentration of local magnetic moments (vacancies or adatoms) can lead to large spin flip rates, if electrons are at the resonance energy of these scatterers and thus spend more time there (see Fig. 2.11). Fig. 2.13 shows the energy dependence of the mechanism calculated for hydrogen adatoms. There are two resonance peaks (singlet and triplet) that merge to one single peak by temperature broadening and electron-hole puddles, leading to a minimum of τ_s at the resonance energy.

The energy of the resonance is dependent on the type of magnetic moment. A mix of different adatoms and vacancies is possible and would lead to an energy dependence that is broadened over several different peaks. Far from the resonant energy, the scatterers exhibit Elliott-Yafet type spin relaxation. At the resonance energy, the orientation of the spin does not matter and the mechanism exhibits isotropic spin relaxation ($\zeta = 1$). When not at resonance, the anisotropy of the Elliott-Yafet type spin relaxation should be seen ($\zeta > 1$).

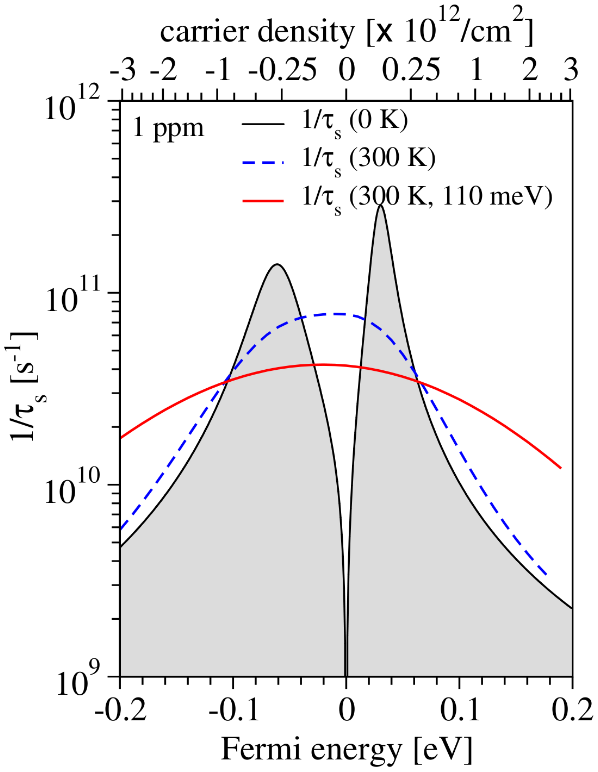

Figure 2.13: Resonant enhancement of spin relaxation in graphene, calculated for 1 ppm of hydrogen adatoms which have two resonances near the Dirac point (Fermi energy = 0). The black trace is for 0 K, the blue trace for 300 K and the red trace is for 300 K with additional broadening by electron-hole puddles with energy fluctuations of 110 meV. Adapted from [11].

2.3.4 Contact induced spin relaxation

This effect is related to the „conductivity mismatch problem“ described in section 2.2.5. As the electrical resistance in the ferromagnetic electrodes is lower than in graphene, the injected spins tend to be backscattered into the electrodes as shown in Fig. 2.14. A high contact resistance reduces the effect, but the resistance values needed to completely eliminate the effect are not feasible for real samples [62]. This effect is inappropriately named as it does not actually relax spins, but it is a spin sink that reduces a spin accumulation in graphene. The name „contact induced spin relaxation“ is used as it is the established nomenclature in the literature.

In section 2.2.5 it was already established that a low contact resistance reduces the spin injection efficiency P. Furthermore, spins backscattering into the contacts will change the trace of a non-local Hanle measurement and result in incorrect fit parameters for τ_s and D. This problem was systematically studied by T. Maassen *et al.* [62]. The magnitude of the problem scales with the contact resistance as well as the sample geometry. The effects are reduced for a large spin channel width W as well as a large injector detector separation d.

To estimate the impact of the contact induced spin relaxation, the parameters R and d are compared with the spin relaxation length L_s. The parameter $R = (R_C/R_{sq})W$, where R_C is the contact resistance and R_{sq} is the graphene sheet resistance, was introduced by Popinciuc *et al.* [75]. The relation of the parameters ${\tau_s}^{fit}$ and D^{fit} obtained from Hanle fitting and the actual values in dependence of R, d, and L_s is displayed in

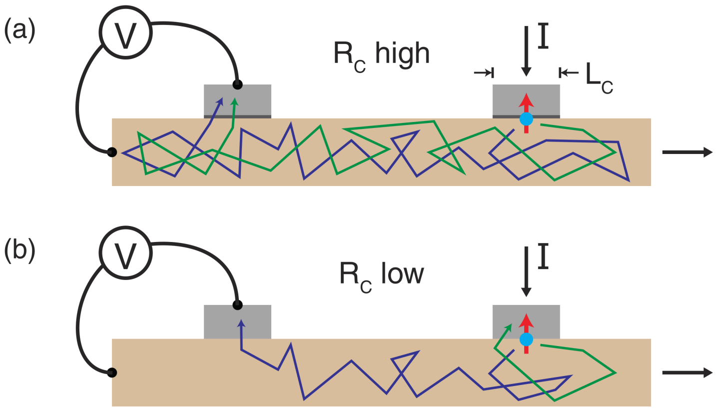

Figure 2.14: Illustration showing the mechanism of contacts acting as spin sinks by spins backscattering into the contact. Depicted is a non-local spin valve, where electrons move in the spin channel by diffusion. In a), a large contact resistance R_C prevents the electrons from quickly entering the contacts. In b), a low R_C leads to the green electron backscattering into the injector contact. Adapted from [62].

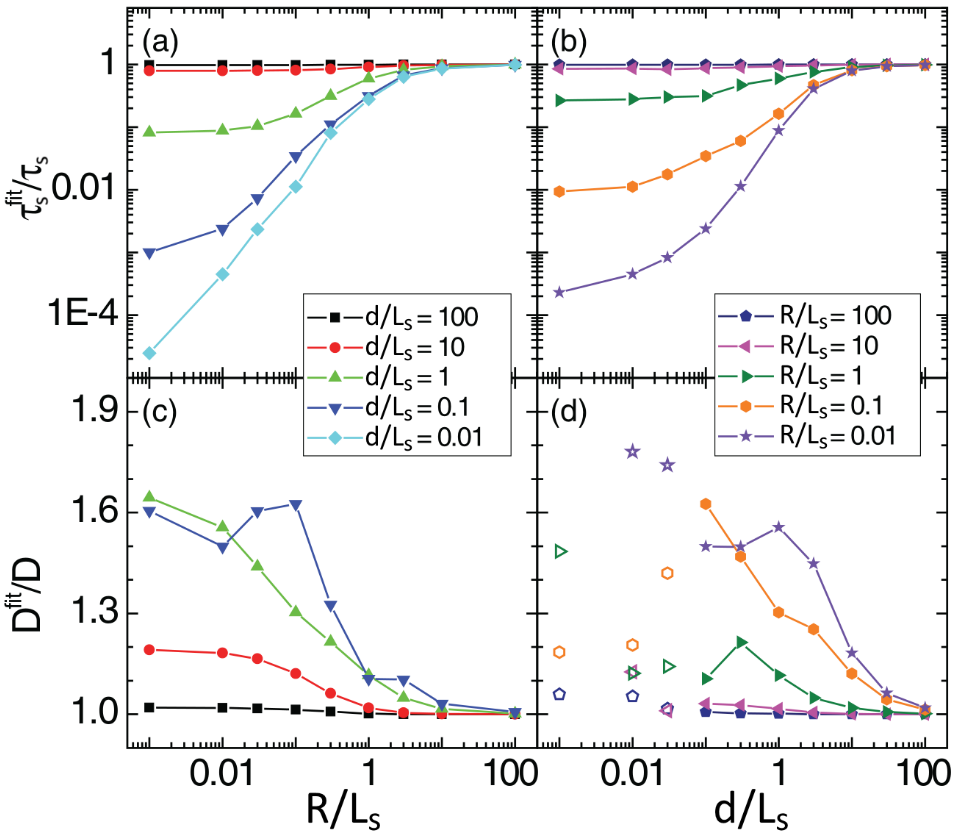

Figure 2.15: The change in ${\tau_s}^{fit}$ and D^{fit} fitted for different d/L_s as a function of R/L_s [(a) and (c)] and for different R/L_s as a function of d/L_s [(b) and (d)]. Adapted from [62].

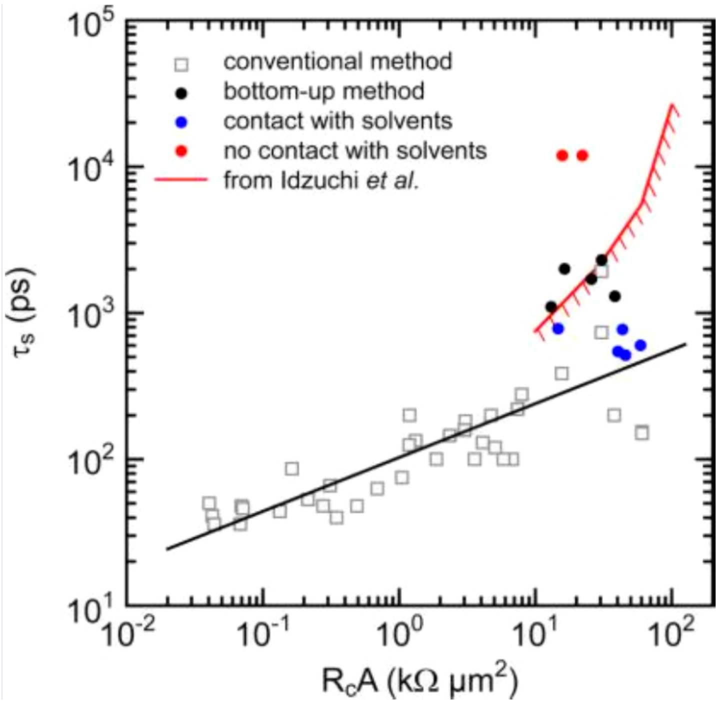

Figure 2.16: Spin lifetime versus contact-resistance-area product of respective injection and detection electrodes at room temperature. The white squares represent samples prepared by the conventional method, where the electrode is directly deposited onto the graphene layer. The colored dots represent samples fabricated with the „bottom up“ method invented by M. Drögeler *et al.* Adapted from [18].

Fig. 2.15.

How much the contact induced spin relaxation is actually limiting τ_s in samples was studied by F. Volmer *et al.* and M. Drögeler *et al.* [18, 52, 57, 63, 64]. For graphene non-local spin valve devices prepared with the conventional method (electrodes directly deposited on graphene), they observed a linear scaling of τ_s with the contact resistance area product $R_C A$ (see Fig. 2.16). This indicates that the contacts are a major obstacle when probing the spin lifetime of graphene with Hanle measurements in a non-local spin valve geometry.

To reduce the invasive nature of the contacts, M. Drögeler *et al.* invented the „bottom up“ fabrication method [52], where the inverted contact stacks are first deposited on a substrate and then a graphene sheet is placed on top. This avoids the problems of growing homogeneous tunnel barriers on graphene (see section 3.5) and keeps the graphene free from contamination by the chemicals needed for lithography processing. In samples prepared by this method, M. Drögeler *et al.* have been able to measure spin-lifetimes exceeding 12 ns, which is so far the highest reported value [18].

As the „bottom up“ fabrication method also features much cleaner hBN encapsulated graphene, it is unclear if the improvements in τ_s are only attributed to less invasive contacts. The scaling of the 'conventional method' data points (white squares) in Fig. 2.16 does not *show* a saturation, but a saturation might still be reached at the highest $R_C A$ values. It then remains an open question if the spin sink behavior of the contacts in the conventional sample design can be sufficiently reduced by high $R_C A$ contacts.

The conclusion of the research on contact induced spin relaxation is that this effect was most likely the limiting factor for τ_s in the graphene samples of past experiments. To minimize the influence of the contacts, a sample design using the conventional fabrication method should then maximize $R_C A$ as well as the distance between injector and detector contacts. Wide graphene flakes are also helpful.

When invasive contacts are the dominating spin sink, the spin relaxation would appear isotropic. An energy scaling will be observable, as the graphene sheet resistance R_{sq} and thus the R parameter changes with the charge carrier concentration. The maximum value for R_{sq} is at the Dirac point, where R would be lowest. This will result in a minimum of τ_s at the Dirac point and an increase of τ_s for higher carrier concentrations.

2.4 How to measure the anisotropic spin relaxation in graphene

While the idea to measure the anisotropy of τ_s to identify the spin relaxation process in graphene is not new, there are just three publications where this was attempted. The first experiment was done in 2008 by N. Tombros *et al.* of the van Wees group, which used the rotating electrode technique [19]. In 2014, a similar experiment was performed by M. H. D. Guimarães *et al.*, also of the van Wees group [53]. Finally in 2016, a new method called „oblique spin precession“ was introduced by B. Raes *et al.* of the Valenzuela group [20, 76]. A third method is presented in this dissertation that we call „xHanle“, which has so far not been used to to measure the anisotropy of the spin lifetime in pristine graphene.

2.4.1 Rotating electrodes

This experiment starts with a regular Hanle measurements in a non-local geometry, with the magnetic field perpendicular to the graphene plane (z direction). The spins are injected and detected in-plane, and the Hanle signal is used to extract τ_{xy}. The magnetic field in z is then increased until the injector and detector electrodes are completely rotated out-of-plane, which is ~1 T for the data in Fig. 2.17a). Now, spins are injected with an out-of-plane orientation s_z that can be detected by the z-oriented detector electrode. There is no more Hanle precession, as the spin orientation is now parallel to the magnetic field direction.

The detected signal for rotated electrodes $R_{nl,z}$ is then compared to the height of the Hanle center peak at $B = 0$, $R_{nl,xy}$. Both signals follow equation 2.30, with the only difference that $R_{nl,z}$ is calculated by using $L_{s,z}$ and thus τ_z, while $R_{nl,xy}$ is calculated by using $L_{s,xy}$ and thus τ_{xy}. Any difference between $R_{nl,z}$ and $R_{nl,xy}$ would then be the result of anisotropic spin relaxation.

The problem with this method is that the signal at high magnetic fields will sit on top

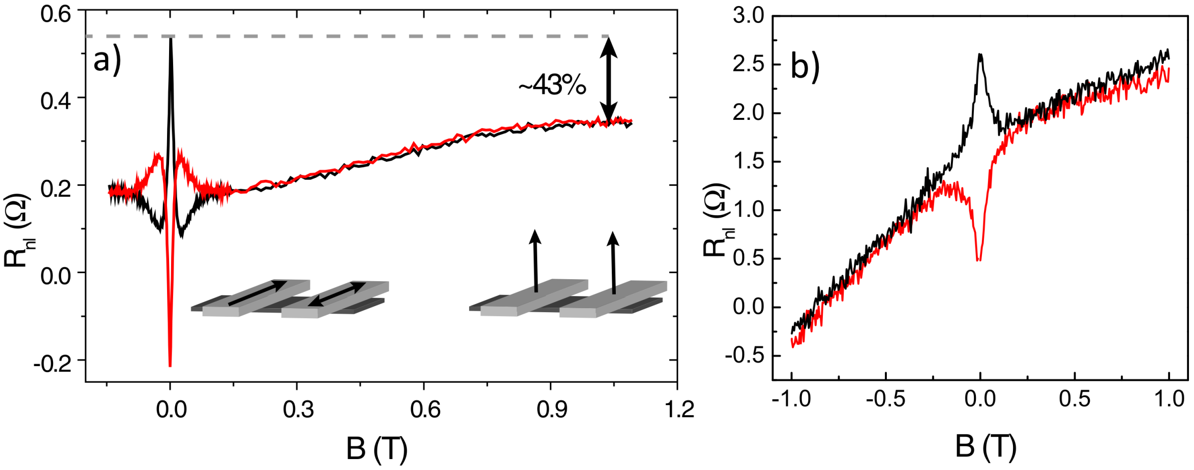

Figure 2.17: a) Schematic of the rotating electrode technique. At $B = 0$ the electrodes are oriented in-plane and the signal is proportional to τ_{xy}. At $B \sim 1\,\mathrm{T}$ the electrodes are oriented out-of-plane and the signal is proportional to τ_z. Adapted from [53]. b) Hanle signal of our sample S5B2, demonstrating a large B-dependent background.

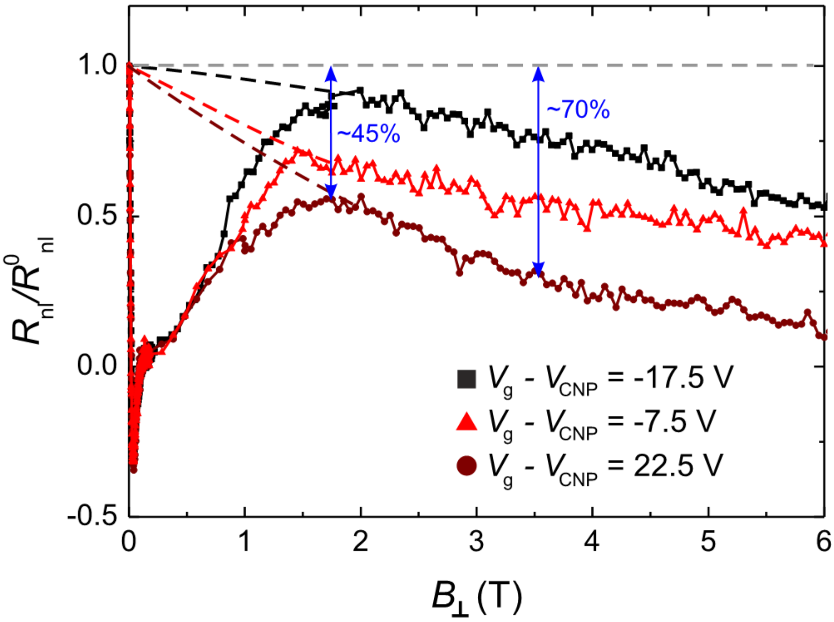

Figure 2.18: Rotating electrodes measurement by B. Raes *et al.* of a sample that was measured with the oblique spin precession method to have isotropic spin relaxation. The difference of $R_{nl,xy}$ and $R_{nl,z}$ is not due to anisotropic spin relaxation but because of the magnetoresistance of the graphene. Adapted from the supplementary material of [76].

of an unknown B-field dependent background. An example of data with an exceptionally large background is shown in Fig. 2.17b). The cause for such a background is for example an inhomogeneous spin injection because of pinholes, as has been demonstrated by F. Volmer *et al.* [77] and D. Schiermeier in his bachelor thesis [78].

Further additions to the background come from the magnetoresistance of graphene. Fig. 2.18 shows data of a sample that was measured with the oblique spin precession method to have isotropic spin relaxation [76]. As can be seen, the high field signal does not recover the zero field value and does not saturate. The background is also gate dependent, which is attributed to the magnetoresistance varying with the carrier concentration.

In conclusion, the rotating electrodes technique is unsuitable for a precise measurement of the spin relaxation anisotropy in graphene because of an unavoidable magnetic background. In the first publication by N. Tombros *et al.* [19] that use the rotating electrodes technique, it is stated that on average $R_{nl,z}$ is 20% lower than $R_{nl,xy}$. However, a precise calculation of ζ is impossible because of background fluctuations as large as the spin signal.

In the publication of M. H. D. Guimarães *et al.* [53], no complications with the background are reported and it is claimed that $R_{nl,z}$ saturates. The data to support this is shown in Fig. 2.17a). However, a measurement to higher field values as is shown in Fig. 2.18 is missing, raising doubts about the validity of the claims. The reported anisotropy in the publication of M. H. D. Guimarães *et al.* is $\zeta \approx 0.75$.

2.4.2 Oblique spin precession

This method was introduced in 2016 by B. Raes *et al.* of the Valenzuela group [76]. The idea is to use an oblique magnetic field to induce a spin precession that also has an out-of-plane component. The experiments starts with a regular Hanle measurement in a non-local geometry, with the magnetic field perpendicular to the graphene plane (z direction). The spins are injected and detected in-plane, and the precession because of the z-oriented magnetic field is also in-plane. From this Hanle signal, τ_{xy} is extracted. Then, the magnetic field is tilted in the z-y plane towards the y axis with the angle β (see Fig. 2.19). The spins are still injected and detected in-plane, but the precession around the oblique magnetic field is not in-plane. As is shown in Fig. 2.19, this precession also has an out-of-plane component that is sensitive to τ_z.

To extract τ_z from the oblique spin precession with an in-plane detector electrode is done by dephasing the spins. At a sufficiently large magnetic field, the Hanle oscillations can no longer be detected as the spins have dephased due to diffusive broadening. For an oblique magnetic field ($\beta \neq 90°$), a spin component proportional to $\cos\beta$ parallel to the magnetic field direction will still be detectable (see Fig. 2.19). As the detector electrode is in-plane, the detected signal is projected with a further $\cos\beta$ term onto the y-axis.

Fig. 2.20 shows magnetic sweeps for different tilt angles β of the experiment by B. Raes *et al.* [76]. At $B = 175\,\mathrm{mT}$ (vertical dashed line) the spin signal is completely dephased. Fig. 2.21 shows a sweep of the field angle β at a fixed magnetic field of

$B = 175\,\mathrm{mT}$. The data are plotted vs. $\cos^2\beta^*$, with β^* signifying the effective field angle that includes a slight rotation of the electrodes towards the z-direction because of the z-oriented magnetic field. In this plot, isotropic spin-lifetimes would appear linear, which is the case in Fig. 2.21. The gray lines indicate simulated plots for anisotropic spin relaxation of the stated ζ.

Fig. 2.22 is a summary of the measured ζ at various gate voltages V_g relative to the charge neutrality point V_{CNP}. B. Raes *et al.* measured ζ to be between ~0.9 and ~1.03. They conclude to have isotropic spin relaxation in their samples. A follow-up paper published in 2017 discusses alternative methods to extract τ_z from the data, for example from the shape of the normalized traces of Fig. 2.20 [20]. However, these are not superior to the method of $\cos^2\beta^*$ plotting.

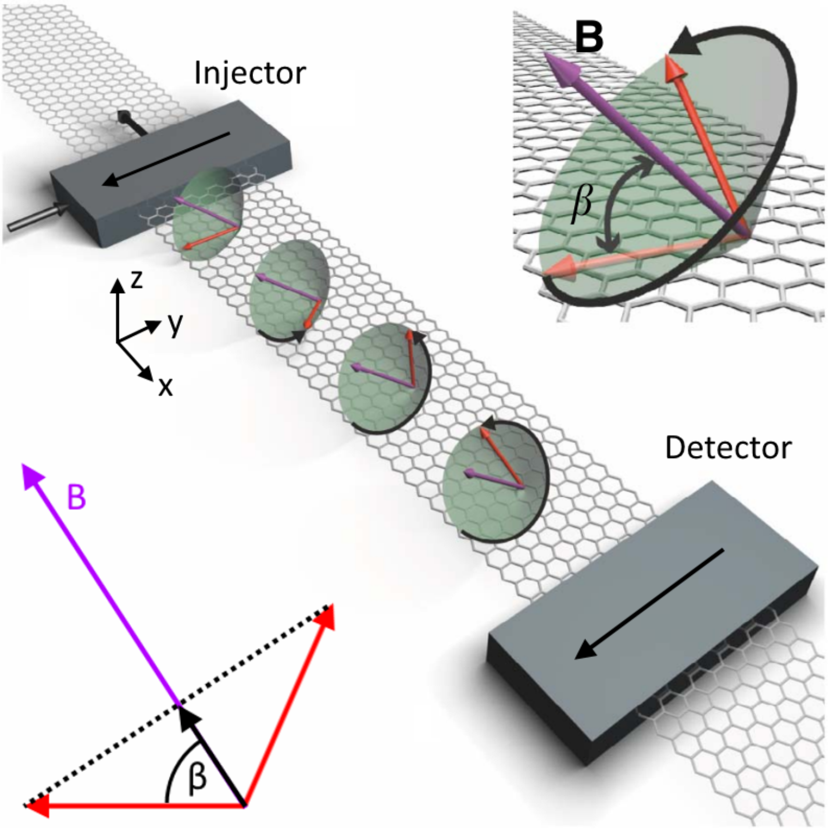

Figure 2.19: Schematic illustration of the oblique spin precession experiment. The red arrows represent the electron spin, the purple arrows represent the magnetic field B. In the lower left corner, the black arrow indicates the detectable spin signal parallel to the magnetic field for dephased spin precession. Adapted from [76].

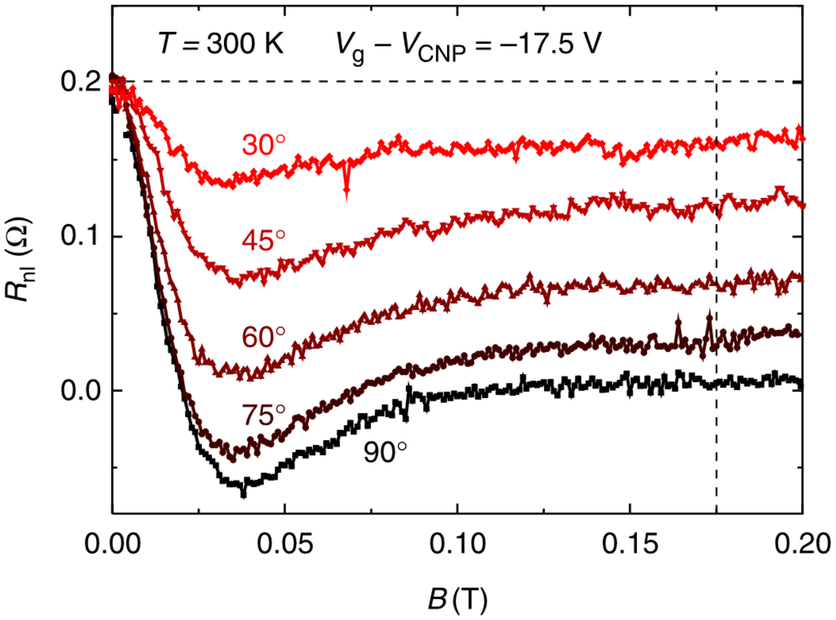

Figure 2.20: Oblique spin precession traces measured by B. Raes *et al.* at various inclination angles β of the magnetic field. The data at $\beta = 90°$ correspond to the regular Hanle experiment with z-oriented magnetic field. Adapted from [76].

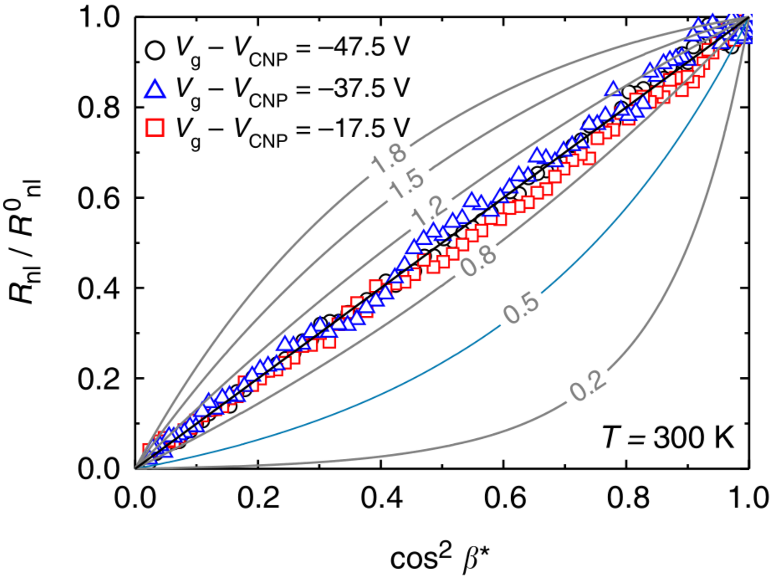

Figure 2.21: Oblique spin precession data measured by B. Raes *et al.* Sweep of the field angle β in the z-y plane at a constant field of 175 mT, plotted vs. $\cos^2 \beta^*$ to see the deviation from isotropic spin-lifetimes that is linear in this plot. Gray lines show the simulated traces for various degrees of anisotropy ζ. Adapted from [76].

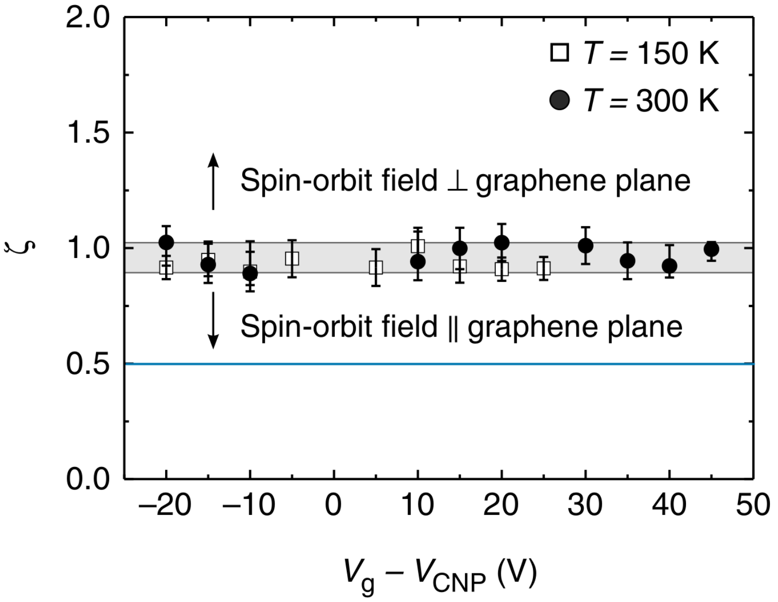

Figure 2.22: Extracted spin relaxation anisotropy ζ from the oblique spin precession experiment by B. Raes *et al.* ζ is displayed as a function of the gate voltage V_g relative to the charge neutrality point V_{CNP}. Adapted from [76].

2.4.3 xHanle

Another method to extract the anisotropy of the spin relaxation is to perform two Hanle measurements, where in one measurement the magnetic field is in the z-direction and in the other in the x-direction (see Fig. 2.23). A Hanle measurement with the magnetic field in z-direction, which we call „zHanle", is considered the „regular" Hanle. The Hanle measurement with the magnetic field in x-direction we call „xHanle".
In a zHanle measurement, the spins precess exclusively in-plane and experience τ_{xy}. When doing a xHanle measurement, the spins precess in the z-y plane where they experience both τ_{xy} and τ_z. By comparing zHanle to xHanle, τ_z can be extracted. For isotropic spin relaxation, there is no difference between zHanle and xHanle.

The concept of the xHanle experiment is well known and was for example briefly mentioned by B. Raes *et al.* as an alternative to the oblique spin precession experiment [20]. While the experiment is in principle easy to perform, the difficulty is to obtain data where the spin relaxation anisotropy can be extracted with sufficient accuracy. The effect of τ_z on the xHanle oscillations is strongest in the secondary peaks, which are only visible at large injector detector distances. To still measure a signal at these distances requires a good spin injection efficiency. Also, the electrodes must be designed to prevent the magnetic orientation to rotate into the x-direction. This dissertation presents the first xHanle experiment in pristine graphene that was performed with sufficient accuracy

to extract τ_z.
In 2017 the xHanle method was used to measure the anisotropy of graphene-transition metal dichalcogenide (TMDC) heterostructures. L. A. Benítez *et al.* published an experiment for graphene on WS_2 [79], while T. S. Ghiasi *et al.* published an experiment for graphene on $MoSe_2$ [80]. Graphene functionalized in this way has an extremely large anisotropy of $\zeta \approx 11$. The accuracy of the xHanle experiments in both publications suffered from rotating electrodes, but as the anisotropy of graphene-TMDC heterostructures is so large, a difference to pristine graphene was still clearly visible.

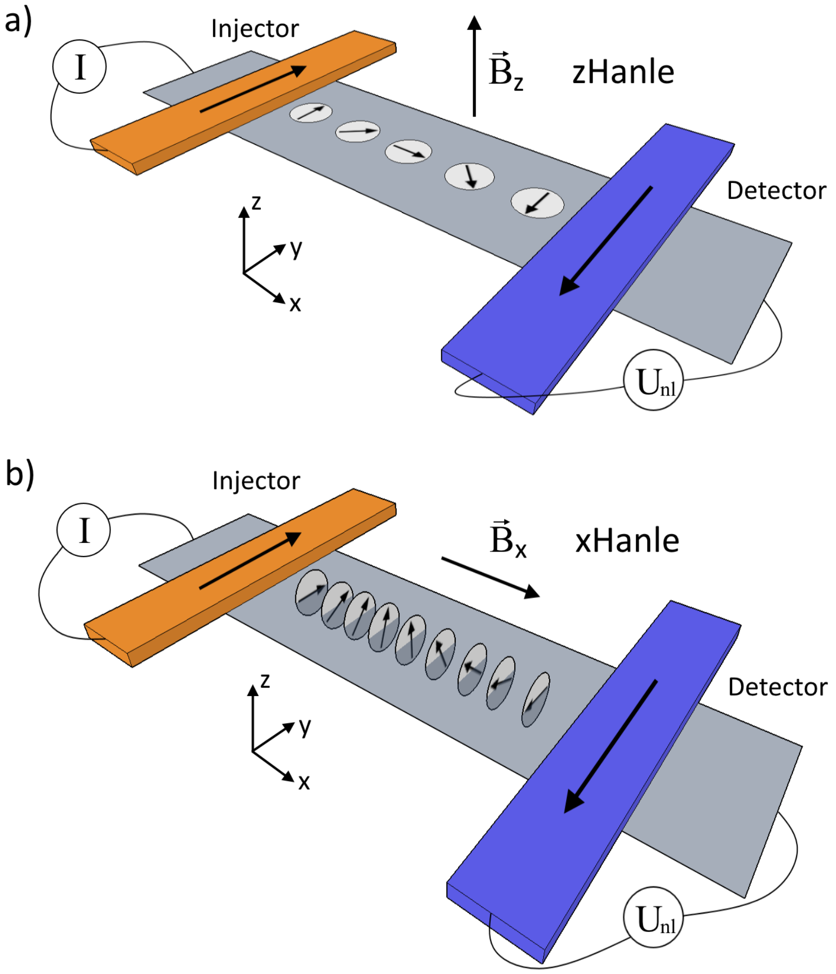

Figure 2.23: a) A Hanle measurement where the magnetic field is in z-direction we call zHanle. Here, the spins precess in the x-y plane. b) When the magnetic field is in x-direction, we call it xHanle. Now the spins precess in the z-y plane.

Chapter 3

Sample preparation and experimental setup

This chapter discusses the process of preparing samples, starting with the exfoliation of graphene. The next step is the lithography, where the impact of resist type and exposure dose is covered. Connected to the lithography are the dimensions and contour of the magnetic contacts, which determines the magnetic shape anisotropy. Once the resist mask is created, material can be deposited on the sample by thermal evaporation to form the contacts. The fabrication of reliable tunnel contacts is the most difficult part in this procedure. The chapter ends with a description of the cryostat and the measurement setup, explaining the precautions that must be taken when working with samples that are sensitive to electrostatic discharge.

3.1 Graphene exfoliation

Graphene flakes were fabricated by using a variant of the standard „Scotch tape“ mechanical exfoliation method, invented by Novoselov *et al.*[24] in 2004. This method, though rather low-tech, still produces the graphene of the highest quality. The tape we used was not Scotch tape but a blue foil normally used for dicing wafers (dicing tape type Ultron 1008R-9.0 by Minitron Electronic GmbH). This blue tape has the advantage over Scotch tape to leave less glue residues on the substrate. As source material for cleaving, natural graphite of the type „Flaggy Flakes“ from NGS Naturgraphit GmbH was used. Lena Bachhuber did a bachelor thesis comparing the various types of graphite and found Flaggy Flakes graphite has a far better mobility than Kish, Graphenium and HOPG graphite [81]. The detailed process of exfoliation is described in section A.1, a quick summary is as follows:

A piece of graphite is pressed on the sticky side of the tape and then removed, leaving cleaved-off thin graphite sticking to the tape. The tape is then folded so that it sandwiches the thin graphite. By pulling the tape apart, the thin graphite is cleaved again and this process is repeated five to ten times until the graphite is sufficiently thin. The tape with the cleaved graphite then gets pressed onto a substrate material, which after removal, leaves some graphite and graphene of varying thickness. The graphene and graphite stick to the substrate due to van-der-Waals forces. The transfer of graphene from tape to substrate requires a good amount of pressure that is usually applied by rubbing the tape onto the substrate with a plastic object. Without this rubbing, the amount of material that is transferred is far less. A special hot exfoliation technique was used that does not require rubbing for a good transfer. This technique was established by Josef Kamann [82].

The substrate is then put under a microscope to find any graphene flakes of the desired thickness and shape that might have transferred. The thickness of the graphene can be identified by its optical contrast. Fig. 3.1 shows an optical micrograph displaying single and bilayer graphene. The change in contrast is exemplified where the two single layer flakes overlap to form bilayer graphene. In the experiments presented in this work, only single layer graphene was used.

The properties of the substrate play an important role to enhance the visibility of graphene. We use p^{++}-doped silicon chips with an oxidized surface layer of 285 nm thickness, which by optical interference enhances the contrast of graphene. As seen in Fig. 3.1, the chips have a 50 μm spaced grid of markers, consisting of a Cr wetting layer and 60 nm Au. These markers are used to map the position of graphene flakes and for alignment during lithography. Before use, the chips are cleaned with acetone, propanol, and oxygen plasma.

To retain the good quality of exfoliated graphene, no plasma etching was used to shape the graphene flakes or remove any unwanted graphite chunks in their vicinity. This reduces the number of flakes on a chip that are suitable for further processing. However, it is possible to remove graphite chunks by scratching with a sharp needle (tip radius 1 μm) on a probestation, which will not damage the nearby graphene. Two examples are shown in Fig. 3.2. As can be seen in Fig. 3.2 d) and e), the precision of this method is good enough to remove the upper graphene flake that was just a few μm apart from the lower flake. The method can also be used to correct lithography errors after deposition, for example a short between to leads caused by a piece of graphite.

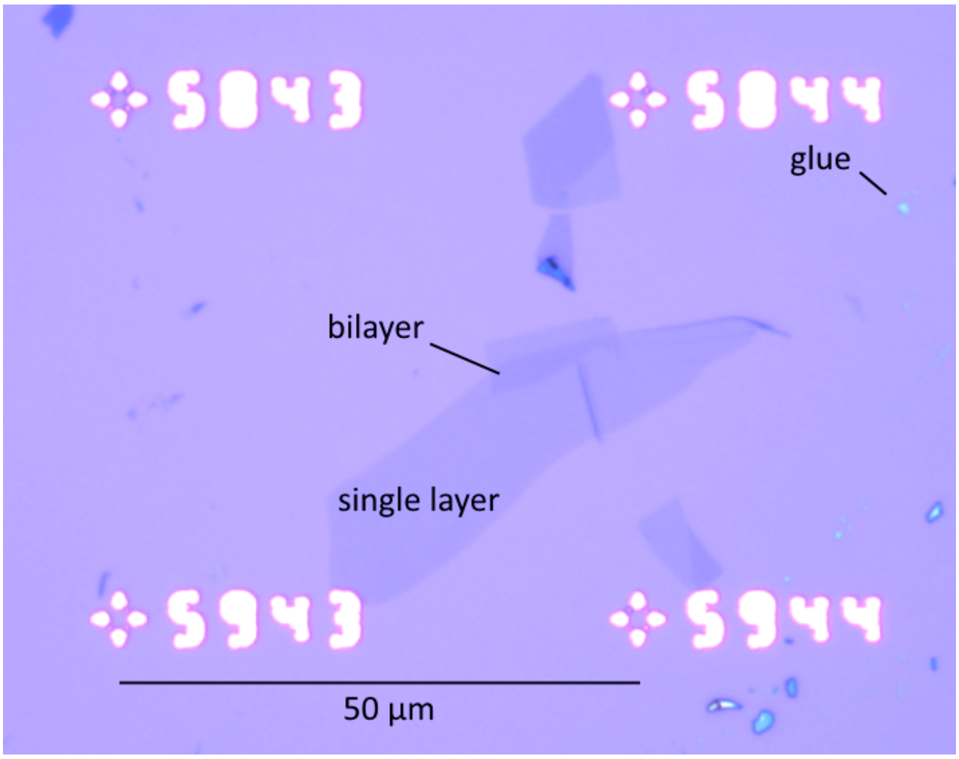

Figure 3.1: Optical micrograph of exfoliated graphene flakes. The number of layers can be distinguished through the contrast. Where the two single layer flakes overlap, there is bilayer graphene. In the upper right corner, there are remains of glue from the tape.

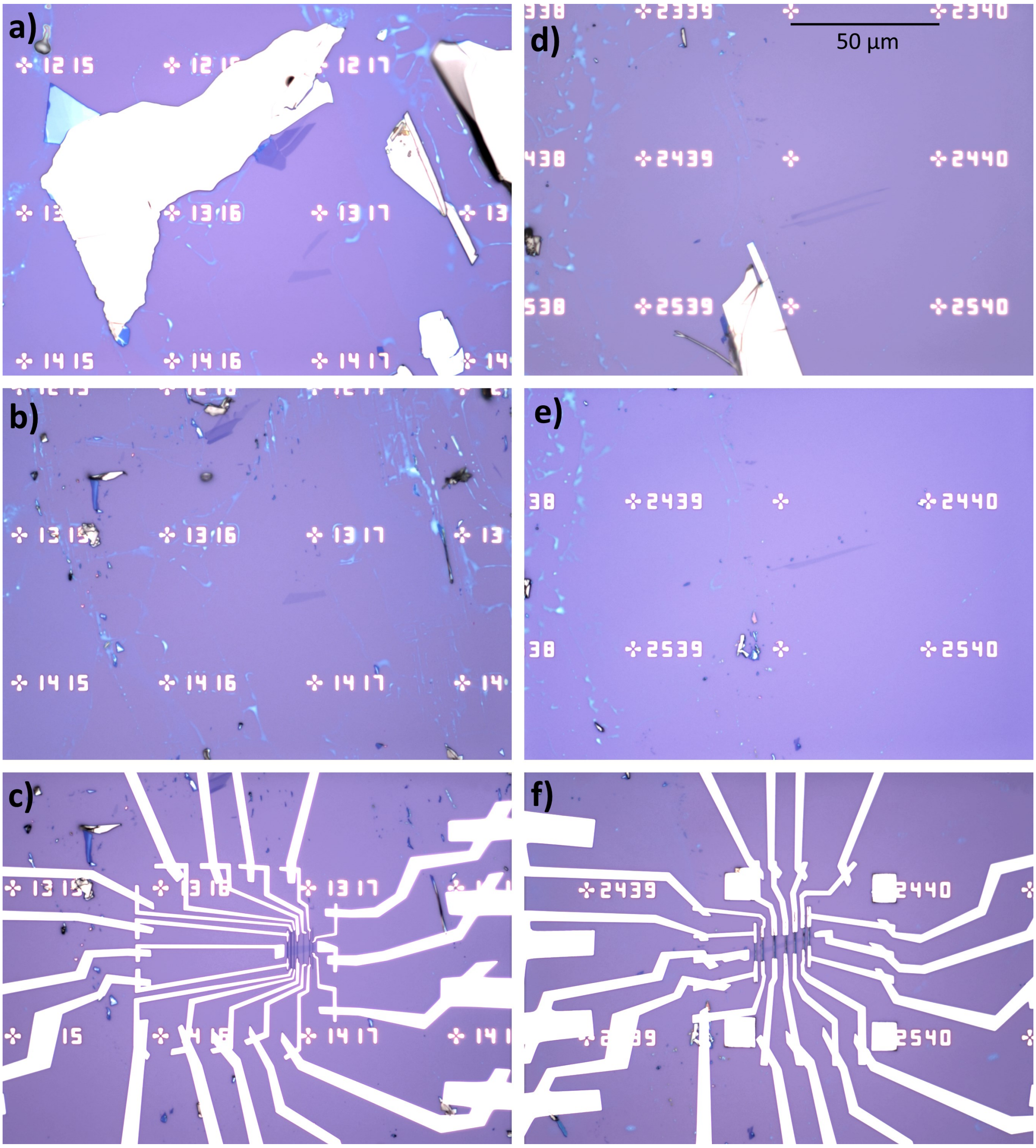

Figure 3.2: Optical micrograph of exfoliated graphene flakes before (a, d) and after (b, e) removal of unwanted graphite in their vicinity by scratching with a sharp probestation needle. Finished sample (c, d). The graphite surrounding the graphene of sample S2F3 in a) would make contacting the flake very difficult. Contacting just one of the two parallel flakes of sample S2F4 in d) from both sides is impossible, so the top one had to be removed.

3.2 Lithography

To electrically contact the exfoliated graphene flakes, electron beam lithography (EBL) was used. The process is depicted in Fig. 3.3. First, the chip is spin-coated with an electron beam sensitive positive resist. In our case, that is either poly(methyl methacrylate) (PMMA) or CSAR (Allresist AR-P 6200). The resist is then patterned with an electron beam using a scanning electron microscope. This is depicted in Fig. 3.3a). The pattern defines where the material will be deposited on the substrate in a later step. We used the software eDraw to design the pattern. After the exposure, the sample is dipped in developer for a specific duration which removes the exposed resist (see Fig. 3.3b)). The developer for PMMA is MIBK (methylisobutylketon) mixed with 3 parts chlorobenzene, for CSAR, the developer is AR 600-546.

The trenches in the resist are wider near the substrate because of reflected and scattered electrons that broaden the exposed area. This is called an undercut and is a desired feature, as this makes the lift-off more reliable. An undercut can also be achieved by using two layers of resist, where the bottom resist is more sensitive. In the next step shown in Fig. 3.3c), a material, in this case a metal, is deposited on the resist and the substrate. The final step shown in Fig. 3.3d) is the lift-off, where the resist and with it the material on top is removed with a solvent. The sample is then washed and blow-dried to leave the finished metal structures on the chip.

Fig. 3.4 shows the eDraw file of sample S6C3 and Fig. 3.5 and 3.6 the finished sample after lift-off. There are 16 Co contacts on the graphene, which are contacted by Pd leads on both ends to enable anisotropic magnetoresistance (AMR) measurements. The outermost contacts to the graphene sheet are also made of Pd. This results in 34 bondpads on the chip.

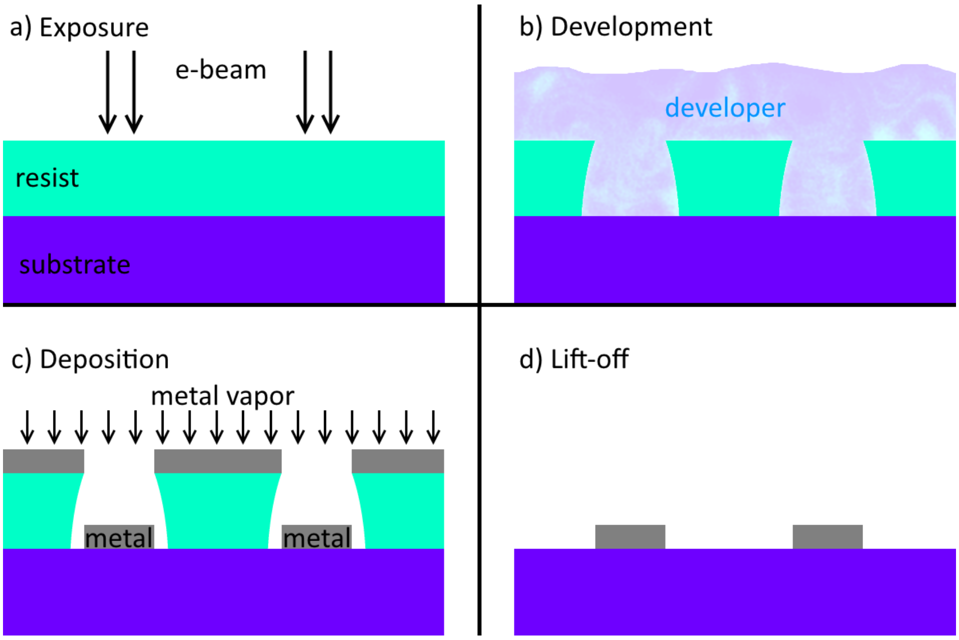

Figure 3.3: Step by step lithography process, side view of the chip. a) The substrate is covered with an electron beam sensitive resist and exposed. b) The substrate is dipped in developer which removes the resist that has been exposed. c) Metal is deposited on the substrate and on the resist. d) The resist is removed with a solvent, lifting off and removing the metal on top of the resist.

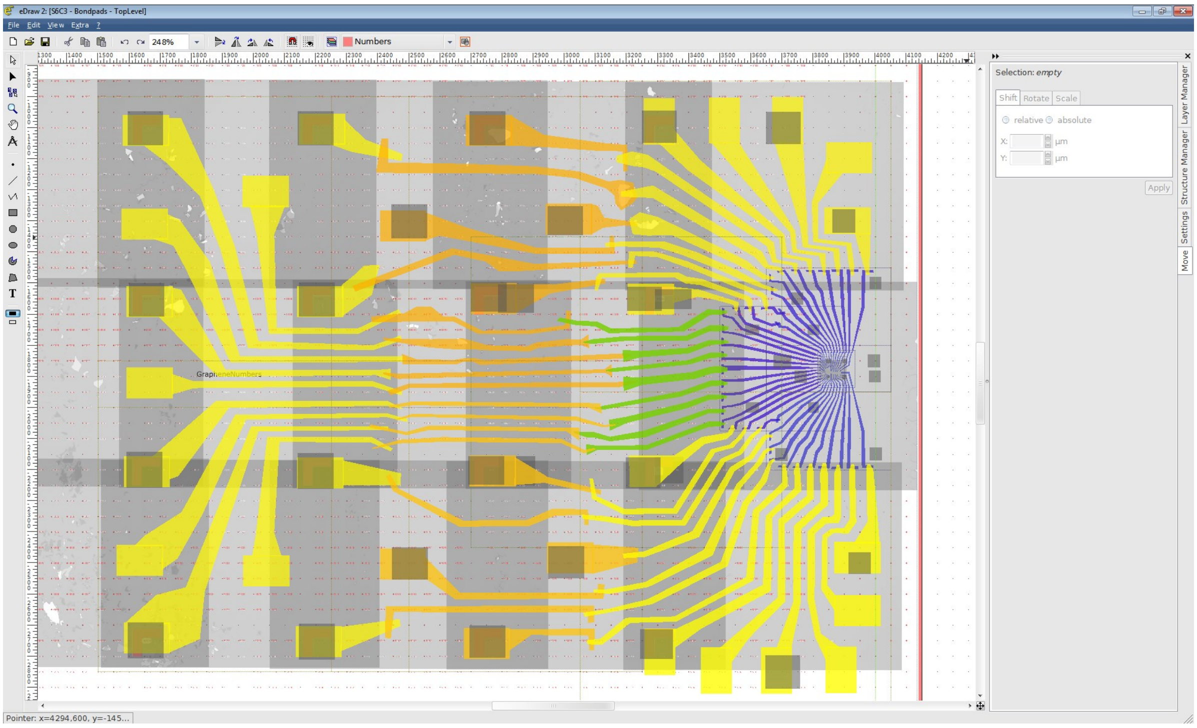

Figure 3.4: eDraw file of sample S6C3.

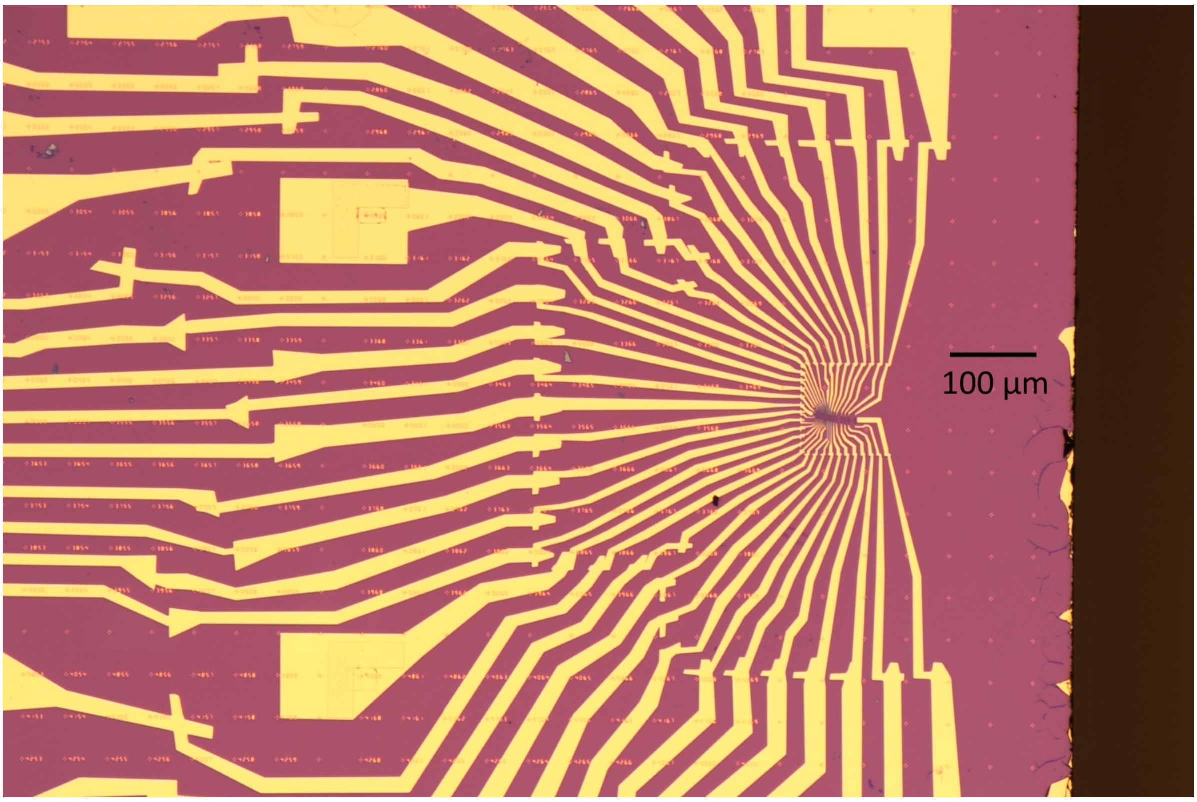

Figure 3.5: Optical micrograph of sample S6C3 after lift-off at 10x magnification.

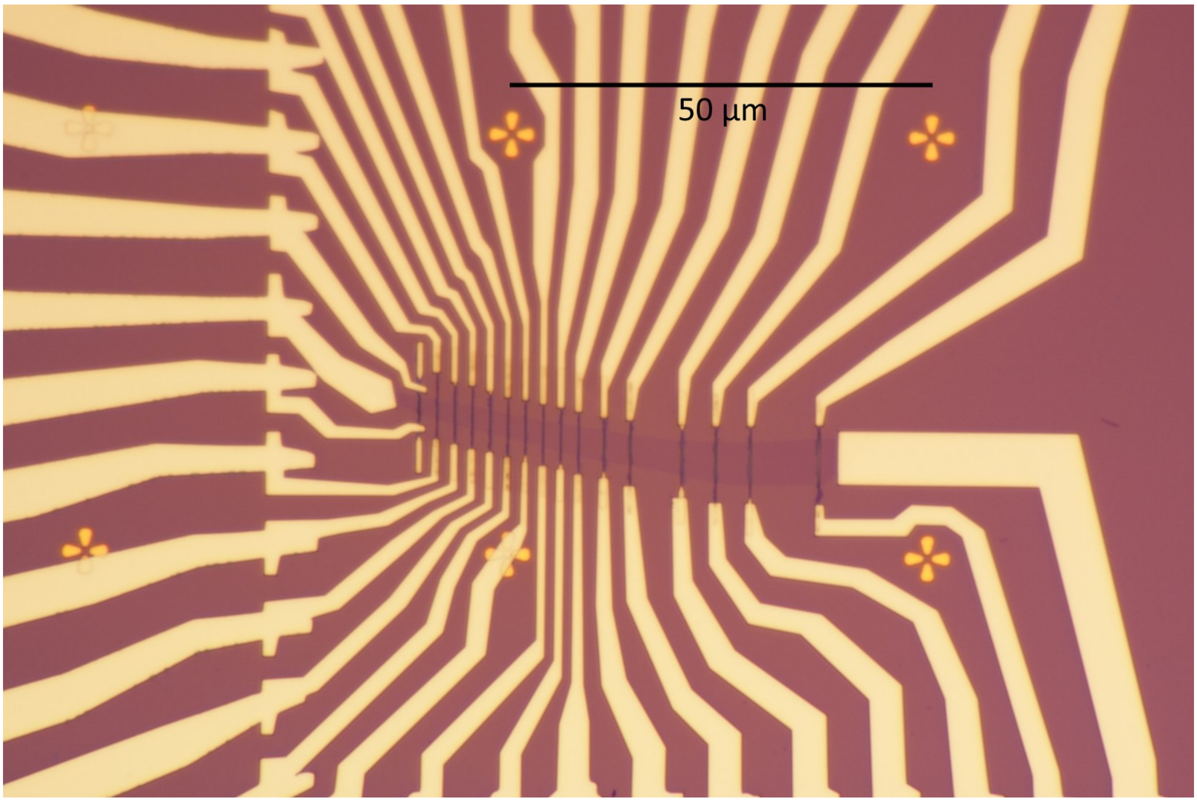

Figure 3.6: Optical micrograph of sample S6C3 after lift-off at 50x magnification. The lithography for the Co contacts used PMMA and suffered the problematic lift-off further discussed in section 3.4. In the upper left corner there is a short circuit that was later removed by scratching with a probestation needle in the same way that graphite was removed in Fig. 3.2

3.3 Magnetic properties of the contacts

Controlling the magnetic orientation of the electrodes is an essential part of any spin transport experiment. Ideally, one wants the magnetic orientation to be either parallel or antiparallel. This is done by having stripe-shaped parallel electrodes, where the magnetic shape anisotropy keeps the magnetization aligned to the easy axis which is in the stripe direction. To be able to switch the electrodes into an antiparallel orientation, the stripes are of different width as this changes the strength of the shape anisotropy. Narrow electrodes increase the magnetic shape anisotropy which makes the magnetization more resistant to an external field (hard switching). Conversely, wide electrodes reduce the magnetic shape anisotropy and the magnetization is easier to manipulate with an external field (easy switching). The usual setup is then to have one narrow and one wide electrode. The wide electrode changes the direction of the magnetization at a field value whereas the narrow electrode is still stable, enabling an antiparallel orientation.

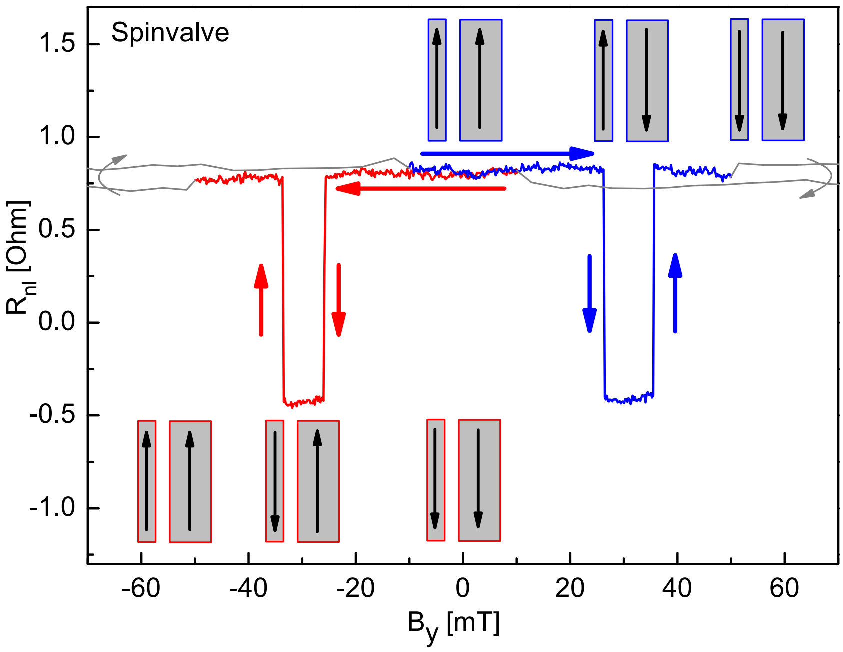

Figure 3.7: Spinvalve signal of sample S7F2 at 100 K and gate = 12 V, with depiction of the electrodes and their magnetization direction at the corresponding field values. The wide electrode changes magnetization direction before the narrow electrode, enabling an antiparallel state. The blue trace is the up-sweep, the red trace is the down-sweep. The gray trace shows the preparation of the electrodes that was done at a higher sweep rate, which induces an offset because of the DC measurement setup.

This is depicted in Fig. 3.7, that shows a spinvalve measurement with the corresponding electrode magnetizations.
When designing electrodes for the xHanle experiment, an additional requirement is stability vs. a transverse magnetic field. Ideally, one wants to do the xHanle experiment in a field range where the measurement field does not influence the electrode orientation. This range is defined by the least stable (widest) electrode, so all electrodes should be as narrow as possible. Narrow electrodes, because of their increased magnetic shape anisotropy, have better stability than wide electrodes. All electrodes can have the same width, but then a solution must be found to give them different coercive fields to still be able to prepare an antiparallel state. This can be achieved by varying the shape of the tips.

Fig. 3.8 and Fig. 3.9 show anisotropic magnetoresistance (AMR) data of two Co electrodes at T = 200 K with shapes that have the same width in the middle but different tip designs. The leads connect to these Co electrodes at the middle part, so the magnetization behavior of this middle part is what the AMR data display. The sweep axis of the magnetic field is along the stripe direction of the electrodes (y axis), to measure at which field strength the electrodes reverse their magnetization (coercive field). As both magnetization directions are parallel to the current flow, there would be no change in the AMR signal. To make the switching process visible in the magnet sweep, an additional

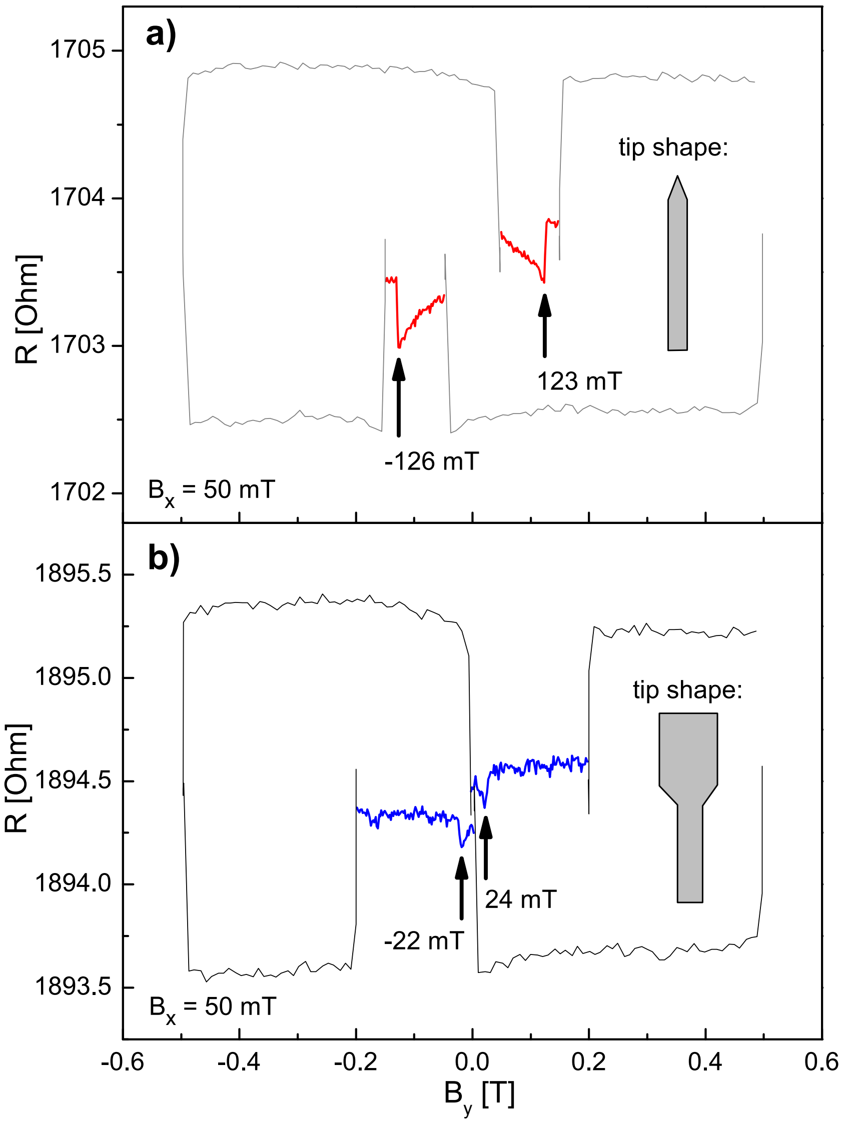

Figure 3.8: AMR measurement to detect the difference in coercive fields of Co electrodes with different tip designs.The switching events are marked by arrows. a) Pointed tips. b) spatula shaped tips with a width of 450 nm. The middle part of both electrodes is ~73 nm. The thin gray lines mark data that were recorded with an increased sweep rate of the magnetic field. This speeds up the measurement but results in an enhanced offset because of magnetic induction.

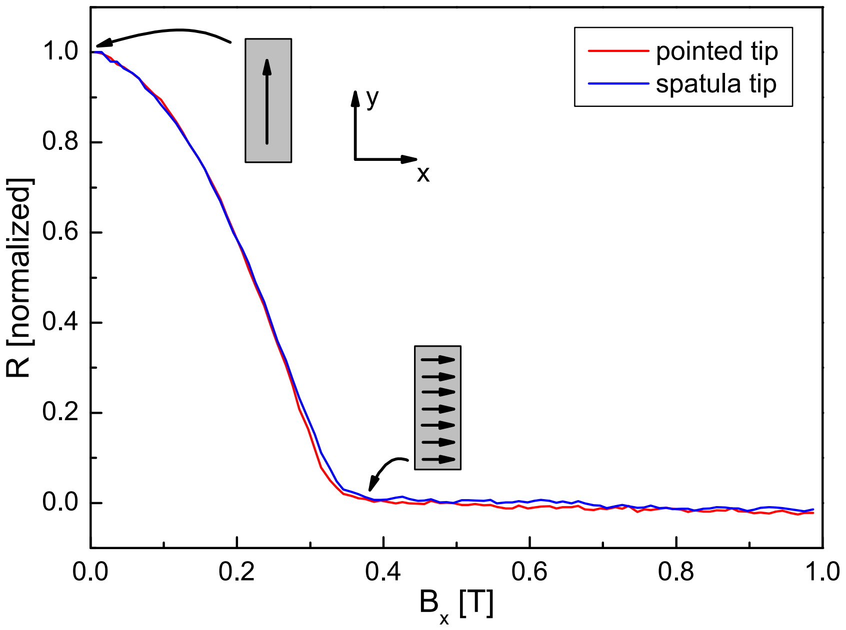

Figure 3.9: AMR data to test the stability of the electrodes of Fig. 3.8 vs. a transverse magnetic field in x direction. The long axis of the electrodes is in y direction. Both electrodes behave identical.

fixed field in x direction of 50 mT is applied. This distorts the absolute values of the coercive fields, but it is sufficient to test if differences in the coercive fields exist or not. The switching event is marked by arrows. The big jumps in the signals before and after the switching event are due to magnetic induction because of a change in the sweep rate and are not an AMR signal of the electrodes. Data recorded at a higher sweep rate is colored gray and should be disregarded. It is displayed to have a complete picture of the magnet sweep.
Fig. 3.8a) shows AMR data of a Co stripe with a narrow, sharp tip that suppresses the formation of a seed area for a magnetization reversal, increasing the coercive field. The width of this Co stripe is ∼73 nm. Fig. 3.8b) shows AMR data of a Co stripe with a spatula-shaped tip that acts as a seed area for a magnetization reversal, lowering the coercive field. The width of the stripe is ∼73 nm in the middle, the spatula shaped tips at both ends have a width of 450 nm. The coercive field can be further tuned by varying the width of the spatula part. The data demonstrates a successful manipulation of the coercive fields by the tip shape.
Fig. 3.9 shows the AMR data of both these electrodes vs. a transverse field in x direction. As can be seen, both electrodes have identical stability, demonstrating that the stability vs. a transverse field of the middle part of the electrode is unaffected by the tip design. The look of this electrode design when implemented in a graphene spin transport device can be seen in Fig. 3.15a). The picture shows a graphene flake with Co contacts on top that are not yet contacted by Pd leads at each end.

The sweep rate for the gray part of the data in Fig. 3.8 was increased to speed up

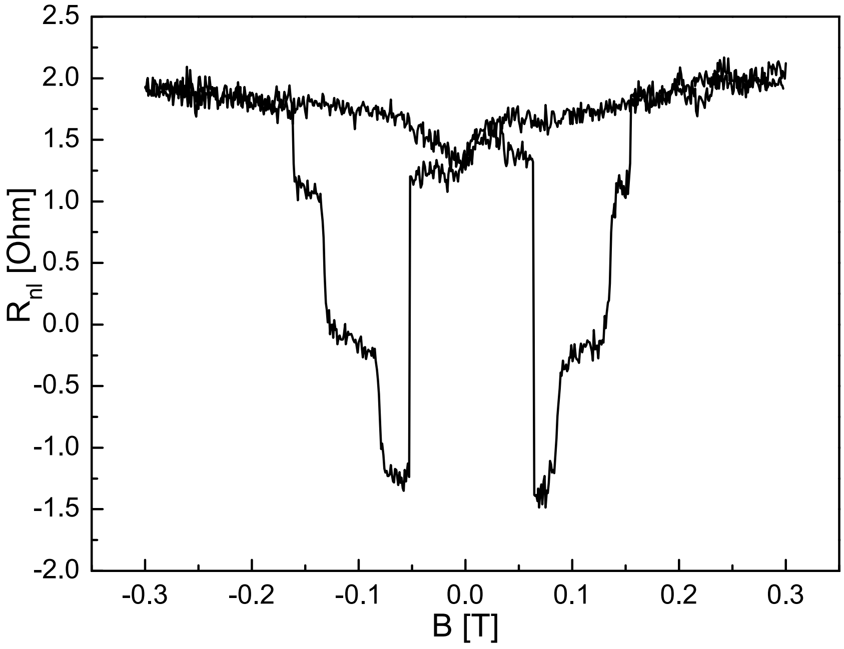

Figure 3.10: Spinvalve data of sample S6C3 at 200 K showing partially switching electrodes. Both Co electrodes have a width of ~63 nm and a thickness of 30 nm. The coercive fields are different because of differently shaped tips.

the measurements for field ranges where no change in the signal is occurring. This was exercised for measurements that require a high magnetic field resolution like in Fig. 3.8, but also a high field value to ensure proper magnetic orientation. Using the high resolution for the whole field range would have increased the measurement time from ~5 minutes to 20+ minutes without providing any additional information.

Induction effects are present in the data because of the DC setup used. The strength of the offset is dependent of the position of the wiring and which coil of the 3D vector magnet is used. It scales linearly with the sweep rate of the magnet and, depending on the circumstances, can be negligible. The offset changes sign when the sweep direction is inverted and can this way be extracted and removed from the data if necessary. However, this is mostly a cosmetic change and was not done for any data presented here.

Instead, the magnetic induction was treated in different ways. Fig. 3.10 and Fig. 3.11 are examples of spin valve measurements that were recorded with a constant sweep rate over the whole field range. Here, the induction offset is negligible as it is lower than the noise in the data. Fig. 3.12 is an example of a spin valve with changes in the sweep rate. Once the existence of the different sweep rates is known, the part of the data with increased sweep rate can be easily identified by the difference in noise. Fig. 3.7 is a measurement of the same contacts but at a different gate voltage where the data at increased sweep rate is marked by being differently colored (gray). For the red and blue colored low sweep rate data, no offset is visible. Fig. 3.8 is the data where the induction effect causes the most noticeable offset, but it was no hindrance for the analysis of the data.

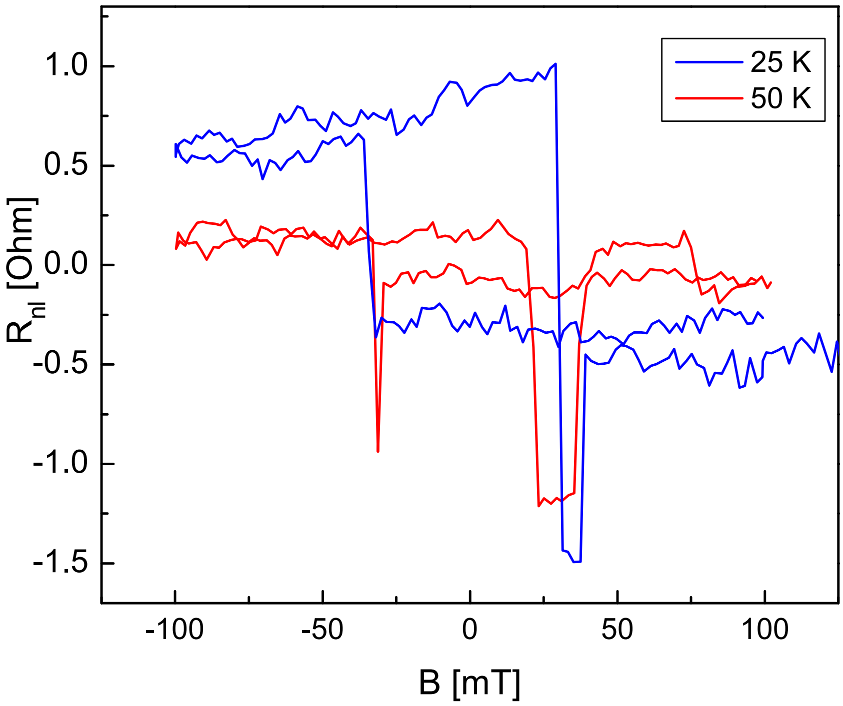

Figure 3.11: Spinvalve data of sample S7F2 at 25 K and 50 K and gate = 0 V, showing partially switching electrodes.

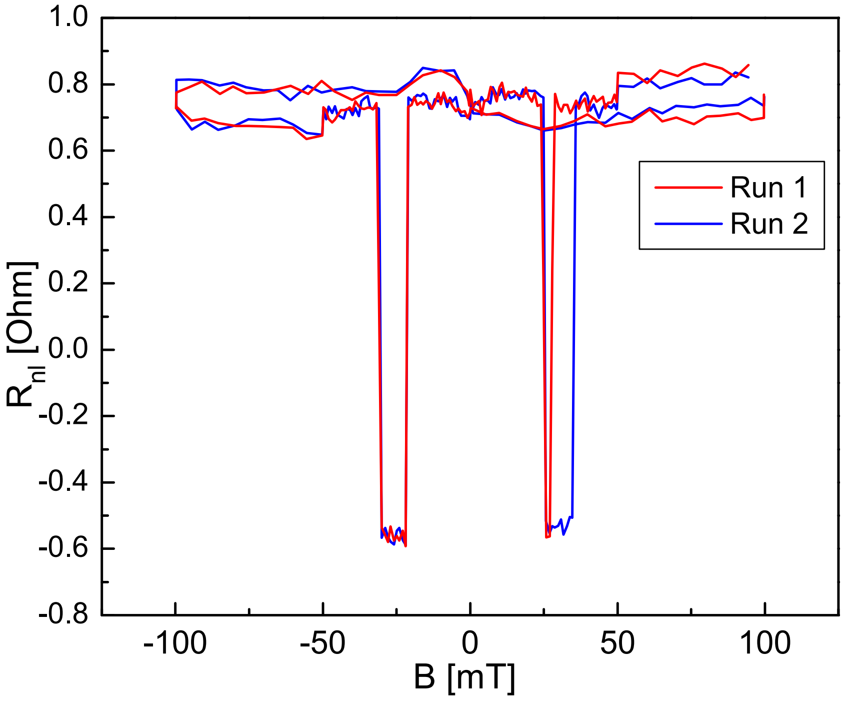

Figure 3.12: Spinvalve data of two consecutive measurements of sample S7F2 at 100 K and gate = 0 V. The coercive fields are not stable and can change.

To have the best magnetic properties for the xHanle experiment, it would seem logical to have electrodes as narrow as the lithography allows. However, there are also parameters that favor wider electrodes. Arguments connected to the tunnel barrier are discussed in detail in section 3.5.2. Here we discuss the magnetic properties.

Narrow electrodes may have a segmented magnetization where switching is not synchronized. Then the magnetization direction is non-trivial and more states than just parallel and antiparallel exist. The preparation of a complete antiparallel state might not be possible anymore. An example of this is shown in Fig. 3.10, that displays a spinvalve measurement of sample S6C3 at 200 K. Both Co electrodes have a width of ~63 nm and a thickness of 30 nm. This sample also suffered from the PMMA lift-off problems detailed in section 3.4, which may have further worsened the switching behavior. The measurement was done with Co electrodes as injector and detector and nonmagnetic Pd electrodes for the reference contacts to the graphene. When the spinvalve signal looks like this, the magnetization state of the electrodes is unclear, which hinders proper analysis of any other spin experiments. Ideally, the signal should look like in Fig. 3.7 where the magnetization is either parallel or antiparallel. The data in Fig. 3.7 is from sample S7F2 at 100 K where the electrodes have a width of 300 nm and thickness of 20 nm.

Two more parameters that influence the switching behavior are the film thickness and the temperature. For the material stack of MgO/Co/Au, the Co needs to have a minimum thickness of 30 nm for clean switching at liquid helium temperatures. Sample S7F2, where the Co thickness is only 20 nm, needs 100 K or more for sufficiently reliable switching. Fig. 3.11 shows spinvalve data of sample S7F2 below 100 K that demonstrates this unreliable switching. Fig. 3.12 shows two consecutive spinvalve measurements at 100 K that demonstrate that the coercive fields in this sample are not always stable and may change slightly. This needs to be checked before automating a measurements procedure that includes the preparation of an antiparallel state.

3.4 Evaporation chamber

To realize the experiments detailed in this work, much effort was put into the improvement of the tunnel barriers that are needed for good spin injection into graphene. The characteristics of the evaporation chamber are an important aspect of that and will be discussed in this section. We used a custom-made, ultra-high vacuum chamber that we refer to as the „UHV chamber“. A schematic of the chamber is shown in Fig. 3.13.

As the name implies, the chamber was built for operation at ultra high vacuum (UHV) and can reach pressures below 10^{-10} mbar. The main chamber is kept at pressure by a turbomolecular pump and an ion pump. Samples are transferred in via a load lock. The sample suspension can be rotated, tilted, and can also be cooled to −120°C with liquid nitrogen.

There is an e-gun in the chamber that can evaporate MgO, Co, Ti and Al. The MgO and Co are in a graphite crucible, the Ti is in an $\mathrm{AlO_x}$ crucible and the Al is in the pocket

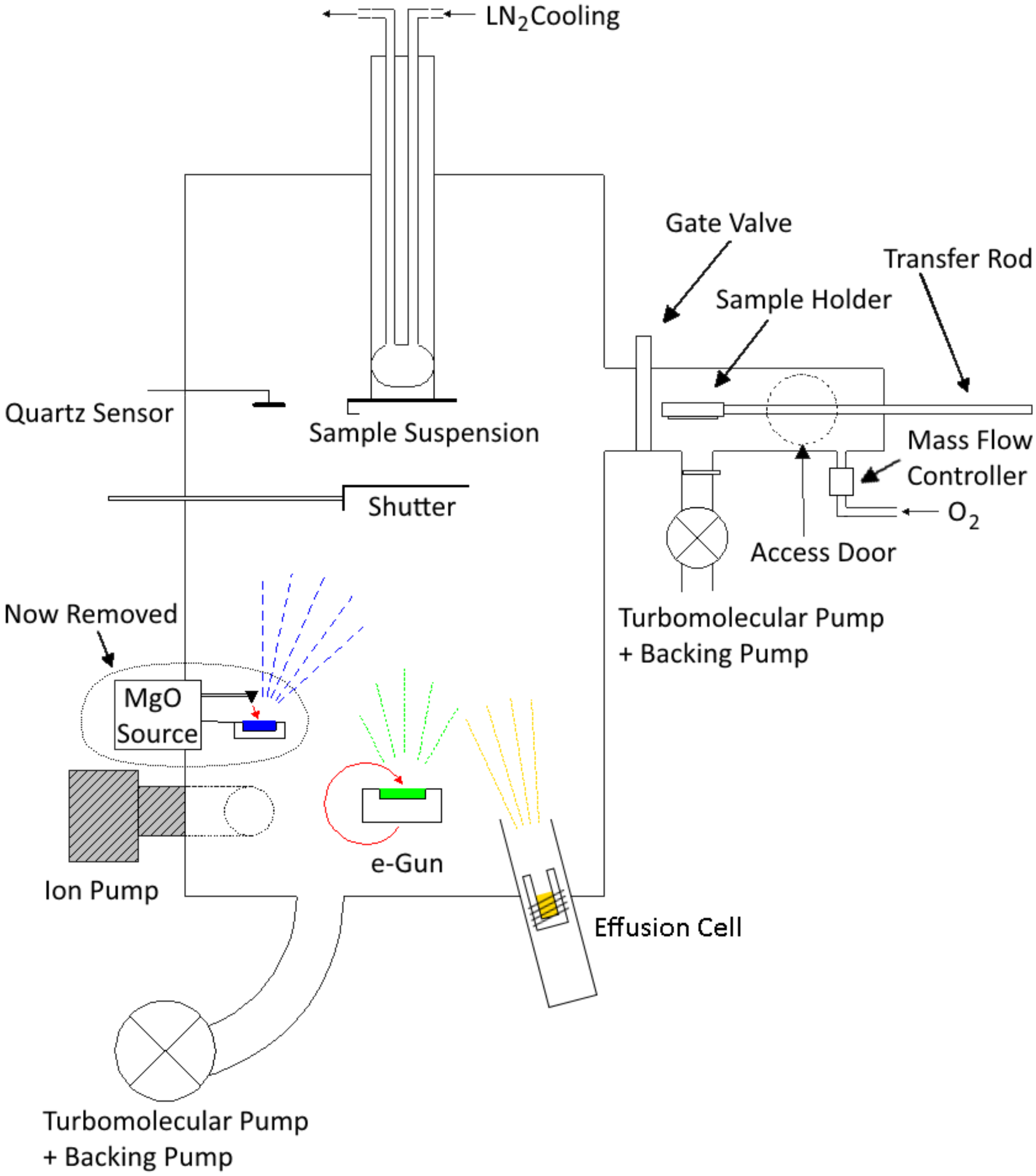

Figure 3.13: Schematic of the UHV evaporation chamber. Adapted from [83]

made of Cu without a crucible. The crucible type is important as for example Co will not work well in an AlO_x crucible. Charging effects and/or magnetic fields make it very difficult to focus the electron beam into the AlO_x crucible when the Co is still in shot form. The Co source also radiates quite a lot of heat when at deposition temperature, which is enough to damage PMMA resists. An example can be seen in Fig. 3.14 that shows an AFM picture of Co electrodes that were fabricated using PMMA resist. The additional material on top of the Co at the edges comes from the wall of the PMMA trench that did not lift off properly but collapsed on the structure. Cooling the sample suspension is not enough to eliminate the problem, as can be seen in Fig. 3.14a). An improvement of the lift-off can be observed when the amount of heat that the sample receives is reduced by depositing less Co, as a comparison between Fig. 3.14a) (30 nm Co) and Fig. 3.14b) (20 nm Co)shows. At a thickness of 10 nm Co combined with cooling, the lift-off is clean (see Fig. 3.15). The solution to grow thicker Co films using PMMA resists is then to do the deposition at intervals with enough time for cooling in between. One can also use the more heat resistant CSAR resist instead of PMMA to avoid the problem.

Complementing the e-gun, there are also several effusion cells in the chamber to evaporate Au, Pd, Fe and Dy. The load lock can be filled with pure oxygen, the amount controlled by a mass flow controller, to create oxides of deposited films. This was used to create AlO_x and TiO_x tunnel barriers.

The thickness of deposited materials is monitored by a water cooled quartz sensor that is read out by a thickness controller. To deposit really thin films, we found it best to directly monitor the change in frequency of the quartz. The Al films we deposited were as thin as 1.5 Hz. Because of this, in the log book the thicknesses of tunnel barriers are written with the unit „Hz“ and not „nm“. However, the frequency change of the quartz is non linear and depends on its lifetime (base frequency). Consequently, the accuracy of deposition monitoring by a direct quartz readout is limited and constant recalibration is needed.

The first experiments with MgO were made using MgO evaporated from a custom made source built by Mirko Ribow and Georg Woltersdorf from the Back work group that is shown in Fig. 3.16. A filament of tungsten is heated by a current that acts as an electron source, while a high voltage between the filament and the MgO accelerates the electrons to hit the MgO. After switching to e-gun evaporated MgO, the custom built source was removed from the chamber. This custom made source works, but we found the evaporation of MgO from the e-gun to be superior for several reasons. The deposition rate is higher, it is easier to refill the material and there is no alignment problem as the Co is deposited from the e-gun as well. Care must be taken with the power setting of the e-gun, as the lowest current setting of 5 mA at 10 kV is already enough to damage the MgO crystals. The electron beam is then wobbled to reduce the effective power.

The MgO evaporated from the e-gun needs to be calibrated frequently. The MgO does not melt to form a flat surface, and apparently different pieces of MgO crystal have different evaporation trajectories. For example, our first calibration resulted in 1 nm = 27.7 Hz, the second calibration a few months later was 1 nm = 46.7 Hz. The correlation of quartz frequency to material thickness can be calibrated for one piece of MgO crystal,

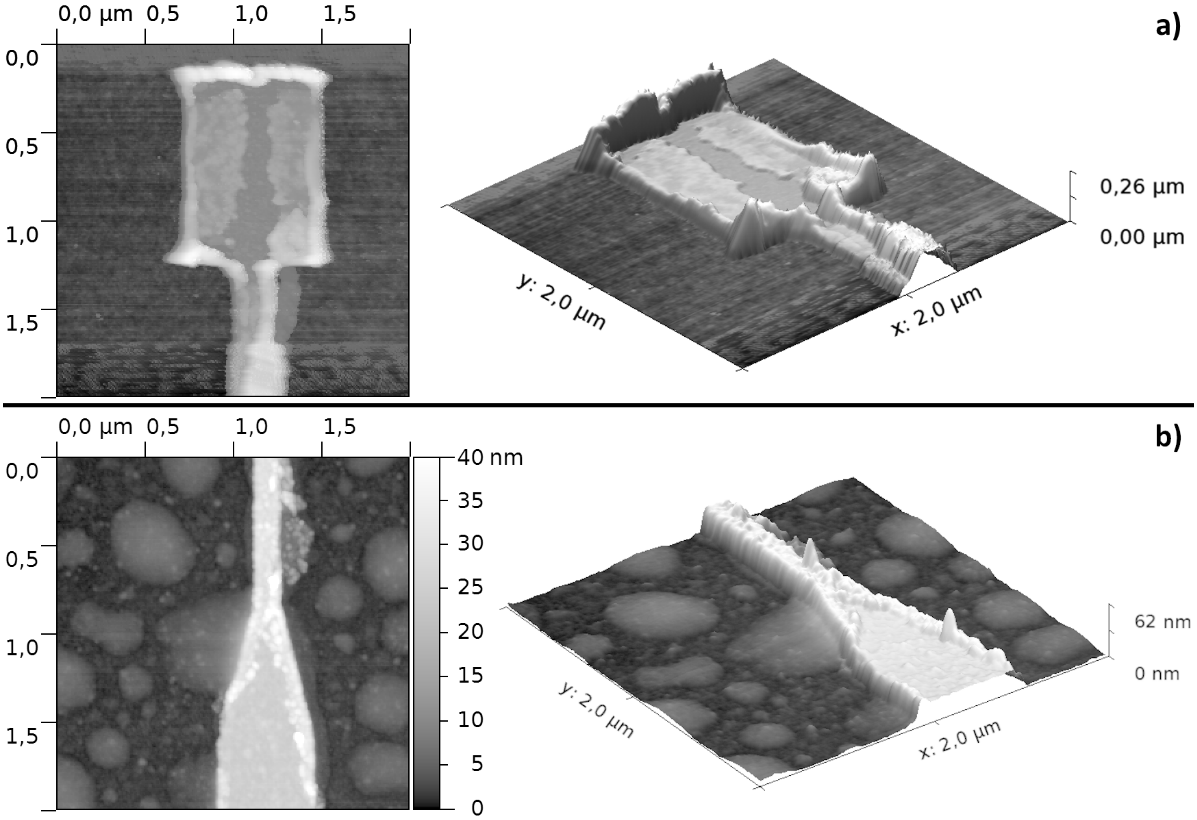

Figure 3.14: AFM images showing part of a Co electrode. The additional material on top of the Co at the edges comes from the wall of the PMMA resist that did not lift off properly but collapsed on the structure. This is caused by the heat of the Co source in the UHV chamber that damages the PMMA.
a) Sample S3D6. Two layer resist PMMA 200k 7% chlorobenzene 6000 rpm (bottom) and PMMA 950k 2% chlorobenzene 6000 rpm (top). Material stack (from bottom): ~0.125 nm Ti, oxidized, ~1 nm MgO, 30 nm Co, 10 nm Ag. During Co deposition the sample suspension was cooled to −110°C. The color scale is nonlinear for better visibility, the 3D plot z-axis is to scale.
b) Sample S2D5. The tunnel barrier of ~0.125 nm Ti, oxidized (bottom) and ~1 nm MgO (top) was deposited on the whole chip before the lithography. The MgO is hygroscopic and will absorb water when exposed to air, which results in bubbles forming at the surface. Resist is PMMA 950k 5% anisol 6000 rpm, deposited material is 20 nm Co without cooling. The 3D plot z-axis is not to scale for better visibility.

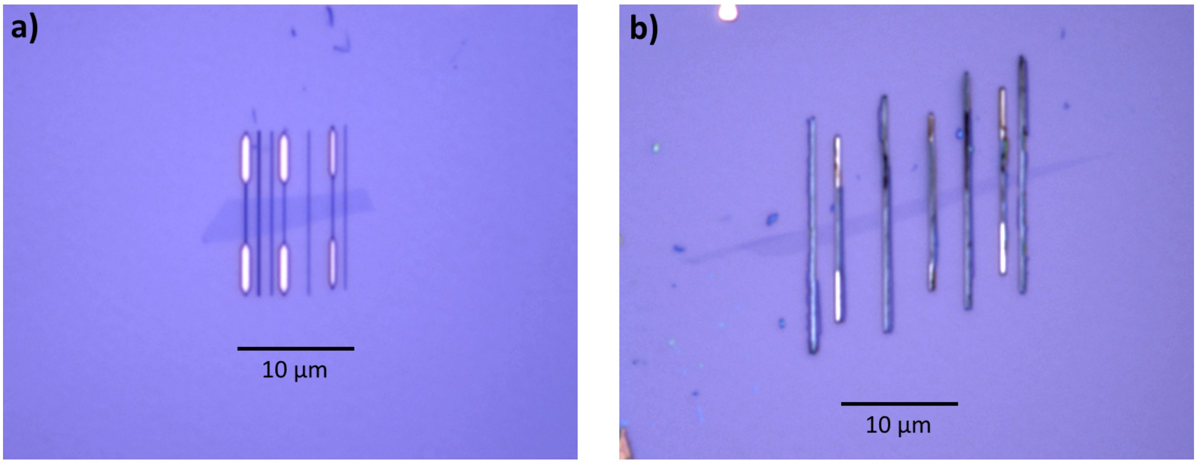

Figure 3.15: Optical micrograph of Co electrodes on graphene using a PMMA lithography after a clean lift-off (a) and a problematic lift-off (b). The lift-off in (a) is clean because of a shorter exposure to the Co source.

a) Sample S2F3. Resist is PMMA 200k 3.5% chlorobenzene 6000 rpm, deposited material stack (from bottom) is: ~0.125 nm Ti, oxidized, ~2 nm MgO, 10 nm Co, 5 nm Pd. During Co deposition the sample suspension was cooled to −106°C.

b) Sample S2F4. Two layer resist PMMA 200k 7% chlorobenzene 6000 rpm (bottom) and PMMA 950k 2% chlorobenzene 6000 rpm (top). Material stack (from bottom): ~0.125 nm Ti, oxidized, ~1 nm MgO, 30 nm Co, 3 nm Ag. No cooling of the sample suspension during deposition.

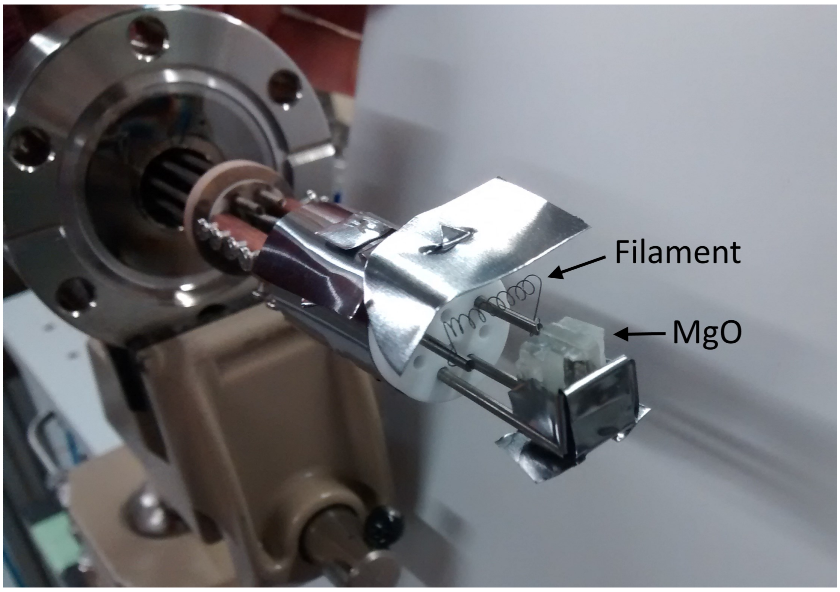

Figure 3.16: The custom made MgO source built by Mirko Ribow.

but if a different crystal piece is used for evaporation, the calibration will be wrong. This is a problem as the e-gun has enough power to easily break MgO crystals, voiding the calibration.

As has been reported by Frank Volmer [84], a good 10^{-10} mbar pressure or better is needed to grow high quality MgO tunnel barriers. Otherwise contamination of residual H_2O vapor will react with the very hygroscopic MgO to form $Mg(OH)_2$ [85–87]. An essential measure to keep our UHV chamber at a low 10^{-10} mbar pressure is to store the sample holder in the load lock and not outside exposed to air. The pressure can be further improved by evaporating Ti, using its getter effect.

Anytime MgO is exposed to air it will absorb water. This can be seen in Fig. 3.14b) that shows the AFM image of a sample where the whole chip is covered with ∼1 nm of MgO. Large bubbles cover the surface besides the Co electrode, which form because of the hydroxylation of MgO. This is also a concern for the MgO crystals that are used as an evaporation source. When the material is exposed to air because of material refill or chamber maintenance, the absorbed water needs to be removed by heating before it can be used for material deposition. Heating over 250°C in UHV is enough to reverse the hydroxyilation reaction [87].

For the evaporation of Pd circuit paths and bondpads, we used a different chamber, a Univex 450 by Leybold. This chamber is referred to as „Univex A“ in our work group. The Univex A is a standard evaporation chamber that does not need further explanation.

3.5 Tunnel barriers made of AlO_x, MgO and TiO_x

To avoid the conductivity mismatch problem explained in section 2.2.5, tunnel barriers were used under the magnetic electrodes. As previously stated, fabricating reliable tunnel contacts was the most difficult obstacle to tackle for the realization of the experiments presented in this thesis. When the project was started, the established work group standard were unreliable AlO_x tunnel barriers. It was first tried to improve the reliability of these contacts, but failing that, a change of material seemed a more promising approach. Other work groups in the field were successfully using TiO_x [53] or MgO [63, 67] barriers. The best spin signals to date were reported by Han *et al.* [88], who employed MgO tunnel barriers, so it was decided to try to reproduce their recipe. Since that recipe included a TiO_x seed layer, also testing samples with a full TiO_x tunnel barrier could be done without much extra effort. These experiments revealed complications connected to the oxidization of Ti which were not easily solvable and also prevented the use of TiO_x as a seed layer. It was then opted to fabricate MgO barriers without the TiO_x seed layer and implement the recipe detailed by F. Volmer *et al.* [84].

Working samples, meaning a spin signal could be detected, were produced with AlO_x, MgO and TiO_x tunnel barriers. However, only the recipe for fabricating MgO barriers could be sufficiently developed to produce samples where every single contact showed

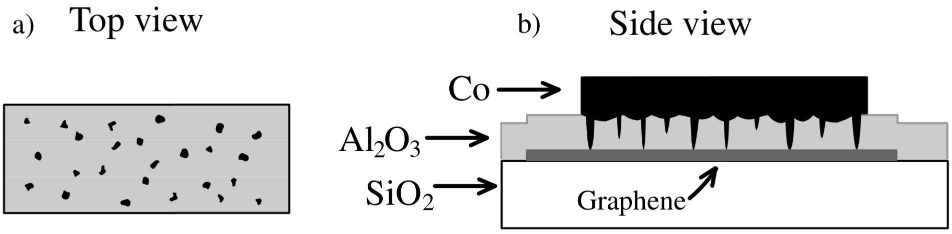

Figure 3.18: Sketch to illustrate an AlO_x tunnel barrier on graphene with pinholes. Adapted from [90].

a spin signal. Use of AlO_x and TiO_x barriers stopped before the sample design was advanced enough for a successful xHanle experiment, so there is no xHanle data from a sample using these barriers.

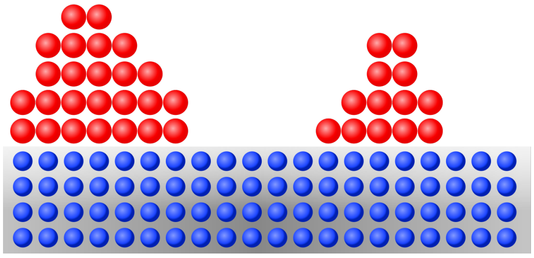

Figure 3.17: Thin film growth in the Volmer-Weber mode. The red atoms are the deposited material, the blue atoms are the substrate. Picture source: Wikimedia Commons

The challenge of growing tunnel barriers is to get an atomically thin film that is also smooth and homogeneous. The tunnel current has an inverse exponential correlation with the barrier thickness. If the barrier thickness is not homogeneous, „hot spots“ will form where the barrier is thinnest. At these hot spots, the current density can get dangerously large and damage the barrier, creating a short circuit. A homogeneous barrier prevents this by evenly distributing the tunnel current over the contact area.
Matters are further complicated because graphene is not the best substrate on which to grow a homogeneous thin film. The sp^2 hybridized C atoms are chemically inert and many materials deposited on top cannot form strong connections. This allows the deposited atoms to easily move around. As a result, the atoms will form islands instead of a smooth film [89]. This is called the Volmer-Weber growth mode and is depicted in Fig. 3.17. In the worst case, this leads to tunnel barriers with pinholes, as shown in Fig. 3.18.

Several methods can be used to counter this mechanism. Cooling the substrate hinders the island formation by reducing surface diffusion of the deposited atoms [91]. A high deposition rate also helps to reduce island formation, as the atoms have less time to move around [89]. Another possibility is to first deposit highly reactive atoms that form strong bonds like Ti as a seed layer [89].

As graphene is a very thin material, its morphology strongly follows the texture of the sustaining substrate [92]. Trapped gases and water between the graphene and the substrate can be removed by annealing, in effect making the graphene cling more tightly to the substrate and adapting to its roughness even more [93]. Because of this increase in roughness of the graphene, the mobility of deposited atoms is reduced, enabling smoother

films [91].
The following sections now report how these methods where explored with the different tunnel barrier materials and their respective success or failure.

3.5.1 AlO_x

The recipe for AlO_x tunnel barriers on graphene was first developed by Daniel Pachniowski [45] and then further improved by Bastian Birkner [94] and Andreas Sandner. Then followed the bachelor thesis of Philipp Nagler, whose objective it was to chart the correlation of the surface roughness of AlO_x films on graphene to the sample temperature during deposition [91]. Also tested was the effect of pre deposition annealing of the graphene. AFM measurements of 2.5 Hz of Al + oxidization resulted in surface roughness (RMS) values of $\sim$850 pm for no cooling and no annealing down to $\sim$250 pm for cooling below -60°C or pre annealing for 20 minutes at 400°C. For pre annealed graphene, cooling did not further improve the film smoothness as at a roughness of $\sim$250 pm the roughness of the SiO_2 substrate is already the limiting factor. It should be mentioned that we later discovered an error in the sample cooling system and the actual temperatures were not as low as stated.
The result of the experiments by Philipp Nagler was then that the film smoothness of AlO_x was at the highest attainable level on the given substrate. However, this did not improve the insufficient reliability of the tunnel contacts and we saw no further option to remedy the situation but to switch to a different barrier material.
The detailed fabrication recipe for AlO_x tunnel barriers in its final form can be found in section A.2. We produced working samples with the tunnel barrier covering the whole chip and also samples with the tunnel barrier just underneath the magnetic electrodes (local contacts). Cooling or pre-annealing is required, but not both. Working samples have been produced with pre-annealing and no cooling and also cooling and no pre-annealing.
There are many oddities related to the AlO_x produced by this recipe, the most important one being that the recipe does not work anymore (no spin signal). As functioning MgO tunnel contacts were already available when that occurred, there was no need to investigate the problem and the explanations we can give here are mostly speculation.
As has been stated, the contacts were unreliable. The problem with reliability is twofold. For one, on a given sample a significant number of contacts would not show a spin signal. Second, if a pair of contacts did show a spin signal, it happened that the signal degraded over the course of the measurement. It is unclear if the failure rate was augmented by a problematic measurement setup. Specifically, the nanovoltmeters in combination with the Ithaca current amplifier produce voltage spikes large enough to damage the tunnel barrier. This is further discussed in section 3.7.
We speculate that the fundamental problem of our AlO_x tunnel barriers is that the material that forms the tunnel barrier is not clean AlO_x but also „dirt“. There are several indicators supporting this speculation:

- When Daniel Pachniowski did the pioneering work to establish the AlO_x recipe in our workgroup, he struggled to get the contact resistance below the MΩ range [45]. For the following experiments by Bastian Birkner, the objective then was to evaporate as little Al as possible. This led to the direct readout of the quartz frequency and Al thicknesses of 1.5 to 2.5 Hz. A thickness calibration by Bastian Birkner related 1 nm Al to 14 Hz (UHV logbook entry), a later calibration by Philipp Nagler related 1 nm Al to 24 Hz. As the lattice parameter of Al is 0.40 nm (fcc), the resulting film thickness for 2.5 Hz deposited amorphous Al is then in the (sub)mono layer range.
  Considering the known problem of Volmer-Weber growth on graphene, it is hard to imagine that a mono layer of Al will form a continuous film. Oxidization will most likely not fix that. However, spin signals could be measured with such contacts, raising the question if the evidently existing tunnel barrier is formed because of additional contaminating materials.

- Following Bastian Birkners work was the bachelor thesis of Philipp Nagler. The surface roughness values that he measured for 2.5 Hz of Al + oxidization go up to ∼850 pm and the observed surface textures indicate an amount of oxidized material that is more than can originate from a mono layer of Al.

- The AlO_x recipe stopped working after the UHV chamber was optimized for a low pressure that is needed to grow high quality MgO. A possible explanation is that residual gases in the chamber were needed as contamination for the AlO_x recipe to work.

Philipp Nagler also did a thickness test for five chips of one evaporation run for 2.5 Hz Al with cooling during deposition and subsequent oxidization in the load lock [91]. The measured thickness of ∼1 nm on average is consistent with a working tunnel barrier, but inconsistent with the calibration of 2.5 Hz Al in the mono layer range. However, there was an unusually high variance in the thickness values that point to a questionable sample preparation technique.
The AlO_x thickness ranged from 0.5 to 1.5 nm for 20 data points. The variance on each chip was not that high (0.5 - 0.8 nm, 1.05 - 1.5 nm). We find it unlikely that this high variance originates from a deposition inhomogeneity of the Al source. The speculated contamination material that is included in the barrier might be the cause, as the contamination process is unknown and could be inhomogeneous. Another possibility is connected to the lithography processing. Photo resist was used to define an edge for the AFM step measurements, combined with oxygen plasma for cleaning. The oxygen plasma slightly etches the surface, which is a problem when one wants to measure a nanometer high step edge. This etching could be the source of the high variance in the height measurement. Not using oxygen plasma is not an option as the resist cannot be completely removed by solvent, leaving a thin nanometer high film. An example AFM image of that situation is shown in Fig. 3.19. The edge can be identified, but the height measurement is questionable. The same chip after oxygen plasma treatment can be seen

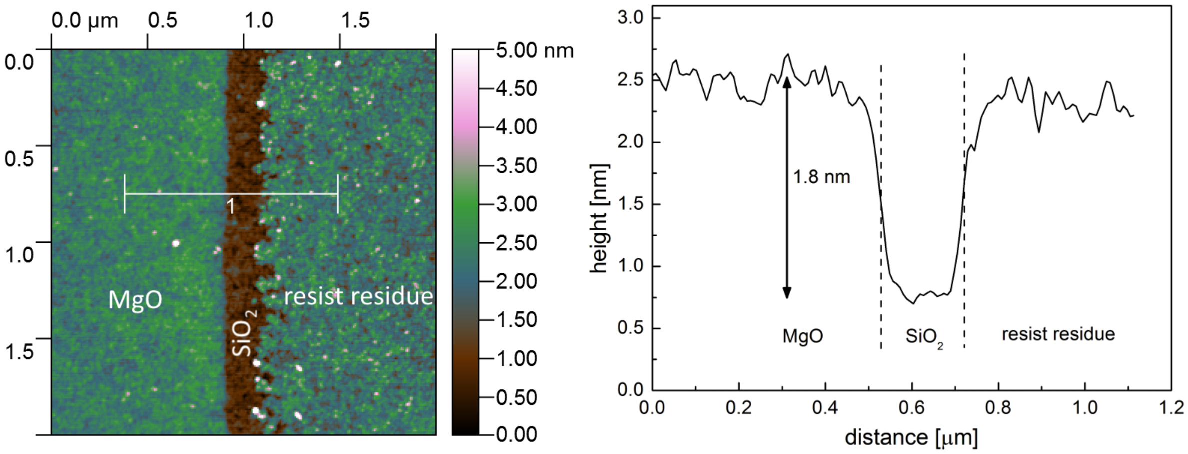

Figure 3.19: AFM image of a ∼1.8 nm MgO (left) step edge defined by optical photoresist. The photoresist (right) is not completely removed by the solvent. The graph on the right shows the height profile of the area marked in the AFM picture.

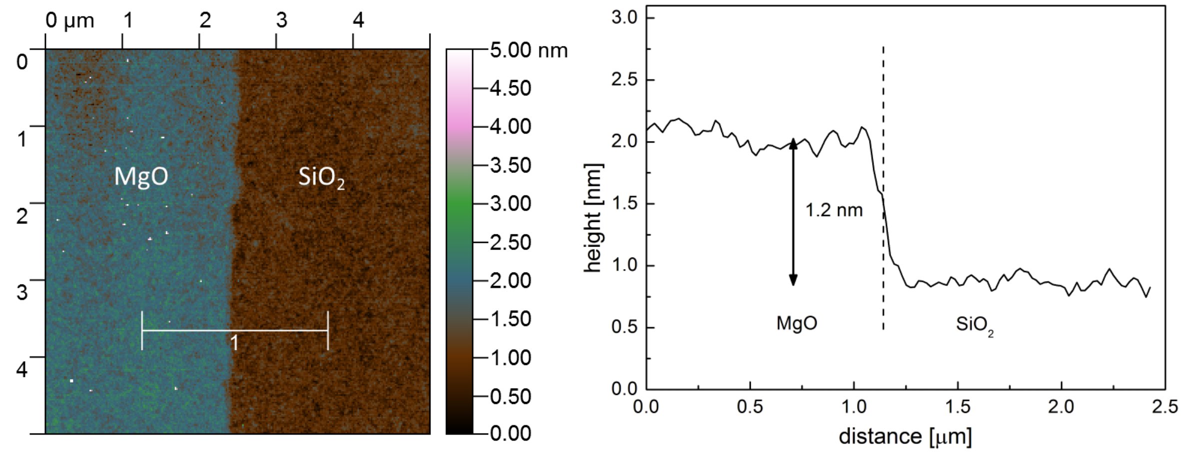

Figure 3.20: AFM image of the same ∼2 nm MgO (left) step edge as shown in Fig. 3.19, after cleaning with oxygen plasma. The resist is completely removed, but the step edge is now only ∼1.2 nm. The graph on the right shows the height profile of the area marked in the AFM picture.

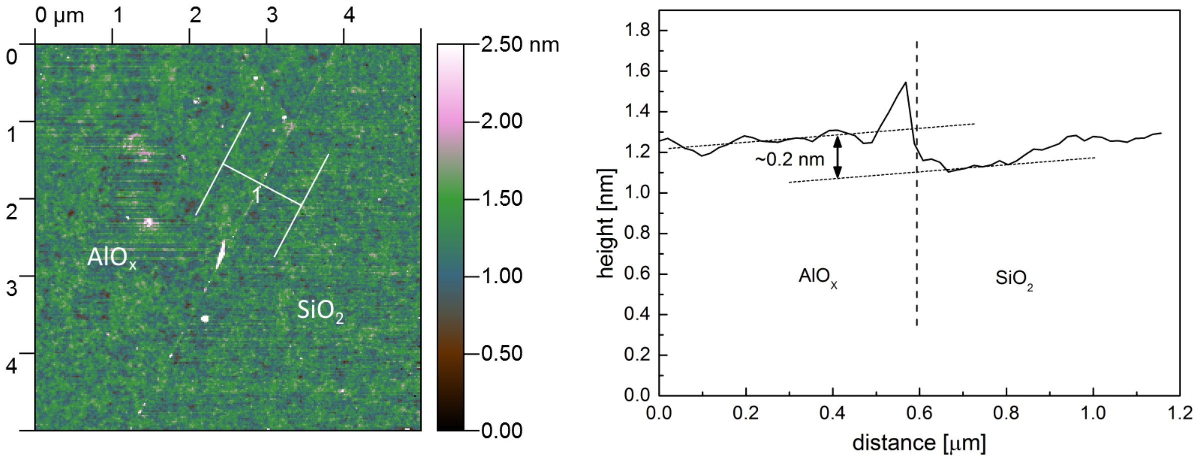

Figure 3.21: AFM image of 2.5 Hz Al, oxidized in air, deposited at room temperature. Step edge created by graphite scratching. The graph on the right shows the height profile of the area marked in the AFM picture.

in Fig. 3.20, showing a clean edge. However, the edge height is noticeably lower, most likely because of the plasma treatment.

We later developed a cleaner method to create step edges in thin films. The material is deposited on a chip with exfoliated graphite flakes. A step edge is then formed by removing a graphite flake using the scratching technique described in section 3.1. This method was used to calibrate the MgO film thickness and no unusually high variance occurred, testifying the reliability of the method. With this improved method we redid the height measurement of 2.5 Hz of Al and subsequent oxidization, the result can be seen in Fig. 3.21. We measured a step edge of ∼0.2 nm, which is consistent with the calibration of 2.5 Hz Al being in the (sub)mono layer range. However, the substrate was at room temperature during the deposition of the Al and not cooled. Also, the Al was oxidized at air and not in the load lock.

The consistency with the thickness calibration could be explained with the deposition temperature and oxidization method, as past calibration samples would have been produced in the same fashion. In contrast, the AlO$_x$ samples Philipp Nagler measured were processed like the actual tunnel barriers. It is shown in section 3.5.2 that MgO grows a thicker film when deposited on a cooled substrate. This might also be the case for Al. However, a spinvalve signal has been observed on a sample with an AlO$_x$ tunnel barrier that was grown without cooling and just pre annealing, so the difference cannot be too significant. Unfortunately, we did no further thickness calibration with an AlO$_x$ sample processed like the actual tunnel barriers, so this question cannot be answered.

3.5.2 MgO

In 2010 W. Han *et al.* [88] published an article about tunneling spin injection into graphene. They used Co electrodes with TiO_x seeded MgO barriers and report a non-local spin signal of 130 Ω at a contact distance of 2.1 μm, which is by far the largest signal reported even today. Because of our stated problems with the established AlO_x tunnel barriers, we decided to give MgO barriers a try.

Mirko Ribow and Georg Woltersdorf built the MgO source for us that is pictured in Fig. 3.16, which is designed after MgO sources already in use at the neighboring work group of Prof. Back. During the bachelor thesis of Max Kadur [83], we could replicate the correlation of the surface roughness of MgO films on graphene to the thickness of the TiO_x seed layer as reported by W. H. Wang *et al.* [89]. However, we found the TiO_x seed layer to be electrically problematic, most likely due to oxidization issues. This is further discussed in section 3.5.3.

Another key element of the recipe detailed in the work of W. Han *et al.* [88] is the angle evaporation technique to eliminate the chance of side contacts. This technique is illustrated in Fig. 3.22 and requires a resist with an undercut. The barrier material is deposited in two steps at two different angles. In a third step, the electrode material is deposited with a high tolerance for misalignment errors.

We tried to implement this method as well but did not achieve the desired results. We think the issue was a damaged PMMA mask because of too much heat from the evaporation sources as described in section 3.4. The CSAR resist might have solved the problems but was not yet available at the time of these experiments. To eliminate side contacts as a possible source of error, we instead used a TiO_x hard mask. Here, the graphene is covered with a ∼5 nm TiO_x masks in a separate lithography step, with stripe shaped holes in the TiO_x where the contacts will be deposited later. A sample with a TiO_x hard mask is shown in Fig. 3.28. After switching to e-gun evaporated MgO, the issue of side contacts ceased to be a problem (see section 3.4) and no preventive measures were needed anymore.

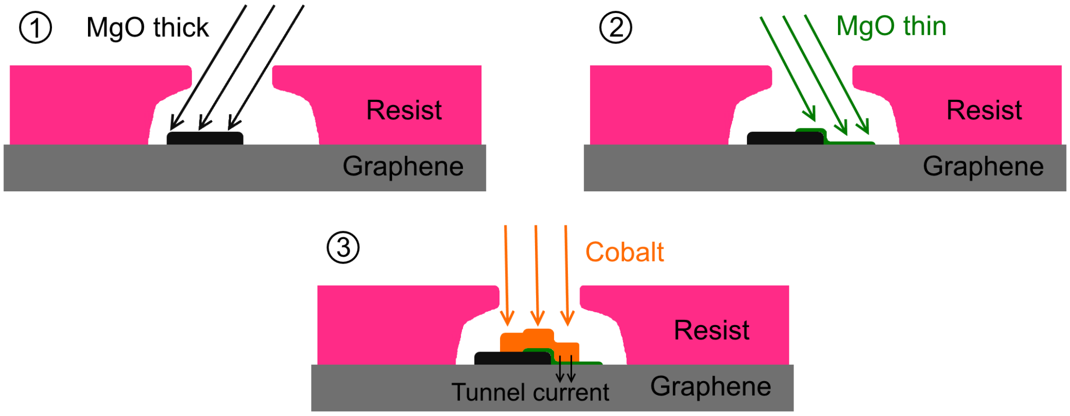

Figure 3.22: Angle evaporation technique. The electrons only tunnel where the thin MgO is.

As we were unsuccessful in resolving the issues related to the TiO_x seed layer, we opted to switch to the recipe of F. Volmer *et al.* [84] for fabricating MgO tunnel barriers. The final fabrication recipe as implemented by our work group is described in detail in section A.3. The major changes were to not use a TiO_x seed layer, switch to evaporating the MgO out of the e-gun, improve the pressure in the UHV chamber and let the sample degas in the chamber for at least a day before material deposition.

M. Kadur also tested the effect of graphene pre annealing on the smoothness of the MgO film [83]. MgO on unannealed graphene was measured with a RMS roughness of $\sim$480 pm, which could be improved to $\sim$410 pm by pre annealing at 400°C for 40 minutes. A Ti seed layer (1 ML) would further improve the RMS roughness to $\sim$250 pm. We later changed the pre-annealing to 200°C for 1 h as reported by J. Balakrishnan to be the optimal annealing procedure [95].

The induced roughness of annealed graphene on SiO_2 is an integral part of our MgO recipe. This was exemplified when we tried to produce spintransport devices with graphene that was transferred on hexagonal boron nitride (hBN). On hBN the graphene is smoother than on SiO_2. We deposited the same amount of MgO on these samples as we did for graphene on SiO_2. The electrical resistance of the contacts was then very low and no spin signal could be observed. We attribute this to holes in the MgO barrier because of Volmer-Weber growth. Compared to graphene on SiO_2, graphene on hBN exhibits an increased surface diffusion of the deposited MgO atoms. The conclusion is that the MgO growth on graphene is very dependent on the underlying substrate.

We also tried depositing MgO on a cooled substrate (-113°C) to further improve the smoothness without a TiO_x seed layer. The results of this experiment are quite puzzling. While the roughness of the MgO on the cooled sample is similar to the MgO on the not cooled sample, there is a huge difference in thickness. The amount of MgO deposited was the same for both samples (60 Hz from custom made MgO source). The step height on the not cooled sample was $\sim$0.7 nm, while the cooled sample had a step height of $\sim$4 nm. We have no explanation why there is so much more deposited material on the cooled sample. Also note that for this test the MgO was deposited on SiO_2 and not on graphene.

When MgO is used as a tunnel barrier in TMR junctions, the consensus is that sample heating during deposition results in a better barrier quality [96]. Because of these publications and the unexplainable increase in material thickness, we did no further experiments with MgO deposited on a cooled substrate.

An oddity of the MgO recipe is that the reliability of the contacts is related to the width of the contact stripes. The test samples we made to tune the barrier thickness had electrode widths of 200 nm and more. With these wide electrodes and an MgO thickness of $\sim$1.45 nm, we fabricated samples where every single contact showed a spin signal. This was first achieved with sample S6B3 four years after starting the project.

To get a better stability of the magnetization under transverse magnetic fields however, we wanted to make the electrodes as narrow as possible (see section 3.3). Using CSAR resist, we fabricated electrodes with a width of $\sim$63 nm. Unfortunately, this thin contour makes the electrodes unreliable with approximately 50% failure rate. This might be tied to residues of the photo resist. As reported by F. Volmer *et al.*[57], insufficient dosage during lithography will leave contamination from the resist residue on the graphene that will increase island formation during material deposition. Large areas get higher effective dosage during exposure than smaller ones because of the proximity effect. As a result, the barrier under narrow contacts is likely to have more pinholes because of more resist residue.

Fabricating samples with an increased exposure dosage for narrow contacts would be needed to confirm if this speculation is true. However, this was not tested as there are two other characteristics of narrow contacts that make them unsuitable for our experiment. As discussed in section 3.3, the magnetic switching can become unreliable. The second argument is that wider contacts can have a thicker tunnel barrier, which makes them more reliable and more importantly reduces contact-induced spin relaxation.

As has been discussed in section 2.3.4, contact-induced spin relaxation decreases for contacts with a high resistance area product. However, there is a limit on the feasible electrical resistance of a contact before a measurement becomes too noisy. At the same absolute electrical resistance, a wide contact has a higher resistance area product than a narrow contact (assuming the same length for both contacts) and thus less contact-induced spin relaxation.

In summary, narrow contacts suffer in reliability concerning a working spin injection/detection as well as magnetic switching. We did not do extensive testing at what dimensions these problems start to appear, but we can give 200 nm as an upper bound. An argument for wide contacts is that they enable the use of a thicker tunnel barrier, which increases the reliability and minimizes contact-induced spin relaxation. At the same time, narrow contacts are needed for the xHanle experiment to increase the magnetic stability vs transverse magnetic fields.

The xHanle experiment was successfully performed on sample S7F2, which has contacts with a width of 300 nm. That width seems to be a good compromise of the oppositional requirements. The spin injection efficiency of the MgO contacts on sample S7F2 was $P \approx 15\%$.

3.5.3 TiO$_x$

TiO$_x$ was successfully used as a tunnel barrier on graphene by Guimarães *et al.* [53, 97]. Our experiments on TiO$_x$ started by using it as a seed layer for MgO as reported in the article by W. Han *et al.* [88]. However, in our samples even the smallest amount of TiO$_x$ would make the contacts electrically problematic. We think this is related to the oxidization process we use, as oxidizing the Ti in the TiO$_x$/MgO stack leads to an increase in thickness compared to Ti/MgO that is far more than expected.

We checked the Ti source and calibration and found nothing out of the ordinary. The Ti was calibrated to 1 nm = 41 Hz. Then we tested the increase in thickness through oxidization by growing two identical samples of 0.12 nm (5 Hz) Ti, 0.58 nm (50 Hz) MgO and 5 nm Co (from bottom), deposited on SiO$_2$. The MgO was deposited from the custom built MgO source. MgO was included in this experiment as the intention was to test the MgO barrier with TiO_x seed layer, and the MgO might grow differently on Ti compared to TiO_x. On one sample, the Ti was oxidized in the load lock before continuing with the deposition of the other materials. Both stacks were then measured in the AFM for their height.

The stack without oxidization had a height of 7.5 nm, while the oxidized stack had a height of 8.3 nm. If we assume the difference in thickness is only caused by Ti expanding to TiO_x, this means 0.12 nm Ti expanded to 0.92 nm TiO_x. An alternative explanation for the high thickness difference would involve an increase in thickness of the MgO layer because of the oxidation process. For comparison, 1 nm of Ti oxidizing to TiO_2 would result in a film thickness of 1.7 nm, assuming expansion only in one direction. This raises the question of what type of oxide is formed on our samples.

The total stack height was higher than expected for both stacks. This can be explained by the oxidization in air of the Co top layer. Also, it is possible that more MgO is deposited on SiO_2 when a Ti or TiO_x seed layer is present.

Our procedure for the oxidization of Ti was the same that we used for the oxidization of Al (see A.2). We transferred the sample to the load lock of the UHV chamber and flooded with pure oxygen, reaching pressures in the mbar range. The sample was left from 10 to 30 minutes in the load lock depending on the thickness of the deposited Ti layer. Other work groups oxidize Ti at a much lower pressure of 10^{-8} Torr [98] and when TiO_x is used in magnetic tunnel junctions, a special „radical oxidation“ process is used that provides a more thorough oxidization [99]. On the other hand, Guimarães *et al.* report that they fabricate their TiO_x tunnel barriers by twice depositing 0.4 nm of Ti with subsequent oxidation at 10^{-1} Torr [97]. Because of these mixed reports, we are not sure if our oxidization technique is the source of our problems with TiO_x tunnel barriers.

The electrical problems of the TiO_x seed layer are exemplified by comparing sample S5F5 to S5F6. Both samples are processed identically, the only difference is that S5F6 has a TiO_x seed layer while S5F5 does not. Both samples have a TiO_x hard mask to prevent side contacts. They were annealed before and after the deposition of the hard mask at 400°C for 10 minutes. For the TiO_x seed layer on S5F6, 0.073 nm (3 Hz) Ti was deposited and then oxidized. The amount of MgO deposited on both samples was ~0.7 nm (60 Hz) from the custom made MgO source.

A spinvalve signal could be observed in both samples, as shown in Fig. 3.23 and Fig. 3.24. On sample S5F5 there were 16 contacts in total out of which 7 contacts showed a spin signal. However, the non-local spin signal was small, less than $1\,\Omega$ at an injector/detector distance of $2\,\mu$m. The resistance area product of the contacts was a few $k\Omega\mu m^2$ on average, with $0.7\,k\Omega\mu m^2$ the lowest and $42\,k\Omega\mu m^2$ the highest.

On sample S5F6 there were 15 contacts in total out of which only one contact pair showed a spin signal. The non-local spin signal was $\sim 9\,\Omega$ at an injector/detector distance of $1.2\,\mu$m. However, there was a huge background on the signal. The resistance area product of the contacts varied a lot and was in the $M\Omega\mu m^2$ range on average, with $213\,k\Omega\mu m^2$ the lowest and $3.8\,M\Omega\mu m^2$ the highest. Resistance of the majority of contact was not stable and would vary a lot, for example between $213\,k\Omega\mu m^2$ and $373\,k\Omega\mu m^2$ on one contact.

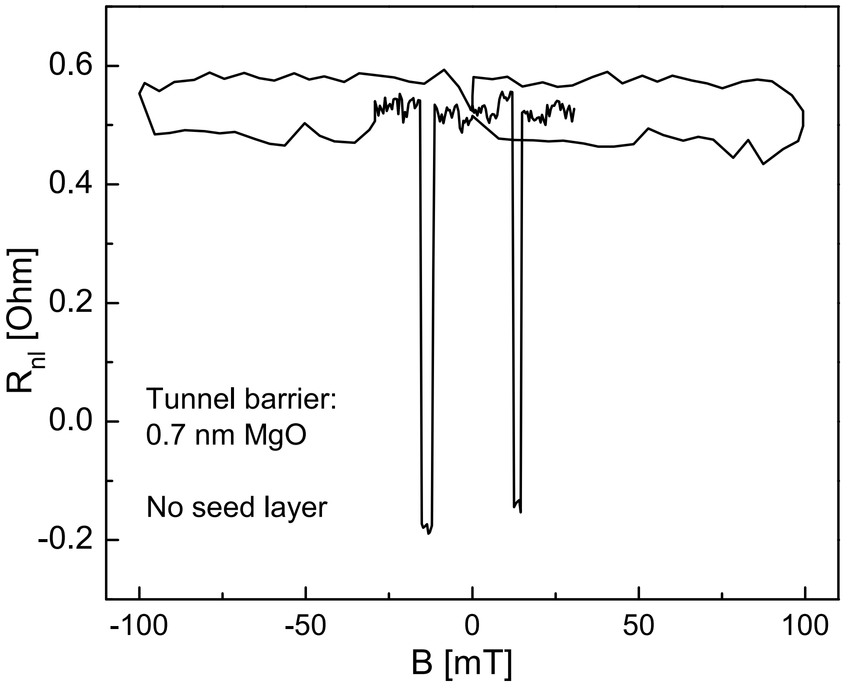

Figure 3.23: Spinvalve data of sample S5F5 at 200 K. Injector/detector distance was 2 μm.

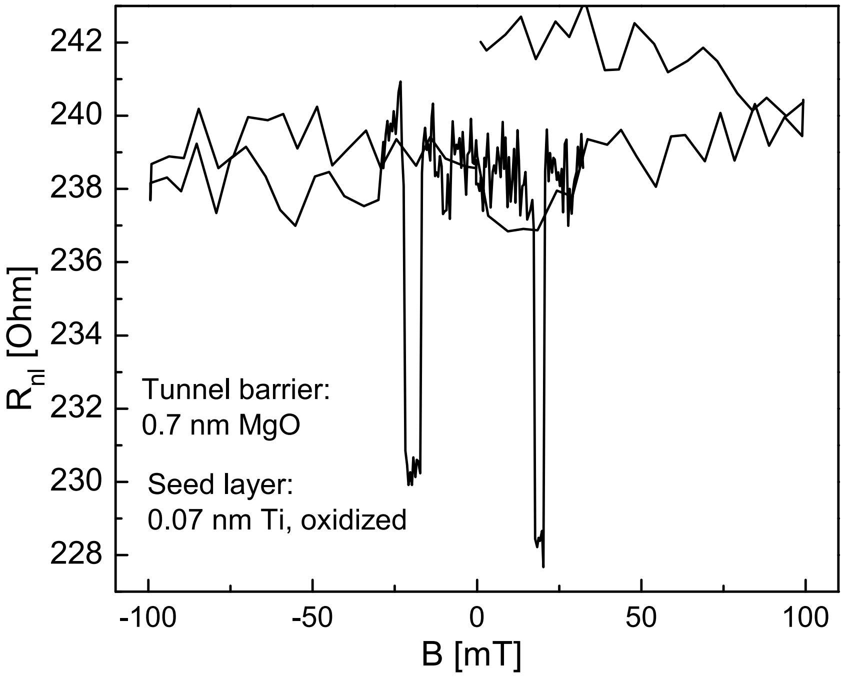

Figure 3.24: Spinvalve data of sample S5F6 at 200 K. Injector/detector distance was 1.2 μm.

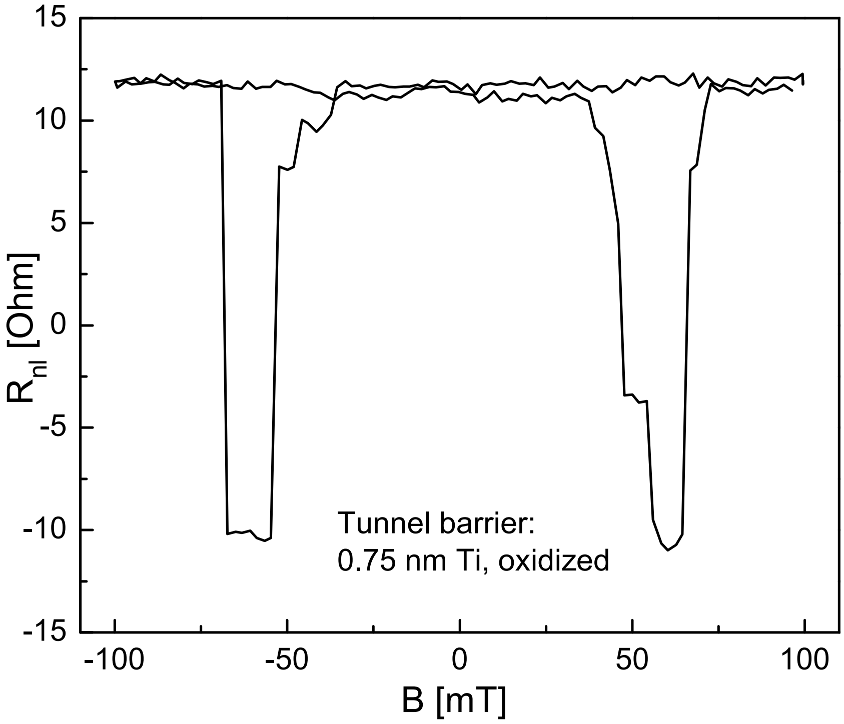

Figure 3.25: Spinvalve data of sample S5B2 at 93 K. Injector/detector distance was 1.5 μm. The signal is quite large, the spin injection efficiency is estimated to $P \approx 15\%$. The unreliable switching can be attributed to the insufficient thickness of the 15 nm Co layer.

As can be seen from this comparison, adding the TiO$_x$ seed layer on sample S5F6 increased the resistance area product by two orders of magnitude. This huge effect is astonishing, considering only 0.073 nm (3 Hz) of Ti were deposited. Further noted should be the „telegraph noise“ change in resistance of the contacts on sample S5F6, which was a commonly observed feature of contacts containing TiO$_x$. By comparison, the change in resistance of contacts on sample S5F5 was $\sim$1%.

The increase in contact resistance from sample S5F5 to S5F6 could be caused by a difference in growth of the MgO that results in less pinholes and/or the additional TiO$_x$ in the barrier stack. We believe the TiO$_x$ is responsible for most of the contact problems. As has been mentioned at the start of this section, the increase in thickness through oxidization of Ti is disproportionally large. If we assume our AFM two stack comparison data is correct, 0.073 nm of Ti expand to 0.55 nm TiO$_x$. This additional tunnel barrier thickness would be consistent with the increase in contact resistance.

To test if it is the TiO$_x$ that is responsible and not the difference in growth of MgO on a TiO$_x$ seed layer, we fabricated samples with just a TiO$_x$ tunnel barrier. We have grown samples with a tunnel barrier as thin as 0.27 nm (11 Hz) Ti, oxidized, and observed contact resistances close to MΩ. These measurements indicate that there is something amiss with our TiO$_x$.

Our results for samples with TiO$_x$ tunnel barriers have been very inconsistent. Despite the MΩ contact resistance of the sample with 0.27 nm Ti, we produced one sample (S5B2)

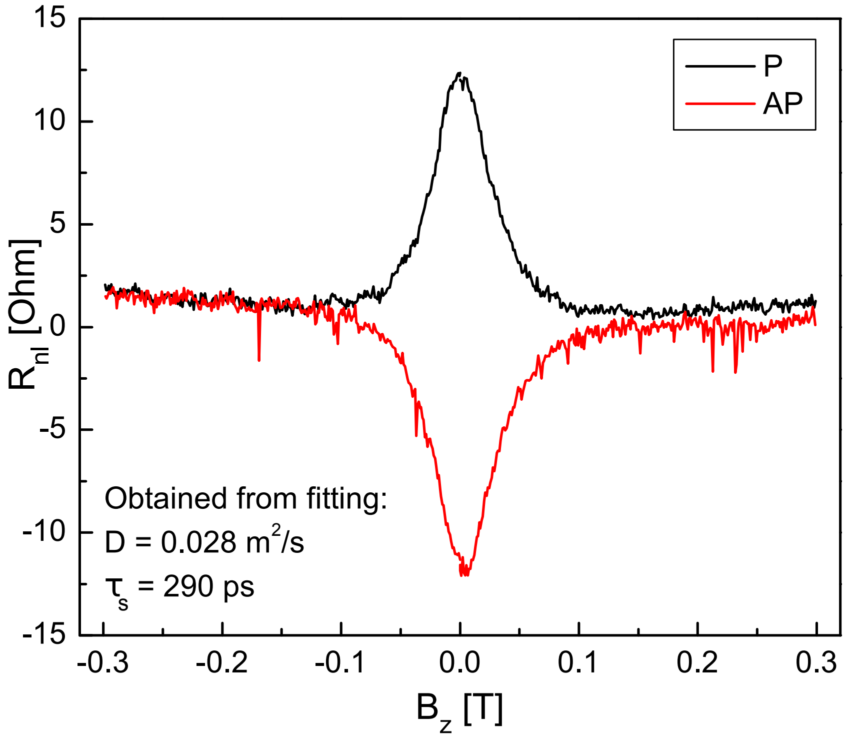

Figure 3.26: zHanle data of sample S5B2 at 93 K. Raw data, no smoothing.

with a thicker tunnel barrier but lower contact resistance. The tunnel barrier consisted of 0.75 nm Ti, oxidized, and contact resistance was between $0.5\,\mathrm{k}\Omega\mu\mathrm{m}^2$ and $12\,\mathrm{k}\Omega\mu\mathrm{m}^2$ for the three contacts that showed a spin signal. A sample spinvalve measurement is shown in Fig. 3.25, Fig. 3.26 shows a zHanle measurement. The signal was very good, the spin injection efficiency of the contacts could be estimated to $P \approx 15\%$, which is identical to the MgO contacts of sample S7F2. However, the distance between the contacts was $1.5\,\mu$m and not sufficiently long for a successful xHanle measurement.

We were not able to produce another sample like S5B2 with working TiO_x contacts. Also, our TiO_x when used as a seed layer will not improve the MgO contacts. When this was demonstrated by comparing S5F5 to S5F6, we did not produce any more samples containing TiO_x.

3.6 Preparing a graphene spin transport device

Preparing a sample starts by cleaning silicon chips with an oxidized surface that have already been prepared with markers. Then graphene is exfoliated onto those chips and they are placed under a microscope to find suitable single layer flakes. The flakes should be as long as possible and roughly oriented along either axis of the markers on the chips. The Co stripes are then also oriented along one of the axis, which makes their alignment to the magnets of the measurement setup easier. Once a suitable graphene flake is found, unwanted graphite in the surrounding area is removed by scratching with a probestation needle. The chip will then be annealed in vacuum.

The annealing might change the graphene flake. If there are any folded edges, they will probably curl up further, possibly tearing the graphene. This can be seen in Fig. 3.27. By annealing early in the fabrication process, flakes that become unusable through the procedure get sorted out before much work was wasted on them. The annealing is required to make the deposited tunnel barrier smoother and prevents the graphene flakes from being washed away during spin coating.

The next step now depends on what sample design is chosen. The tunnel barrier can be deposited over the whole chip or just under the contacts (local barrier). For measurement purposes, the local barrier is generally superior as then non magnetic reference contacts can connect to the graphene without a tunnel barrier. Also, the barrier material covering the whole graphene might cause unwanted doping. For MgO barriers, local contacts are of a better quality because the MgO is not exposed to air [84]. AlO_x on the other hand can benefit from being deposited on the whole chip because then the graphene is not yet contaminated by residues from the lithography.

We used the local contacts for samples intended to produce data. To test and tune the tunnel barrier, we occasionally used the chip wide barrier deposition when we thought side contacts might be a problem. Samples only intended for tunnel barrier testing, local or non-local, also had a simpler design using just one lithography step. Then the Co was also used for the bond pads and all contacts to the graphene were magnetic and had a tunnel barrier. A picture of this design can be seen in Fig. 3.28.

The two step lithography for samples intended to produce data would create the Co stripes in the first step and then connect them with Pd in the second step. This enables AMR measurements of the Co stripes as well as non magnetic reference contacts to the graphene.

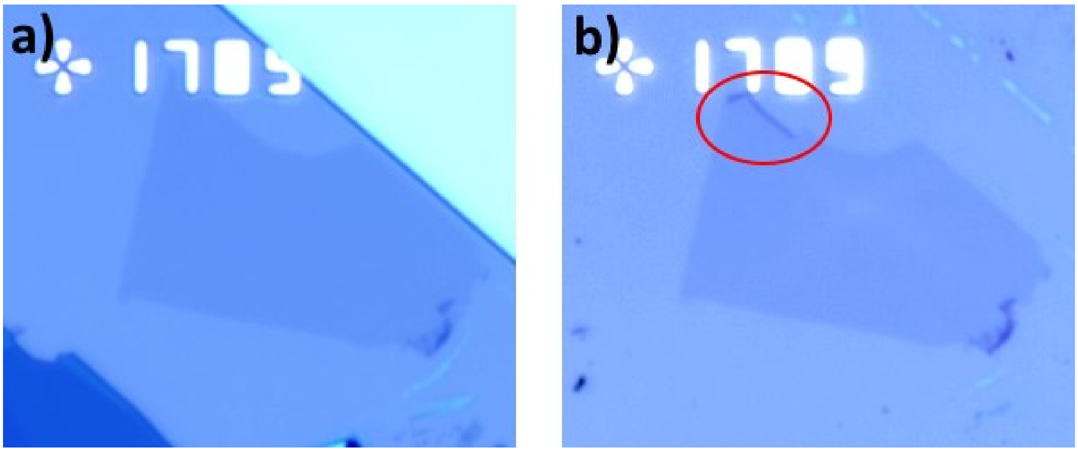

Figure 3.27: Sample S7F1 a) before and b) after annealing. The red circle indicates where the graphene edge curled up during annealing. In b) the unwanted graphite next to the graphene was removed by scratching with a probestation needle.

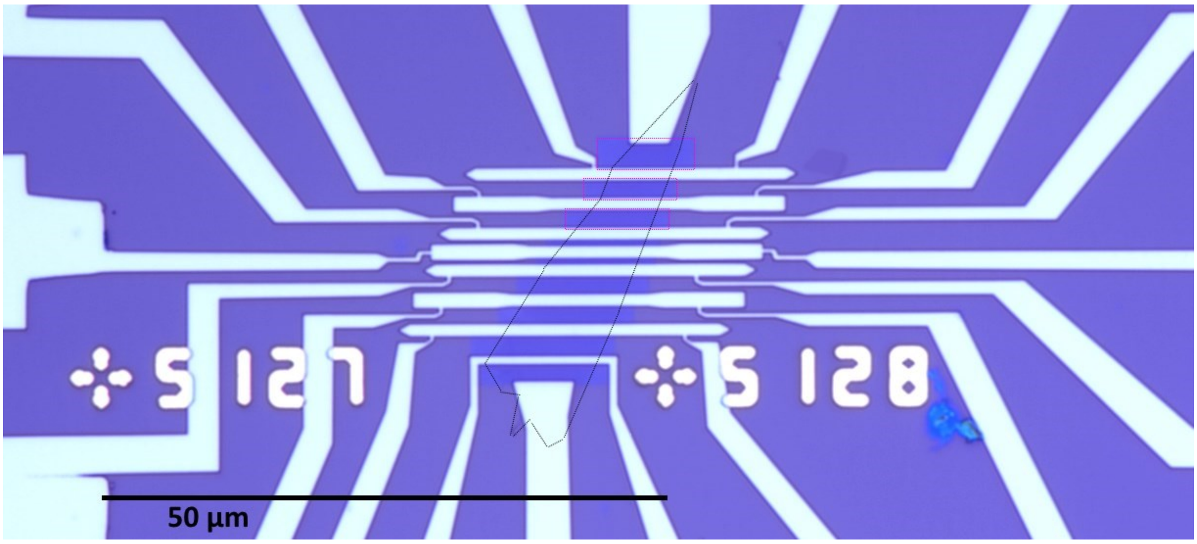

Figure 3.28: Sample S5F6 with a simpler one step lithography intended for tunnel barrier testing. Covering part of the graphene flake is a TiO_x hard mask to prevent side contacts. The graphene flake is marked by a black outline. In the top part, the TiO_x hard mask is marked with a pink outline. The hard mask is also present in the lower part, but not marked.

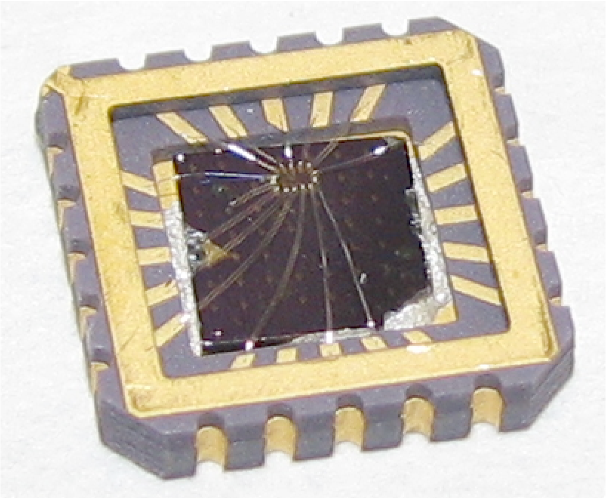

Figure 3.29: Finished sample, glued into the chipcarrier and bonded. The large markers on the chip can be seen without a microscope.

The material Pd is chosen instead of the commonly used Au because the contacts to graphene have a lower electric resistance. It must be noted however that this may prohibit further annealing of the sample. In our samples, the contacts where Pd was on top of Co had an unwanted change of the magnetic behavior after annealing. This is probably due to material diffusion at the interface, as Pd can become ferromagnetic by a small doping with other materials [100].

After lithography and material deposition are finished, the chip is glued into a chipcarrier as seen in Fig. 3.29. The chipcarrier has a conducting surface to connect to the SiO_2 and use it as a backgate. For a good electrical connection, one corner of the chip (lower right one in Fig. 3.29) is broken off with the help of a diamond scriber to have a clean non-oxidized Si surface which is then contacted with two component conductive Ag glue. As the two component Ag glue is quite plastic, care must be taken to avoid gluing the chip in a skewed position.

Alternatively, a drop of PMMA on the chip backside can be used as glue to avoid the skewed chip problem. PMMA also has the advantage that it hardens almost instantly when put on a hotplate (5 sec on 150°C hotplate). To ensure that the silicon is conductively connected to the chipcarrier surface, a little bit of the Ag containing part of the two component glue still needs to be applied to the broken off corner of the chip.
Once the glue has hardened, the bondpads on the chip are connected to the chipcarrier by aluminum wire bonding. The power and force settings should be as low as possible to prevent damaging the chip, which might cause a backgate breakdown. After bonding, the sample is ready for measurement.

3.7 Measurement setup

For the measurements, we used a liquid helium cryostat with a 3D vector magnet built by *Cryogenics* that allows temperatures down to 1.6 K, schematically shown in Fig. 3.30. The vector magnet consists of three superconducting magnet coils capable of 1 T, one big coil for the z axis and two identical smaller ones inside the z coil for the x and y field. While the oblique spin precession experiment requires two coils, the xHanle experiment requires all three coils. The y magnet is needed to switch the magnetic orientation of the electrodes from parallel to antiparallel. The z and x magnet are used for zHanle and

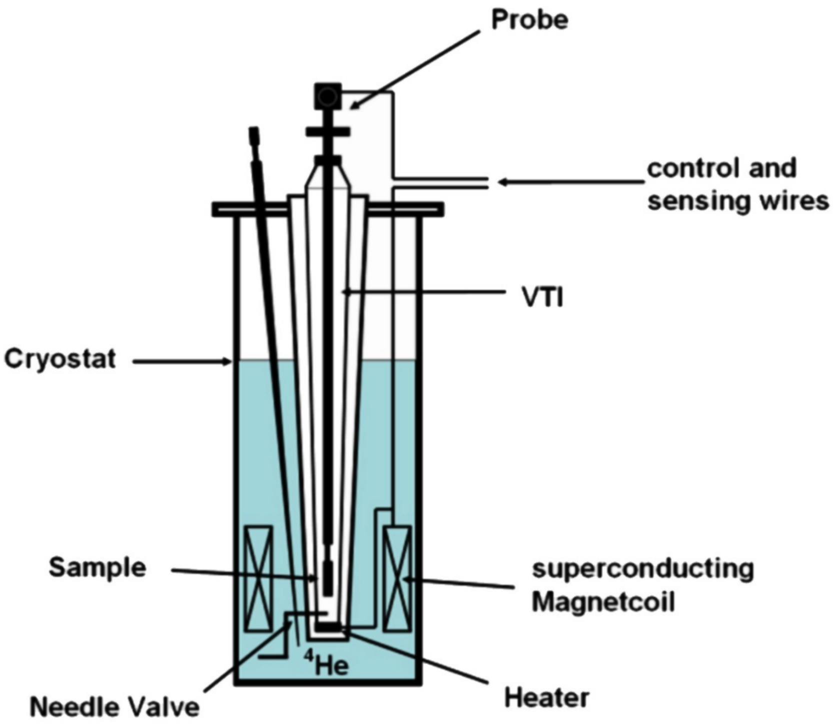

Figure 3.30: Schematic of the cryostat. Adapted from [101]

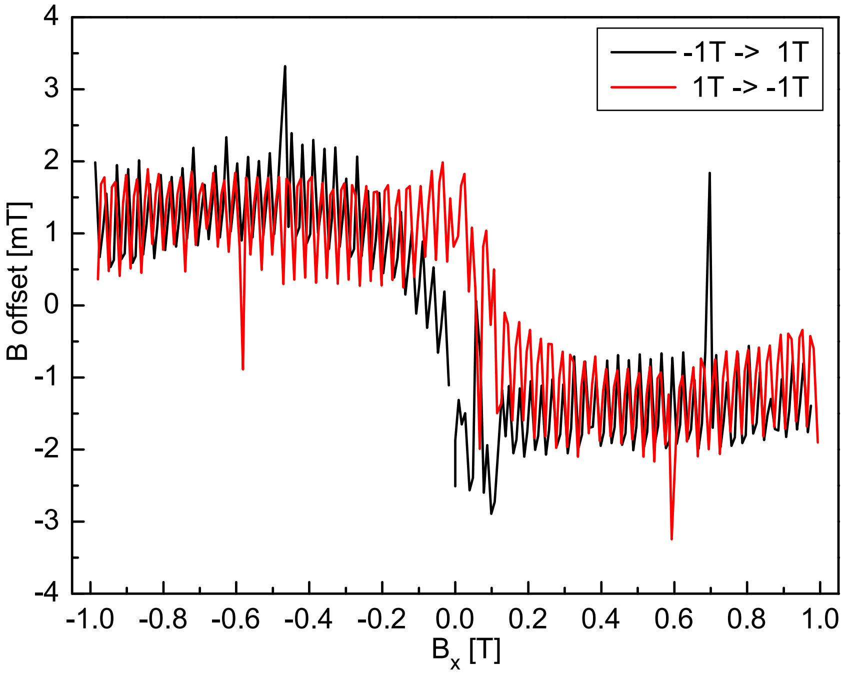

Figure 3.31: Deviation of the x magnet coil from a linear current-to-field behavior. The different sweep directions show that the offset is dependent on the magnetic field history of the magnets.

xHanle, while z and y magnet together are used for the oblique magnetic field. zHanle, xHanle and the oblique spin precession were measured using different magnets, so we needed to check for calibration errors, sample misalignment, and stray fields to properly analyze the data.

Our magnet setup does not yet have a permanently installed Hall sensor, which would be the ideal solution to accurately set the magnetic field. We checked the calibration of the magnets with a Hall probe that was placed in the setup instead of a sample. In the field range of 25 mT which was used for the xHanle measurement, the x and y magnets produced a field that was only 89% of what was expected. For larger fields the output was at 96%. The z magnet was calibrated correctly. Because of this calibration error, the xHanle measurement range was actually 22 mT and not 25 mT.

We also tested for magnetization shifts due to hysteresis or trapped fields in the superconducting coil. The deviation from a linear current-to-field behavior of the x magnet is shown in Fig. 3.31. For field values above ±250 mT, the offset is constant, while in the field range from -250 to 250 mT the offset is dependent on the magnetic field history of the magnets. We repeated the magnetic cycle that we used for the Hanle measurements in section 4.2.1 and found offset fields of about 1-2 mT in the x and y magnet were possible. When the x or y magnet is set to zero, this offset remains present as stray fields and must be accounted for when processing the data.

To measure the samples, a DC setup was used. This is schematically shown in Fig. 3.32 for the non-local spin transport measurement. In this setup, the current is set by the current source and not separately measured. Previously, this setup also contained a current amplifier (DL Instruments Ithaco 1211) placed between the graphene and ground which allowed to automatically log the current at the injector contact. However, the current amplifier when used together with the nano volt meters (Agilent 34420A) turned out to create voltage spikes exceeding several volts. Tunnel barriers can get damaged by these, so the current amplifier was removed.

The tunnel barriers we used on our samples were at times very fragile. It happened occasionally that the contact resistance changed after reconnecting the sample (turn off the current, ground the contacts, reconnect, turn the current back on). The change in contact resistance also meant a reduction or loss of the spin signal. Consequently, we avoided as best as possible to reconnect a sample for fear of possible damage. During measurement however, contacts were robust enough to withstand an injector bias of up to 1 V.

A few samples were also destroyed by a backgate breakdown that happened at elevated voltage. A voltage bias of up to 30 V was generally considered safe for our backgates, up to 60 V was risky and going up to 80 V would result in a backgate breakdown on most samples. These values were confirmed in a study by Barbara Klinger [102], who found the problem to be caused by the aluminum wire bonding. For future samples, the backgate reliability can be increased by using a different bonding machine, increasing the thickness of the bond pads and careful placement of the bonds in the middle of the pads.

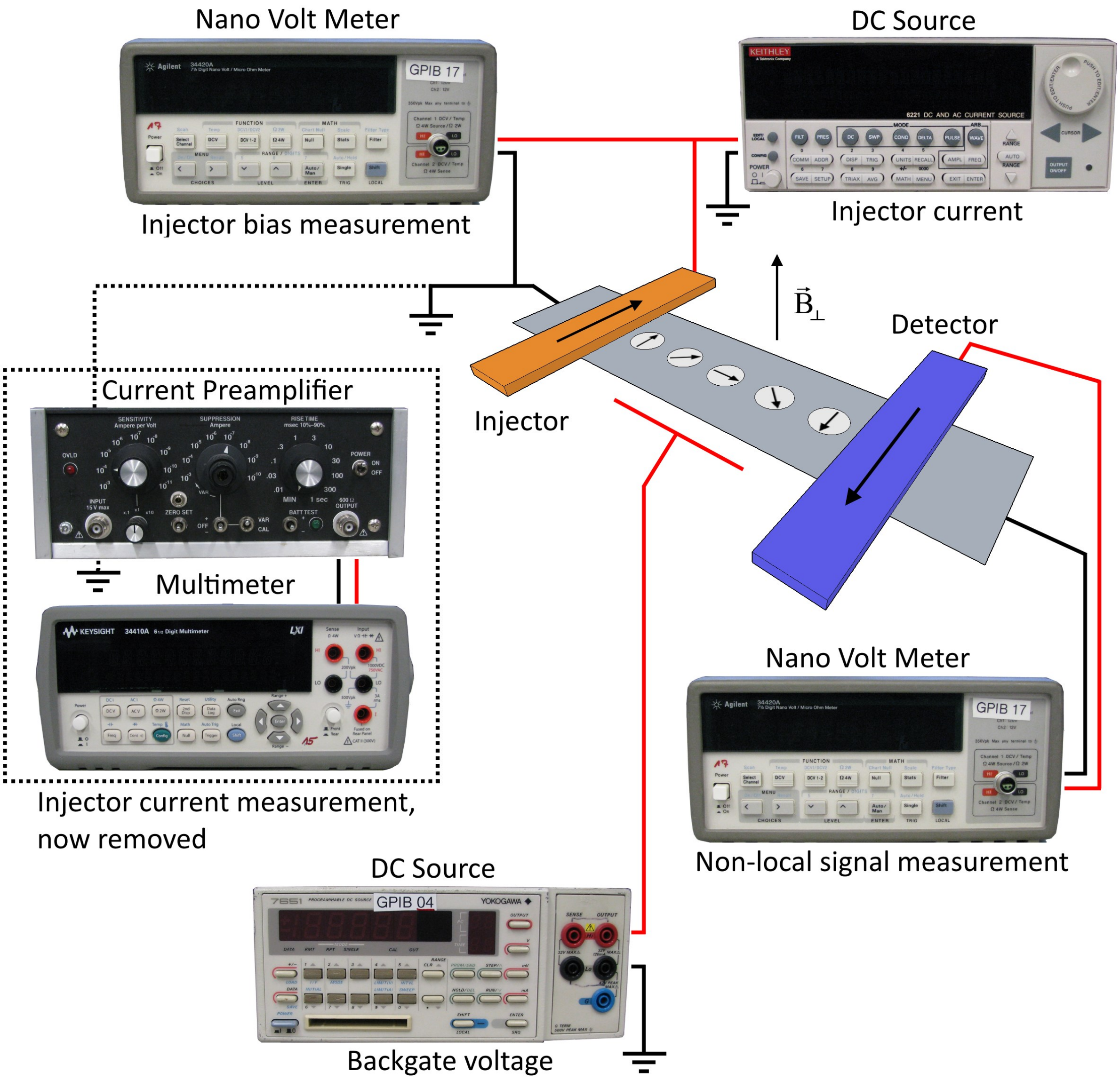

Figure 3.32: Schematic showing the DC setup to measure the non-local spin signal with an injector and detector circuit.

Chapter 4

Experiments on anisotropic spin relaxation

In this chapter the experiments on anisotropic spin relaxation are discussed, schematically pictured in Fig. 4.1. The xHanle experiment and the oblique spin precession experiment are performed on the same sample. To fit the xHanle data, a numerical simulation is used that can calculate spin precession with anisotropies in the spin-lifetimes under magnetic fields in any direction. A small anisotropy is observed in both experiments, but the values are slightly different. The two experiments are then compared in terms of reliability and precision.
A non-trivial magnetization of the electrodes is discovered that serves as an example to demonstrate that the xHanle experiment is more reliable. For the discussed sample and experimental setup, the xHanle experiment is more precise, primarily due to said non-trivial magnetization of the contacts. An argument is made that even for an ideal sample and setup, the xHanle experiment should offer a higher precision.
Finally, it is discussed what conclusions can be drawn from the data about the dominant spin relaxation mechanism in the sample. The data can be explained by the combined action of isotropic mechanisms, such as relaxation by the contacts and resonant scattering by magnetic impurities, and an anisotropic Rashba spin-orbit based mechanism.

This chapter is based on the publication „Measuring anisotropic spin relaxation in graphene“, S. Ringer, S. Hartl, M. Rosenauer, T. Völkl, M. Kadur, F. Hopperdietzel, D. Weiss, J. Eroms, arXiv:1711.06472 (2017).

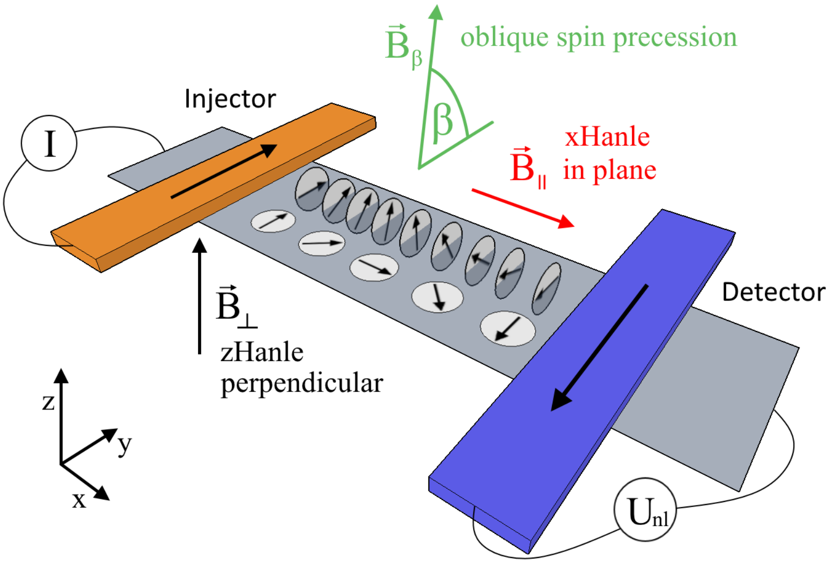

Figure 4.1: Sample schematic illustrating the different orientations of the magnetic fields. The non-local detection scheme, where the charge current path is outside the detector circuit removes spurious effects. The conventional zHanle experiment (black) rotates the spins only in the x-y-plane. The oblique spin precession experiment (green) was introduced in Ref. [76]. In the xHanle experiment (red) the spins also experience the relaxation time τ_z.

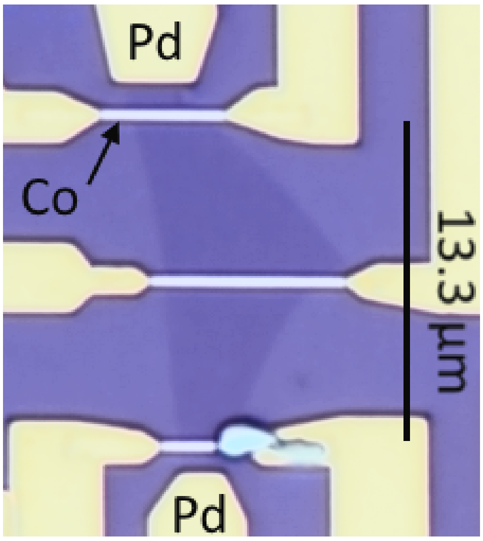

Figure 4.2: Optical micrograph of sample S7F2, showing the graphene flake with contacts. Cobalt electrodes (light gray) serve as ferromagnetic injectors and detectors. Pd electrodes (yellow) provide the spin-independent reference probes and also contact the Co electrodes for AMR measurements.

4.1 Sample characterization

4.1.1 Basic sample characterization and stray fields

The data presented in this chapter is from sample S7F2. Unfortunately, there were no other sample where the experiments could be performed successfully. This was due to failing tunnel contacts, insufficient magnetic properties of the contacts (see for example sample S6C3 discussed in section 3.3), or back gate breakdowns.
Sample S7F2 has a single layer graphene flake that is shown in Fig. 4.2. There are five contacts to the graphene, two Pd end contacts and three Co electrodes. The ferromagnetic Co electrodes are contacted by Pd leads on both ends to enable anisotropic magnetoresistance (AMR) measurements. The outermost contacts to the graphene sheet are made of Pd to have non-magnetic reference contacts which enable non-local spin valve measurements with only two switching contacts. To avoid the conductivity mismatch problem (see section 2.2.5), we use a 1.4 nm thick MgO film underneath the magnetic Co contacts. The exact recipe for the fabrication of sample S7F2 is listed in section A.3. For the anisotropy experiments, only the top and bottom Co electrodes were used. The top electrode was used as the injector and has an area resistance of $46\,\mathrm{k}\Omega\mu\mathrm{m}^2$, the bottom electrode was used as the detector and has an area resistance of $13\,\mathrm{k}\Omega\mu\mathrm{m}^2$. The edge to edge distance between the electrodes is $13.3\,\mu$m. The middle electrode was used in the experiments detailed in chapter 5 and has an area resistance of $27\,\mathrm{k}\Omega\mu\mathrm{m}^2$.

Fig. 4.3 shows a backgate sweep of the graphene sheet resistance, with the Dirac point

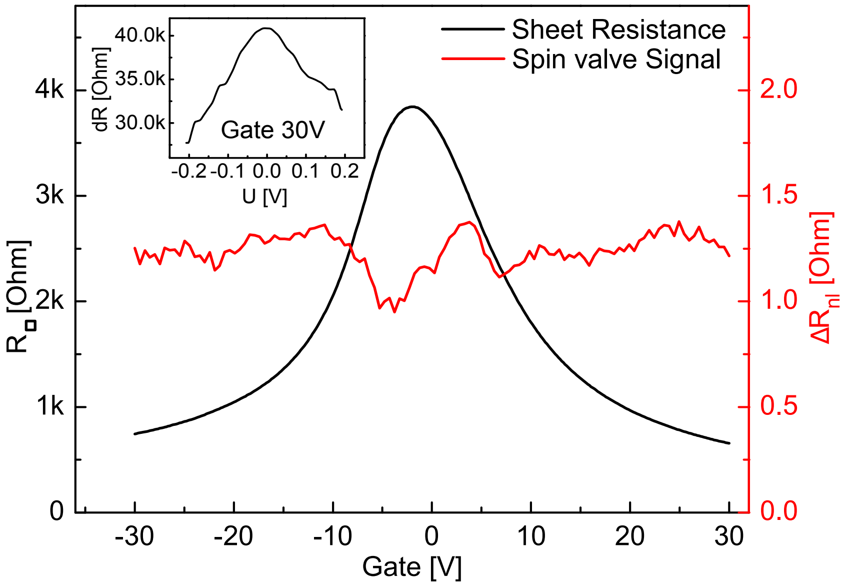

Figure 4.3: Gate dependence of the sheet resistance $R_\square$ and the non-local spinvalve signal ΔR_{nl}. The Dirac point is at -2 V. Inset shows the differential resistance of the injector tunnel contact as a function of current bias.

at $V_g = -2\,\mathrm{V}$, indicating low extrinsic doping. For this measurement, the outermost Pd electrodes were used to bias the sample and the voltage drop was detected between the Co electrodes that are used as injector and detector for the anisotropy experiments. From this data, the carrier mobility in graphene μ was calculated to be between 3500 - 5000 $\mathrm{cm}^2/\mathrm{Vs}$ (depending on backgate voltage). The inset in Fig. 4.3 shows the differential resistance $dR = dV/dI$ of the injector contact. The non-ohmic behavior is an indication for high quality tunnel barriers.

Spin transport measurements were carried out in a non-local DC setup schematically shown in Fig. 4.1 at $T = 100\,\mathrm{K}$. Below this temperature, switching the electrodes into an antiparallel state produced inconsistent results, which can be attributed to incomplete switching of the electrodes. This is further discussed in section 3.3. Fig. 4.4 shows a spin valve measurement at 100 K with properly switching electrodes and a spin valve signal of about $\Delta R_{nl} = 1.2\,\Omega$.
The red graph in Fig. 4.3 displays the gate dependence of the spin valve signal at an injector current of $4\,\mu\mathrm{A}$, used for all spin experiments in this chapter. The graph shows that the spin signal depends only weakly on V_g. At the injector detector distance of $13.3\,\mu\mathrm{m}$, non-local spinvalve signals ΔR_{nl} of 1.0 - 1.4 Ω (depending on backgate voltage, see Fig. 4.3) could be achieved. At negative injector bias there exists a regime where the back gate can be used to change the spin polarization of the injector current. This will be addressed in chapter 5. The anisotropy experiments discussed in this chapter were done at an injector bias where no change in the polarization of the injected spins occurs.

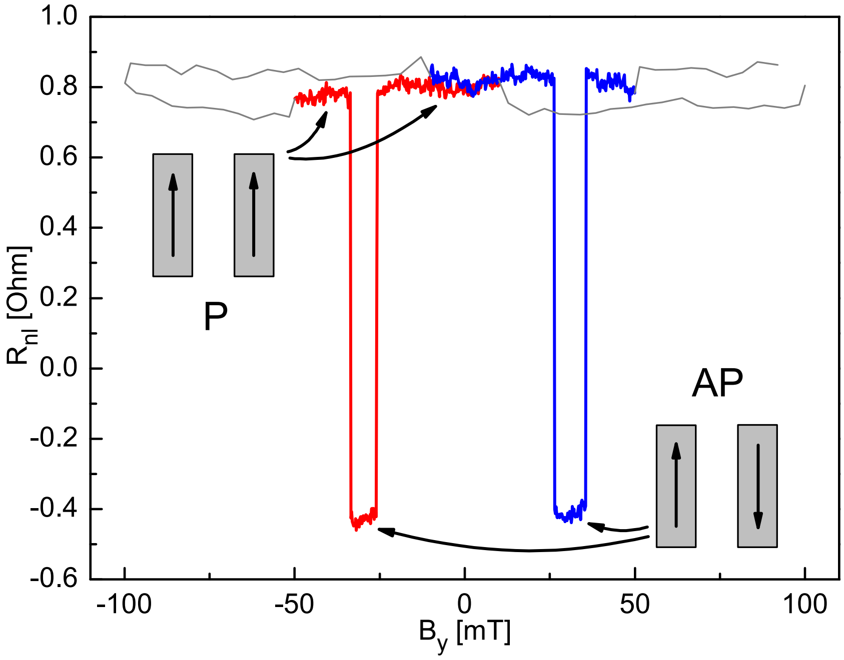

Figure 4.4: Spin valve signal at $V_g = 12$ V with illustrations to show the parallel (P) and antiparallel (AP) magnetic orientation of the electrodes. Distance of the injector and detector contacts was 13.3 μm with an injector current of 4 μA.

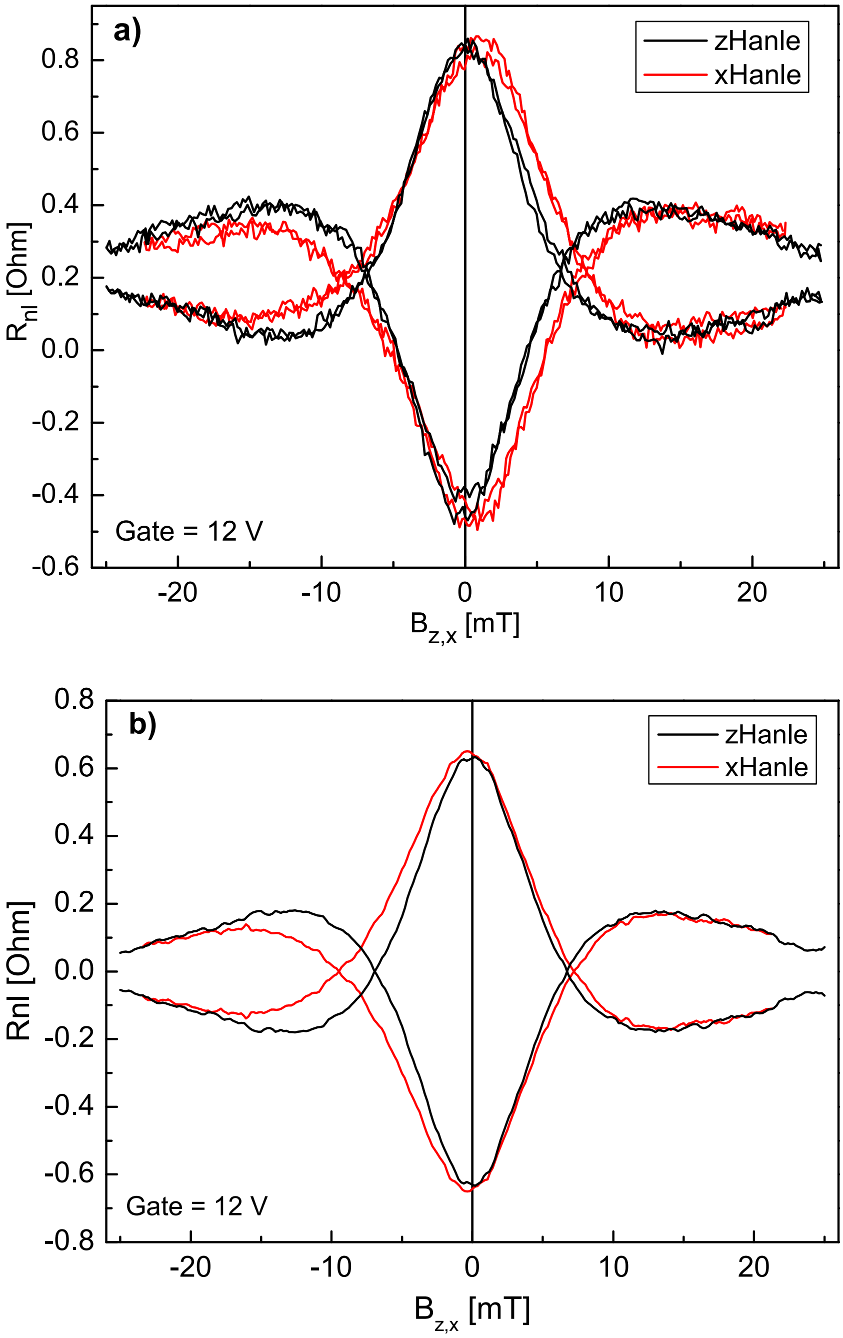

Figure 4.5: a) Raw data and b) smoothed data of zHanle (black) and xHanle (red). Traces for both parallel and antiparallel magnetization were taken in both sweep directions. In b), the xHanle trace is shifted to have the center peak at $B = 0$ for a better comparison with the zHanle trace.

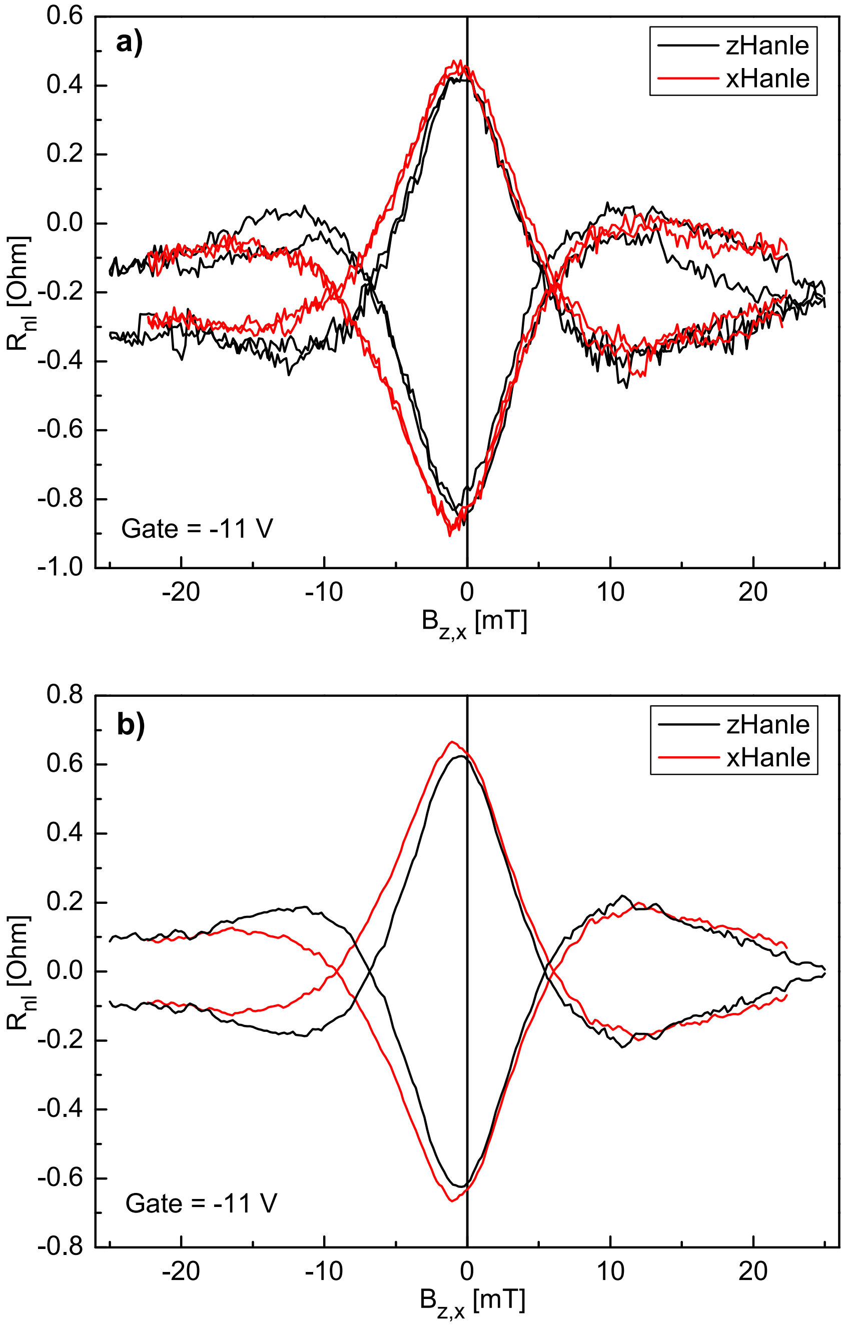

Figure 4.6: a) Raw data and b) smoothed data of zHanle (black) and xHanle (red). Traces for both parallel and antiparallel magnetization were taken in both sweep directions. In b), the xHanle and zHanle traces are not shifted to show the center peak offset field.

As has been stated in section 3.7, unwanted stray fields of 1-2 mT were present in the xy plane during measurement. We will now analyze our spin transport data to see what effect these had on our experiment.

Fig. 4.5a) and Fig. 4.6a) show the raw data of zHanle (black) and xHanle (red) at $V_g = 12\,\mathrm{V}$ and $V_g = -11\,\mathrm{V}$, respectively. As can be seen, there is a distinctive difference between the zHanle and xHanle traces, which will be discussed in more detail in subsection 4.2.1. Measurements were done as an up and down sweep, starting at 25 mT for the zHanle and 22 mT for the xHanle. There is no visible displacement between the up and down sweep, so magnetic hysteresis on this 25 mT/22 mT loop can be neglected.

In Fig 4.5a), the xHanle peak is shifted by 0.8 mT from zero field, which indicates a remanent magnetization of the x magnet. This stray field in x was also present during zHanle measurements and slightly reduced the peak amplitude. This is more obvious to see in Fig. 4.5b), where the up and down sweep is averaged, the background removed and the shift of the xHanle corrected. The z magnet is more accurate and has a smaller remanent magnetization. The maximum observed shift of a zHanle peak was 0.4 mT. This is shown if Fig. 4.6b), where the smoothed traces are not shifted to better show the offset of the center peaks.

For accurate fitting of both zHanle and xHanle, the remanent magnetization has to be accounted for. To calculate the spin precession under influence of an external field in arbitrary direction, including stray fields, misalignment, and the anisotropy of spin relaxation, we employ the diffusion equation for the spin density $\vec{s}$ [35]:

$$\frac{\partial \vec{s}}{\partial t} = \vec{s} \times \vec{\omega} + D\frac{\partial^2 \vec{s}}{\partial x^2} - \tau_s^{-1}\vec{s} \tag{4.1}$$

with

$$\tau_s^{-1} = \begin{pmatrix} \tau_{xy}^{-1} & 0 & 0 \\ 0 & \tau_{xy}^{-1} & 0 \\ 0 & 0 & \tau_z^{-1} \end{pmatrix} \tag{4.2}$$

the anisotropic spin relaxation rate, D the spin diffusion constant and $\vec{\omega}$ the Larmor precession frequency vector, which is parallel to the magnetic field vector. While for Hanle experiments in isotropic media an analytical solution exists that is commonly used to fit the data [35], we resort to a numerical finite element solution using the commercial software package COMSOL to account for anisotropic spin-lifetimes. The simulated traces are then compared with experimental data of zHanle and xHanle. The parameters of the simulation are varied until the best possible match is obtained. The implementation of the spin diffusion equation into COMSOL was developed by Stefan Hartl in his bachelor thesis [103].

We will first analyze the zHanle data, which is the standard characterization method in spin transport experiments. We include stray fields of various strength and can assess the magnitude of the stray fields by the quality of the fit. Fig. 4.7a) shows the smoothed zHanle data with two fit traces, one whith a stray field in y-direction of 1 mT and the other with 2.5 mT. The stray field in x of 0.8 mT is the same for both fits. As can be seen, the 1 mT trace gives a perfect fit, while the 2.5 mT trace is noticeably worse in comparison. We conclude from these fits that our assessment of a maximum stray field

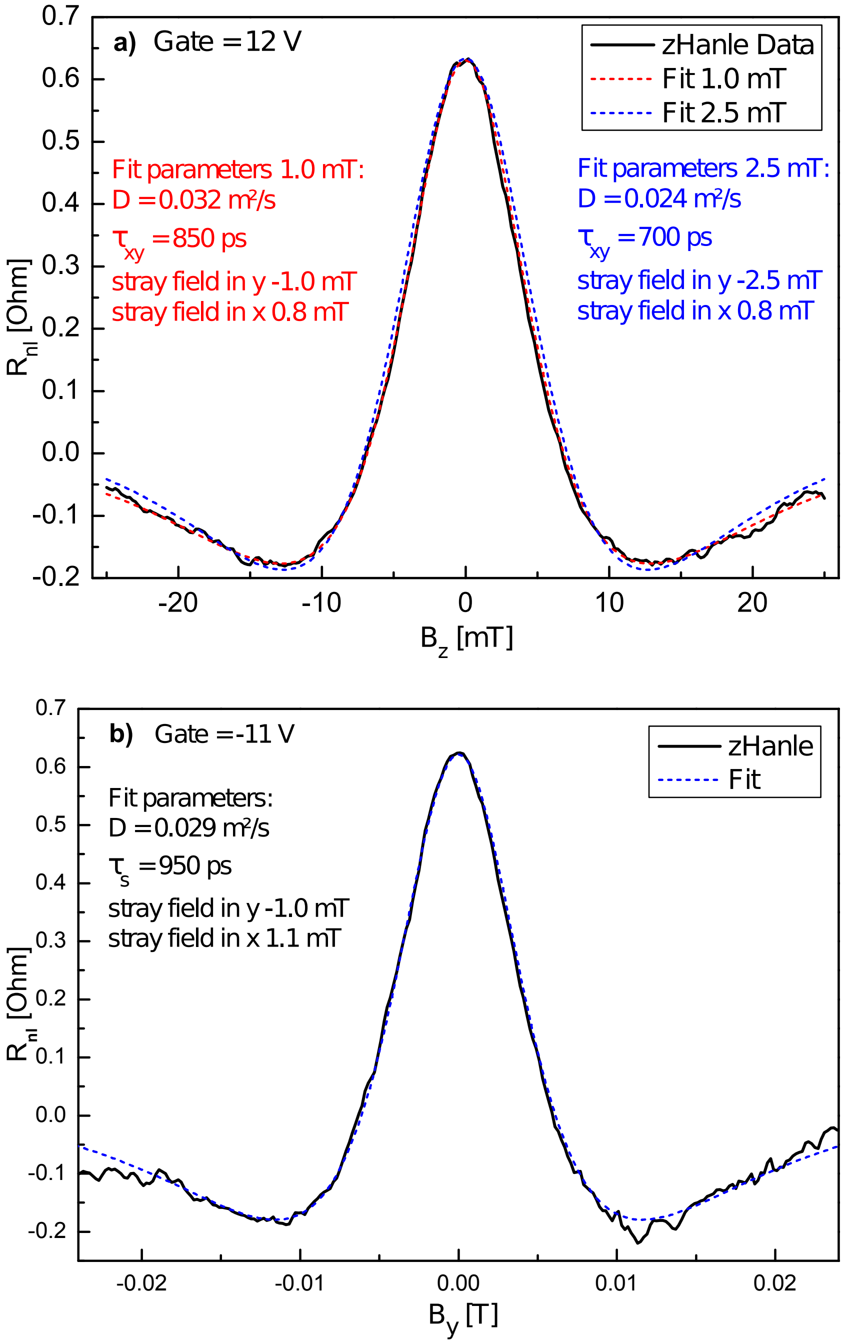

Figure 4.7: a) Smoothed data of zHanle (black line) at gate = 12 V with fit traces for a stray field in y of 1 mT (red dots) and 2.5 mT (blue dots). b) Smoothed data of zHanle (black line) at gate = -11 V with fit traces for a stray field in y of 1 mT (blue dots).

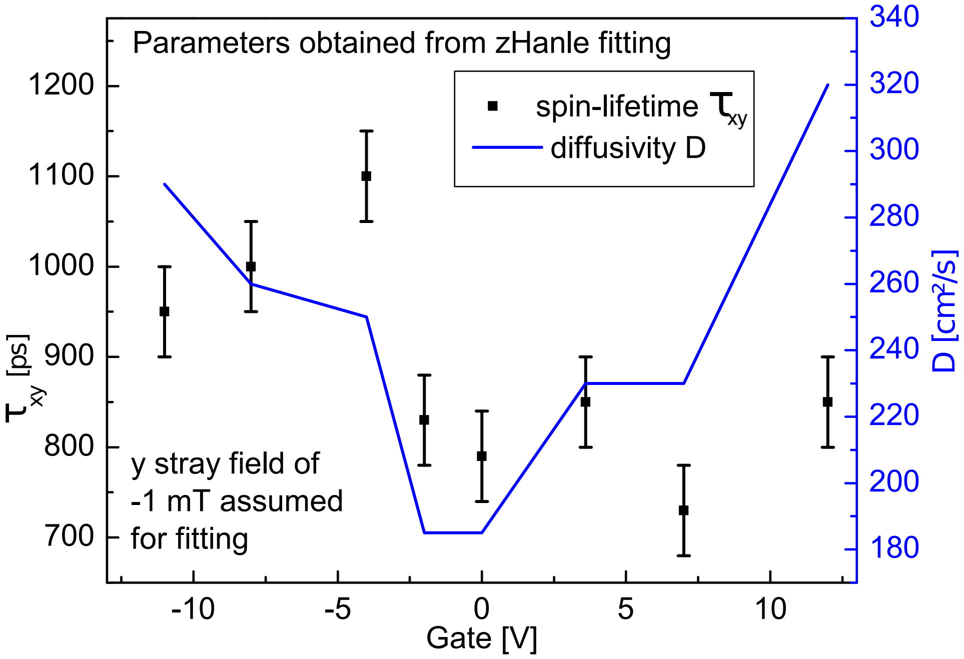

Figure 4.8: In plane spin-lifetime τ_{xy} and diffusivity D vs. gate voltage, extracted from fitting zHanle data with -1 mT stray field in y.

strength of 2 mT is correct.

The stray field in x reduces the amplitude of the zHanle signal and has little influence on the shape. It can accurately be obtained by comparing the amplitude of the center peak of the zHanle and xHanle trace. The stray field in y has no influence on the center peak but reduces the height of the secondary peaks, in zHanle as well as in xHanle. Because of this, when fitting zHanle data for various stray fields in y, the parameters D and τ_{xy} have to be adjusted for stray fields exceeding 1 mT to keep the amplitude of the secondary peaks. Consequently, the fit results for D and τ_{xy} depend on the stray field strength. For our data, a stray field in y of 1 mT gives the best fit and for this stray field strength adjustments to D and τ_{xy} are not yet necessary.

It should be noted that the effect of the stray fields on the Hanle signal is unchanged when the direction of the stray field is inverted, as long as the sample is perfectly aligned. The effects of stray fields on a misaligned sample are discussed in section 4.2.2.

We fitted the zHanle data for several gate voltages and extracted the parameters for spin diffusivity and spin-lifetime. Fig. 4.8 shows the fitted in plane spin-lifetime τ_{xy} and diffusivity D plotted against the backgate voltage. The spin-lifetimes range from 730 ps to 1100 ps and show no correlation with the gate voltage. The spin diffusivity was a free parameter for the zHanle fit, giving 185 cm^2/s as the lowest value at the Dirac point and 320 cm^2/s as the highest value at $V_g = 12$ V. We also extracted D_e, the electron diffusivity, from the charge transport measurements shown in Fig. 4.3. Theses values are lower than the spin diffusivity ($D_e = 235$ cm^2/s at $V_g = 12$ V). Using the electron diffusivity as a fixed parameter for zHanle fitting produced significantly worse fits, so this was disregarded.

4.1.2 Magnetic orientation of the electrodes

For a correct analysis of the xHanle data, it is important to know how exactly the electrodes rotate towards an external magnetic field in x direction. Ideally, the magnetic field for the xHanle measurement is limited to a range where there is no rotation. Narrow electrodes increase the magnetic shape anisotropy that keeps the magnetization aligned to the long axis and delays rotation. The rotation can be further delayed by lowering the temperature. Additionally, a large distance between the injector and detector contacts narrows the Hanle curve, reducing the required magnetic field.

The Co electrodes of sample S7F2 have a width of 300 nm. Different coercive fields are achieved by shaping the tips of the electrodes as detailed in section 3.3. AMR measurements were carried out to see at what field values these electrodes rotate at 100 K. According to the AMR data displayed in Fig. 4.9, at $B_x = 200\,\mathrm{mT}$ the electrodes are almost fully rotated into the x direction. This rotation is independent of the tip shape, so the AMR data are the same for all electrodes.

The peak width of the Hanle feature scales inversely with the travel time of the electrons. A long distance between injector and detector contact is therefore needed in order to narrow the Hanle feature to a field range well below 200 mT. The xHanle measurements were done at magnetic fields only up to 22 mT to keep electrode rotation minimal. For our injector-detector distance of 13.3 μm, most of the Hanle feature was in that field range.

According to the AMR data shown in Fig. 4.9b), the electrodes do exhibit a slight rotation in the field range of ~22 mT that is used for the xHanle measurement. To further quantify this rotation, we look at the background signal of the xHanle, obtained by adding the P and AP trace. As can be seen in Fig. 4.10, that background is almost constant. A rotation of the electrodes would be indicated by an upwards inclination of the background signal with increasing B-field, which is not the case. This is in disagreement with the AMR data of Fig. 4.9b), where the change in signal from 0 to 22 mT is about 8% of the total signal change.

To validate this disagreement, we fitted the normalized AMR data in x direction with a $cos(\delta)^2$ function to extract the rotation angle of the electrodes (see supplementary of [76]). We assume a linear dependence between the rotation angle δ and the magnetic field in x direction. As shown in Fig. 4.11, for a field range <50 mT this gives a good fit. According to the fit, the electrode rotation at 22 mT is then ~ 17°. Using the extracted function $\delta = 180° \cdot 4.4 \cdot B$ (B field in Tesla), we simulated the xHanle data of Fig. 4.10 for rotating electrodes according to the AMR data. The result is shown in Fig. 4.12. The upwards inclination of the background signal with increasing B-field can be clearly seen. The biggest difference is between the flipped AP trace and the P trace at 22 mT. These features can not be seen in Fig. 4.10, validating that the AMR data does not match the xHanle data.

The difference in the data can be explained by differences in the interface and bulk magnetization of the electrodes. Spin injection and detection are sensitive to the interfaces of the electrodes, while AMR probes the bulk magnetization. It is known that a MgO-

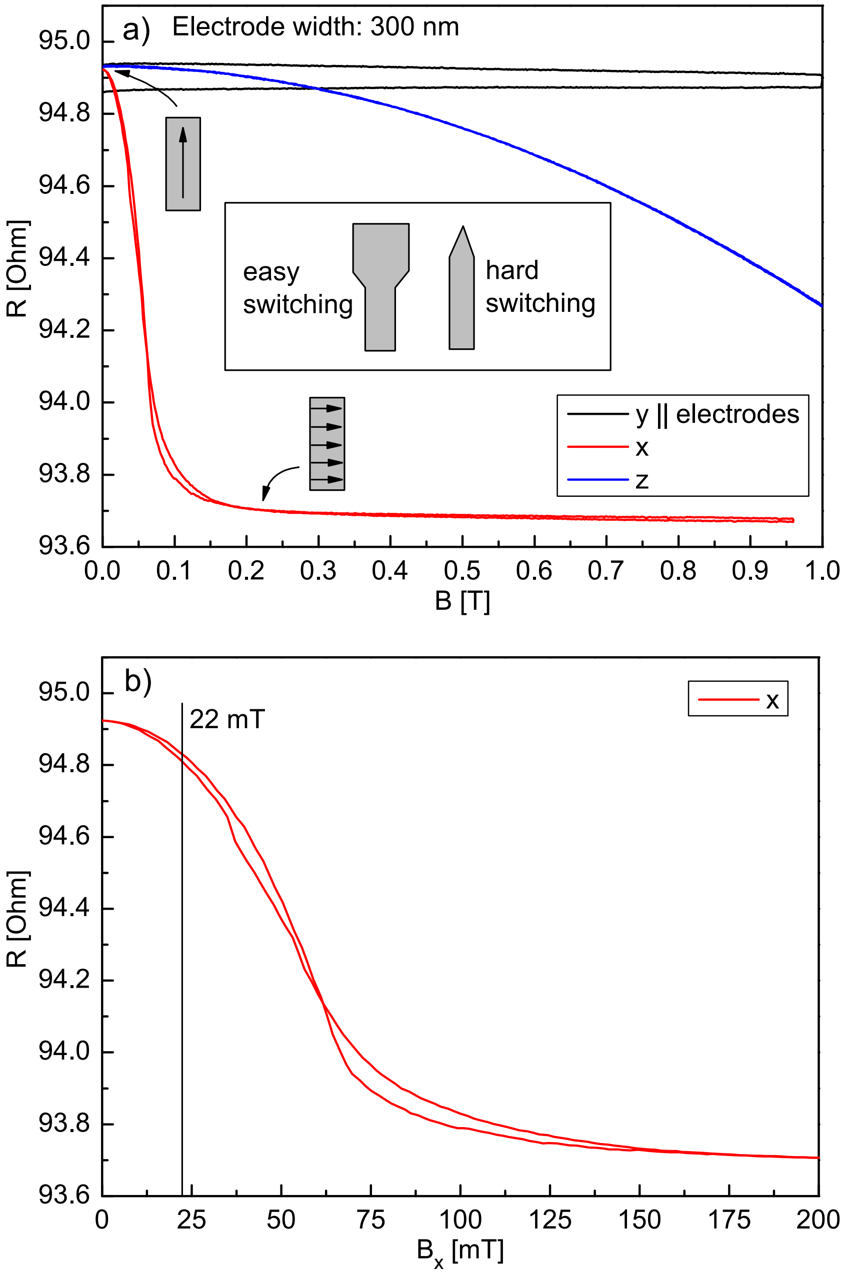

Figure 4.9: a) AMR data of Co electrodes with the external field applied in x, y and z-direction. Illustrations show the orientation of the magnetization in the electrodes. Inset illustrates the shape of the electrode tips, to achieve different coercive fields while using the same body width. b) AMR data of the x direction on a magnified scale.

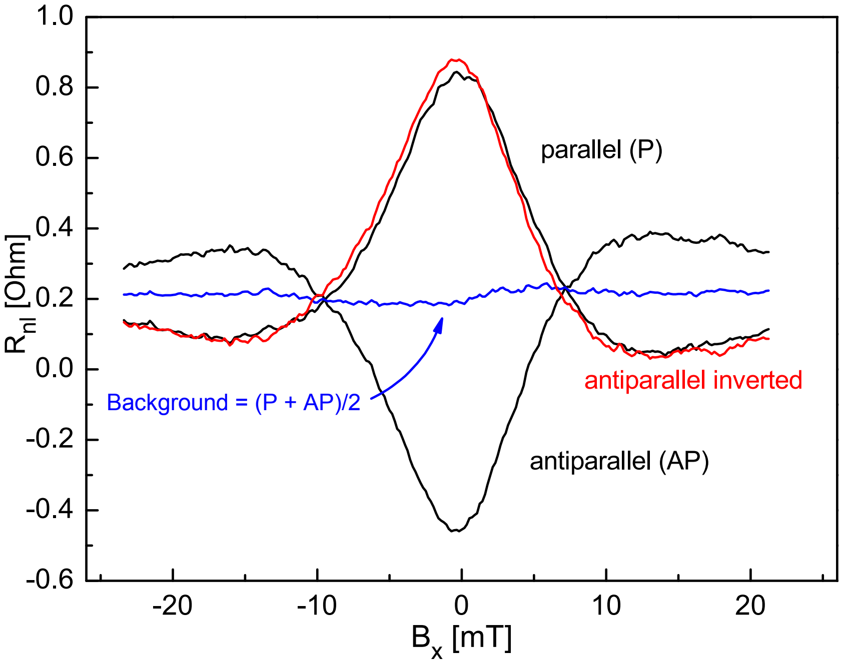

Figure 4.10: xHanle data with extracted background ($\frac{P+AP}{2}$, blue) to check for possible rotation of electrodes. Inverted AP signal in red to check for proper AP alignment and a possible change in the stray fields caused by the switching.

Co interface induces a strong magnetic coupling on the neighboring Co layers [104]. In our sample, this coupling seems to make the interface magnetization more resistant to rotation than the bulk. We therefore believe the conclusion of the data in Fig. 4.10 to be correct and there is little or no rotation of the interface magnetization in the field range of 22 mT.

We can estimate the signal loss because of electrode rotation. The signal scales with $cos(\delta)^2$ (injected s_y scales with $cos(\delta)$ and detected s_y scales with $cos(\delta)$), where δ is the rotation angle with $\delta = 0°$ being the y direction. For $\delta = 6°$ the signal loss is then 1%, which can be considered as the threshold where a slight rotation can be neglected and treated as equivalent to no rotation. We would then conclude that $\delta = 6°$ is the maximum electrode rotation at 22 mT according to the xHanle data in Fig. 4.10.

Further evidence of differences between interface and bulk magnetization is found when trying to fully rotate the electrode in x direction, which is discussed at the end of this section. The interpretation of the xHanle data discussed in section 4.2 also supports the existence of the magnetic coupling at the MgO-Co interface.

Fig. 4.10 also shows the flipped xHanle antiparallel trace, for a direct comparison with the parallel trace. First, this can be used to compare amplitudes of the P and AP signal to ensure that the electrodes have switched properly. As is shown in Fig. 3.11 in section 3.3, incomplete switching can occur at temperatures below 100 K. The traces are identical enough to verify that a complete antiparallel orientation was indeed obtained.

The second information to be gained by comparing the traces is to see if the remanent fields of the y magnet may have changed because of the switching procedure from par-

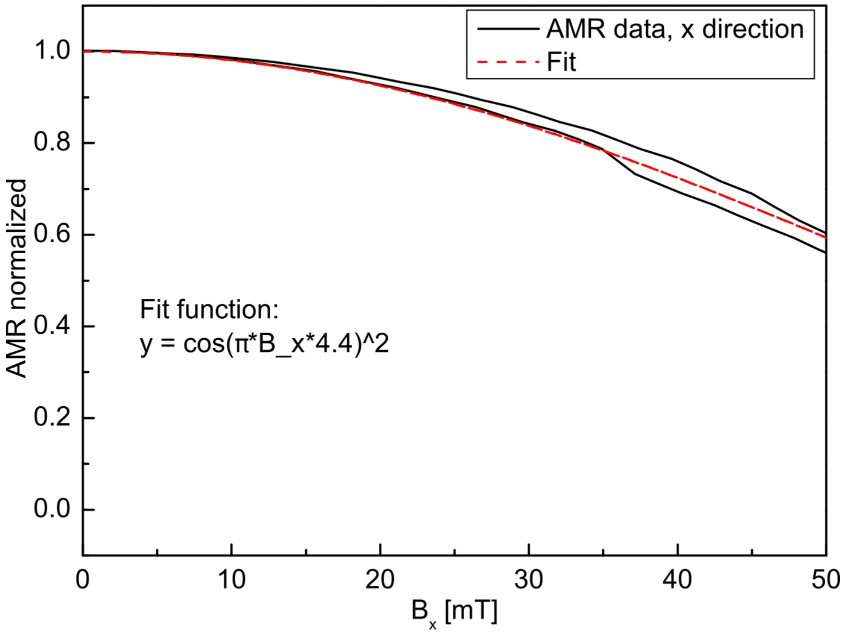

Figure 4.11: Fit of the normalized AMR data in x direction for magnetic fields <50 mT with a cosine function.

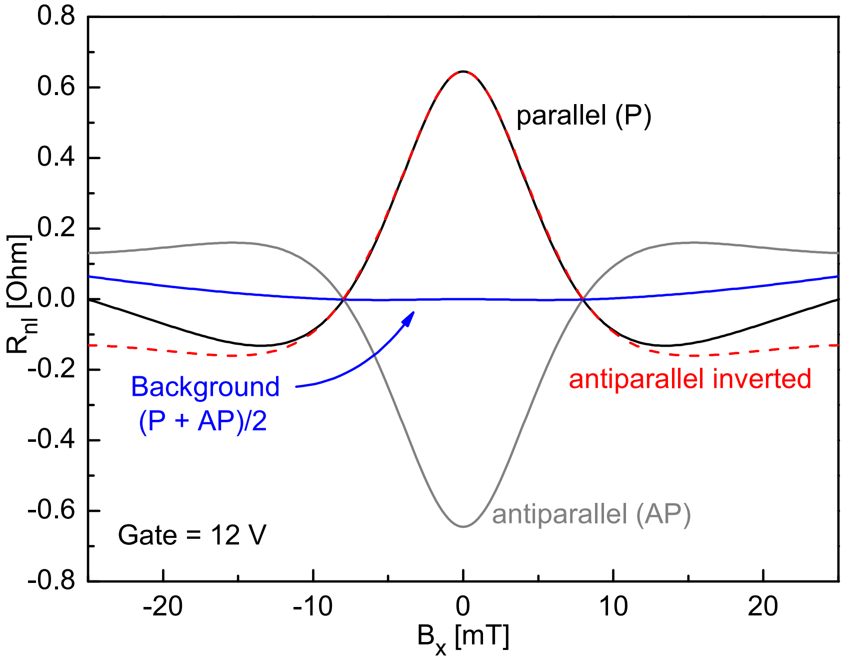

Figure 4.12: Simulated xHanle data for electrodes rotating into the x direction according to the AMR data of Fig. 4.11. The simulation uses the parameters obtained from the $V_g = 12\,\mathrm{V}$ measurement shown in Fig. 4.10.

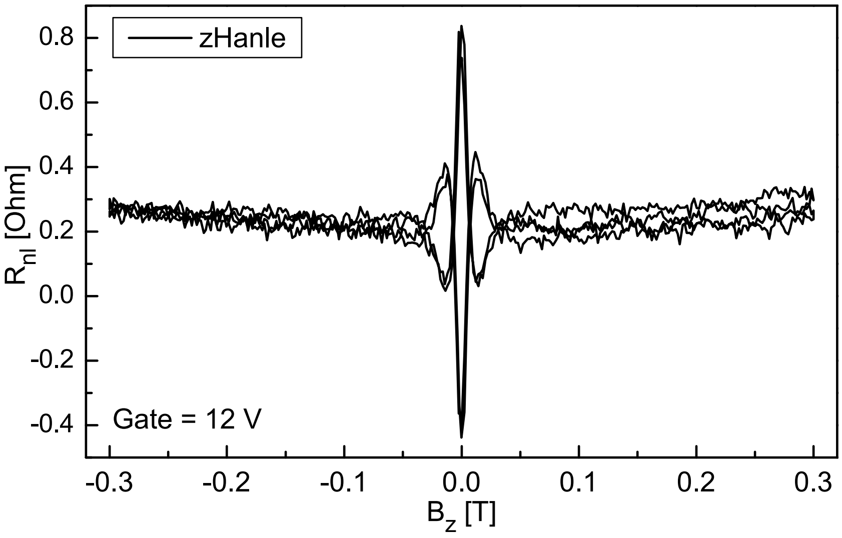

Figure 4.13: zHanle measured up to 300 mT (raw data) to see the background at higher fields in parallel and antiparallel configuration.

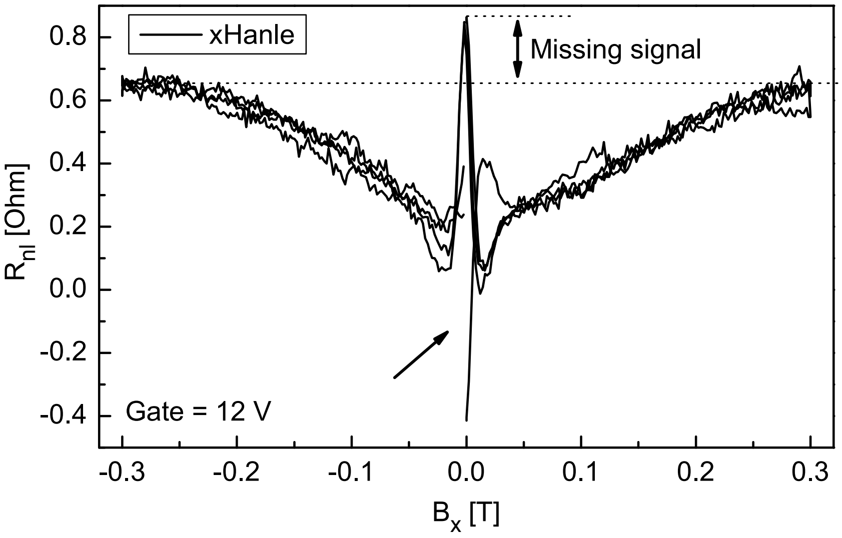

Figure 4.14: xHanle measured up to 300 mT (raw data) to see the rotation of the electrode magnetization. The upper double arrow indicates the difference between actual and expected signal at fields above 200 mT. The lower arrow indicates the missing data of the AP downsweep, because the high B_x field flipped the electrodes back to P.

allel to antiparallel. As the remanent fields depend on the magnetic field history of the magnet, it is a reasonable assumption that performing any field sweep with the magnet may change them. However, the traces are identical enough that we can assume changes in the remanent fields, if present at all, to be small enough to be negligible.

To check our setup, we performed zHanle and xHanle up to 300 mT. The slight symmetric increase of the background in the zHanle data shown in Fig. 4.13 can be attributed to the Co electrodes slowly rotating into the external field towards the z direction. We cannot fully rotate the electrodes towards z as our magnet is limited to 1 T. According to the AMR data in Fig. 4.9 however, 300 mT is enough to rotate the electrodes completely towards the x direction. In this case, the injected spins should remain in plane and propagate without precession. Since B_z remains zero, no orbital magnetoresistance effects that could possibly influence the detected signal should be expected. Therefore, we expect that for complete rotation of the electrodes towards x, the xHanle signal fully recovers the zero field parallel state value.

The 300 mT xHanle is shown in Fig. 4.14 where the non-local signal at 300 mT is noticeably smaller than the zero field value. Since at high B_x the spin orientation remains in the graphene plane all the time, no anisotropy of the spin-lifetime is expected, so the signal loss must have a different origin. The most likely explanation for the signal loss is an imperfect magnetic alignment at the MgO-Co interfaces. Contrary to what the AMR data in Fig. 4.9 suggest, the interface magnetization is probably not yet fully aligned to the external field at 300 mT. This is more evidence that the interface magnetization that is probed by the spin experiment behaves differently than the bulk magnetization that is probed by the AMR. The cause for the difference is again the magnetic coupling of the MgO-Co interface [104] that makes the interface magnetization more resistant against an external field than the bulk magnetization. The linear background seen in the 22 mT xHanle data in Fig. 4.10 is consistent with that finding. We conclude that AMR data alone are not sufficient to characterize the electrodes for spin experiments.

4.2 xHanle measurements

4.2.1 Discussion of Hanle data

We now discuss in more detail the data of zHanle (black) and xHanle (red) at $V_g = 12\,\mathrm{V}$ shown in Fig. 4.5b) and Fig. 4.6b). For isotropic spin-lifetimes where the in-plane spin relaxation time τ_{xy} is the same as the out-of-plane spin relaxation time τ_z, xHanle and zHanle should give identical results. In our data the traces are not identical, which could be caused by anisotropic spin lifetimes.

For xHanle, the magnetic field is aligned along the x axis (see Fig. 4.1), and the spins precess in the y-z plane. Therefore, the xHanle trace is sensitive not only to τ_{xy}, but also to τ_z. To extract the spin-lifetime anisotropy, we first determine τ_{xy} from the zHanle

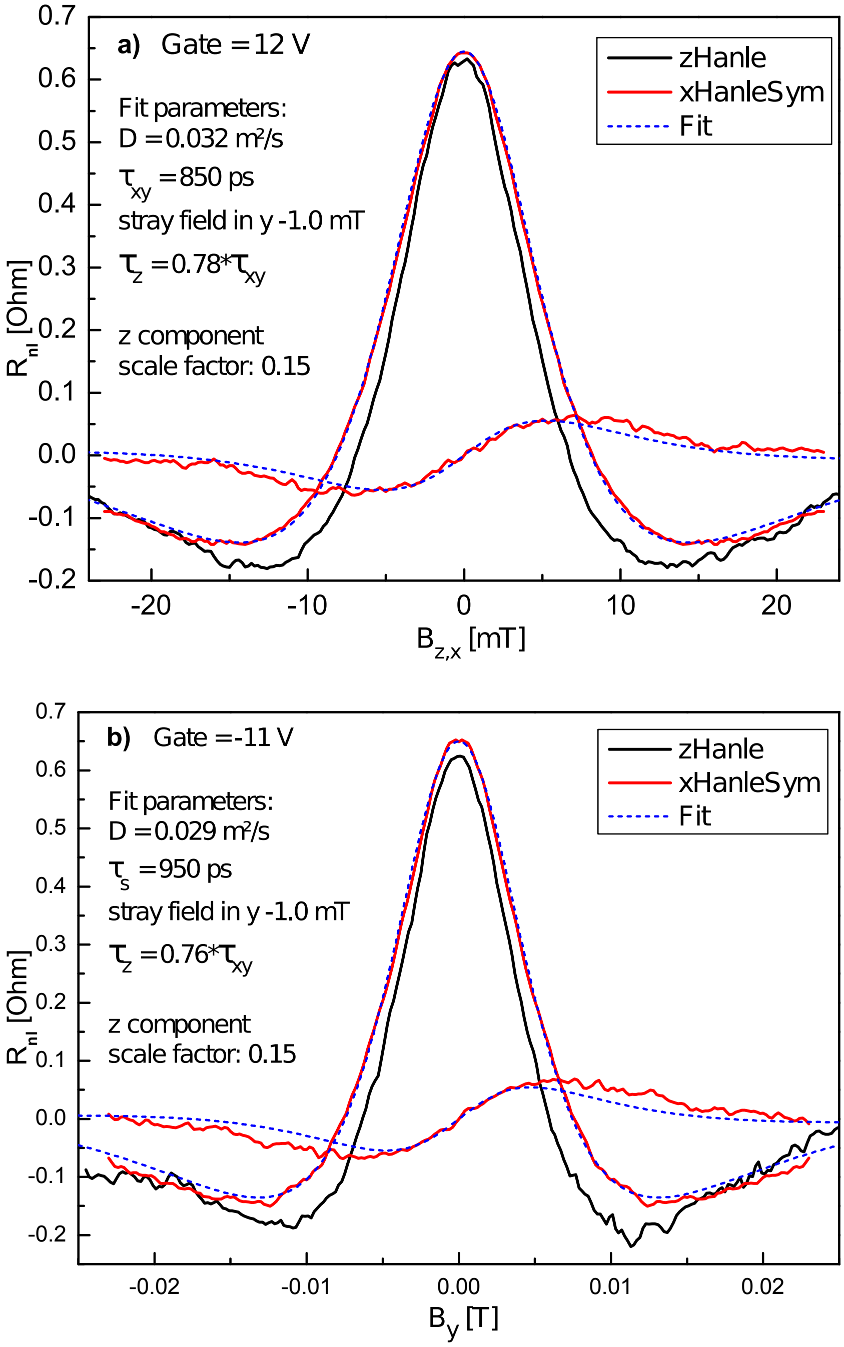

Figure 4.15: zHanle data (black) and symmetrized and antisymmetrized xHanle data (red), with fit traces for the xHanle (blue dashed lines) at a) gate = 12 V and b) gate = -11 V.

data as detailed at the end of section 4.1.1. Then we use these parameters to fit the xHanle data, with τ_z the only remaining free parameter. By comparing τ_z to τ_{xy}, we get the anisotropy parameter $\zeta := \frac{\tau_z}{\tau_{xy}}$.

In the data in Fig. 4.5b) we notice a clear asymmetry with respect to $B = 0$ in the xHanle trace, not present in the zHanle data. This is unexpected and could be due to sample misalignment in combination with stray fields. We simulated Hanle curves for this situation and found that a sample rotation error of more than 12° would be required to produce an asymmetry of the observed magnitude. As this is far more than our estimated error of 3°, and the resulting trace does not match the shape of our data, we disregard this scenario. This is discussed in more detail in the next section 4.2.2.

The most likely cause for the asymmetry of the xHanle signal is then a magnetization misalignment of the electrodes. The mechanism is depicted in Fig. 4.19. Since the zHanle curve is *not* asymmetric, we conclude that the magnetization of the detector electrode contains a small z component in addition to the y component expected from shape anisotropy. Considering that the Co electrodes have a film thickness of 20 nm and are deposited on a near perfectly flat Si wafer, this z tilted magnetization must be a local effect at the MgO-Co interface.

In section 4.1.2 we have compared AMR data with Hanle data and suspected a magnetic coupling at the MgO-Co interface to be present in our sample. It is know that a Co-MgO(100) interface induces a large perpendicular magnetic anisotropy in the neighboring Co layers [104]. This magnetic anisotropy favors a magnetic orientation in z direction, orthogonal to the shape anisotropy of the electrode which favors a y direction. Depending on their respective strength, a tilted magnetic orientation at the interface between the z and y axis is then a possible result. In principle, this can be calculated if the strength of each anisotropy is known. However, the strength of the interface magnetic anisotropy is heavily dependent on crystallinity and oxidization state. Both parameters are unknown for our sample.

To split the xHanle data into their y and z components as detected/injected by the electrode, we symmetrize and antisymmetrize the curves with respect to $B = 0$. The result is shown in Fig. 4.15. We get a large symmetric part that is the projection on the y component of the electrode magnetization and a smaller asymmetric part for the projection on the z component of the magnetization. For isotropic spin relaxation, the symmetric part would be identical to the zHanle as the zHanle is also projected on the y component of the magnetization. The remaining difference between zHanle and the symmetrized xHanle is now due to the anisotropy in spin relaxation. The symmetrized xHanle can be fitted very well with an anisotropy of $\zeta = 0.78$ in Fig. 4.15a) and $\zeta = 0.76$ in Fig. 4.15b). The antisymmetrized xHanle is fitted with the same parameters using only the scaling factor as a free variable. The scaling factor can then be used to estimate the tilt angle between injection and detection magnetization, which is $\sim 9°$. Including the data of other gate voltages not shown here, we get an average of $\zeta = 0.78$ for the anisotropy.

Summarizing this subsection, we note that the xHanle experiment not only yielded the anisotropy $\zeta = 0.78$, but also allowed us to detect a small degree of z-magnetization in the electrodes.

4.2.2 Fitting procedure for zHanle and xHanle

To prepare the data for fitting, we averaged the up and down sweep and subtracted the antiparallel from the parallel trace (then divide by two) to eliminate the background. The data was also shifted where necessary to have the center peak at zero field. A constraint for the fitting is that xHanle and zHanle need to be fitted with the same diffusivity D and τ_{xy}. We also assumed identical stray fields for both fits. The fitting procedure was then to first fit the zHanle to obtain these parameters and then use them in the xHanle fit.
As the result of B. Raes's oblique spin precession experiment [76] was that spin-lifetimes are isotropic, we first tried to fit the xHanle data by assuming isotropic spin-lifetimes while modeling the differences to the zHanle data with sample misalignment and stray fields in y. The obvious problem to fit the xHanle data is that the trace is asymmetric regarding the magnetic field direction. We found that a combination of stray fields in y and a misaligned sample that is rotated in the x-y plane can indeed produce an asymmetric xHanle trace. However, misalignment or a y stray field alone do *not* produce an asymmetry, the combination of both is needed for that.

Fig. 4.16 shows a fit of the xHanle data with a parameter sweep of the misalignment angle, with a stray field in y of 1 mT. Assuming isotropic spin-lifetimes, this is the

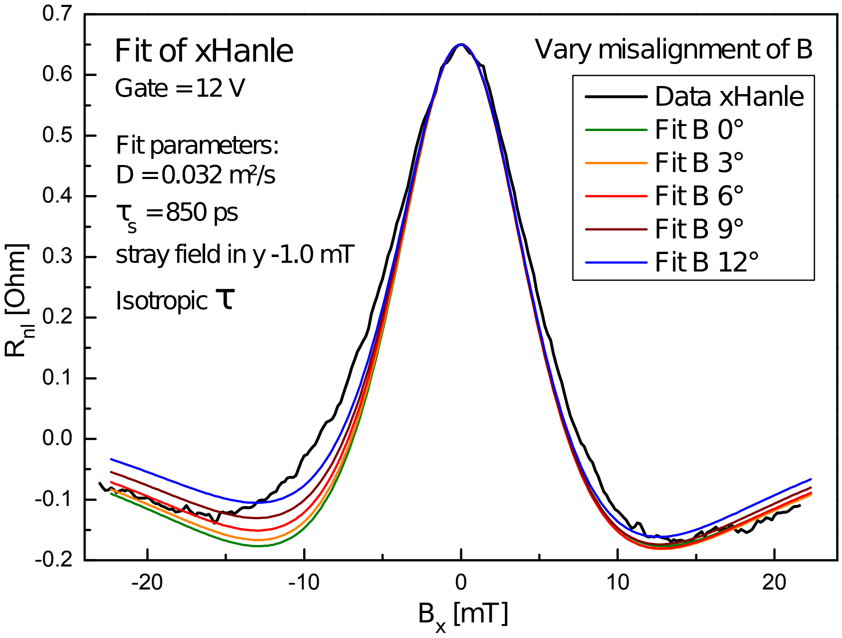

Figure 4.16: xHanle data (black), with fit traces assuming isotropic spin-lifetimes. Parameter sweep of the sample misalignment angle.

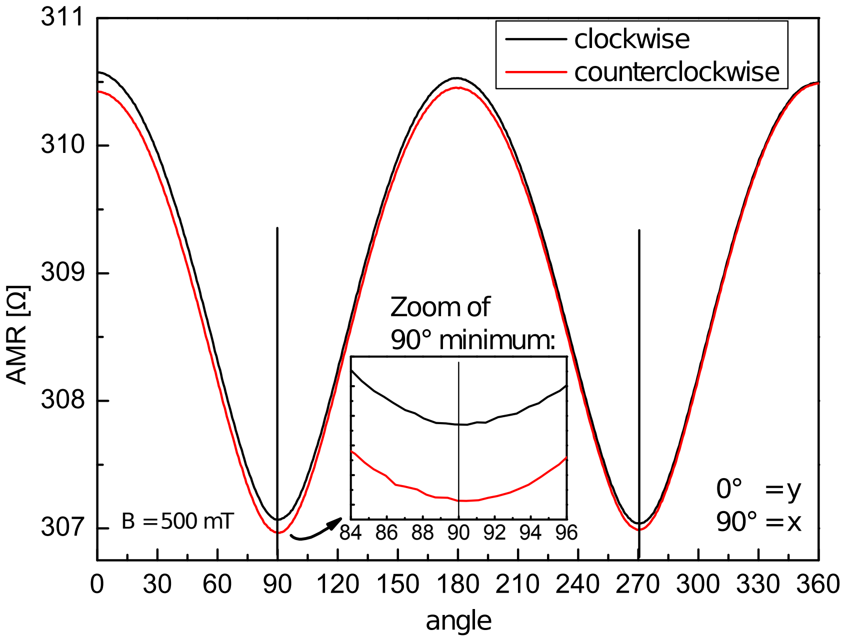

Figure 4.17: AMR data of a circular sweep of the B field in the x-y plane at 500 mT, to test the alignment of the sample. Clockwise and counterclockwise sweeps were performed to account for possible magnetic hysteresis. A slight signal drift is visible because of temperature drift.

closest we could get to fit the data. Higher stray fields in y did not give a better fit. As can be seen, the data on the positive B side can be fitted reasonably well, while the negative B side gives no good fit even for unreasonably large misalignment angles. Large misalignment angles produce a trace with considerable asymmetry, but the shape does not fit.

We measured the misalignment of our sample by doing an AMR circle sweep in the x-y plane, shown in Fig. 4.17. According to this data, the misalignment is about 1°. Including errors [1], we assume our sample was misaligned to the B_x field direction by a maximum of 3°. As the simulation shows, that angle is not enough to create an asymmetry of the magnitude seen in the xHanle data. Therefore, we conclude that the asymmetry in the xHanle data can not be explained by stray fields and sample misalignment.

We also examined the effect of stray fields in x for zHanle or in z for xHanle. We found that these stray fields reduce the height of the center peak of the Hanle feature, but have nearly no effect on the shape of the secondary peaks.

Next, we did not require $\tau_z = \tau_{xy}$, but allowed τ_z as a free parameter for the xHanle fit. This produced a good fit for either the positive B side data *or* the negative B side data. A good fit of *both* sides would require a separate τ_z for each side, as they are asymmetric. However, there is no known effect where the anisotropy changes when the

---

[1] The errors in this case is that the sample was taken out of the measurement setup after the xHanle data was collected and was remounted for the AMR circle sweep. The sample holder orientation is reproducible with an error of 2°.

magnetic field is reversed. The asymmetry of the xHanle data has a different origin. The best explanation for the asymmetry is a z component in the magnetization of one of the electrode interfaces. This z component could be a tilted magnetization or actual magnetic domains with a z orientation. The other electrode could have a z component as well, but the difference in tilt angle in the zy plane needs to be $\sim 9°$ as per the xHanle fit. For example, one electrode could have a tilt angle of $\phi = 14°$ while the other has $\phi = 5.5°$.

By analyzing the data, we can narrow down the possible values for the z tilt. By fitting the oblique spin precession data, which is discussed at the end of section 4.3.2, we discovered that the z component follows the external z field. This places a lower bound of $\phi = 8.53°$ on the z tilt of the tilted electrode, as the z component of other electrode, if existing, would point in the same direction. The upper bound for the tilt can be discerned from the spin valve data and the xHanle data. If there was a significant z component in both electrodes, that would result in a peak at $B_y = 0$ in the spin valve data because of spin precession. The first electrode injects spins with a z component and these spins would be detected by the z component of the detector electrode at $B_y = 0$. Because of the y field used in the spin valve experiment, the z component of the spins would precess in the zx plane and then cease to be detected at higher magnetic fields because of dephasing. A Hanle feature would be visible in the spin valve data. What amount of z component in the electrodes is possible, before this Hanle peak is strong enough to be detected, can be calculated.

In the spin valve signal of Fig. 4.4, the peak at $B_y = 0$ would need to be at least $\sim 0.05\,\Omega$ to be noticeable above the background. This threshold would be reached for 27.6% z domains (tilt angle $\phi = 20.9°$) in one electrode and 17.9% z domains (tilt angle $\phi = 12.3°$) in the other electrode. The tilt angle difference must be 8.53° to fit the asymmetry in the xHanle data. From the spin valve signal of $1.2\,\Omega$ detected by the y component we can calculate the peak amplitude of the z component Hanle oscillations: $\frac{1.2\,\Omega}{(1-0.276)(1-0.179)} \cdot 0.276 \cdot 0.179 \cdot 0.5 = 0.05\,\Omega$. The last factor of 0.5 is because the z signal is a Hanle dephasing. As we see no peak at $B_y = 0$ in our spin valve data, the electrode z tilt must be less than 20.9°.

An even lower bound for the electrode z tilt can be found by simulating xHanle traces for various tilt angle combinations shown in Fig. 4.18. In zHanle, the z spins do not precess and would be a static offset. In xHanle, these z spins *do* precess and increase the amplitude of the oscillations. This is most obvious for the center peak. In our data, an exact comparison of the center peak amplitudes of zHanle and xHanle is difficult because they might also be changed by stray fields in x and z, respectively. On average, the amplitudes of the zHanle and xHanle are similar and we see no obvious offset of zHanle data and xHanle data in Fig. 4.5a) and 4.6a). This places an upper bound of $\phi = 14°$ (20% z domains) on the electrode tilt with the corresponding $\phi = 5.5°$ in the second electrode (9% z domains). With these values, the xHanle amplitude is not yet significantly changed (dotted blue trace in Fig. 4.18).

For the fitting of our data, we assumed a tilt angle of $\phi = 8.53°$ in one electrode and no z component in the other electrode (dotted red trace in Fig. 4.18). We cannot discern which electrode has the z component, but we assume for ease of understanding

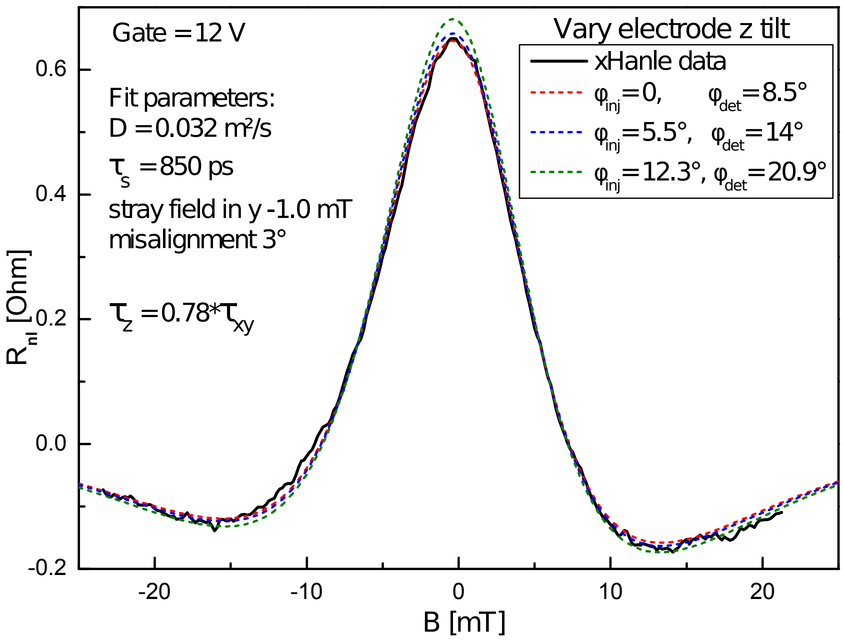

Figure 4.18: xHanle data (black), with dotted fit traces for different magnitudes of tilt angle ϕ in injector and detector interface magnetization. The red and blue fit traces can be considered viable, while the green fit trace clearly does not represent the data.

and writing that it is the detector electrode. As both electrodes have the same width and are deposited in the same lithography step, this raises the question of how can there be a difference. Ideally, they should be identical, but there is evidence that they are not. For example, the resistance area product of the two electrodes is quite different, one being at $13\,\mathrm{k}\Omega\mu\mathrm{m}^2$ and the other at $46\,\mathrm{k}\Omega\mu\mathrm{m}^2$. This difference is most likely caused by the inhomogeneity of the MgO tunnel barrier, where the current flows through local hot spots where the barrier is thinnest.

The MgO grows polycrystalline, and the Co on top of the MgO is then most likely polycrystalline as well. While the magnetization direction of the electrode interfaces can be expected to be the same on average, there are likely local fluctuations because the strength of the MgO-Co exchange coupling depends on the local crystal structure. Such a local fluctuation can get amplified disproportionately in the spin signal when it is at a tunneling hotspot. The difference in z component in our electrode interface magnetization is then the result of statistical fluctuations.

How a z component in the magnetization can cause an asymmetric Hanle signal is schematically shown in Fig. 4.19. For an xHanle experiment in isotropic media where the spins propagate in the x direction with parallel electrodes in y and a magnetic field in x, the spin signal at the detector electrode is proportional to:

$$s_y(x,t) \sim \int_0^\infty dt \frac{1}{\sqrt{4\pi D t}} e^{-(x-\mu E t)^2/4Dt} e^{-t/\tau_s} \cos(\omega_0 t) \tag{4.3}$$

This formula is also commonly used to fit zHanle. The trigonometric function that defines the shape of the Hanle trace is a cosine, and accordingly we call this a cosine

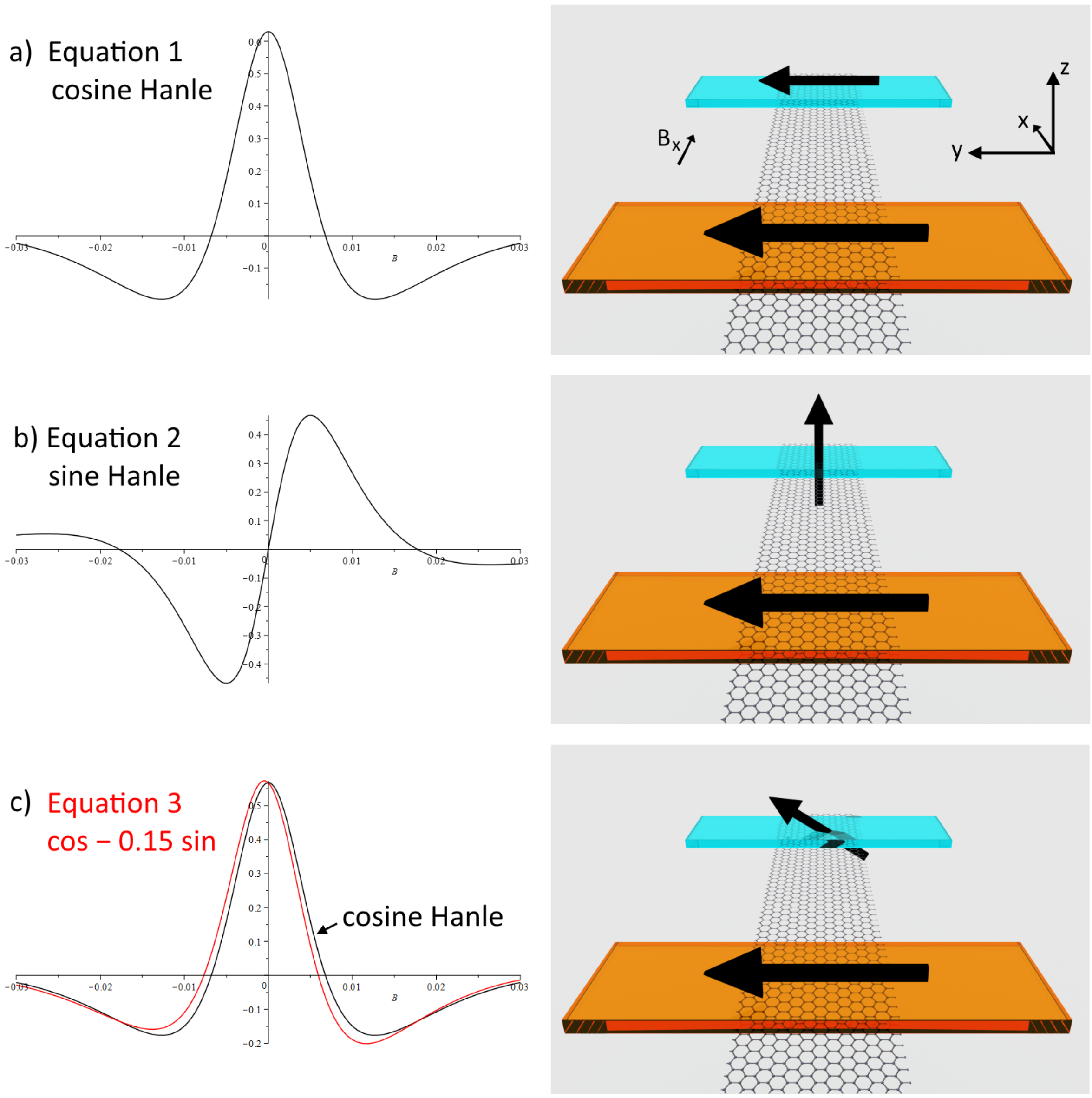

Figure 4.19: a) cosine shaped Hanle, b) sine shaped Hanle, c) cosine shaped Hanle in black that is symmetric and in red a linear combination of cosine and sine Hanle that is asymmetric. Pictures beside the graphs illustrate the corresponding orientation of the electrode magnetization, assuming an xHanle experiment.

shaped Hanle as depicted in Fig. 4.19a).

Now we consider the same xHanle in isotropic media, but the detector electrode is pointed in the z direction. We detect the z component of the spin that is described by the following equation:

$$s_z(x,t) \sim \int_0^\infty dt \frac{1}{\sqrt{4\pi Dt}} e^{-(x-\mu Et)^2/4Dt} e^{-t/\tau_s} \sin(\omega_0 t) \tag{4.4}$$

This formula describes Hanle where the injector and detector are not parallel but perpendicular to each other. The trigonometric function that defines the shape of this Hanle trace is a sine, and accordingly we call this a sine shaped Hanle as depicted in Fig. 4.19b).

If injector and detector are neither parallel nor perpendicular but at an angle in between, then we have a linear combination of cosine and sine shaped Hanle. This mixed case is described by the following formula:

$$s_{y,z}(x,t) \sim \int_0^\infty dt \frac{1}{\sqrt{4\pi Dt}} e^{-(x-\mu Et)^2/4Dt} e^{-t/\tau_s} (\cos(\omega_0 t) + a \cdot \sin(\omega_0 t)) \tag{4.5}$$

The tilt angle ϕ between injector and detector electrode is being represented by the scaling factor a, with $\phi = \arctan(a)$. A mixed Hanle trace with $a = 0.15$ and $\arctan(a)$ $= 8.53°$ is shown in in Fig. 4.19c) in red, with a cosine shaped Hanle in black for comparison. As can be seen, the red trace is asymmetric.

Equation 4.3 is symmetric in B while equation 4.4 is antisymmetric in B. The mixed Hanle of equation 4.5 that is a linear combination of the two can therefore be separated into these two parts by symmetrization and antisymmetrization. By symmetrizing the xHanle data we can extract the y part of the xHanle and compare that to the zHanle to extract the anisotropy of the spinrelaxation. The zHanle data is projected on the same y component of the electrodes. We first fit the zHanle to obtain the fit parameters, then the y part of the xHanle is fitted with the same parameters and the only free variable is the anisotropy of the spin lifetime. To do that, we used a COMSOL simulation as detailed in section 4.1.1, as the formulas 4.3 - 4.5 do not account for an anisotropic spin relaxation.

Antisymmetrizing the xHanle data gives the z component of the spin signal that can be used to extract the scaling factor a and thus the tilt angle ϕ of the detector electrode magnetization. We use the same fitting parameters as for the y component of the xHanle and fit with a sine shaped Hanle, allowing only a as a free variable. It should be noted that knowing a is *not* needed to extract the anisotropy out of the xHanle data. But it *is* needed for a correct interpretation of the oblique spin precession data.

Estimating the tilt angle from the antisymmetrized xHanle data is not very accurate because of our problems with remanent B fields in the x magnet as stated in section 3.7. This is demonstrated in Fig. 4.20 that shows the antisymmetrized xHanle data for various small offsets to account for a possible remanent field. As can be seen in Fig. 4.20a), for no offset a scaling factor of 0.3 would give a good fit, while for an offset of 0.6 mT a scaling factor of 0.15 is the best possible fit. It must be concluded that for this

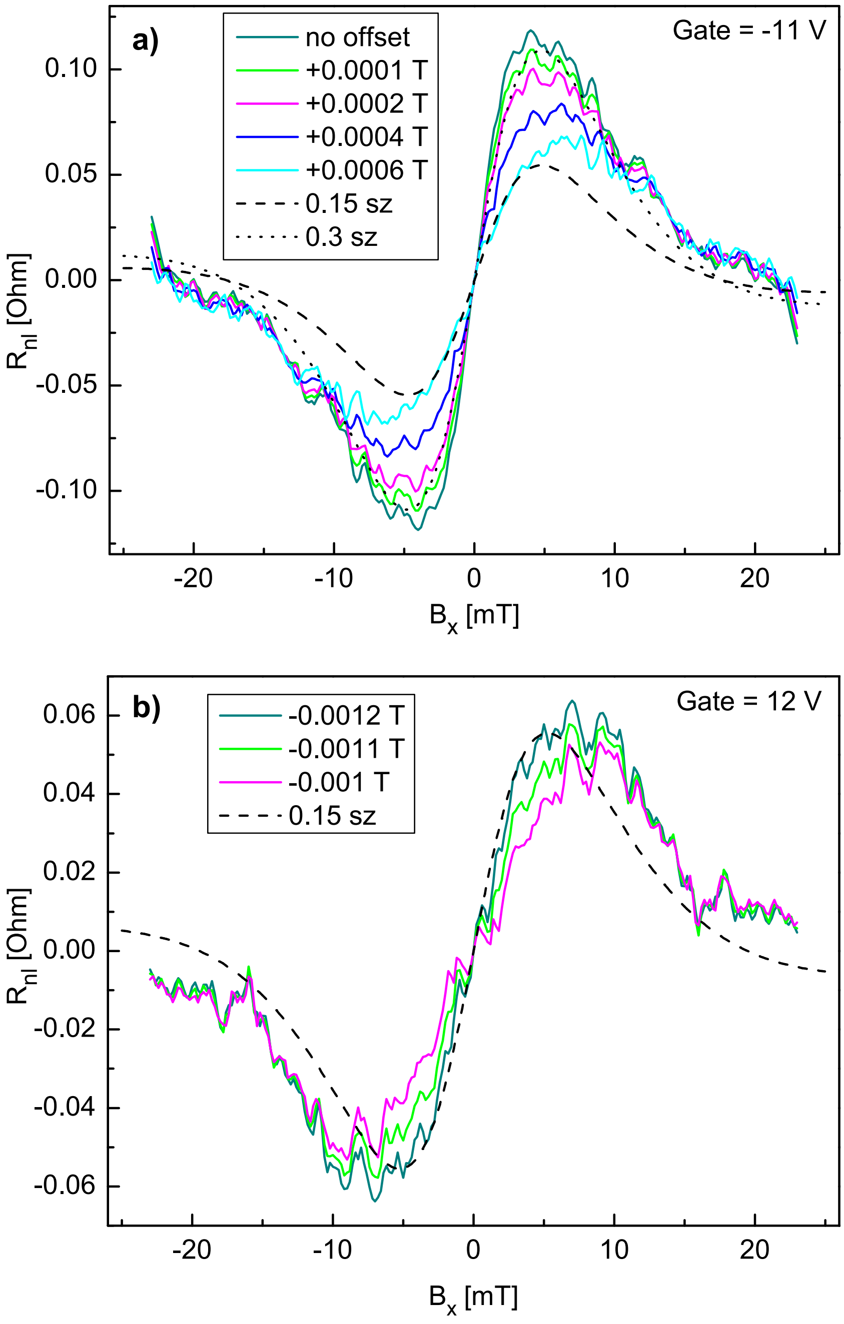

Figure 4.20: Antisymmetrized part of the xHanle data, calculated from different offset fields to correct for remanent magnetization.

kind of analysis, our magnet setup is not accurate enough for a reliable result.
As our measurements were reproducible, we can assume that the z component of the interface magnetization and thus the scaling factor a is a fixed parameter that does not change because of the gate or the external magnetic field. We considered the antisymmetrized data from all gate voltages under different offset corrections and tried to find offset fields were all data could be fitted with the same scaling factor a. We found that a scaling factor of 0.15 that corresponds to a tilt angle of 8.53° can fit all data reasonably well. We cannot say whether the z component of the magnetization is a tilt of the whole magnetization or domains with a z direction. Mathematically, they are identical. In equation 4.5, instead of $(\cos(\omega_0 t) + a \cdot \sin(\omega_0 t))$ which is the domain representation, one could also use $(\cos(\omega_0 t - \phi)/\cos(\phi))$, which would be the tilt angle representation. In case of domains, the percentage of z oriented domains is $\frac{a}{1+a}$ and the percentage of y oriented domains is $1 - \frac{a}{1+a}$. For $a = 0.15$ this would mean that 13% of the domains that contribute to the spin detection are z domains.

4.3 Oblique Spin Precession measurements

4.3.1 Discussion of oblique spin precession data

Finally, we performed the oblique spin precession experiment of B. Raes *et al.* [76] on our sample. As outlined in section 2.4.2, in this experiment an external field is applied at an angle β to the y-axis (see also Fig. 4.1). When the field strength is varied at fixed β, we obtain a set of Hanle curves, shown in Fig. 4.21. At large enough field strength, the spin component perpendicular to the external field is fully dephased, leaving only the component parallel to the external field. The projection of the original spin direction onto the external field direction results in a $\cos\beta$ term in the signal. During diffusion to the detector electrode, the spins are subject also to the out of plane spin relaxation time, if $\beta \neq 0$. When entering the detector electrode, the spins are now projected onto the magnetization of the detector electrode, resulting in a further $\cos\beta$ term.

For isotropic spin relaxation, the non-local signal at the detector is therefore expected to follow a $\cos^2\beta$-dependence, while $\zeta \neq 1$ will lead to a deviation from that behavior. In Fig. 4.22, we plot the spin signal of a continuous sweep of the angle β at a fixed total external field of 100 mT. To account for differences between the actual electrode magnetization direction and the y-axis direction, the data in Fig. 4.22 are plotted vs. $\cos^2\beta_{\text{eff}}$, where β_{eff} is the angle between external field and the electrode magnetization direction. The $\cos^2$-scaling allows identifying any deviation from isotropic spin-lifetimes easily. The colored lines show simulated traces for various degrees of anisotropy, applying Eq. (7) in Ref. [76] (see next section 4.3.2 for the full expression).
The magnetization direction in the injector and detector electrodes deviates from the y-direction, which would be expected from shape anisotropy, due to rotation of the

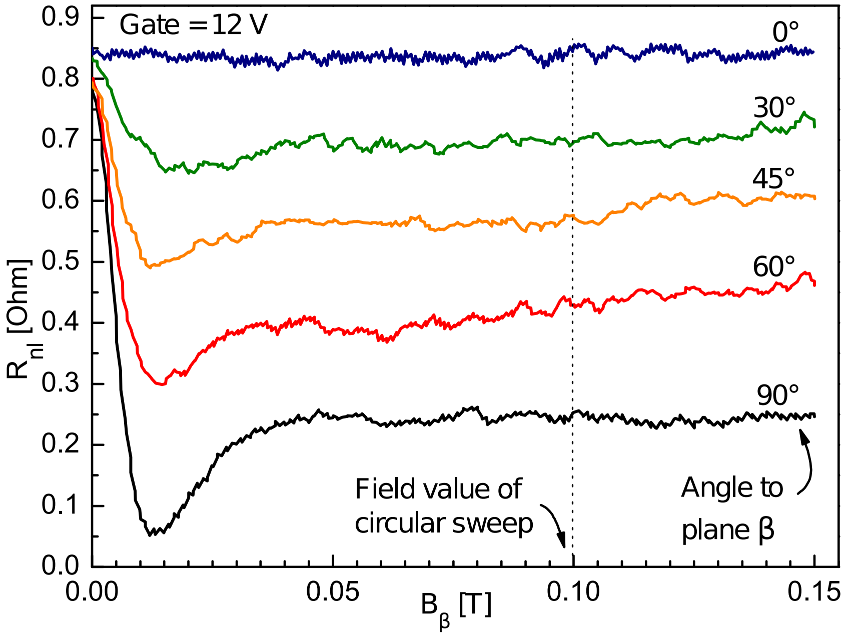

Figure 4.21: Oblique spin precession traces at various inclination angles β of the magnetic field. The data at $\beta = 90°$ correspond to the zHanle experiment.

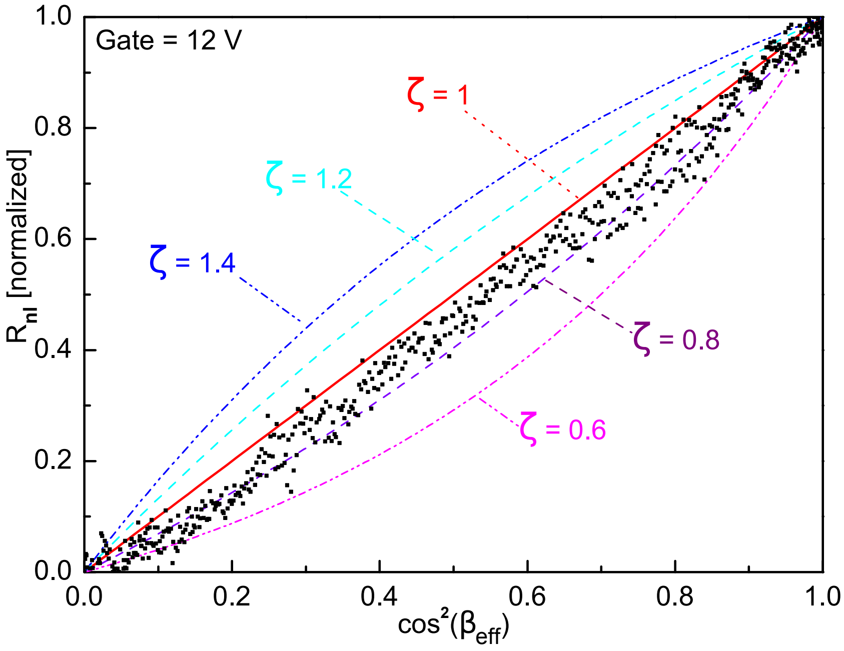

Figure 4.22: Sweep of the field angle β in the z-y plane at a constant field of 100 mT, plotted vs. $\cos^2 \beta_{\text{eff}}$ to see the deviation from isotropic spin-lifetimes that is linear in this plot. Colored lines show the simulated traces for various degrees of anisotropy.

electrode magnetization in the external field. Also, there is the partial z-magnetization ascribed to the MgO/Co-interface, which we detected in the xHanle experiment. This leads to correction terms that enter into the $\cos^2 \beta_{\text{eff}}$ term. More details on fitting procedure and formula are discussed in the next section 4.3.2.

As can be seen, the data fall roughly between the linear (isotropic) trace and the $\zeta = 0.8$ trace. A fit of the data gives an anisotropy of $\zeta = 0.91$. Importantly, the z-magnetization component at the MgO/Co-interface could only be detected in the xHanle experiment, but is crucial for the correct determination of ζ in the oblique spin precession experiment. Not accounting for the z component would have given an incorrect anisotropy of $\zeta = 1.08$ (see next section 4.3.2). Including the data of other gate voltages not shown here, we get an average of $\zeta = 0.91$ for the anisotropy.

It must be noted that the partial z-magnetization ascribed to the MgO/Co-interface in our sample leads to large error bars in ζ obtained from the oblique spin precession fit due to lack of precision at which the tilt angle can be determined. In a sample without this problem, the oblique spin precession experiment can achieve a better accuracy.

Summarizing this subsection, we note that the z-magnetization in the electrodes has a large influence on the oblique spin precession experiment. This is specific to our sample and not a general problem if it can be avoided by proper material selection. The anisotropy yielded by our oblique spin precession experiment is $\zeta = 0.91$, but the accuracy is questionable.

4.3.2 Oblique spin precession fitting

To prepare the oblique spin precession data for fitting, it needs to be normalized to a scale of 0 to 1. β is the angle of the magnetic field to the x-y-plane. For $\beta = 90°$ the spin signal should be 0, so any remaining signal is background that needs to be subtracted from the data. The data is then divided by its peak value which is at $\beta = 0°$ to normalize it to 1. To fit the data, we used the formula provided by B. Raes [76]:

$$\frac{R_{nl}^{\beta}(B)}{R_{nl}(B=0)} = \sqrt{\left(\cos^2(\beta) + \frac{1}{\zeta}\sin^2(\beta)\right)^{-1}} \cdot e^{-\sqrt{\frac{L^2}{\tau_{xy} D}}\left(\sqrt{\cos^2(\beta)+\frac{1}{\zeta}\sin^2(\beta)}-1\right)} \cdot \left[\cos^2(\beta-\gamma)\right] \tag{4.6}$$

Here, $\frac{R_{nl}^{\beta}(B)}{R_{nl}(B=0)}$ is the normalized non-local spin signal. The formula in Ref. [76] has an additional term for the magnetoresistance of the graphene that we omitted as we operate at a low enough magnetic field. L is the distance of the injector and detector contact, D is the diffusivity and $\zeta = \frac{\tau_z}{\tau_{xy}}$ is the anisotropy of the spin relaxation time. When the field component perpendicular to the plane increases, the electrodes will start to turn into the z direction as shown in the AMR data in Fig. 4.9a) (blue trace). In equation 4.6 this is accounted for by γ, which is the field dependent angle of the symmetric turning of the electrodes in the z direction because of the z component of the external field. This γ does *not* account for the z component of the interface magnetization that exists in our

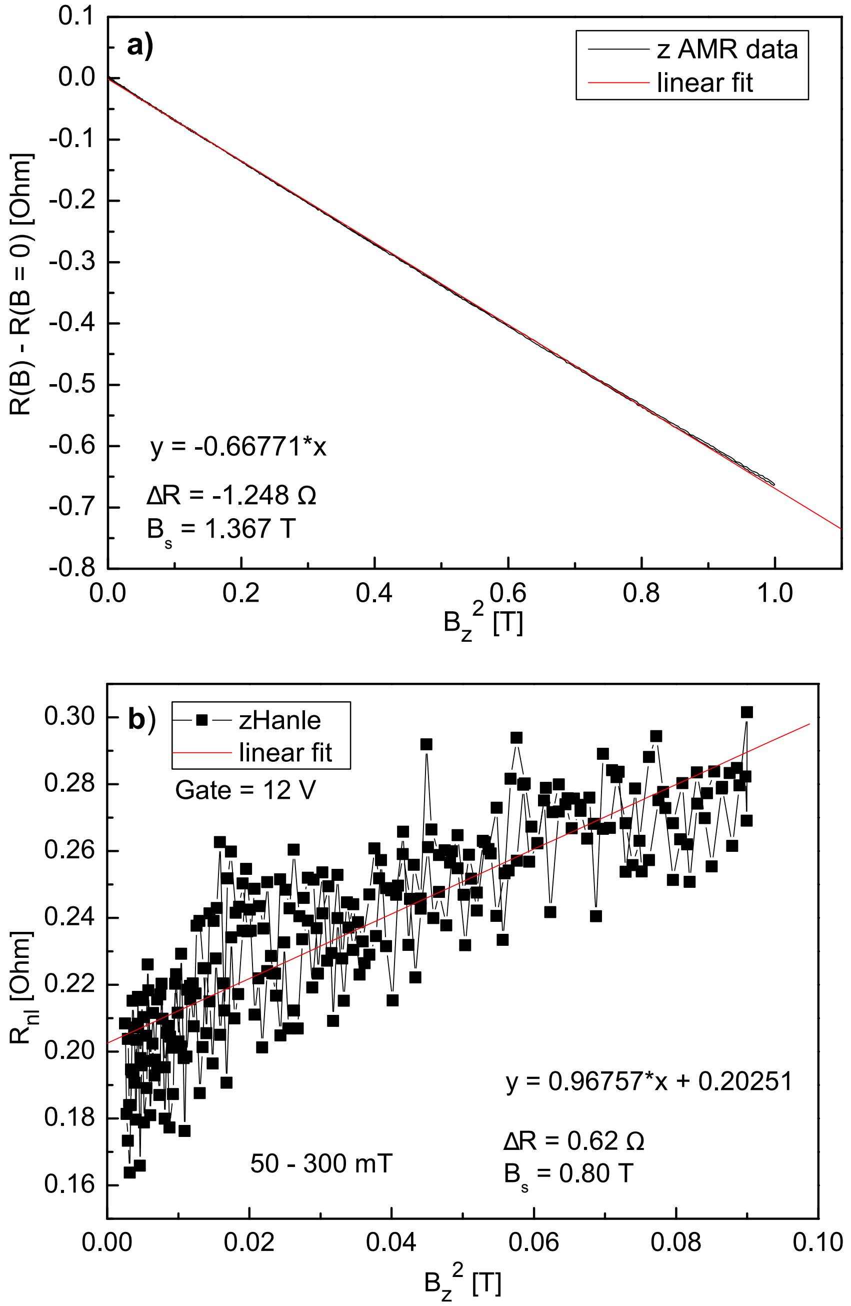

Figure 4.23: a) z direction AMR data plotted vs. the quadratic magnetic field. Linear fit in red. As can be seen, the data closely follow the parabolic shape that the model assumes. b) zHanle data of 50 - 300 mT plotted vs. the quadratic magnetic field. Linear fit in red.

electrodes independent of an external field. That z component that we represent with a tilt angle ϕ is not yet accounted for in equation 4.6, but is added later in equation 4.9. To calculate the field dependent γ, B. Raes *et al.* use the Stoner-Wohlfarth model [34], which provides a very good approximation for coherent magnetization rotation at low B. From this model, they derive an expression for γ that is given in the supplemental material of Ref. [76]:

$$\gamma = \arcsin[\frac{\sin(\beta)}{B_s/B + \cos(\beta)}] \tag{4.7}$$

Here, $B_s = 2\kappa_{\text{eff}}/M_s$ is the saturation field that is a composite of the saturation magnetization M_s and an effective anisotropy constant κ_{eff}. The B in the equation is also a constant as the oblique spin precession experiment operates at a fixed field strength, which is 100 mT in our case. Then we have an expression for γ that only depends on β. This relationship for γ is known to closely follow experimental results [105, 106], even for magnetic fields approaching B_s.

To determine B_s from AMR or similar data where the magnetization is rotated by a perpendicular field, the following formula can be used:

$$\rho(B) - \rho(B = 0) = \frac{\Delta\rho}{B_s^2} B^2 \tag{4.8}$$

We use the AMR data where the field is applied along the z axis, which is the blue trace in Fig. 4.9a). Then $\rho(B)$ is the field dependent electrical resistance and $\Delta\rho$ is the maximum resistance difference of the AMR data. From the y data (red) in Fig. 4.9a) we see that $\Delta\rho = -1.248\,\Omega$. We plot $\rho(B) - \rho(B = 0)$ vs. B^2 as shown in Fig. 4.23a) and do a linear fit, where the inclination of the linear fit is equivalent to $\frac{\Delta\rho}{B_s^2}$. As can be seen, the data closely follow the parabolic shape that the model assumes up to 1 T. So we have $-0.66771 = \frac{\Delta\rho}{B_s^2}$, which gives us $B_s = 1.367$ T. The field strength of the oblique spin precession experiment at 100 mT is small enough compared to B_s that this model can be used to calculate the electrode rotation. In comparison, B. Raes *et al.* operated at 175 mT with electrodes that have $B_s = 1.12$ T [76].

We have to note that AMR probes the bulk magnetization and the B_s we extracted from the AMR data will give us a γ that describes the rotation of the bulk. Since we know that because of the magnetic coupling at the MgO-Co interface, the interface magnetization behaves differently than the bulk (see section 4.1.2), we can expect the interface to rotate differently than the bulk. We can see the rotation of the interface in our 300 mT zHanle data and can use that to extract a B_s for the interface. In Fig. 4.23b) we plot the dephased zHanle signal vs. B^2 and do a linear fit. We used the zHanle data of field values above 50 mT to ensure a dephased signal. The $\Delta\rho$ is then equivalent to the amplitude of the center Hanle peak, which is $0.62\,\Omega$. The fit results in $B_s = 0.80$ T. The saturation field for the interface magnetization is lower than for the bulk, meaning the interface magnetization is easier to rotate into the z direction. This is consistent with our assumption of the MgO-Co magnetic coupling at the interface, considering that the coupling favors an out of plane magnetization. To further process the data, we used $B_s = 0.80$ T.

We extended equation 4.6 to account for the z component of the interface magnetization:

$$\frac{R^{\beta}_{nl}(B)}{R_{nl}(B=0)} = \sqrt{\left(\cos^2(\beta) + \frac{1}{\zeta}\sin^2(\beta)\right)^{-1}} \cdot e^{-\sqrt{\frac{L^2}{\tau_{xy} D}}\left(\sqrt{\cos^2(\beta)+\frac{1}{\zeta}\sin^2(\beta)}-1\right)} \cdot$$
$$\cdot \left[\cos(\beta-\gamma)\cdot\cos(\beta-\gamma-\frac{\beta}{|\beta|}\phi)/\cos(\phi)\right] \tag{4.9}$$

Here, $\phi = \arctan(a)$ is the tilt angle that corresponds to a scaling factor of a for the z component. The term $\frac{\beta}{|\beta|}$ is there to change the sign of ϕ, as the z component switches direction when the external z field switches direction. That this is the case can be seen in Fig. 4.24, where the oblique spin precession signal is plotted vs. β for a range of $\beta = 90°$ to $\beta = -100°$. The measurement started at $\beta = 90°$ and at $\beta = 0°$ the z component of the external field changes direction.

The continuous red fit trace in Fig. 4.24 uses equation 4.9, with $\phi = 8.53°$ and ζ as a free parameter. The dashed red trace also uses equation 4.9, but here ϕ does not change sign, meaning the z component of the interface magnetization does *not* follow the external field. As can be seen, this does not fit the data. The conclusion is that the z component of the electrode magnetization follows the external field and switches direction.

The blue trace in Fig. 4.24 is for comparison. It uses equation 4.6 that assumes no z component in the electrode magnetization, again with ζ as a free parameter. The

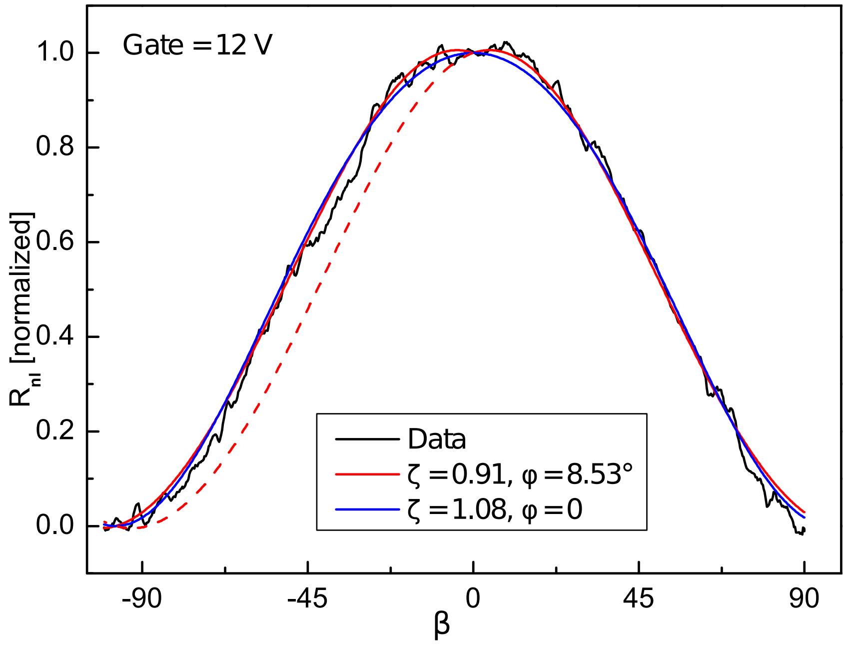

Figure 4.24: Oblique spin precession data. The red fit assumes an interface magnetization z tilt of $\phi = 8.53°$ where the z component switches direction as soon as β changes sign. The dashed red line is the continued trace where the z component does not switch direction. The blue fit assumes no z component with $\phi = 0°$.

differences between the red and the blue fit trace are small, but it does seem that the red trace gives a better fit near $\beta = 0°$, supporting our tilted electrode thesis. It must be noted, however, that the way the data is normalized can change which trace seems to give the better fit.
The blue fit would give a higher $\zeta = 1.08$ compared to $\zeta = 0.91$ of the red fit. This demonstrates how big the influence of the z component of the electrode magnetization is when fitting for the spin-lifetime anisotropy. As has been stated at the end of section 4.2.2, our method to estimate the magnitude of the tilt angle ϕ is not very accurate. This inaccuracy is passed on to ζ when fitting the oblique spin precession data. If we underestimated the tilt and ϕ is larger than 8.53°, ζ would be smaller. If we overestimated the tilt and ϕ is smaller than 8.53°, ζ would be larger.

4.4 Comparison of the anisotropy parameter: Estimation of uncertainty

Fig. 4.25 shows the extracted anisotropy parameters of the oblique spin precession experiment and the xHanle experiment of all measured gate voltages. As can be seen, the anisotropy parameters obtained from the xHanle experiments do not match those from the oblique spin precession experiments. On average, the xHanle experiment gives an anisotropy ζ slightly below 0.8, while the oblique spin precession gives ζ a bit larger

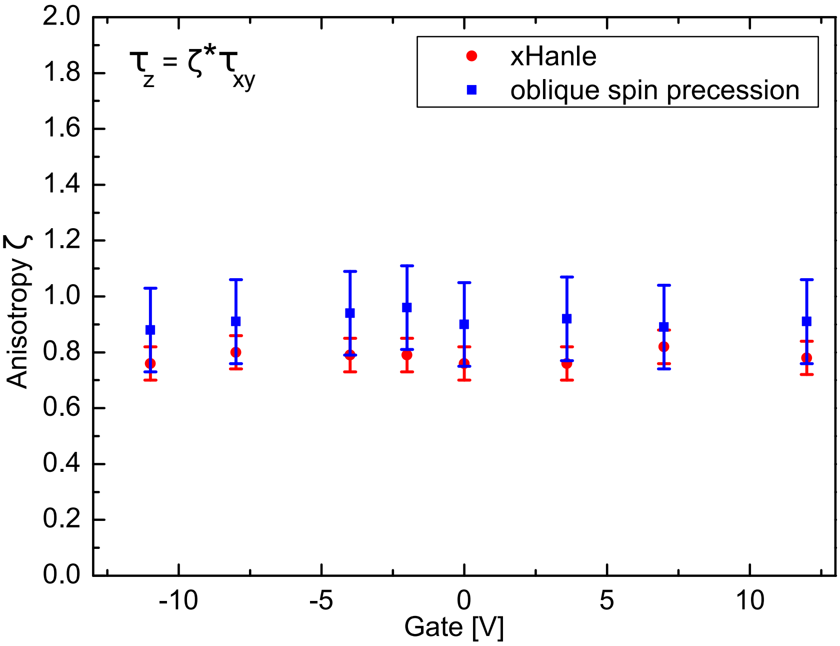

Figure 4.25: Extracted anisotropy ratio ζ from xHanle data (red) and oblique spin precession data (blue) as a function of gate voltage.

than 0.9. There is no correlation to the gate voltage.
To address this disagreement in the obtained anisotropy values, we now estimate the uncertainty of the xHanle and the oblique spin precession data. In Fig. 4.25, the xHanle ζ is displayed with error bars of ± 0.06 for an average ζ of 0.78. This value results from two sources of uncertainty. The first is the uncertainty of the fit, which was done by manually adjusting the parameters and judging if the fit is good or not. This could be determined with an accuracy of $\zeta \pm 0.02$.
The fit for the symmetrized xHanle data is shown in Fig. 4.26, which is the fit we deemed to be optimal and gives $\zeta = 0.78$. This fit can be compared with Fig. 4.27, that shows a fit for $\zeta = 0.76$ in Fig. 4.27a) and a fit for $\zeta = 0.80$ in Fig. 4.27b). The fit for $\zeta = 0.76$ matches the shape very well for $B < \pm 10\,\mathrm{mT}$, but it does not match the amplitude of the local minima at $B = \pm 15\,\mathrm{mT}$. At these points the anisotropy would have the biggest influence, so matching these was a requirement for a good fit. The fit for $\zeta = 0.80$ matches the amplitude of the minima, but does not give a good fit for the shape. The fit for $\zeta = 0.78$ in Fig. 4.26 is the best compromise for matching shape and minima amplitude. As the shape of the Hanle curves was sometimes distorted due to drift or varying magnetic configuration (monitored by the difference between P and AP curves), we found that total accuracy of the fit, including both fitting precision and distortion, amounted to ± 0.04.

The second source of uncertainty for the xHanle is the stray field in y. We fitted for a constant stray field of $1\,\mathrm{mT}$ for xHanle and zHanle. If the stray field during xHanle measurement was different by $\pm 1\,\mathrm{mT}$ to the stray field during zHanle measurement, that

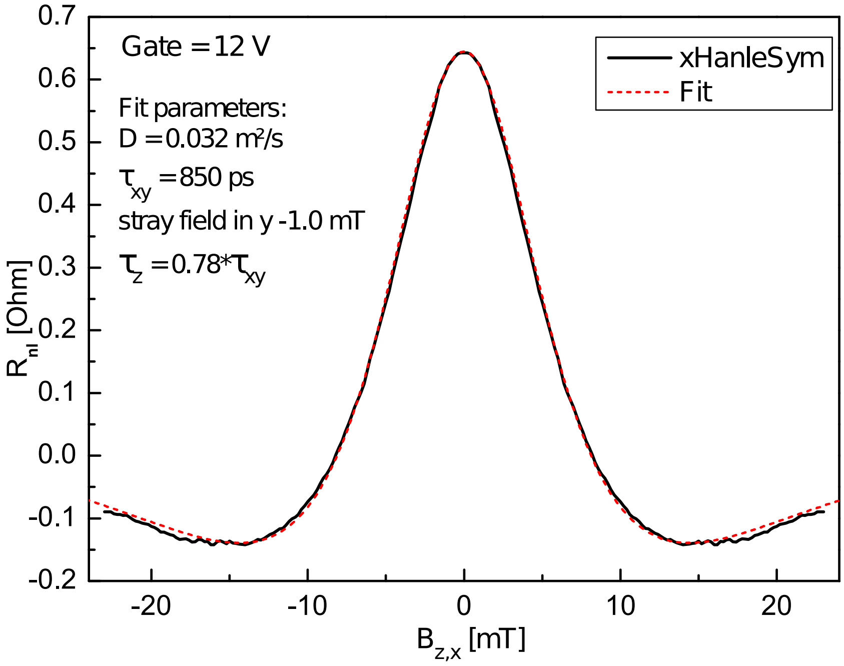

Figure 4.26: Symmetrized xHanle data (black), with fit trace for $\zeta = 0.78$ which was judged a good fit.

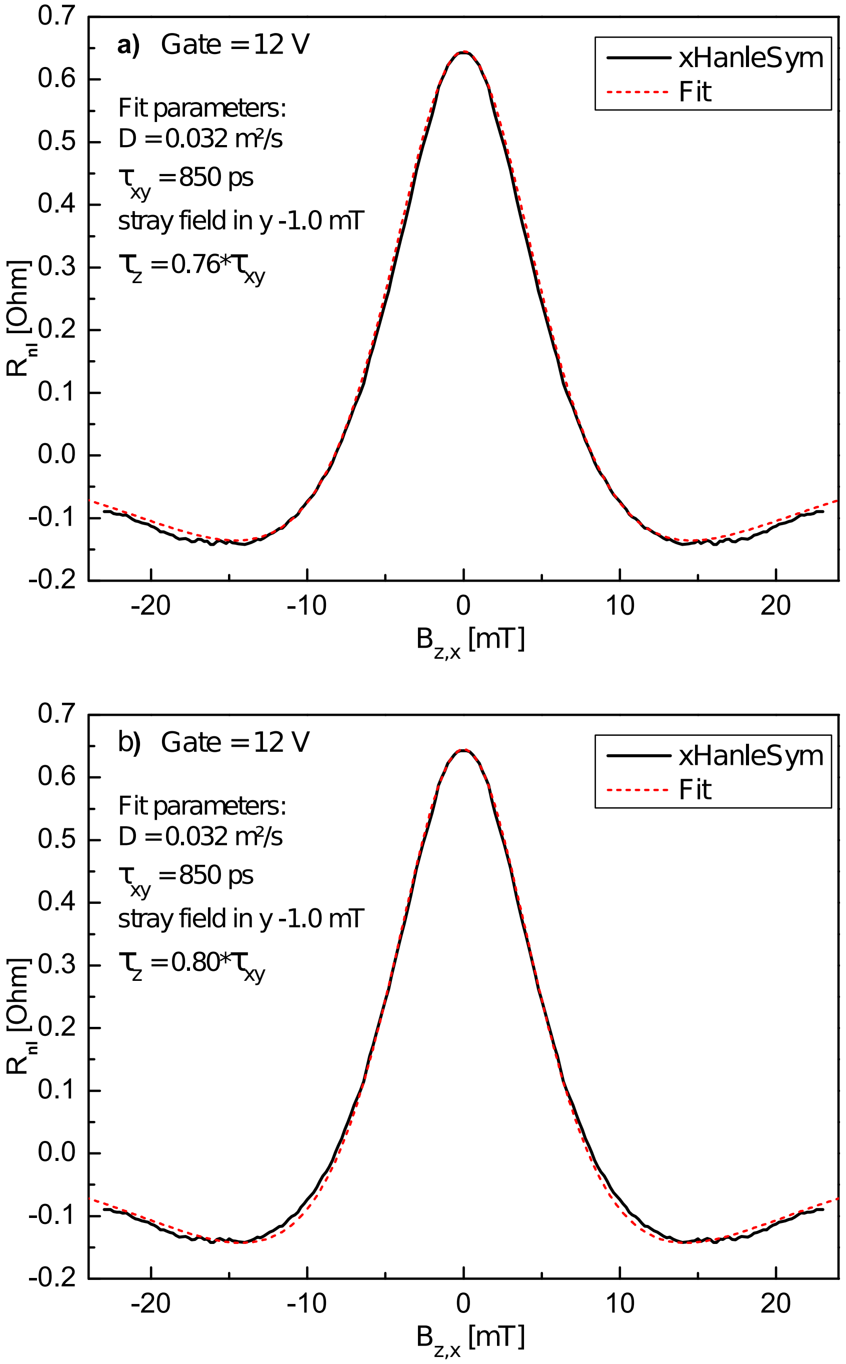

Figure 4.27: Symmetrized xHanle data (black), with fit traces for a) $\zeta = 0.76$ and b) $\zeta = 0.80$, which were judged as not so good fits.

would result in an error for ζ of ± 0.02. However, the occurrence of this error is unlikely, as the measurement sequence was:
Measure zHanle P, measure xHanle P, prepare AP orientation, measure zHanle AP, measure xHanle AP.
Here P signifies the parallel orientation of the electrodes and AP the antiparallel orientation. A change to the stray field in y would most likely occur after the y magnet was used, which in this sequence only happens during the preparation of the AP orientation. Assuming this, the zHanle AP and xHanle AP measurement would have had a changed stray field. As these data are averaged with their P counterparts, the resulting average stray field for zHanle and xHanle would be the same.
For the total error of ζ obtained from the xHanle we then give ± 0.06, which we estimate is the worst case scenario. As we think an error from the stray fields is unlikely, this number also includes minor other error source we did not think about.

The uncertainty of the parameter ζ calculated from the oblique spin precession method is ± 0.15 for an average ζ of 0.91. The uncertainty is so high because there are several sources of uncertainty for the oblique spin precession.
We have five minor sources of error, which we estimate each to contribute an error of ± 0.01 - 0.02 to ζ. The first is that we rotate the magnetic field by using the linear combination of two magnetic coils. Because of remanent magnetization in our magnets, we estimate that our magnetic field angle β has some inaccuracies. B. Raes *et al.* [76] use a single magnet coil and instead rotate the sample, which is more accurate to determine β.
The second minor source of error is the fitting of the oblique spin precession data, which was done by hand and will have comparable inaccuracies as the xHanle fitting. However, the oblique spin precession data has to be normalized before it can be fitted, which we count as the third minor source of error.
A forth source of error is the correction for the dynamic tilting of the electrodes that is expressed by γ. We calculate our B_s from the data shown in Fig. 4.23b), and these data are quite noisy. The change in ζ because of γ with -0.07 is not insignificant, so this needs to be considered as a potential source of minor uncertainty.
The fifth source of error is in the formula used for fitting, equation 4.9. More specifically, the formula contains the term $\sqrt{\frac{L^2}{\tau_{xy} D}}$. As displayed in Fig. 4.8, we determined τ_{xy} with a certain amount of uncertainty. This uncertainty is then inherited by equation 4.9.
The biggest source of uncertainty in determining ζ from the oblique spin precession data comes from the tilted magnetization at the electrode interface that we describe with the tilt angle ϕ. We used $\phi = 8.53°$ for the fit and this is responsible for a shift in ζ of -0.16. As detailed in section 4.2.2, estimating ϕ from the available data cannot be done with great accuracy. This is exemplified by the data in Fig. 4.20a), where a scaling factor of 0.3 ($\phi = 16.6°$) can also fit the data. We consider this high volatility unlikely and assume an uncertainty of ± 0.08 because of the tilted magnetization. That would correspond to an error in ϕ of $\pm 5°$.

The disagreement of the obtained ζ from the xHanle experiment and oblique spin precession experiment can now be solved by including the error bars into the discussion. They overlap for $\zeta \approx 0.8$, which we conclude to be the anisotropy in our sample.

4.5 Discussion

The summary of the arguments in section 4.4 is that the xHanle experiment is more precise than the oblique spin precession experiment. A general advantage of the xHanle experiment is that it measures the P and AP configuration, while the oblique spin precession experiment measures only the P configuration. First, this gives the xHanle experiment twice the amplitude over noise of the spin signal. Second, subtracting the AP from the P trace is a very reliable method to remove any background signal. The oblique spin precession experiment relies on normalization to remove any background.
The weakness of the oblique spin precession experiment is its sensitivity to the exact orientation of the electrode magnetization. On top of the permanent z component caused by the MgO-Co interface, the dynamic tilting because of the external field needs to be accounted for in the fit formula (see section 4.3.2). At our comparatively weak external field of 100 mT, the dynamic tilting correction is responsible for a shift in ζ by roughly -0.07 and must be considered as a potential source of inaccuracy. Combined with the uncertainties related to determining the tilt angle of the permanent z component, this leads to significant error bars for ζ extracted from fitting the oblique spin precession data. The inaccuracies originating from the permanent z component are the largest contribution to the error bars and can be avoided by proper material selection. The other factors however, still apply.
It follows from the arguments that the xHanle experiment is generally more precise than the oblique spin precession experiment and also more robust to non-ideal conditions. As has been stated in section 4.3, the permanent z tilt in the detector electrode was only identified because of the xHanle experiment, but the knowledge of its existence was crucial for correct interpretation of the oblique spin precession data.

As was stated at the end of section 4.4, we conclude that the anisotropy in our sample is $\zeta \approx 0.8$. This is in contrast to the oblique spin precession experiments by B. Raes *et al.*, who claim an isotropic spin relaxation time in graphene [76]. They observe a range for ζ from $\sim$0.9 to $\sim$1.03. Our values of $\zeta \approx 0.91$ extracted from the oblique spin precession data are still in that range, but not our values extracted from the xHanle experiment.
The disagreement between both results could be due to an overall higher spin relaxation rate in the experiment in Ref. [76], likely because of stronger contact induced spin relaxation. The resistance area product of their contacts are not explicitly stated, but estimates of contact area and electrical resistance are provided and allow to assume 1 - 10 $k\Omega\mu\mathrm{m}^2$. This is nearly an order of magnitude lower than the resistance area product of our sample and according to F. Volmer *et al.* [64] indicates enhanced contact

induced spin relaxation. Also, the width of their graphene flake is between 1.5 μm to 1 μm compared to our very wide flake, which further enhances the invasiveness of the contacts (see section 2.3.4). As spins backscattering into the contacts is an isotropic spin sink, the total spin relaxation anisotropy in the sample of B. Raes *et al.* would be shifted more towards isotropic than in our sample.

For our sample, we assume that the spin relaxation stems from a mix of Rashba type spin-orbit fields that have $\zeta = 0.5$ and isotropic contributions like contact induced spin relaxation and resonant scattering by magnetic impurities. The individual relaxation rates are added to a total spin relaxation rate in the following way:

$$\frac{1}{\tau_{total}} = \frac{1}{\tau_1} + \frac{1}{\tau_2} + \dots \quad . \tag{4.10}$$

Assuming the anisotropic contributions are only of the Rashba type, we can use this formula to separate anisotropic and isotropic contributions. That gives us $\tau_{iso} = 1.18$ ns for the isotropic part and $\tau_{Rashba,xy} = 3$ ns and $\tau_{Rashba,z} = 1.5$ ns for the anisotropic Rashba part.

The spin lifetime of the isotropic part is consistent with the model of resonant scattering by magnetic impurities, such as adsorbed hydrogen [11, 61], assuming a low concentration of scatterers. The sample was measured at a pressure of ~10 mbar, making a small concentration of hydrogen atoms or other species on the graphene surface plausible. As is discussed in section 2.3.3, this mechanism would exhibit a gate dependence when the energy approaches the resonance and no gate dependence at other energies. However, we do not see any significant gate dependence neither in the spin lifetime nor in the anisotropy within the gate range of our experiment. A likely explanation is that the energy range probed in our experiment ($E_F = 116$ meV at $V_g = 12$ V) is not enough to see the gate dependence of resonant scattering by magnetic impurities. For the speculated hydrogen adatoms, we would expect a very broadened peak due to the SiO_2 substrate. This peak might be further broadened by additional peaks from other species of adatoms. That there are also other spin relaxation mechanisms present would further diminish the energy dependence of resonant scattering by magnetic impurities in the total spin lifetime.

Contact induced spin relaxation, while still present, should be comparatively weak in our sample because of the high resistance area product of the contacts (see section 2.3.4).

The local Rashba spin orbit fields caused by the few adatoms are not significant enough to matter. For the global Rashba spin orbit fields of the SiO_2 substrate, there are contradicting publications. C. Ertler *et al.* calculated the spin relaxation time to be at least a few μs with a maximum at the CNP [56], while D. Van Tuan *et al.* obtain a few hundred ps with a minimum at the CNP [71]. More recent DFT calculations suggest a Rashba spin-orbit coupling of λ_R in the range of tens of μeV for graphene on crystalline SiO_2 [2]. Using the D'yakonov-Perel' mechanism, this works out to Rashba spin lifetime on the order of 1..10 ns, in agreement to our experimental data.

---

[2] K. Zollner and J. Fabian, private communication

4.6 Conclusion and outlook

In conclusion, with the xHanle experiment we demonstrated an additional way to measure the anisotropy of the spin-lifetime in graphene that we believe to be so far the most accurate method. This tool can also be used to probe the spin relaxation in similar 2D materials that have recently started to attract interest like black phosphorus [107]. The data collected from the xHanle experiment pointed to a non-trivial magnetization of the contacts which is in line with the other experiments we performed. We attribute this non-trivial magnetization to a perpendicular magnetic anisotropy caused by the MgO-Co interface. Not accounting for this magnetization would have led to a false interpretation of the data from the oblique spin precession experiment. For the xHanle experiment, this magnetic coupling at the MgO-Co interface was actually beneficial, as it prevented the rotation of the interface magnetization during the xHanle experiment.
Compared to the oblique spin precession experiment, the xHanle is potentially more accurate, especially under non-ideal conditions. The weakness of this experiment is that it needs to operate at low magnetic field values to prevent a rotation of the electrodes. At these low field values, possible stray fields from the remanent magnetization of the magnets are relevant enough to influence the measurement.
The oblique spin precession experiment is still a valid method to measure the spin relaxation anisotropy. It is possible to perform with any setup and sample that is capable of the xHanle experiment and therefore should be executed as well to have a second set of data for verification. The weakness of the oblique spin precession experiment is its sensitivity to the orientation of the interface magnetization. A magnetic coupling at the interface exist in other material combinations as well, so testing for this possibility should be part of a thorough experiment.
The graphene sample in this study showed an anisotropy in the spin-lifetime of $\zeta \approx 0.8$ that was clearly visible in xHanle but could not be identified with this precision in the oblique spin precession experiment. We conclude that the spin relaxation mechanism in our sample is a combination of isotropic and anisotropic parts. We attribute the isotropic part to resonant scattering at adatoms and also contact induced spin relaxation. The anisotropic part is due to Rashba spin orbit fields originating from the SiO_2 substrate.

To improve upon the data provided by this dissertation, future xHanle experiments should focus on measuring at a wider range of gate voltages. The proposed spin relaxation mechanisms present in our sample do have a gate dependence that needs to be observed for confirmation. The results of the study by Barbara Klinger [102] can be used to improve the robustness of our samples regarding a backgate breakdown.
To observe anisotropic spin relaxation mechanisms in graphene, the influence of the contacts needs to be minimized. This can be achieved by using thick tunnel barriers and large contact areas to maximize the resistance area product, as well as long distances between the contacts. A more sophisticated approach is to fabricate samples with the bottom up technique introduced by M. Dögeler *et al.*, who could demonstrate the absence of contact induced spin relaxation in these samples [18].

To test if our conclusions about the precision of xHanle and oblique spin precession experiments are correct, a comparison should be performed in a sample that does not have a z tilted electrode interface magnetization because of magnetic coupling. In a good sample it should be possible to obtain the same anisotropy value from both experiments. Then, with more data, a statistical analysis can be done to accurately asses the precision of each experiment. Also, doing both experiments in a system with an expected large spin relaxation anisotropy like graphene on transition-metal dichalcogenides [13, 79, 80] can provide better data to evaluate their precision.

Chapter 5

Spin field-effect transistor action via tunable polarization of the spin injection in a Co/MgO/graphene contact

In this chapter the properties of the Co/MgO/graphene tunnel contacts regarding spin polarization are discussed. While characterizing sample S7F2 for the anisotropy experiments of chapter 4, an unexpected spin valve inversion was observed. Further investigation revealed that the spin polarization of the injector contact can be tuned by both the injector current bias and the gate voltage. The spin polarization can be turned off and even inverted. This behavior enables a novel type of spin transistor where the signal is switched off by turning off the spin injection using the field-effect.
As the measurements are done in a lateral spin valve geometry, there is the problem of distinguishing between contributions from the spin channel and contributions from the tunnel contacts. Most likely the source of the spin valve inversion is the band structure of the injector contact.

This chapter is based on the publication „Spin field-effect transistor action via tunable polarization of the spin injection in a Co/MgO/graphene contact“, S. Ringer, S. Hartl, M. Rosenauer, T. Völkl, M. Kadur, F. Hopperdietzel, D. Weiss, J. Eroms, arXiv:1803.07911 (2018).

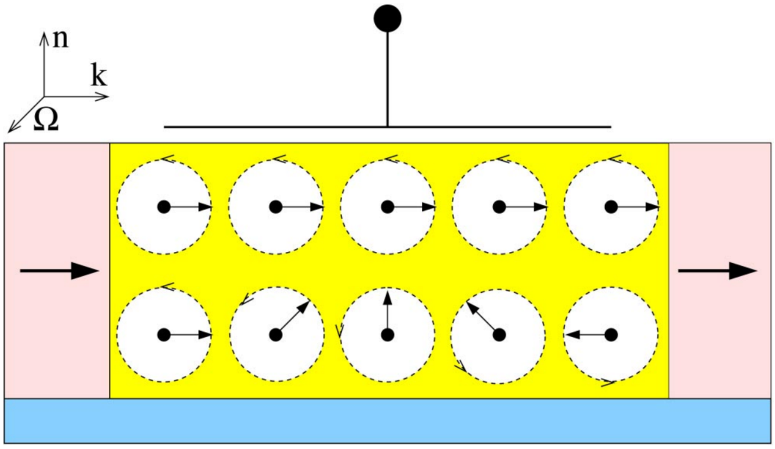

Figure 5.1: Scheme of the Datta-Das spin field-effect transistor. The source (spin injector) and the drain (spin detector) are ferromagnetic metals or semiconductors, with parallel magnetic moments. The injected spin-polarized electrons with wave vector k move ballistically along a quasi-one-dimensional channel formed by, for example, an InGaAs/InAlAs heterojunction in a plane normal to n. Electron spins precess about the precession vector Ω, which arises from spin-orbit coupling and which is defined by the structure and the materials properties of the channel. The magnitude of Ω is tunable by the gate voltage V_g at the top of the channel. The current is large if the electron spin at the drain points in the initial direction (top row)-for example, if the precession period is much larger than the time of flight-and small if the direction is reversed (bottom). Adapted from [4]

5.1 Introduction

Spintronics can be utilized in many applications. The commercial success of spintronics has so far been limited to devices used for data storage, but concepts exist for also building spin based logic circuitry [5–7]. The paradigmatic device, the spin field effect transistor (spinFET) was proposed by Datta and Das in 1990 [5]. This device is a three terminal spin valve, where the electric field of a gate is used to switch between a high resistance and a low resistance state (see Fig. 5.1). The basic structure is a local spin valve with an injector and detector connected by a spin channel. Here, the spin channel is the important part of the design. It needs to have a gate-tunable spin-orbit interaction that rotates the spins as they travel from injector to detector. Changing the gate voltage changes the rotation speed, so that spins arrive at the detector either parallel for a low resistance or antiparallel for a high resistance.

The advantage of a spinFET over a regular spin valve is that no magnetic fields are required to change the state. However, the Datta-Das spinFET has requirements for the spin channel that are contradicting. The strong spin-orbit interaction that is needed to rotate the spins is detrimental to the spin lifetime in the channel. Because of these design difficulties, an attempt to fully realize the Datta-Das spinFET was only presented more than two decades after the original proposal [108]. An easier to realize approach to a spinFET that we present here is to have an injector where the spin polarization can be manipulated by a gate. Then, a material with a low spin-orbit interaction and long spin lifetimes such as graphene can be used for the spin channel.

While electric tunability of spin injection has been demonstrated in magnetic tunnel junctions [109–113], this aspect has only recently become the focus of graphene spintronics. Bias-dependent reversal of the spin polarization was reported by Kamalakar *et al.* [114] and by Gurram *et al.* [115] using hexagonal boron nitride (hBN) as a tunnel barrier and cobalt electrodes. However, no gate dependence was shown.

In this chapter, we report on a gate and bias-tunable spin polarization in a Co/MgO/graphene device. We find that at an elevated negative injector bias U_{inj}, the spin polarization vanishes and afterwards changes sign. At this bias setting, which we call spin neutrality point, both sign and magnitude of the spin polarization can be controlled by a voltage V_g applied to the back gate of the sample. Importantly, the spin signal at the detector electrode can even be turned off by gate control, thus enabling a true three-terminal spintronic device.

5.2 Sample characterization

The inversion of the spin polarization was observed in a contact on sample S7F2. This sample was also used for the anisotropy experiments of chapter 4, but in a different contact configuration. The setup for the spin transistor experiments is shown in Fig. 5.2.

There are three tunnel contacts on the sample, marked I, II and III in Fig. 5.2. The experiments on spin lifetime anisotropy used contact I as injector and contact III as detector. The experiments in this chapter also use contact I as injector, but now contact II is used as detector. The injector detector distance is then 6 μm (edge to edge). The other parameters of the sample have already been stated in section 4.1.1 and remain unchanged. They are repeated here for completeness.

We use exfoliated single layer graphene on $p^{++}Si/SiO_2$, where the highly doped silicon serves as a back gate, using the 285 nm thick SiO_2 as a dielectric. The injector and detector contacts are Co with ~1.4 nm of MgO as a tunnel barrier, the end contacts are Pd. At the injector electrode, a DC current bias I_{inj} is applied and the bias voltage U_{inj} is simultaneously measured. Using the non-local spin valve geometry detailed in section 2.2.6, we record a non-local voltage signal U_{nl} and the corresponding non-local resistance $R_{nl} = U_{nl}/I_{inj}$ at the detector electrode.

We define the outer Pd electrode as ground for the injector circuit. A positive U_{inj} or I_{inj} therefore means an electron current flowing from graphene to the Co electrode. Similarly, the detector circuit is connected with the positive terminal of the nanovoltmeter to the Co detector electrode. Since we are using a DC setup, the bias dependence can be studied in this experiment, at the expense of sensitivity to unavoidable magnetic induction signals. The spin valve signal ΔR_{nl} is defined as $\Delta R_{nl} = R_{nl,P} - R_{nl,AP}$, for R_{nl} in the parallel (P) or antiparallel (AP) configuration. All measurements in this chapter were performed at $T = 200\,\mathrm{K}$, using the cryostat described in section 3.7. As the measurement setup did not contain a device to automatically record the injector current, this parameter was noted manually and then later added to the measurement data.

At a distance between the injector and the detector contacts of $6\,\mu$m, we achieve a spin valve signal of $R_{nl} \sim 7\,\Omega$ at an injector current of $I_{inj} = +5\,\mu$A, as can be seen in Fig. 5.3. The resistance area products of the injector and detector electrodes are $45.9\,\mathrm{k}\Omega\mu\mathrm{m}^2$ and $27.0\,\mathrm{k}\Omega\mu\mathrm{m}^2$, respectively. In Fig. 5.4 we see in black a back gate sweep of the graphene sheet resistance, with the Dirac point at $V_g = -2\,\mathrm{V}$. From these data, the carrier mobility was calculated to be between $\mu = 3500 \ldots 5000\,\mathrm{cm}^2/\mathrm{Vs}$, depending on back gate voltage. The red trace in Fig. 5.4 displays the gate dependence of the spin valve signal, at an injector current of $I_{inj} = +4\,\mu$A. At this injector current the gate dependence follows qualitatively the shape for high quality tunnel contacts as described by W. Han *et al.*[88]. The differential resistance $dR = \frac{dU_{inj}}{dI_{inj}}$ of the injector contact is shown in the inset of Fig. 5.4 and displays clearly non-ohmic behavior, another indicator for high quality tunnel barriers.

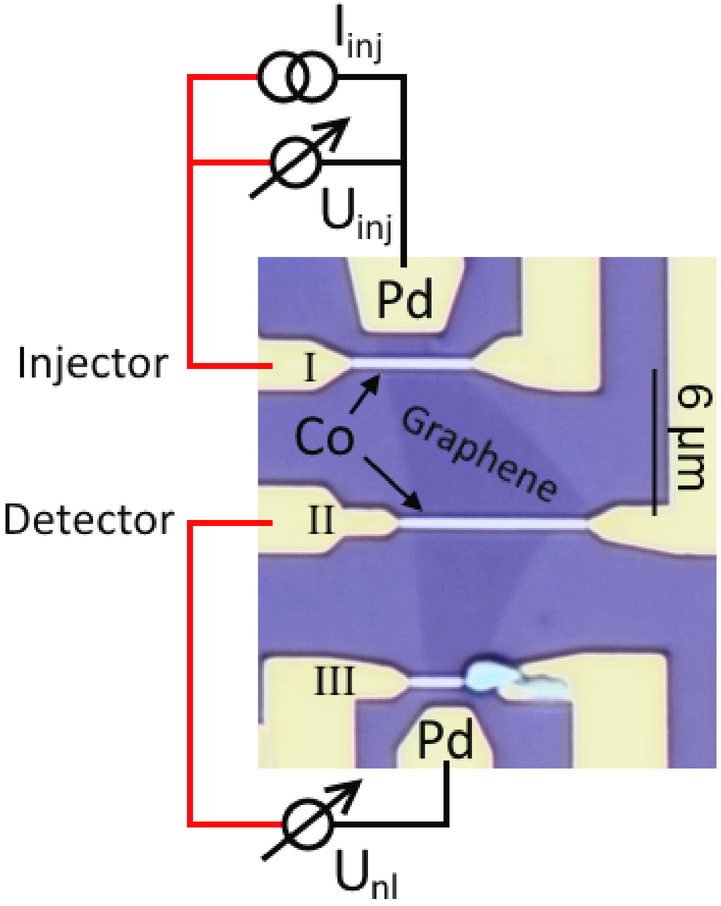

Figure 5.2: Sample schematic showing a graphene flake with contacts in the non-local spin valve measurement setup. The polarity of current source and voltage detectors is indicated by red (positive) and black (negative) leads.

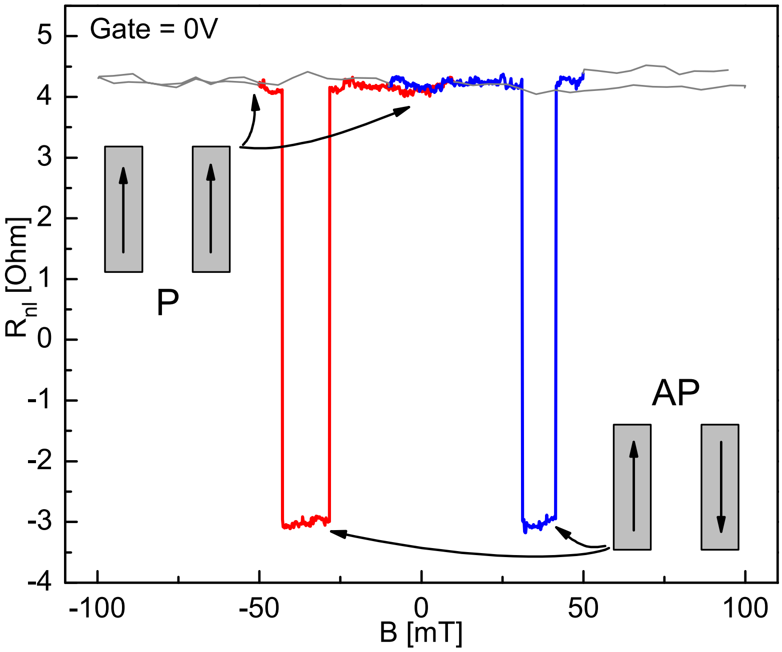

Figure 5.3: Spin valve signal at $V_g = 0\,\mathrm{V}$ with illustrations to show the parallel (P) and antiparallel (AP) magnetic orientation of the electrodes. Distance of the injector and detector contacts was $6\,\mu\mathrm{m}$ with an injector current of $I_{inj} = +5\,\mu\mathrm{A}$. The grey trace shows the preparation of the electrodes that was done at a higher sweep rate, which induces a slight inductive offset because of the DC measurement setup.

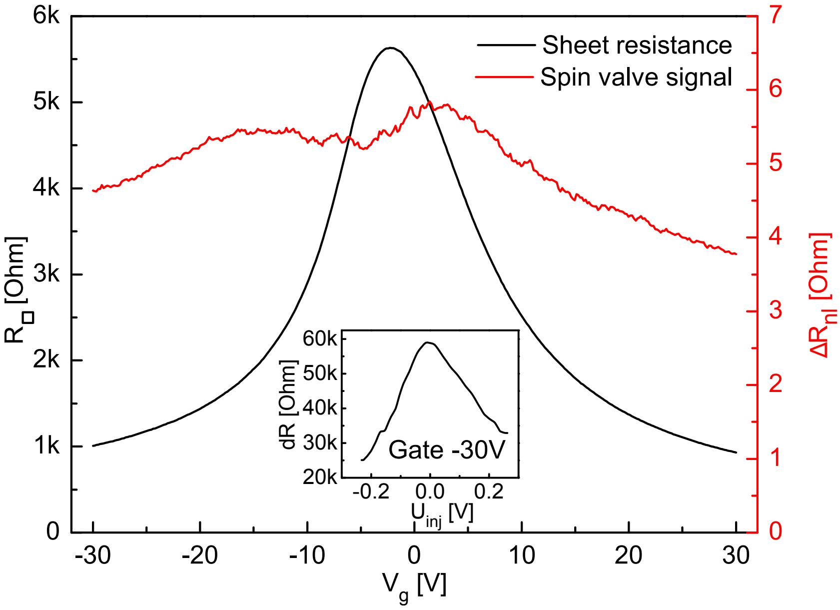

Figure 5.4: Gate dependence of the non-local spin valve signal ΔR_{nl} with an injector current of $I_{inj} = +4\,\mu\mathrm{A}$ (red) and the sheet resistance (black). The Dirac point is at $V_g = -2\,\mathrm{V}$. Inset shows the differential resistance of the injector tunnel contact as a function of voltage bias.

5.3 Injector bias and gate dependence of the non-local spin signal

Now we apply a negative bias current of $I_{inj} = -4\,\mu$A. Surprisingly, the observed polarity of the spin valve signal now depends on the gate voltage V_g, as shown in Fig. 5.5 (insets). When we fix the electrode magnetization to either P or AP and record the gate reponse of R_{nl}, we observe the black (P) and red (AP) curves in Fig. 5.5. The traces cross, which indicates that the back gate can change the polarity of the detected spins.
The transition between these two states is best observed in Fig. 5.6 which displays the gate dependence of the non-local spin valve signal ΔR_{nl} , calculated from the data in Fig. 5.5. A positive ΔR_{nl} then represents the expected spin valve signal while a negative ΔR_{nl} signifies an inverted spin valve signal. As can be seen, the transition between regular and inverted spin signal occurs at $V_g = -2\,$V. The transition is continuous and approximately linear. That the Dirac point is at the same back gate voltage as the spin neutrality point is a coincidence. Applying a different injector current will move the spin neutrality point, as shown below. In the region where ΔR_{nl} is negative the scaling with the gate voltage is distinctly different than in the region where ΔR_{nl} is positive. As Fig. 5.6 shows, in this configuration the sample acts as spin field effect transistor, where the back gate can be used to turn ΔR_{nl} on, off or invert it.

Finally, we study the bias dependence of the spin valve signal. Fig. 5.7a) displays the dependence of ΔR_{nl} on the injector bias U_{inj} at a gate voltage of $V_g = 30\,$V (black squares) and $V_g = -30\,$V (red triangles). The inset shows the U_{inj}-I_{inj} dependence of the injector contact for the corresponding gate voltages. Fig. 5.7b) and c) display the direct response of the detector voltage U_{nl} to the injector bias U_{inj}, for $V_g = 30\,$V in Fig. 5.7b) and $V_g = -30\,$V in Fig. 5.7c). As Fig. 5.7a) shows, for positive U_{inj}, ΔR_{nl} is always positive, while at negative U_{inj}, ΔR_{nl} changes sign at a certain value of U_{inj}. This inversion point can be tuned by the gate voltage, or, equivalenty, an injector bias of $U_{inj} \approx -150\,$mV sets the operating point for gate-controlled spin transistor action.

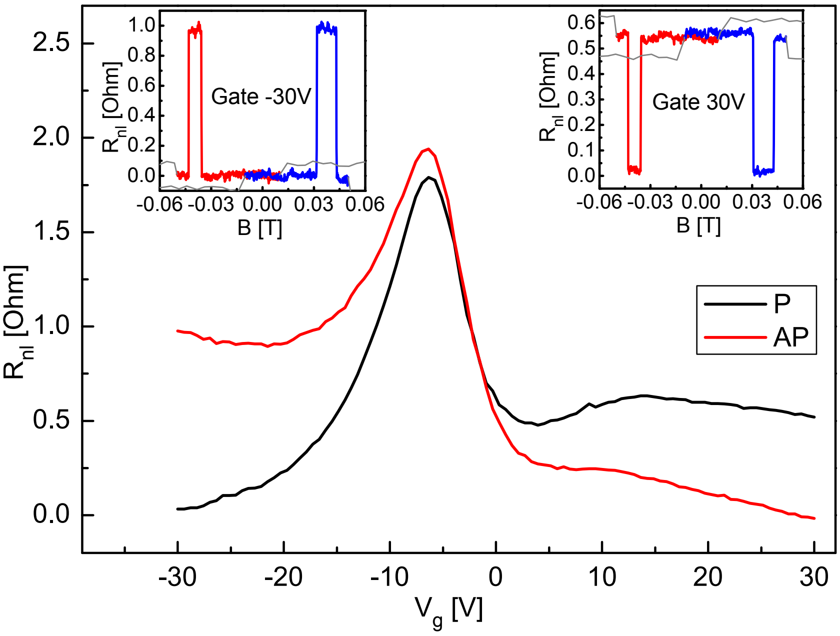

Figure 5.5: Gate dependence of the non-local resistance of parallel (P, black) and antiparallel (AP, red) configuration, at a fixed injector current of $I_{inj} = -4\,\mu$A. Insets show the spinvalve signal at $V_g = 30\,$V and $V_g = -30\,$V.

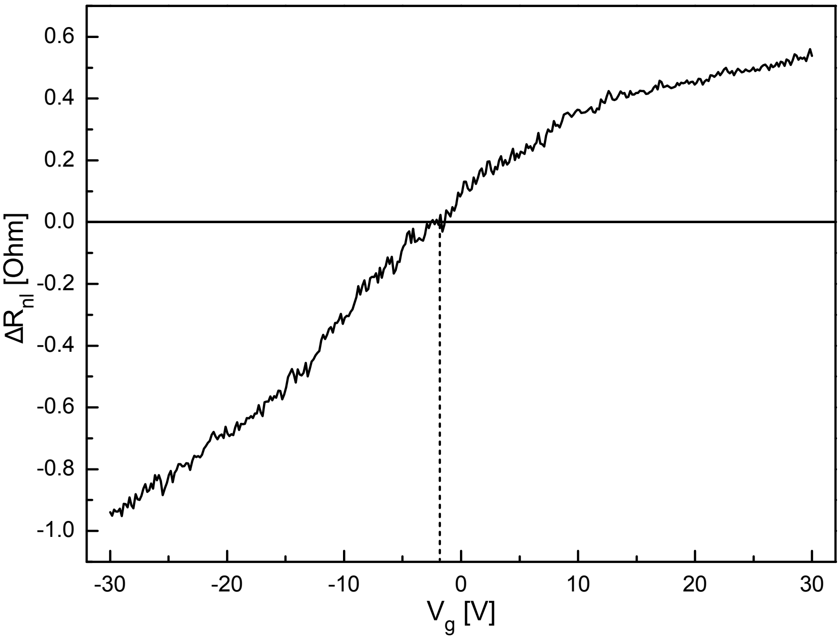

Figure 5.6: Gate dependence of the non-local spin valve signal ΔR_{nl} at a fixed injector current of $I_{inj} = -4\,\mu$A in black.

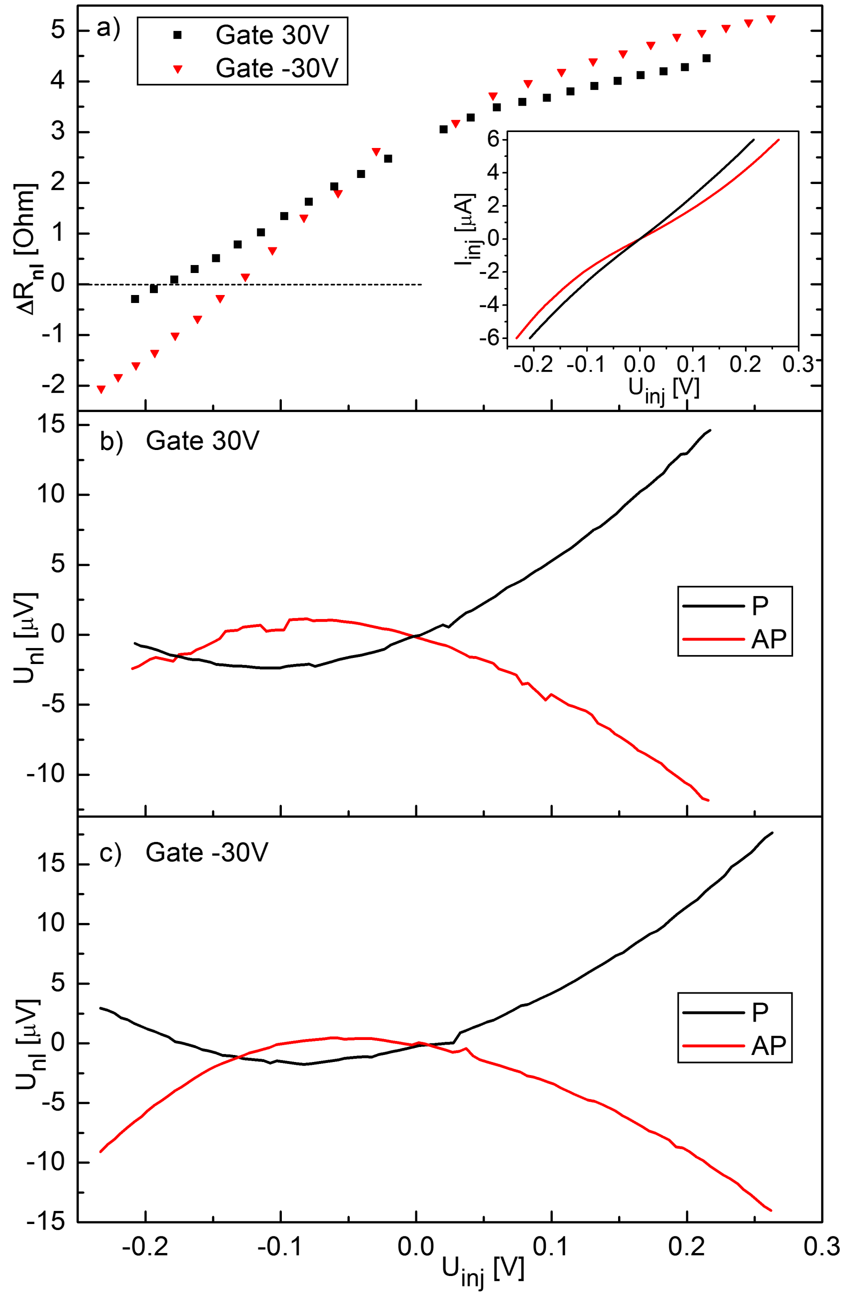

Figure 5.7: a) Plot of the spinvalve signal ΔR_{nl} in dependence of the injector bias for $V_g = 30\,\mathrm{V}$ (black squares) and $V_g = -30\,\mathrm{V}$ (red triangles). Negative values indicate an inverted spin valve. The injector current was varied between 0.5 and 6 μA with steps of 0.5 μA for each current polarity and gate voltage. b) & c) Plot of the voltage signal measured at the detector electrode in dependence of the injector bias for parallel (P, black) and antiparallel (AP, red) configuration, for gate voltages of b) $V_g = 30\,\mathrm{V}$ and c) $V_g = -30\,\mathrm{V}$.

5.4 Discussion

As the measurements are performed in a lateral spin valve geometry and the back gate also affects the spin channel, we need to distinguish between contributions from the spin channel and contributions from the tunnel contacts. Since the spin valve inversion is only enabled by a negative injector current, this is a clear indicator of a contact effect. However, when applying a back gate voltage, contributions from the spin channel to the amplitude of ΔR_{nl} cannot be excluded. We note that the gate dependence of the spin injection polarization can pose a problem when a measurement of $\Delta R_{nl}(V_g)$ is used to extract spin transport parameters of the graphene channel, as practiced in some publications [65, 66].

The reversal of the spin polarization is originating from a property of the injector contact and appears at an injector bias of $U_{inj} \approx -150\,\text{mV}$. Since the effect can be manipulated by the back gate, it must have a connection to the Fermi level in graphene. For low-resistance contacts, the Fermi level in graphene under the electrodes is pinned [63]. This pinning is lifted when the contact resistance is high enough, which we assume to be the case in our sample. The pinning of the Fermi level under the electrodes might be the reason for an absence of a gate dependence in other publications that report a bias-dependent spin valve reversal in graphene [115].
In fully crystalline magnetic tunnel junctions, a reversal of the spin polarization can be caused by the band structure [116]. A similar mechanism might be present in our case, though it must be noted that in our sample the MgO/Co layers are only polycrystalline. A further possible origin are defects in the barrier, where resonant tunneling at a specific energy can result in spin valve inversion [117]. This does not match with the featureless bias dependence in our sample as shown in Fig. 5.7.
When in contact with a ferromagnet, the band structure of graphene can be spin split through a magnetic proximity effect [118]. This can then lead to an inverted spin valve when tunneling from p to n doped graphene, as observed by Asshoff *et al.* [113]. However, this magnetic proximity effect requires the graphene to be in direct contact with a ferromagnet, which is not the case in our samples. We have a tunnel barrier of $\sim 1.4\,\text{nm}$ MgO that separates the Co from the graphene. The non-ohmic differential resistance shown in Fig. 5.4 proves that the barrier is mostly pinhole free, so there is no point of contact between Co and graphene. Furthermore, the induced spin splitting in graphene by the magnetic proximity effect results in a low spin polarization and a weak spin valve signal, as reported by Asshoff *et al.* [113]. This does not match our sample, where the spin signal can be quite large as shown in Fig. 5.3.
Considering the available facts, the most likely explanation for the spin polarization reversal is then a feature in the density of states (DOS) of cobalt. While the polarization P_N derived from the spin-resolved density of states (DOS) of cobalt [119] stays constant in an energy window of about 700 meV below the Fermi level, for spin injection one has to consider the effective spin polarization g_{eff} weighted by v^{α}, where v is the electron velocity, and $\alpha = 1$ or 2 for a ballistic or diffusive situation, respectively [120].

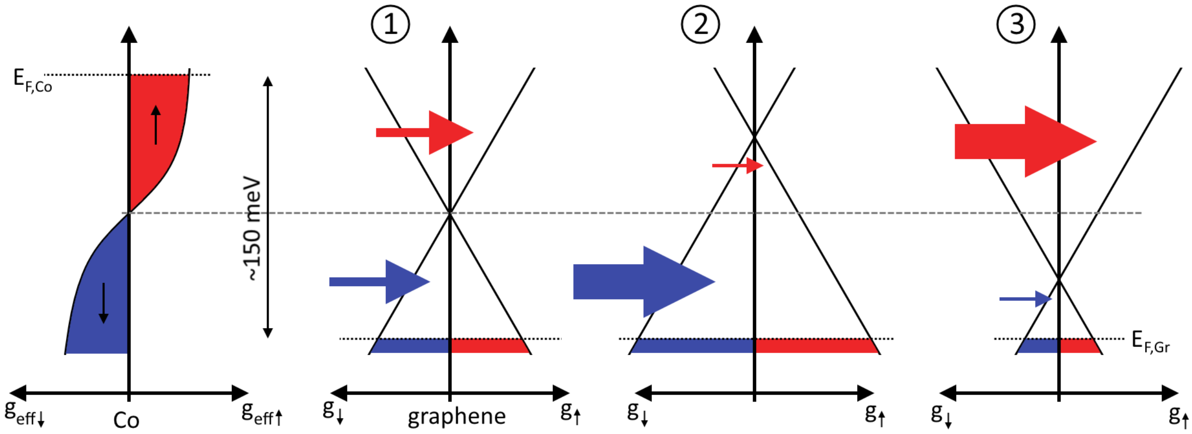

Figure 5.8: Speculative mechanism of the observed spin polarization reversal, showing the tunneling of electrons from Co to graphene. The DOS of Co has a reversal in the effective spin polarization g_{eff} in the energy range $\sim 150\,\mathrm{meV}$ below the Fermi level $E_{F,Co}$. We assume p doped graphene, where the injector bias of $\sim 150\,\mathrm{mV}$ aligns the Dirac point to the reversal point of g_{eff} in Co. In 1), there is no gate voltage applied and there is an equal number of states for spin up and spin down to tunnel into. This is the spin neutrality point, as the tunnel currents for spin up and spin down are of equal magnitude. In 2), a negative gate voltage is applied, which increases the p doping in graphene. Now the spin down electrons have more states to tunnel into, while spin up electrons have less. This results in a spin down polarization in graphene. In 3), a positive gate voltage is applied, which weakens the p doping of graphene. Now the spin up electrons have more states to tunnel into, while spin down electrons have less. This results in a spin up polarization in graphene.

Mazin calculated this quantity for Fe and Ni, showing a sign change of P_{Nv^2} around the Fermi level for Nickel, fundamentally different from P_N of Ni, while for Fe, both P_{Nv^2} and P_N show similar behavior around E_F [120]. The quantities P_N, P_{Nv} and P_{Nv^2} were calculated for Co/graphene by Sipahi *et al.* [121]. They observe that, while P_N in the bulk Co layers retains its sign over a wide energy range, the velocity-weighted polarization can show a strong energy dependence.

Since it is known that the spin polarization for the bulk and the interface can be quite different, depending on its detailed conditions [122], for our sample the velocity weighted DOS would have to be calculated for the Co/MgO interface. A similar situation was reported by Lou *et al.*, who see a strong bias dependence in a Fe/GaAs spin valve device. They are offering the band structure at the Fe/GaAs interface as a possible explanation [123].

That such a calculation for our sample can reveal the responsible mechanism is not guaranteed. We have an unknown crystal structure in our non-epitaxial sample, which makes a comparison to first-principles calculations not meaningful [124]. If we speculate that a polarization reversal of the effective spin polarization g_{eff} exists in Co at the Co/MgO interface, we can offer an explanation that matches our data. As shown in Fig. 5.8, g_{eff} of Co would need to have a reversal of the spin polarization in the energy range

$\sim 150\,\mathrm{meV}$ under the Fermi level. To match our data with this mechanism, the graphene needs to have a p doping. The p doping is of such a strength that at an applied injector bias of $\sim 150\,\mathrm{mV}$, the Dirac point in graphene is aligned with the reversal point of g_{eff} in Co. When no gate voltage is applied, this would result in equal tunneling currents of spin up and spin down electrons, and thus no spin polarization in graphene. Applying a gate voltage can then be used to move the Dirac point up or down. As there are less states near the Dirac point and more states away from it, the band structure of graphene can be used to tune the relative strength of spin up and spin down tunneling currents. This mechanism matches the gate polarity and approximately linear gate dependance shown in Fig. 5.6.
The explanation given in Fig. 5.8 assumes a p doping of the graphene. The relevant graphene is the area under the contacts, where the proximity to the MgO is likely to induce a doping, but we do not know if this doping is of p or n type. Assuming the proposed mechanism is correct, the data shown in Fig. 5.6 would only match a p doping. Depending on the actual shape of the DOS for g_{eff} in Co, the mechanism proposed in Fig. 5.8 could still work with weakly n doped graphene, if the gate can still shift the graphene into a p doping. An inability to induce a p doping in the graphene under the contacts would prevent a spin polarization reversal. The doping might be another explanation why other groups that observe a spin valve inversion do not report a gate tunability.

We note that a sign reversal of the spin-polarization under bias change was observed in Co/hBN/graphene by two groups [114, 115], but no gate dependence was reported. This shows that the observed electric control of the spin polarization is not restricted to a specific material combination. Instead, it can be found in different Co/insulator/graphene systems and thus seems to be a more universal feature.

5.5 Conclusion

In conclusion, we report on a tunable spin polarization of injected spins through a Co/MgO/graphene contact. For a certain range of negative injector bias the spin polarization can be controlled by the back gate, turning the device into a spin field effect transistor. We offer a conclusive explanation based on a speculative DOS at the Co/MgO interface. Calculating this DOS would need to include a velocity weighting, to account for the tunneling probability of the states. A comparison of our data to characteristic features of alternative mechanisms makes the proposed explanation the most likely. For the proposed mechanism to match our data requires a p doping of the graphene under the contacts, which could be induced by the MgO tunnel barrier.
In addition to the possible application as a spin transistor, we note that the gate dependence of the spin polarization has to be taken into account when studying the correlation of the spin lifetime to other gate dependent parameters of graphene.

Chapter 6

Summary

In this dissertation, we presented measurements on the spin relaxation anisotropy in graphene. The intention was to improve on the experiments published by N. Tombros *et al.* [19] and M. H. D. Guimarães *et al.* [53], who employed the rotating electrodes technique as detailed in section 2.4.1. Here, a large magnetic field >1 T is applied to rotate the electrodes out-of-plane (z direction) to measure the out-of-plane spin relaxation time τ_z. The accuracy of this method suffers severely from the magnetoresistance of graphene and other possible magnetic background signals.

The xHanle method described in section 2.4.3 offers several potential benefits over the rotating electrode technique, while also presenting new experimental difficulties to overcome. Here, a Hanle measurement is performed with the magnetic field aligned along the length of the spin channel (x direction). This causes the precessing spins to also experience τ_z during their rotation. By comparison with a regular Hanle measurement (zHanle, magnetic field in z direction), the anisotropy parameter $\zeta := \frac{\tau_z}{\tau_{xy}}$ can be extracted.

The improvements over the rotating electrodes technique is that no large magnetic fields are required, and any background can be eliminated by subtracting the antiparallel (AP) from the parallel (P) measurement traces. The experimental difficulty of the xHanle method is to prevent the electrodes from rotating during the measurement. The most accurate data are obtained when the electrode rotation can be prevented completely. We managed to achieve this by a combination of a long injector detector distance as well as careful electrode design.

The long travel distance of the electrons reduces the magnetic field range of the Hanle measurement. The electrodes can be designed as narrow as possible to increase their resistance towards a perpendicular magnetic field. Then, one electrode needs to have spatula shaped tips, which decreases the coercive field required for a magnetization reversal. A difference in the coercive fields of the electrodes is needed to prepare an antiparallel magnetic alignment. By applying these methods, we tried to improved the xHanle experiment sufficiently to achieve the so far most accurate measurement of the spin lifetime anisotropy in graphene. We believe to have succeeded in this task.

During the preparation of the experiments, B. Raes *et al.* published their work on the oblique spin precession method in 2016 [76], as detailed in section 2.4.2. This method is a substantial improvement over the rotating electrodes technique to measure the spin relaxation anisotropy. Here, a Hanle measurement is performed where the magnetic field is tilted to an oblique angle in the z-y-plane, with y being the long axis of the electrodes. Then, the precessing spins also experience τ_z during their rotation, which is the same basic idea as the xHanle method. However, the signal is detected in a different way.
The magnetic field is sufficiently increased to dephase the Hanle signal, which is 175 mT in the experiment of B. Raes. When the magnetic field is at an oblique angle, there will be a remaining spin signal parallel to the field, which can be detected. By recording this signal for several magnetic field angles, ζ can be extracted.
The immediate question concerning our work was then if this method is more accurate than an xHanle experiment. Luckily, the method can be performed with the same sample design that is required for xHanle. We then proceeded to perform the oblique spin precession experiment and the xHanle experiment with the same sample, to have a direct comparison.

While analyzing the data of the xHanle experiment, we discovered a non trivial magnetization of the Co at the MgO-Co interface of the electrodes. We conclude this to be the case based on three different indicators. As discussed in section 4.1.2, we performed AMR measurements on the electrodes to characterize their rotation behavior to perpendicular magnetic fields. Using that information, we then performed an xHanle experiment up to 300 mT where the AMR data indicate a complete rotation of the electrodes in x direction. The detected signal at 300 mT should then be equivalent to the zero field signal.
However, this was not the case. There was ∼20% less signal at 300 mT then for zero field, which we attribute to an incompletely rotated electrode magnetization. As the AMR data clearly indicate complete electrode rotation at 300 mT, we conclude that the interface magnetization behaves differently than the bulk and is more resistant to rotation. The AMR measurement is only sensitive to the bulk magnetization while the interface magnetization is relevant for the spin injection.
The second indicator to support this finding is the background of the 22 mT xHanle data. Any rotation of the electrodes would tilt the background, which we do not observe. This is again in disagreement with the AMR data, which display a ∼7% difference in the signal of 0 mT and 22 mT. The disagreement is again solved by an interface magnetization that is more resistant to rotation than the bulk.
The third indicator is the analysis of the xHanle data. Here, an asymmetry is observed that we attribute to a tilted interface magnetization of one electrode. The tilt is $\sim 9^\circ$ in z direction and would be caused by the perpendicular magnetic anisotropy at the MgO-Co interface [104]. This explanation gives the best fit of the data, as discussed in detail in section 4.2.2.

Our analysis of the xHanle and oblique spin precession data is then relying on the assumption that our interpretation of the non-trivial interface magnetization is correct. In the xHanle experiment, the spurious effects of this magnetization can be eliminated by symmetrizing the data. In the oblique spin precession experiment however, a correct fit of the data requires knowing the exact tilt angle of the magnetization. Any inaccuracy in determining this tilt angle will be inherited by the fit results of the oblique spin precession data. It then follows that the oblique spin precession experiment cannot be performed with the maximum possible accuracy in our sample because of the tilted magnetization at the MgO-Co interface.

The measured spin relaxation anisotropy in graphene, averaged over several back gate voltages, is then $\zeta = 0.78 \pm 0.04$ from the xHanle experiment, while the oblique spin precession gives an average of $\zeta = 0.91 \pm 0.15$. We explain the discrepancy between the two values with an insufficient accuracy of the oblique spin precession experiment, as detailed in section 4.4. When error bars are included, the results of the two experiments overlap.

The uncertainty in ζ obtained from xHanle results from possible fitting errors and undetermined small magnetic stray fields. The uncertainty in ζ obtained from oblique spin precess is mostly due to the tilted electrode magnetization, where the tilt angle cannot be accurately determined. Other, smaller contributions are the inaccuracy of the magnets, fitting errors and the inaccuracy of parameters in the quite extensive fit function. It then follows that in our sample, the xHanle experiment is more accurate than the oblique spin precession experiment.

An open question that our data cannot answer is which experiment would be more accurate under ideal conditions. We believe the xHanle experiment is potentially more accurate, based on the fact that here P and AP state are measured while the oblique spin precession experiment can only measure the P configuration. Subtracting the AP from the P data is a reliable method to remove any magnetic background and also gives a better signal to noise ratio than using just the P state data. In contrast, the oblique spin precession experiment relies on normalization to remove a background signal.

When discussing accuracy under non-ideal conditions, the obvious problem of the oblique spin precession experiment is a possible tilted electrode magnetization. The crucial point is, this cannot be identified in the oblique spin precession data and was only discovered because of a simultaneous xHanle experiment. As a perpendicular magnetic anisotropy can be present at the interface of other material combinations besides Co-MgO, for example Fe-$\mathrm{AlO_x}$ [104], this is a potentially huge source of error that needs to be accounted for in any oblique spin precession experiment.

In our xHanle experiment there was little ($<8°$) or no rotation of the electrodes during the measurement, which is the ideal condition. A slight rotation of 8° for both electrodes will result in a 2% change in the signal and is the threshold that can still be considered as equivalent to no rotation. If that can be guaranteed, the experiment is quite robust to other interferences. A magnetic background can be reliably removed by subtracting the AP from the P data and symmetrization eliminates any spurious effects of a tilted magnetization, without a need to know the tilt angle. However, we did not investigate how much accuracy is lost when more than 8° electrode rotation cannot be prevented. This rotation then needs to be accounted for in the fitting procedure, with a need to know the rotation angle of both electrodes. In that case, the oblique spin precession experiment could offer a better accuracy.

The obtained accuracy of our xHanle experiment is close to ideal. The only possible improvement is the reduction of magnetic stray fields by a better magnet control. This would need a permanently installed 3D Hall sensor in our measurement setup. We then conclude that the spin relaxation anisotropy in our graphene sample is $\zeta \approx 0.8$, as per the xHanle data.

We will now discuss the spin relaxation in our graphene sample based on the the measured anisotropy parameter of $\zeta \approx 0.8$. There is no single spin relaxation mechanism that has this exact anisotropy, so we can conclude to have a mix of mechanisms with $\zeta < 0.8$ and $\zeta > 0.8$. Since we use a SiO_2 substrate, we expect a Rashba type spin-orbit field to be present that results in spin relaxation with $\zeta = 0.5$ (see section 2.3.2). For the mechanisms with $\zeta > 0.8$, the likely candidates are resonant scattering by magnetic impurities (see section 2.3.3) and contact induced spin relaxation (see section 2.3.4), which both have $\zeta = 1$. The measured $\tau_{xy} \approx 850\,\mathrm{ps}$ is nearly two orders of magnitude lower than the worst case estimate of 50 ns for spin relaxation based on the intrinsic spin-orbit fields of graphene (see section 2.3.1), so we can exclude this mechanism as a limiting factor.

Since we now only consider contributions to τ_s with $\zeta = 0.5$ and $\zeta = 1$, we can use equation 4.10 discussed in section 4.5 to separate the anisotropic and isotropic parts of the total spin lifetime. Using the xHanle data at $V_g = 12\,\mathrm{V}$ ($\tau_{xy} = 850\,\mathrm{ps}$, $\zeta = 0.78$, $\tau_z = 660\,\mathrm{ps}$), we get $\tau_{iso} = 1.18\,\mathrm{ns}$ for the isotropic part and $\tau_{Rashba,xy} = 3\,\mathrm{ns}$ and $\tau_{Rashba,z} = 1.5\,\mathrm{ns}$ for the anisotropic Rashba part. These values are in agreement with the models of the respective relaxation mechanisms, as detailed in section 4.5.

The anisotropy was measured for back gate values ranging from $V_g = -11\,\mathrm{V}$ to $V_g = +12\,\mathrm{V}$, with the Dirac point at -2 V. The farthest energy offset from the Dirac point in graphene is then $E_F = 116\,\mathrm{meV}$ at $V_g = 12\,\mathrm{V}$. In this energy range, there is no significant change of the anisotropy parameter ζ (see Fig. 4.25 in section 4.4). The in-plane spin lifetime τ_{xy} varies between 730 ps and 1.1 ns, but without a clear trend (see Fig. 4.8 in section 4.1.1). Since the proposed spin relaxation mechanisms all have an energy dependence, it must be concluded that the probed energy range was not large enough to see it.

The next question is whether the isotropic part of the spin relaxation is dominated by contact induced spin relaxation or by resonant scattering by magnetic impurities. We compare our sample with the results of T. Maassen *et al.* [62] concerning contact induced spin relaxation, as discussed in section 2.3.4. The parameters of our sample are $R > 20$, $d/L_s \approx 3$ and $R/L_s \approx 5$, which according to Fig. 2.15 means the contacts still have a small influence. We then conclude that the contacts are most likely not the dominant mechanism for the isotropic part of the spin relaxation.

In summary, the spin relaxation in our sample is limited in equal parts by the SiO_2 substrate and resonant scattering by magnetic impurities.

While characterizing the sample for the anisotropy measurements, we observed an unexpected spin valve inversion. Further investigation revealed that the spin polarization of the injector contact can be tuned by both the injector current bias and the gate voltage. The spin polarization can be turned off and even inverted. First, this needs to be accounted for when using the back gate to probe the spin dependent properties of the graphene spin channel. Second, this behavior can be used to build a novel type of spin transistor, where the signal is switched off by turning off the spin injection using the field-effect. In contrast to the Datta and Das spin field effect transistor [5], this design does not need a spin channel with a large spin-orbit coupling. We present measurements displaying this transistor behavior in section 5.3.

The source of the effect is most likely the band structure of the injector contact stack Co/MgO/graphene. Since the effect can be tuned by the back gate, the band structure of graphene must be involved. We offer a possible explanation of the effect displayed in Fig. 5.8 in section 5.4. This explanation would match our data, but it is based on a speculative band structure at the Co/MgO interface that needs to be verified by a calculation.

Since a spin valve inversion is also observe by other groups that use a different material combination [114, 115], the effect might be more universal.

Appendix: Fabrication details

A.1 Graphene exfoliation

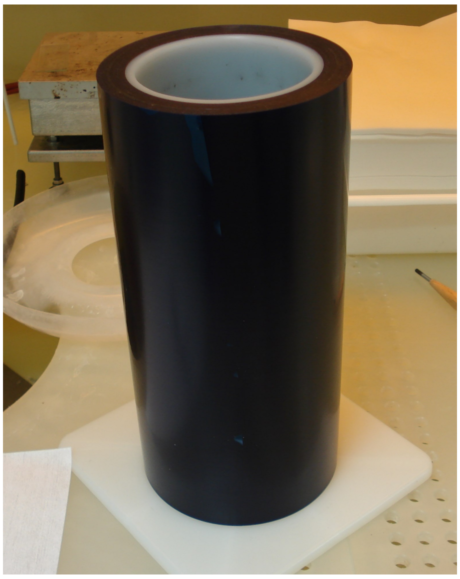

Figure A.1: Dicing tape type Ultron 1008R-9.0 by Minitron Electronic GmbH used for exfoliation.

The exfoliation technique used is a variant of the standard „Scotch tape method“. Instead of Scotch tape, a blue foil normally used for dicing wafers was employed. In our work group we have several different types of this dicing tape, the difference being mainly the type of glue on the tape. The glue that is the stickiest also leaves the most residue when removing the tape, while the least sticky glue leave nearly no trace after tape removal. All of the blue tape glues are less sticky than scotch tape and leave less residue.

While no residue after tape removal is desirable, the flip side is that exfoliation produces less graphene flakes when the glues is less sticky. This finding is the result of a discussion in our workgroup about our experiences with the various tapes for exfoliation and is not backed by scientific data.

The tape that was used in this thesis is shown in Fig. A.1 and is the first one we acquired and has the stickiest glue (dicing tape type Ultron 1008R-9.0 by Minitron Electronic GmbH). A special „hot exfoliation“ method was used that was established by Josef Kamann [82]. The advantage of this technique is that heating and cooling instead of rubbing is used to get a good connection of tape and chip. The heating and cooling is far easier to accurately reproduce than the rubbing, which benefits the consistency of the procedure. This method could not be used with the other less sticky tapes we acquired later (manufacturer: Nitto) as they behave differently when heated.

For this work the Nitto tapes were not used, even though it might have been desirable to further reduce the amount of glue residue on the chip. By the time the Nitto tapes became available, the hot exfoliation technique was sufficiently developed to constantly yield good results. Getting similar results with the Nitto tapes would have required additional time. As the small amount of glue residues from the Ultron tape were not considered problematic for the intended experiments, spending the required time to bring exfoliation with the Nitto tapes to similar proficiency was deemed unnecessary.

The details of the exfoliation process are as follows:

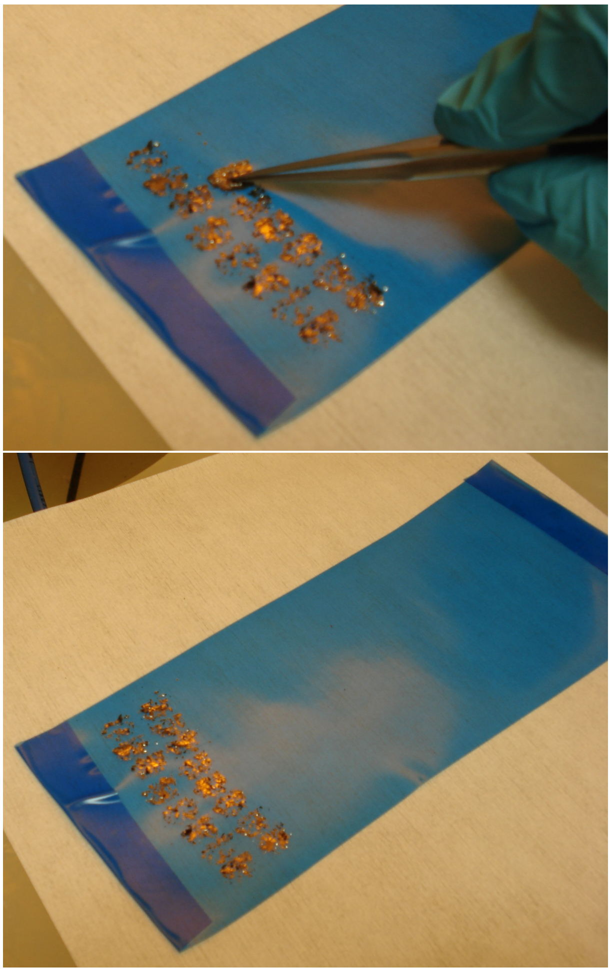

Figure A.2: Decorating the tape with „flaggy flakes“ graphite.

A large piece of „flaggy flakes“ graphite is selected. The side with the smoother surface is softly pressed on a piece of tape with flat metallic tweezers. Careful pressure is applied to the graphite to achieve a good connection to the tape. The graphite is then pulled off, which leaves thin peeled off graphite sticking to the tape. It my be necessary to repeat this a few times before the peel off is large and coherent. The graphite pieces usually have a rough, uneven surface, that is peeled off by the tape. After a few peels, the graphite surface is much more smooth and the graphite films remaining on the tape are larger.

When the graphite peels in nice large pieces, the end of a strip of tape is plastered with thin peeled graphite, as shown in Fig. A.2. The ends of the strip of tape are folded to have a non-sticky handling area. A clean part of sticking tape is folded on top of the peeled graphite and pressed down to get a good connection. The tape is pulled apart again to cleave the graphite. This cleaving process is repeated until the graphite is cleaved thin enough, which can be between roughly 5 to 10 times. What exactly „thin enough“ is needs to be determined by experience. Now a substrate needs to be prepared on which the tape with the cleaved graphite is used for exfoliation.

As a substrate for the exfoliation, a 10 cm diameter silicon wafer with a 285 nm oxidized surface is used. The wafer is processed to have markers of 60 nm gold with a chrome wetting layer underneath. After the markers are evaporated on the wafer, it is cut into 4,5 mm x 4,5 mm chips. Before using the chips for exfoliating graphene, they are cleaned in the following way: Acetone bath in the ultrasonic cleaner for about 30 seconds. Washed with clean acetone from a teflon squeeze bottle, placed in acetone,

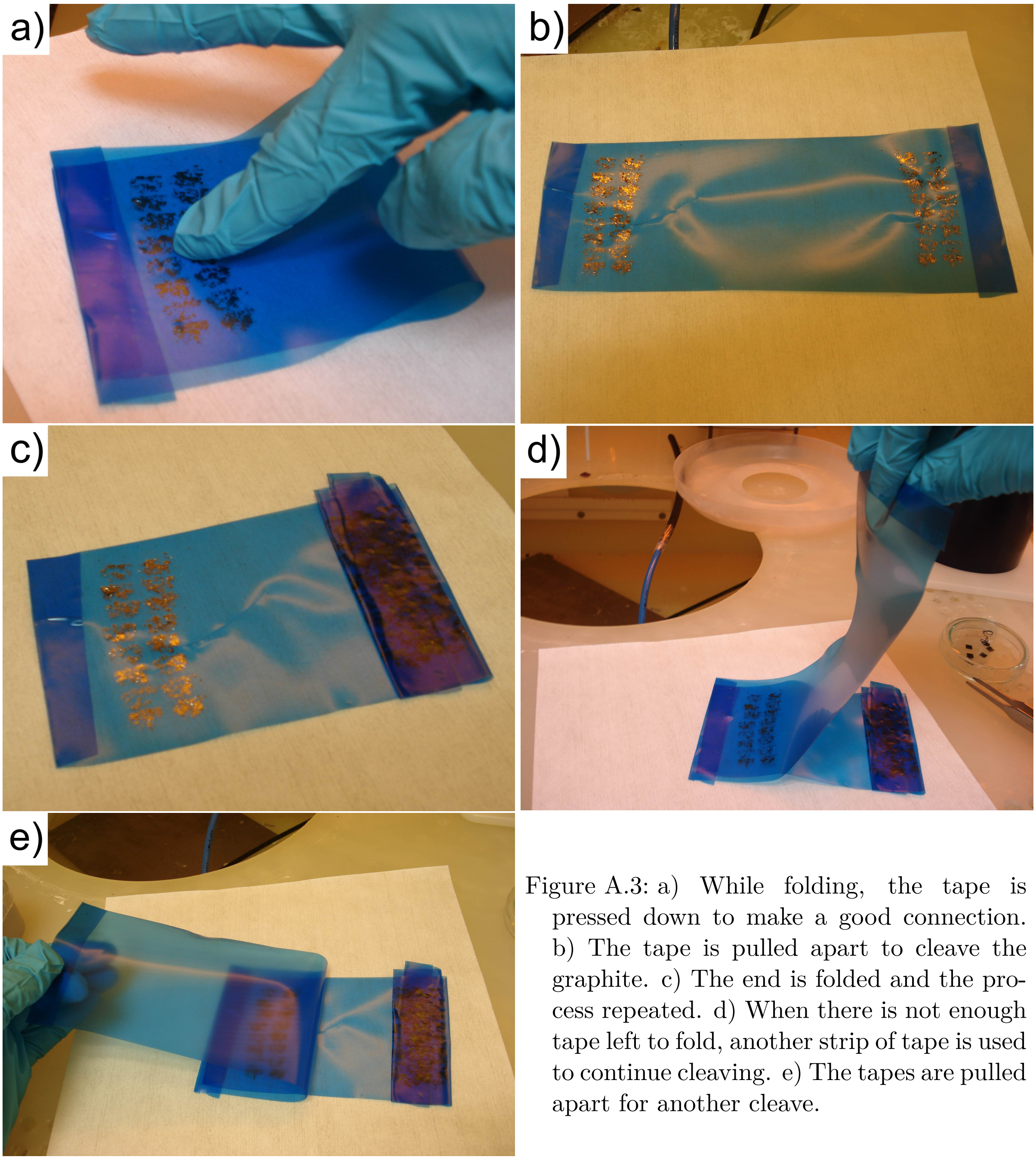

Figure A.3: a) While folding, the tape is pressed down to make a good connection. b) The tape is pulled apart to cleave the graphite. c) The end is folded and the process repeated. d) When there is not enough tape left to fold, another strip of tape is used to continue cleaving. e) The tapes are pulled apart for another cleave.

washed again with acetone, placed in propanol also from a teflon squeeze bottle, then blow dried with nitrogen. After this the chips are placed for 5 minutes in oxygen plasma. The teflon bottles are important as we have discovered that the non teflon bottles leave residues in the acetone and propanol that contaminate the graphene.
Before exfoliating on the chips, they are placed on a hotplate at 150°C to heat them up. Then they are placed on a glass petri dish that was also heated up on the 150°C hotplate, so that the chips don't cool down too fast. Then the tape with the cleaved

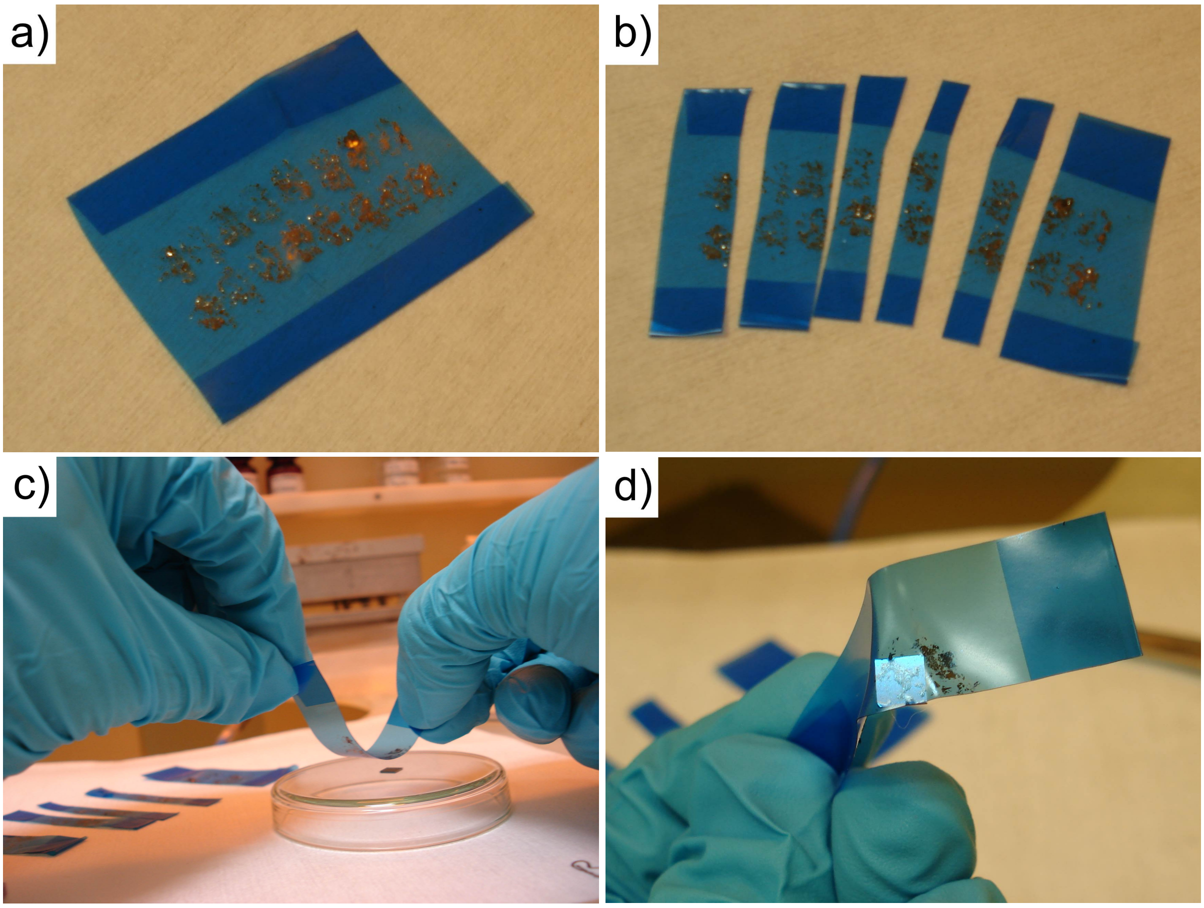

Figure A.4: a) Once the graphite is sufficiently cleaved, the rolled up tape is cut off. b) The tape is inspected for promising clusters of graphite and cut stripes, one per chip. c) The hot chip is placed on a hot upside down petri dish. The tape is carefully placed on the chip, avoiding to cause wrinkles or bubbles. d) The heat will make the tape cling to the chip, forming a very good connection. After waiting a few moments to let it cool, the tape is peeled off.

graphite is placed on the still hot chips. The heat from the chips will soften the tape and shrink it, making it cling tightly to the chips surface. After a few seconds of cooling, the chip can be carefully peeled from the tape.

When doing the exfoliation without heating the chips, it is required to rub the tape on the chips to get the graphite to peel on to the chip. With heating, no rubbing is required. The graphite that remains on the chip is the cleanest possible as it is freshly cleaved on both sides. The thickness of the peeled off graphite film is random and the chips then have to be searched with a microscope to see if single layer graphene has been exfoliated.

A.2 Preparing AlO$_x$ tunnel contacts

This fabrication procedure to prepare AlO$_x$ tunnel barriers on graphene was established by Daniel Pachniowski [45] and then further improved by Bastian Birkner [94], Andreas Sandner, Philipp Nagler [91] and me. According to Tobias Völkl, this procedure has stopped producing working samples (no spin signal) after the UHV chamber was optimized for low pressure operation to deposit better quality MgO.
The procedure for a AlO$_x$ tunnel barrier that covers the whole chip is as follows:

- Before the chip is placed in the evaporation chamber, it is pre annealed in the Annealing Oven AO 600 for 20 minutes at 400°C. There is no photo resist on the chip as the barrier will cover the whole sample.

- The chip is tightened to the sample holder of the UHV evaporation chamber. The sample holder is then put in the load lock and the load lock is pumped until the next day. Then the chip is transferred into the main chamber. This is done to preserve the pressure in the main chamber. The pressure in the load lock before the transfer is 10^{-8} mbar, the pressure in the main chamber is 10^{-10} mbar.

- After transferring, the sample holder is tightened to the sample suspension to have a good thermal connection. The sample suspension is cooled with liquid nitrogen to as low as possible, which is -120°C.

- The evaporation of aluminum is started with the shutter closed. The evaporation is adjusted to a low, stable rate.

- The frequency of the quartz crystal microbalance is readout directly with a frequency counter and displayed in a graph on the computer. The rate controller is not used. A thickness of 1.5 Hz to 2.5 Hz Al is deposited. This is done by two people, one reading the quartz frequency and the other one opening and closing the shutter. The shutter is open for only a few seconds.

- To oxidize the aluminum, the sample is transferred into the load lock. Before transferring, the load lock is conditioned in the following way:
  The turbopump is put on standby at 300 rpm, the backing pump is running as normal. On the mass flow controller, the oxygen flow is set to 80 sccm. After 5 minutes, the oxygen flow is stopped and the turbopump is switched from standby back to normal. The load lock is pumped to 10^{-8} mbar, then the sample is transferred to the load lock.
  For the oxidization of the sample, the valve to the turbopump in the load lock is shut and the torbopump is set to standby (the load lock is not pumped anymore). The oxygen flow is set to 110 sccm and the sample is oxidized for 30 minutes. The pressure will rise to 1.5 mbar during that time. When the oxidization is done, the

oxygen flow is stopped and the valve to the turbopump is opened again. The load lock can then be vented to take the sample out. If that is done immediately, the sample holder will still be so cold that ice will form on the sample. To avoid that, the sample is left in the N_2 flooded load lock for a while to warm up.

- After preparation of the AlO_x tunnel barrier, the lithography for the contacts is done and the desired magnetic metal is deposited.

This fabrication procedure resulted in working samples, not only with the tunnel barrier covering the whole chip, but also with local tunnel barriers just under the electrodes. In that case, the lithography is done before the Al deposition and the pre annealing is done before the lithography. The sample is transferred back into the main chamber after oxidizing the Al in the load lock for the subsequent deposition of Co. There was no apparent difference in the failure rate between the design with the chip covering tunnel barrier and the design with the local tunnel barrier.
Cooling or pre annealing is required, but not both. Working samples have been produced with pre annealing and no cooling and also cooling and no pre annealing.

A.3 Preparing Co electrodes with MgO tunnel contacts

This is the exact fabrication procedure for sample S7F2. It was fabricated in a two step lithography and evaporation process. The first step is described here and deposits the magnetic electrodes with the tunnel barrier. The second step described in the next section A.4 deposits the circuit paths and bondpads made out of Pd. For a faster sample preparation, a one step process was also employed where the circuit paths and bondpads are made of the same material as the electrodes. A sample made in this fashion is S7F1 that is shown in Fig. A.5. These fast process samples were used to test and tune the tunnel barrier.

Pre annealing: Before the lithography, the sample was pre annealed in the Annealing Oven AO 600 for 1 hour at 200°C in vacuum. This makes the graphene cling more tightly to the SiO_2 substrate. The induced roughness decreases the surface mobility of deposited Mg atoms, hindering island formation. Also, the annealing eliminates the risk that spin coating might remove the graphene flake.

Resist spinning: The tunnel contacts were prepared with the positive EBL photo resist CSAR (Allresist AR-P 6200), specifically CSAR 9% spun for 30 s at 4000 rpm. The resulting thickness is about 200 nm. After spin coating, the resist was baked at 150°C for 1 minute.
The CSAR resist has several benefits over PMMA resist. CSAR leaves less residue on graphene after removal, it allows for smaller structures and it is more heat resistant.

The better heat resistance is the most important feature for this fabrication procedure as during deposition in the UHV chamber the sample can get hot enough that PMMA resists start to give problems. Another useful characteristic of CSAR is that it needs less exposure dose than PMMA, so the lithography writes faster.

Electron beam lithography: A Zeiss Auriga electron microscope was used for the lithography. To pattern the resist, an acceleration voltage of 30 kV at a working distance of 10 mm was used. The small structures (electrodes, fine wiring) were written with an aperture of 20 μm, the large structures (coarse wiring, bondpads) were written with an 120 μm aperture. The exposure dosage was 180 μC/cm^2, which is quite high. The high dose is supposed to create an undercut in CSAR that helps with lift-off. Also, a high dose helps in reducing the polymer residue left on the graphene after development of the resist [57]. When using the CSAR resist, it has sometimes happened that unintended lines were written as depicted in Fig. A.5. The sample in Fig. A.5 is fabricated in just one lithography and evaporation step, so CSAR was also used for the circuit paths and the bondpads. The problem seems to only appear when writing larger areas. This looks like a charging effect that might be solvable by additionally spin coating an antistatic agent.

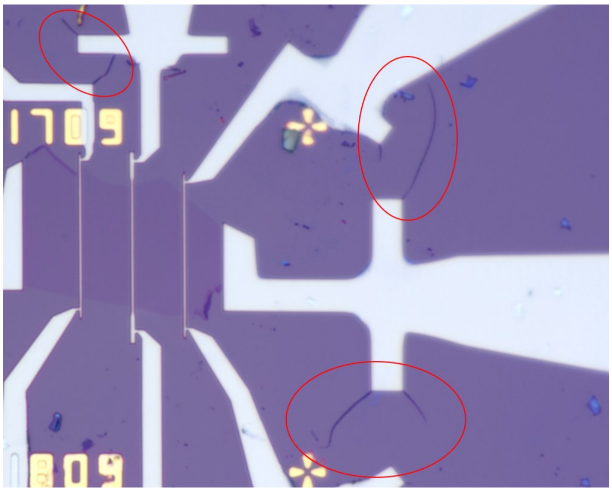

Figure A.5: Unintended lines in the lithography of CSAR caused by charge effects, circled in red. The sample name is S7F1. A short circuit created that way can be fixed by scratching with a probestation needle.

Development: To remove the exposed areas of the resist, the sample was swirled in AR 600-546 for 80 seconds and then rinsed in propanol for 40 seconds.

Material deposition: The MgO tunnel contacts and the Co electrodes were fabricated using the UHV evaporation chamber described in detail in section 3.4. As reported by F. Volmer *et al.* [84], a good 10^{-10} mbar pressure or better is needed to grow high quality MgO tunnel barriers. Also, it is essential to let the sample degas at this pressure for at least a day prior to depositing the materials.

The sample holder is taken out of the load lock where it is stored. Storing the sample holder in vacuum keeps it clean of residues that would deteriorate the pressure in the main chamber. The chip is tightened to the sample holder, which is attached to the transfer rod in the load lock of the UHV evaporation chamber. The load lock is pumped until the next day and then the chip is transferred into the main chamber. This is done to preserve the pressure in the main chamber. The pressure in the load lock before the transfer is 10^{-8} mbar. The sample is then left in the main chamber to degas for at least

a day.
Before the material deposition is started, Ti is evaporated for ~5 min with the shutter closed, to use the getter effect of Ti to further improve the pressure. After waiting one hour, a pressure of $1.4 \cdot 10^{-10}$ mbar was reached. The pressures listed here are from the run where sample S7F2 was fabricated and varied for other samples. With the shutter still closed, the MgO crystals are slowly heated with the e-gun. The minimum current of 5 mA is already enough to heat the MgO crystal to a temperature where it might shatter, so beam oscillation needed to be used to reduce the effective power. The Modus Operandi is to leave the e-gun current at 0 mA after turning it on, with no oscillation at first. At the 0 mA setting, the e-gun already emits a small amount of electrons. These electrons are sufficient to cause the MgO crystals to glow where the e-beam hits and that can be used to position the beam. When a suitable piece of MgO crystal has been targeted, the oscillations are turned on with a large amplitude and then the current is set to 5 mA. The power on the MgO crystal can now be increased by slowly decreasing the oscillation amplitude of the e-beam.
For sample S7F2, the MgO was heated until it evaporated at 66 Hz/min at a pressure of $1.5 \cdot 10^{-8}$ mbar. The rate was observed for a few minutes to verify that it is stable. On sample S7F2, 65 Hz of MgO were deposited. The last calibration of the MgO thickness a month earlier resulted in 1 nm = 46.7 Hz, so 65 Hz equals ~1.4 nm film thickness.
On top of the MgO, 20 nm of Co were deposited. The e-beam current was 20 mA, resulting in a deposition rate of 0.29 Å/s at the beginning that dropped to 0.21 Å/s at the end. The pressure during Co deposition was $5.5 \cdot 10^{-9}$ mbar.
For samples intended to have Pd circuit paths and bondpads, it is essential to cap the Co with an Au layer. Otherwise the Co surface oxidizes when exposed to air, forming an unwanted tunnel barrier to the Pd that is later deposited on top to connect the electrodes. This tunnel barrier will hinder measurements and needs to be avoided. For a single lithography process with Co circuit path and bondpads, a capping layer is not required as the Al wire bonder easily penetrates the surface oxide layer.
The Au source is heated by a coil around the crucible and needs to be heated very slowly. The temperature ramp is set to 13°C/min with a target temperature of 1450°C. At the start, the current output should be limited to 1/3 of the maximum until the actual temperature of the crucible has caught up with the set temperature ramp. At temperatures above 1200°C, the power source needs to be watched as it is operating near it's maximum capacity and might spontaneously cut the power. Simply switching it off and back on again solves the problem. The Au starts to evaporate slowly above 1350°C and the shutter can already be opened. The parameters for Au in the rate controller (parameters: density 19.3 g/cc, z-ratio 0.381, tooling 75) are incorrect and the evaporation rate is actually five times higher. Because of this, log entries are written as „0.6×5 = 3 nm“ and the rate as „0.02×5 Å/s“. After evaporation, the Au source is cooled down at a rate of 30°C/min.

Lift-off: The CSAR resist has a single drawback when compared to PMMA, and that is that the lift-off is not as reliable. The remover chemical for CSAR is AR 600-71 at room temperature. The sample is put into a beaker filled with remover and slowly swirled for

5 - 10 minutes. Then the sample needs to be checked under a microscope to identify areas that did not lift-off properly. Problematic areas need to be treated with water jets from a syringe filled with remover. If that is not successful, a short ultrasonic bath of 5 seconds can be used as a last resort, but that might damage the sample. Alternatively, the probestation can be used to remove unwanted metal connections by scratching with the needles. After the remover bath, the sample is rinsed with clean remover and blow dried with N_2.

A.4 Preparing Pd circuit paths and bondpads

This is the second part of the fabrication process for sample S7F2.

Resist spinning: For the bondpads a two layer resist combination was used, as that increases the reliability of the lift-off. The bottom resist that is spin coated first is PMMA 200k 9%, the top resist is PMMA 950k 2%. Both are dissolved in anisol, spun for 30 s at 6000 rpm and each layer is baked for 8 minutes at 150°C.

Electron beam lithography: A Zeiss Auriga electron microscope was used for the lithography. To pattern the resist, an acceleration voltage of 30 kV at a working distance of 10 mm was used. The small structures (electrodes, fine wiring) were written with an aperture of 20 μm, the large structures (coarse wiring, bondpads) were written with an 120 μm aperture. The exposure dosage was 400 μC/cm^2.

Development: To remove the exposed areas of the resist, the sample was swirled in developer for 40 seconds and then rinsed in propanol for 20 seconds. The developer is MIBK (methylisobutylketon) mixed with three parts chlorobenzene.

Material deposition: For the deposition of the Pd, the Leybold Univex 450 (Univex A) was used. The Pd is evaporated from the e-gun.

Lift-off: The sample was put into a beaker filled with acetone and placed on the 60°C hotplate for a day. Then the sample was checked under a microscope to identify areas that did not lift-off properly. Problematic areas were treated with water jets from a syringe filled with acetone. After the acetone bath, the sample is rinsed with propanol and blow dried with N_2.

Acknowledgments

An dieser Stelle möchte ich mich bei all jenen bedanken, die zum Erfolg dieser Arbeit maßgeblich beigetragen haben:

- Zuerst möchte ich mich beim Elitenetzwerk Bayern bedanken, dessen Stipendium mir die Promotion erst möglich gemacht hat. Weitere finanzielle Unterstützung erhielt ich von der Deutschen Forschungsgemeinschaft (DFG) im Rahmen der Projekte SFB 689 (Project A7) und GRK 1570.

- Ich bedanke mich bei Prof. Dr. Dieter Weiss, der trotz ungesicherter Finanzierung mir ermöglichte die Arbeit am Lehrstuhl anzufangen. Ich bedanke mich für das Vertrauen, dass ich es schaffen werde die Probleme finanzieller und experimenteller Natur zu lösen.

- Besonderer Dank gilt meinem Betreuer Dr. Jonathan Eroms, der mir das Thema der Arbeit vorgeschlagen hatte und mich als geeigneten Kandidaten gesehen hat. Ich bedanke mich für die intensive Betreuung und die gute Zusammenarbeit.

- Ich möchte Prof. Dr. Günther Bayreuther danken, der mir als Betreuer meiner Diplomarbeit eine vernünftige wissenschaftliche Grundlage gegeben hat. Desweiteren möchte ich mich dafür bedanken, dass er sich als Zweitgutachter meiner Dissertation zur Verfügung gestellt hat.

- Bei Prof. Dr. Christoph Strunk und seiner Arbeitsgruppe möchte ich mich dafür bedanken die UHV-Aufdampfanlage benutzen zu dürfen, die ein wesentlicher Bestandteil der Arbeit war. Ein extra Dankeschön an dieser Stelle an Thomas Haller, der mir bei den Umbauten an der Anlange immer behilflich war.

- Ich möchte Dr. Matthias Kronseder und den weiteren Kollegen vom Lehrstuhl Prof. Dr. Christian Back danken für die Unterstützung bei den Problemen mit der UHV-Aufdampfanlage.

- Ich bedanke mich bei Prof. Dr. Jaroslav Fabian und seinen Mitarbeitern Dr. Denis Kochan und Klaus Zollner, die mir bei der Interpretation meiner Messergebnisse geholfen haben.

- Ich möchte Dr. Frank Volmer von der RWTH Aachen University danken, dessen Ratschläge zur Verbesserung unserer MgO Tunnelbarrieren entscheidend für das Gelingen der Arbeit waren.

- Bedanken möchte ich mich auch bei meinem Master-Studenten Matthias Rosenauer, dessen Besuch in Aachen bei Frank Volmer mir sehr wertvolle Informationen gebracht hat. Weiterer Dank gilt den von mir betreuten Bachelor-Studenten Phillip Nagler, Maximilian Kadur, Felix Simbürger und Franz Hopperdietzel, deren aller Arbeit zu meiner Dissertation beigetragen hat.

- Ich bedanke mich bei der gesamten Graphen-Gruppe, die mich bei der Problemlösung unterstützt hat. Insbesondere bedanke ich mich bei Bastian Birkner, der wichtige Grundlagen für meine Arbeit gelegt hat und bei Tobias Völkl, der mir bei der Optimierung der MgO Tunnelbarrieren geholfen hat.

- Weiterer Dank gilt allen meine Kollegen vom Lehrstuhl Weiss, insbesondere meinen Bürokollegen Hubert Maier, Alexei Iankilevitch und Stephan Geißler. Ich bedanke mich für die freundliche Arbeitsatmosphäre und das Alignment-Training.

- Ich möchte unseren Sekretärinnen Claudia Moser und Elke Haushalter danken, die mir in allen bürokratischen Anliegen immer engagiert geholfen haben.

- Ein weiteres Dankeschön geht an unsere Techniker Uli, Flo, Daniel, Connie, Michl und Tom für die Unterstützung bei allen Problemen im Labor und Reinraum.

- Der letzte Dank geht an meine Familie, deren finanzielle Unterstützung mir ein sorgenfreies Physikstudium ermöglicht hat.

Bibliography

[1] G. E. Moore, “Progress in digital integrated electronics”, International Electron Devices Meeting, IEEE, 11 (1975).

[2] G. Bourianoff, M. Brillouet, R. K. Cavin, T. Hiramoto, J. A. Hutchby, A. M. Ionescu, and K. Uchida, “Nanoelectronics research for beyond CMOS information processing [Scanning the Issue]”, Proc. IEEE **98**, 1986 (2010).

[3] D. Reddy, L. F. Register, G. D. Carpenter, and S. K. Banerjee, “Graphene field-effect transistors”, J. Phys. D: Appl. Phys. **44**, 313001 (2011).

[4] I. Žutić, J. Fabian, and S. Das Sarma, “Spintronics: Fundamentals and applications”, Rev. Mod. Phys. **76**, 323 (2004).

[5] S. Datta and B. Das, “Electronic analog of the electro-optic modulator”, Appl. Phys. Lett. **56**, 665 (1990).

[6] B. Behin-Aein, D. Datta, S. Salahuddin, and S. Datta, “Proposal for an all-spin logic device with built-in memory”, Nat. Nanotechnol. **5**, 266 (2010).

[7] H. Dery, H. Wu, B. Ciftcioglu, M. Huang, Y. Song, R. Kawakami, J. Shi, I. Krivorotov, I. Žutić, and L. J. Sham, “Nanospintronics based on magnetologic gates”, IEEE Trans. Electron. Dev. **59**, 259 (2012).

[8] T. Suzuki, T. Sasaki, T. Oikawa, M. Shiraishi, Y. Suzuki, and K. Noguchi, “Room-temperature electron spin transport in a highly doped Si channel”, Appl. Phys. Express **4**, 023003 (2011).

[9] T. Kuczmik, M. Oltscher, A. Bayer, D. Schuh, D. Bougeard, M. Ciorga, and D. Weiss, “Hanle spin precession in a two-dimensional electron system”, Phys. Rev. B **95**, 195315 (2017).

[10] J. Fabian and S. Das Sarma, “Spin relaxation of conduction electrons”, J. Vac. Sci. Technol. B **17**, 1708 (1999).

[11] D. Kochan, M. Gmitra, and J. Fabian, “Spin relaxation mechanism in graphene: Resonant scattering by magnetic impurities”, Phys. Rev. Lett. **112**, 116602 (2014).

[12] J. Bundesmann, D. Kochan, F. Tkatschenko, J. Fabian, and K. Richter, “Theory of spin-orbit-induced spin relaxation in functionalized graphene”, Phys. Rev. B **92**, 081403 (2015).

[13] M. Gmitra, D. Kochan, P. Högl, and J. Fabian, “Trivial and inverted Dirac bands and the emergence of quantum spin Hall states in graphene on transition-metal dichalcogenides”, Phys. Rev. B **93**, 155104 (2016).

[14] K. Zollner, M. Gmitra, T. Frank, and J. Fabian, “Theory of proximity-induced exchange coupling in graphene on hBN/(Co, Ni)”, Phys. Rev. B **94**, 155441 (2016).

[15] W. Han, R. K. Kawakami, M. Gmitra, and J. Fabian, “Graphene spintronics”, Nat. Nanotechnol. **9**, 794 (2014).

[16] D. Pesin and A. H. MacDonald, “Spintronics and pseudospintronics in graphene and topological insulators”, Nat. Mater. **11**, 409 (2012).

[17] N. Tombros, C. Józsa, M. Popinciuc, H. T. Jonkman, and B. J. van Wees, “Electronic spin transport and spin precession in single graphene layers at room temperature”, Nature **448**, 571 (2007).

[18] M. Drögeler, C. Franzen, F. Volmer, T. Pohlmann, L. Banszerus, M. Wolter, K. Watanabe, T. Taniguchi, C. Stampfer, and B. Beschoten, “Spin lifetimes exceeding 12 ns in graphene nonlocal spin valve devices”, Nano Lett. **16 (6)**, 3533 (2016).

[19] N. Tombros, S. Tanabe, A. Veligura, C. Józsa, M. Popinciuc, H. T. Jonkman, and B. J. van Wees, “Anisotropic spin relaxation in graphene”, Phys. Rev. Lett. **101**, 046601 (2008).

[20] B. Raes, A. W. Cummings, F. Bonell, M. V. Costache, J. F. Sierra, S. Roche, and S. O. Valenzuela, “Spin precession in anisotropic media”, Phys. Rev. B **95**, 085403 (2017).

[21] H. P. Boehm, R. Setton, and E. Stumpp, “Nomenclature and terminology of graphite intercalation compounds”, Pure & Appl. Chem. **66**, 1893 (1994).

[22] H. P. Boehm, A. Clauss, G. O. Fischer, and U. Hofmann, “Dünnste Kohlenstoff-Folien”, Z. Naturforschg. **17b**, 150 (1962).

[23] H. P. Boehm, “Graphene - How a laboratory curiosity suddenly became extremely interesting”, Angew. Chem. Int. Ed. **49**, 9332 (2010).

[24] K. S. Novoselov, A. K. Geim, S. V. Morozov, D. Jiang, Y. Zhang, S. V. Dubonos, I. V. Grigorieva, and A. A. Firsov, “Electric field effect in atomically thin carbon films”, Science **306**, 666 (2004).

[25] A. K. Geim, “Graphene: status and prospects”, Science **324**, 1530 (2009).

[26] D. R. Cooper, B. D’Anjou, N. Ghattamaneni, B. Harack, M. Hilke, A. Horth, N. Majlis, M. Massicotte, L. Vandsburger, E. Whiteway, and V. Yu, “Experimental review of graphene”, ISRN Condensed Matter Physics **2012**, 56 (2012).

[27] A. H. Castro Neto, F. Guinea, N. M. R. Peres, K. S. Novoselov, and A. K. Geim, “The electronic properties of graphene”, Rev. Mod. Phys. **81**, 109 (2009).

[28] S. Das Sarma, S. Adam, E. H. Hwang, and E. Rossi, “Electronic transport in two-dimensional graphene”, Rev. Mod. Phys. **83**, 407 (2011).

[29] N. M. R. Peres, “Colloquium: The transport properties of graphene: An introduction”, Rev. Mod. Phys. **82**, 2673 (2010).

[30] A. Sandner, "High-mobility graphene in 2d periodic potentials", dissertation (Universität Regensburg, 2017).

[31] K. S. Novoselov, "Graphen: Materialien im Flachland (Nobel-Aufsatz)", Angew. Chem. **123**, 7123 (2011).

[32] K. S. Novoselov, A. K. Geim, S. V. Morozov, D. Jiang, M. I. Katsnelson, I. V. Grigorieva, S. V. Dubonos, and A. A. Firsov, "Two-dimensional gas of massless Dirac fermions in graphene", Nature **438**, 197 (2005).

[33] A. K. Geim and K. S. Novoselov, "The rise of graphene", Nat. Mater. **6**, 183 (2007).

[34] S. Blundell, "Magnetism in condensed matter. (Oxford Master Series in Physics)", Oxford University Press, USA (2001).

[35] J. Fabian, A. Matos-Abiague, C. Ertler, P. Stano, and I. Žutić, "Semiconductor spintronics", Acta Phys. Slovaca **57**, 565 (2007).

[36] J. Fabian and I. Žutić, "The standard model of spin injection", arXiv:0903.2500 (2009).

[37] S. Parkin, X. Jiang, C. Kaiser, A. Panchula, K. Roche, and M. Samant, "Magnetically engineered spintronic sensors and memory", Proc. IEEE **91**, 661 (2003).

[38] M. N. Baibich, J. M. Broto, A. Fert, F. N. Van Dau, F. Petroff, P. Etienne, G. Creuzet, A. Friederich, and J. Chazelas, "Giant magnetoresistance of (001)Fe/(001)Cr magnetic superlattices", Phys. Rev. Lett. **61**, 2472 (1988).

[39] G. Binasch, P. Grünberg, F. Saurenbach, and W. Zinn, "Enhanced magnetoresistance in layered magnetic structures with antiferromagnetic interlayer exchange", Phys. Rev. B **39**, 4828 (1989).

[40] N. F. Mott, "The electrical conductivity of transition metals", Proceedings of the Royal Society A **153**, 699 (1936).

[41] E. Villamor, M. Isasa, L. E. Hueso, and F. Casanova, "Temperature dependence of spin polarization in ferromagnetic metals using lateral spin valves", Phys. Rev. B **88**, 184411 (2013).

[42] T. Maassen, "Electron spin transport in graphene-based devices", dissertation (University of Groningen, 2013).

[43] A. G. Aronov, "Spin injection in metals and polarization of nuclei", Zh. Eksp. Teor. Fiz. Pisma Red. **24**, 37 (1976).

[44] G. Schmidt, D. Ferrand, L. W. Molenkamp, A. T. Filip, and B. J. van Wees, "Fundamental obstacle for electrical spin injection from a ferromagnetic metal into a diffusive semiconductor", Phys. Rev. B **62**, R4790 (2000).

[45] D. Pachniowski, "Optimierung der Spininjektion in Graphen mit Hilfe von Tunnelbarrieren", unpublished, diploma thesis (Universität Regensburg, 2011).

[46] M. Johnson and R. H. Silsbee, "Interfacial charge-spin coupling: Injection and detection of spin magnetization in metals", Phys. Rev. Lett. **55**, 1790 (1985).

[47] B. Endres, M. Ciorga, R. Wagner, S. Ringer, M. Utz, D. Bougeard, D. Weiss, C. H. Back, and G. Bayreuther, “Nonuniform current and spin accumulation in a 1 μm thick n-GaAs channel”, Appl. Phys. Lett. **100**, 092405 (2012).

[48] R. H. Silsbee, “Novel method for the study of spin transport in conductors”, Bull. Magn. Reson. **2**, 284 (1980).

[49] M. Gmitra, S. Konschuh, C. Ertler, C. Ambrosch-Draxl, and J. Fabian, “Band-structure topologies of graphene: Spin-orbit coupling effects from first principles”, Phys. Rev. B **80**, 235431 (2009).

[50] D. Kochan, S. Irmer, and J. Fabian, “Model spin-orbit coupling Hamiltonians for graphene systems”, Phys. Rev. B **95**, 165415 (2017).

[51] D. Huertas-Hernando, F. Guinea, and A. Brataas, “Spin-orbit coupling in curved graphene, fullerenes, nanotubes, and nanotube caps”, Phys. Rev. B **74**, 155426 (2006).

[52] M. Drögeler, F. Volmer, M. Wolter, B. Terrés, K. Watanabe, T. Taniguchi, G. Güntherodt, C. Stampfer, and B. Beschoten, “Nanosecond spin lifetimes in single- and few-layer graphene-hBN heterostructures at room temperature”, Nano Lett. **14**, 6050 (2014).

[53] M. H. D. Guimarães, P. J. Zomer, J. Ingla-Aynés, J. C. Brant, N. Tombros, and B. J. van Wees, “Controlling spin relaxation in hexagonal BN-encapsulated graphene with a transverse electric field”, Phys. Rev. Lett. **113**, 086602 (2014).

[54] S. Singh, J. Katoch, J. Xu, C. Tan, T. Zhu, W. Amamou, J. Hone, and R. Kawakami, “Nanosecond spin relaxation times in single layer graphene spin valves with hexagonal boron nitride tunnel barriers”, Appl. Phys. Lett. **109**, 122411 (2016).

[55] A. H. Castro Neto and F. Guinea, “Impurity-induced spin-orbit coupling in graphene”, Phys. Rev. Lett. **103**, 026804 (2009).

[56] C. Ertler, S. Konschuh, M. Gmitra, and J. Fabian, “Electron spin relaxation in graphene: the role of the substrate”, Phys. Rev. B **80**, 041405 (2009).

[57] F. Volmer, M. Drögeler, G. Güntherodt, C. Stampfer, and B. Beschoten, “Spin and charge transport in graphene-based spin transport devices with Co/MgO spin injection and spin detection electrodes”, Synth. Met. **210**, 42 (2015).

[58] A. Avsar, I. J. Vera-Marun, J. Y. Tan, G. K. W. Koon, K. Watanabe, T. Taniguchi, S. Adam, and B. Ozyilmaz, “Electronic spin transport in dual-gated bilayer graphene”, NPG Asia Mater. **8**, e274 (2016).

[59] M. Gurram, S. Omar, S. Zihlmann, P. Makk, C. Schönenberger, and B. J. van Wees, “Spin transport in fully hexagonal boron nitride encapsulated graphene”, Phys. Rev. B **93**, 115441 (2016).

[60] D. Huertas-Hernando, F. Guinea, and A. Brataas, “Spin-orbit-mediated spin relaxation in graphene”, Phys. Rev. Lett. **103**, 146801 (2009).

[61] D. Kochan, S. Irmer, M. Gmitra, and J. Fabian, “Resonant scattering by magnetic impurities as a model for spin relaxation in bilayer graphene”, Phys. Rev. Lett. **115**, 196601 (2015).

[62] T. Maassen, I. J. Vera-Marun, M. H. D. Guimarães, and B. J. van Wees, “Contact-induced spin relaxation in hanle spin precession measurements”, Phys. Rev. B **86**, 235408 (2012).

[63] F. Volmer, M. Drögeler, E. Maynicke, N. von den Driesch, M. L. Boschen, G. Güntherodt, and B. Beschoten, “Role of MgO barriers for spin and charge transport in Co/MgO/graphene nonlocal spin-valve devices”, Phys. Rev. B **88**, 161405 (2013).

[64] F. Volmer, M. Drögeler, E. Maynicke, N. von den Driesch, M. L. Boschen, G. Güntherodt, C. Stampfer, and B. Beschoten, “Suppression of contact-induced spin dephasing in graphene/MgO/Co spin-valve devices by successive oxygen treatments”, Phys. Rev. B **90**, 165403 (2014).

[65] C. Józsa, T. Maassen, M. Popinciuc, P. J. Zomer, A. Veligura, H. T. Jonkman, and B. J. van Wees, “Linear scaling between momentum and spin scattering in graphene”, Phys. Rev. B **80**, 241403 (2009).

[66] P. J. Zomer, M. H. D. Guimarães, N. Tombros, and B. J. van Wees, “Long-distance spin transport in high-mobility graphene on hexagonal boron nitride”, Phys. Rev. B **86**, 161416 (2012).

[67] A. G. Swartz, J.-R. Chen, K. M. McCreary, P. M. Odenthal, W. Han, and R. K. Kawakami, “Effect of in situ deposition of Mg adatoms on spin relaxation in graphene”, Phys. Rev. B **87**, 075455 (2013).

[68] R. J. Elliott, “Theory of the effect of spin-orbit coupling on magnetic resonance in some semiconductors”, Phys. Rev. **96**, 266 (1954).

[69] Y. Yafet, “g factors and spin-lattice relaxation of conduction electrons”, Solid State Physics **14**, 1 (1963).

[70] D. C. Elias, R. V. Gorbachev, A. S. Mayorov, S. V. Morozov, A. A. Zhukov, P. Blake, L. A. Ponomarenko, I. V. Grigorieva, K. S. Novoselov, F. Guinea, and A. K. Geim, “Dirac cones reshaped by interaction effects in suspended graphene”, Nat. Phys. **7**, 701 (2011).

[71] D. Van Tuan, F. Ortmann, A. W. Cummings, D. Soriano, and S. Roche, “Spin dynamics and relaxation in graphene dictated by electron-hole puddles”, Sci. Rep. **6**, 21046 (2016).

[72] M. I. Dyakonov and V. I. Perel, “Spin relaxation of conduction electrons in noncentrosymmetric semiconductors”, Sov. Phys. Solid State **13**, 3023 (1971).

[73] D. Kochan, *Private communication.*

[74] S. Adam, P. W. Brouwer, and S. Das Sarma, “Crossover from quantum to Boltzmann transport in graphene”, Phys. Rev. B **79**, 201404 (2009).

[75] M. Popinciuc, C. Józsa, P. J. Zomer, N. Tombros, A. Veligura, H. T. Jonkman, and B. J. van Wees, "Electronic spin transport in graphene field-effect transistors", Phys. Rev. B **80**, 214427 (2009).

[76] B. Raes, J. E. Scheerder, M. V. Costache, F. Bonell, J. F. Sierra, J. Cuppens, J. Van de Vondel, and S. O. Valenzuela, "Determination of the spin-lifetime anisotropy in graphene using oblique spin precession", Nat. Commun. **7**, 11444 (2016).

[77] F. Volmer, M. Drögeler, T. Pohlmann, G. Güntherodt, C. Stampfer, and B. Beschoten, "Contact-induced charge contributions to non-local spin transport measurements in Co/MgO/graphene devices", 2D Materials **2**, 024001 (2015).

[78] D. Schiermeier, "Simulationen zum Spintransport mit räumlich veränderlichen Parametern", unpublished, bachelor thesis (Universität Regensburg, 2018).

[79] L. A. Benítez, J. F. Sierra, W. Savero Torres, A. Arrighi, F. Bonell, M. V. Costache, and S. O. Valenzuela, "Strongly anisotropic spin relaxation in graphene-transition metal dichalcogenide heterostructures at room temperature", Nat. Phys. **14**, 303 (2018).

[80] T. S. Ghiasi, J. Ingla-Aynés, A. A. Kaverzin, and B. J. van Wees, "Large proximity-induced spin lifetime anisotropy in transition-metal dichalcogenide/graphene heterostructures", Nano Lett. **17**, 7528 (2017).

[81] L. Bachhuber, "Magnetotransportmessungen an hochwertigen Graphitkristallen", unpublished, bachelor thesis (Universität Regensburg, 2014).

[82] J. Kamann, *Private communication.*

[83] M. Kadur, "Morphologie dünner Magnesiumoxidschichten auf Graphen", unpublished, bachelor thesis (Universität Regensburg, 2013).

[84] F. Volmer, "Einfluss der Oxid-Barriere auf den Spin- und Ladungstransport in Graphen/MgO/Co-Strukturen", dissertation (RWTH Aachen University, 2015).

[85] P. Liu, T. Kendelewicz, and G. E. Brown, "Reaction of water with MgO(100) surfaces. Part II: Synchrotron photoemission studies of defective surfaces", Surface Science **412–413**, 315 (1998).

[86] E. Carrasco, M. A. Brown, M. Sterrer, H.-J. Freund, K. Kwapien, M. Sierka, and J. Sauer, "Thickness-dependent hydroxylation of MgO(001) thin films", J. Phys. Chem. C **114**, 18207 (2010).

[87] H. S. Craft, R. Collazo, M. D. Losego, Z. Sitar, and J.-P. Maria, "Surface water reactivity of polycrystalline MgO and CaO films investigated using x-ray photoelectron spectroscopy", J. Vac. Sci. Technol. A **26**, 1507 (2008).

[88] W. Han, K. Pi, K. M. McCreary, Y. Li, J. J. I. Wong, A. G. Swartz, and R. K. Kawakami, "Tunneling spin injection into single layer graphene", Phys. Rev. Lett. **105**, 167202 (2010).

[89] W. H. Wang, W. Han, K. Pi, K. M. McCreary, F. Miao, W. Bao, C. N. Lau, and R. K. Kawakami, “Growth of atomically smooth MgO films on graphene by molecular beam epitaxy”, Appl. Phys. Lett. **93**, 183107 (2008).

[90] N. Tombros, “Electron spin transport in graphene and carbon nanotubes”, dissertation (University of Groningen, 2008).

[91] P. Nagler, “Einfluss der Prozess-Parameter auf die Morphologie dünner Aluminiumoxidschichten auf Graphen”, unpublished, bachelor thesis (Universität Regensburg, 2012).

[92] U. Stöberl, U. Wurstbauer, W. Wegscheider, D. Weiss, and J. Eroms, “Morphology and flexibility of graphene and few-layer graphene on various substrates”, Appl. Phys. Lett. **93**, 051906 (2008).

[93] Z. Cheng, Q. Zhou, C. Wang, Q. Li, C. Wang, and Y. Fang, “Toward intrinsic graphene surfaces: A systematic study on thermal annealing and wet-chemical treatment of SiO_2-supported graphene devices”, Nano Lett. **11**, 767 (2011).

[94] B. Birkner, “Spintransport in graphen”, dissertation (Universität Regensburg, 2014).

[95] J. Balakrishnan, “Spin transport studies in graphen”, dissertation (National University of Singapore, 2013).

[96] S. Isogami, M. Tsunoda, K. Komagaki, K. Sunaga, Y. Uehara, M. Sato, T. Miyajima, and M. Takahash, “In situ heat treatment of ultrathin MgO layer for giant magnetoresistance ratio with low resistance area product in CoFeB/MgO/CoFeB magnetic tunnel junctions”, APL **93**, 192109 (2008).

[97] M. H. D. Guimarães, J. J. van den Berg, I. J. Vera-Marun, P. J. Zomer, and B. J. van Wees, “Spin transport in graphene nanostructures”, Phys. Rev. B **90**, 235428 (2014).

[98] I. Vaquila, M. C. G. Passeggi, and J. Ferrón, “Oxidation process in titanium thin films”, Phys. Rev. B **55**, 13925 (1997).

[99] J.-G. Zhu and C. Park, “Magnetic tunnel junctions”, Materials Today **9**, 36 (2006).

[100] R. M. Bozorth, P. A. Wolff, D. D. Davis, V. B. Compton, and J. H Wernick, “Ferromagnetism in dilute solutions of cobalt in palladium”, Phys. Rev. **122**, 1157 (1961).

[101] R. Hössl, “Experimente zur Spininjektion an lateralen Fe/GaAs/Fe-Strukturen”, unpublished, diploma thesis (Universität Regensburg, 2007).

[102] B. Klinger, “Untersuchung von Gatedurchbrüchen an Siliziumdioxid”, unpublished, Zulassungsarbeit (Universität Regensburg, 2017).

[103] S. Hartl, “Finite-Elemente-Simulation von Spin-Transport in Graphen”, unpublished, bachelor thesis (Universität Regensburg, 2016).

[104] H. X. Yang, M. Chshiev, B. Dieny, J. H. Lee, A. Manchon, and K. H. Shin, “First-principles investigation of the very large perpendicular magnetic anisotropy at Fe|MgO and Co|MgO interfaces”, Phys. Rev. B **84**, 054401 (2011).

[105] S. O. Valenzuela and M. Tinkham, “Direct electronic measurement of the spin hall effect”, Nature **442**, 176 (2006).

[106] V. F. Motsnyi, P. Van Dorpe, W. Van Roy, E. Goovaerts, V. I. Safarov, G. Borghs, and J. De Boeck, “Optical investigation of electrical spin injection into semiconductors”, Phys. Rev. B **68**, 245319 (2003).

[107] A. Avsar, J. Y. Tan, M. Kurpas, M. Gmitra, K. Watanabe, T. Taniguchi, J. Fabian, and B. Ozyilmaz, “Gate-tunable black phosphorus spin valve with nanosecond spin lifetimes”, Nat. Phys. **13**, 888 (2017).

[108] H. C. Koo, J. H. Kwon, J. Eom, J. Chang, S. H. Han, and M. Johnson, “Control of spin precession in a spin-injected field effect transistor”, Science **325**, 1515 (2009).

[109] M. Sharma, S. X. Wang, and J. H. Nickel, “Inversion of spin polarization and tunneling magnetoresistance in spin-dependent tunneling junctions”, Phys. Rev. Lett. **82**, 616 (1999).

[110] J. M. De Teresa, A. Barthélémy, A. Fert, J. P. Contour, F. Montaigne, and P. Seneor, “Role of metal-oxide interface in determining the spin polarization of magnetic tunnel junctions”, Science **286**, 507 (1999).

[111] C. Tiusan, F. Greullet, M. Hehn, F. Montaigne, S. Andrieu, and A. Schuhl, “Spin tunnelling phenomena in single-crystal magnetic tunnel junction systems”, J. Phys.: Condens. Matter **19**, 165201 (2007).

[112] F. Godel, M. Venkata Kamalakar, B. Doudin, Y. Henry, D. Halley, and J.-F. Dayen, “Voltage-controlled inversion of tunnel magnetoresistance in epitaxial nickel/graphene/MgO/cobalt junctions”, Appl. Phys. Lett. **105**, 152407 (2014).

[113] P. U. Asshoff, J. L. Sambricio, A. P. Rooney, S. Slizovskiy, A. Mishchenko, A. M. Rakowski, E. W. Hill, A. K. Geim, S. J. Haigh, V. I. Falko, I. J. Vera-Marun, and I. V. Grigorieva, “Magnetoresistance of vertical Co-graphene-NiFe junctions controlled by charge transfer and proximity-induced spin splitting in graphene”, 2D Materials **4**, 031004 (2017).

[114] M. V. Kamalakar, A. Dankert, P. J. Kelly, and S. P. Dash, “Inversion of spin signal and spin filtering in ferromagnet|hexagonal boron nitride-graphene van der Waals heterostructures”, Sci. Rep. **6**, 21168 (2016).

[115] M. Gurram, S. Omar, and B. J. van Wees, “Bias induced up to 100% spin-injection and detection polarizations in ferromagnet/bilayer-hBN/graphene/hBN heterostructures”, Nat. Commun. **8**, 248 (2017).

[116] C. Heiliger, P. Zahn, B. Y. Yavorsky, and I. Mertig, “Influence of the interface structure on the bias dependence of tunneling magnetoresistance”, Phys. Rev. B **72**, 180406 (2005).

[117] E. Y. Tsymbal, A. Sokolov, I. F. Sabirianov, and B. Doudin, “Resonant inversion of tunneling magnetoresistance”, Phys. Rev. Lett. **90**, 186602 (2003).

[118] P. Lazić, K. D. Belashchenko, and I. Žutić, “Effective gating and tunable magnetic proximity effects in two-dimensional heterostructures”, Phys. Rev. B **93**, 241401 (2016).

[119] P. Blaha, K. Schwarz, and P. H. Dederichs, “Electronic structure of hcp metals”, Phys. Rev. B **38**, 9368 (1988).

[120] I. I. Mazin, “How to define and calculate the degree of spin polarization in ferromagnets”, Phys. Rev. Lett. **83**, 1427 (1999).

[121] G. M. Sipahi, I. Žutić, N. Atodiresei, R. K. Kawakami, and P. Lazić, “Spin polarization of Co(0001)/graphene junctions from first principles”, J. Phys.: Condens. Matter **26**, 104204 (2014).

[122] J. Moser, M. Zenger, C. Gerl, D. Schuh, R. Meier, P. Chen, G. Bayreuther, W. Wegscheider, D. Weiss, C.-H. Lai, R.-T. Huang, M. Kosuth, and H. Ebert, “Bias dependent inversion of tunneling magnetoresistance in fe/gaas/fe tunnel junctions”, App. Phys. Lett. **89**, 162106 (2006).

[123] X. Lou, C. Adelmann, S. A. Crooker, E. S. Garlid, J. Zhang, K. S. M. Reddy, S. D. Flexner, C. J. Palmstrøm, and P. A. Crowell, “Electrical detection of spin transport in lateral ferromagnet-semiconductor devices”, Nat. Phys. **3**, 197 (2007).

[124] C. Kim and Y.-C. Chung, “Structural effect of junction interface on magnetic properties in a Co/MgO/Co system: First-principles calculations”, Journal of Applied Physics **103**, 054309 (2008).